Numerical simulation of elastic wave propagation in textile composite structures

by Victor Thierry

A thesis submitted for the degree of Doctor of Philosophy

the Composites Research Group &
the Institute for Aerospace Technology
University of Nottingham
United Kingdom

May 2020

SUPERVISOR
Dr. Dimitrios Chronopoulos

INTERNAL ASSESSOR
Dr. Gabriele Gradoni

EXTERNAL ASSESSOR
Dr. Matthieu Gresil

Abstract

This manuscript presents a novel approach allowing damped ultrasonic wave propagation analysis of textile composite structures modelled at a mesoscopic level (i.e. modelling the yarns and matrix distinctively). Current modelling approaches rely on material homogenisation for analysis at a macroscopic scale and thus overlook the effect of textile architecture on wave propagation. This work aims at predicting wave propagation characteristics in damped textile composite structures and the induced complex phenomena for applications in structural health monitoring.

The developed methodology involves mesoscale modelling of a textile composite structure period using a specialised textile modeller for pre-processing as well as conventional finite element methods. This is combined with the periodic structure theory as well as a mode-based reduction method named Craig-Bampton allowing for solving a reduced eigenproblem deriving from the equation of motion. A multiscale approach is used throughout the thesis to enable the comparison of standard wave propagation analysis of composite structures, using homogenised properties, with the more complex analysis proposed in this thesis. The need for this methodology is demonstrated as well as its validity.

The first axis of this thesis describes the methodology for undamped wave propagation analysis in textile composites. Its advantages, such as the prediction of complex phenomena and the possible applications, are thoroughly described and issues discussed. Its increased accuracy over macroscale prediction methods is exposed. A second axis of the thesis is experimental validation of the methodology by means of linear scans of waves measured by a laser vibrometer and generated by a piezoelectric transducer in 3D woven composite samples. It is shown that the numerical mesoscale methodology provides accurate predictions. The third axis is the prediction of dispersion characteristics in large layered assemblies of textile composites. An attempt toward homogenisation of textile composites using a dispersion curves inversion technique based on genetic algorithms is proposed for this purpose. It is concluded that complex textile composites cannot be approximated by simple macroscale models. The last axis of the thesis introduces a damping model to predict the frequency dependent loss factor of waves propagating in these textile composite structures. The strong influence of mesoscale architecture over loss factor is demonstrated.

Declaration

I, Victor Thierry, declare that this thesis entitled 'Numerical simulation of elastic wave propagation in textile composite structures' is an original work of my own.

Acknowledgements

I wish to thank Dr. Dimitrios Chronopoulos for his great guidance over the years. His excellent advice and interesting suggestions as a supervisor kept me inspired and helped me throughout my research. Special thanks go to the Composites Research Group members and especially to Dr. Louise Brown who gave us advice on TexGen, to Dr. Andreas Endruweit who gracefully provided us the dry fabrics for our experiments and to the lab technicians who helped us manufacture the composite samples.

I also wish to particularly acknowledge Dr. Olivier Mesnil for supervising my placement and for our many stimulating discussions. I also wish to thank all those who helped me navigate through this secondment at the CEA List, and in particular Dr. Arnaud Recoquillay, Dr. Tom Druet, Prof. Alain Lhemery and Dr. Bastien Chapuis.

I would like to thank all my colleagues and friends at the Institute for Aerospace Technology with whom I spent some happy years.

Of course I want to express my sincere gratitude to my parents who supported me over the years without failure. A very special 'thank you' to Floriane with whom I went through the adventure of the PhD with many ups and downs but always aiming for the best.

This work is funded by the INNOVATIVE doctoral programme. The INNOVATIVE programme is partially funded by the Marie Curie Initial Training Networks (ITN) action (project number 665468) and partially by the Institute for Aerospace Technology (IAT) at the University of Nottingham. The author is very grateful for the support provided.

We are grateful for access to the University of Nottingham's Augusta HPC service.

Contents

Nomenclature

1D	One-Dimensional
2D	Two-Dimensional
BZ	Brillouin Zone
CFRP	Carbon Fibre Reinforced Polymer
CMS	Component Mode Synthesis
CPU	Central Processing Unit
DoF	Degree of Freedom
DSM	Dynamic Stiffness Method
FE	Finite Element
FEA	Finite Element Analysis
FFT	Fast Fourier Transform
IBZ	Irreducible Brillouin Zone
LDV	Laser Doppler Vibrometer
MAC	Modal Assurance Criterion
NDE	Non-Destructive Evaluation
PST	Periodic Structure Theory (also called Bloch-Floquet theorem)
PZT	Piezoelectric Transducer
RTM	Resin Transfer Moulding

RVE	Representative Volume Element
SAFE	Semi-Analytical Finite Element
SHM	Structural Health Monitoring
WFE	Wave and Finite Element

Chapter 1

Introduction

World air traffic is growing fast and has more than ever non-negligible impact on the environment. Governments have set ambitious targets for a growth of the industry in a safe and sustainable way using new technologies. Composite materials are made of multiple constituent materials for customised mechanical properties. Fibre reinforced polymers in particular are lightweight and thus are key contributors for more sustainable flights. And even though the first motivation for using these materials lay in operational cost savings due to the reduced fuel consumption, they serve both purposes well. Besides being lightweight, composites also have excellent mechanical properties when compared with traditional materials such as aluminium alloys etc. (e.g. typical tensile strength value for Aluminium Alloy 6061-T6 is 310 MPa, while it can easily reach 600 MPa in the direction of the fibres for a [0/90] carbon fibre fabric composite).

The interest in textile composites over laminates lies in their high resistance to out-of-plane loading and impact where laminates are easily subjected to delamination, such as low speed impact from a dropped tool or high speed hail impact. Another advantage is that complex components are easier to manufacture using a textile reinforcement than stacking multiple thin layers of laminates. However, these new technological improvements do not come without challenges. Some related to future developments, some other can be grouped as safety concerns. One is intrinsic to the early age of composite structures in the aircraft industry. Indeed, Non-Destructive Evaluation (NDE) techniques for these materials have not yet reached their maturity. Another issue lies in the fact that composite materials may be affected by internal damage without showing evidence on the surface, making visual inspection much less effective.

In order to provide safer flights, efforts need to be made on controlling and monitoring techniques for composite structures. Structural Health Monitoring (SHM) is the process of performing non-destructive testing, evaluation and inspection of the structure during flight for damage occurrence and evolution monitoring . This is done by means of embedded sensors, possibly smart materials, data transmission, computational modelling, and processing ability inside the structures [1, 2]. It allows for reducing the operational costs by reducing the aircraft ground handling time and allows for the earliest possible detection of damage as well. For these reasons intensive research is being conducted on SHM of composite structures. One inspection technique gaining in popularity for SHM is ultrasonic guided waves spectroscopy [1, 2], these waves carry frequency that generally exceeds 20kHz and are also designated as Lamb waves. Guided waves are of interest because they can travel over long distances in a thin-walled structure. This ultrasonic inspection technique is already very popular for pipeline monitoring for example [3, 4, 5]. Waves in thin-walled structure are dispersive, so the velocity (and thus time-of-flight) of a wave depends on the frequency. These primary characteristics of waves are called dispersion relations and need to be known in order to apply guided wave techniques.

There exist many analytic and numerical models to obtain the dispersion relations of homogeneous media [6]. However, considering textile composites as homogeneous materials is an oversimplification for dynamical analysis as the internal geometries and mechanical properties influence the way waves propagate and can even induce strange phenomena such as stop-bands (i.e. frequency ranges at which a wave is not allowed to propagate). On the other hand, considering the microstructure of a composite, i.e. considering its fibres independently, would be prohibitive and useless as this scale is negligible in comparison to the wavelengths induced by the frequencies of interest. The intermediate scale is called mesoscopic and is of interest as it takes into account the yarns architecture embedded in the matrix, thus the scale does not oversimplify the geometry nor produce overly expensive computations. Up to now, no methodology had been proposed to obtain the dispersion characteristics in textile composites considered at a mesoscopic scale. And while analytical solutions would be utterly complex to describe this problem, neither it is possible to perform the analysis using a full transient Finite Element (FE) methodology for such a complex problem and large structures.

A great advantage of textile composites is in their periodicity as it allows for applying the Bloch-Floquet wave theory, also called the Periodic Structure Theory (PST), to reduce the problem size to its smallest representative period. Moreover, the inherent periodicity of textile composites has a great influence on the way waves propagate such as constraining the direction of propagation or creating stop-bands, thus considering a textile composite at its period level reveals these phenomena. Semi-analytical methods that take advantage of these periodic properties have been developed as alternatives to analytical or FE methods for dispersion characterisation and often combine the advantages of both. The Wave Finite Element (WFE) method in particular uses both the Bloch-Floquet wave theory and existing FE libraries to simplify the analysis and obtain the dispersion characteristics of complex periodic structures in a robust manner.

In this thesis, methodologies for the numerical simulation of elastic wave propagation in textile composite structures are proposed. Chapter 2 is devoted to a review of the literature, to provide the reader with enough material, context and references to understand and tackle the methodologies and problems presented in following chapters. Chapter 3 describes the methodology combining mesoscale FE modelling of composites and the PST, leading to an investigation of dispersion characteristics in undamped textile composite structures. The mesoscopic properties of the material are taken into account for the first time for this type of analysis. It is shown that standard homogenised composite structure modelling provides inaccurate predictions and that mesoscale modelling is needed. The following chapter (Chapter 4) applies and compares the numerical methodology to experimental results for complex 3D woven composites. Chapter 5 attempts the reconstruction of the elastic moduli of composite materials by inversion of their dispersion curves in order to benefit from the accuracy of predictions provided by the mesoscale methodology and to take advantage of the rapid computational properties of macroscale methodologies. Chapter 6 introduces fast and accurate prediction of the damping properties associated with the dispersion characteristics of these textile composites at a mesoscopic scale. Finally, chapter 7 provides concluding remarks and reflections on possible future work.

Some of the results presented in this thesis have led to publications:

- Chapter 3: V. Thierry, L. Brown and D. Chronopoulos, "Multi-scale wave propagation modelling for two-dimensional periodic textile composites," *Composites Part B: Engineering*, vol. 150, pp.144-156, 2018.

- Chapter 4: V. Thierry, O. Mesnil and D. Chronopoulos, "Experimental and numerical determination of the wave dispersion characteristics of complex 3D woven composites," *Ultrasonics*, vol. 103, p. 106068, 2020.

- Chapter 6: V. Thierry and D. Chronopoulos, "The impact of mesoscale textile architecture on the structural damping in composite structures," *Composite Structures*, vol. 249, p. 112475, 2020.

Chapter 2

Literature review

2.1 Multiscale modelling of textile composites

Composite materials are engineered materials composed of more than one constituent materials. Its constituent materials (or components) remain distinct at a microscale level while forming a single material at a macroscale level. The constituent materials have different characteristics and their assembly should form a material with new or improved characteristics. The components of a textile composite in particular are the fabric used as reinforcement and a binding polymer used as matrix. A fabric is built up by a number of yarns assembled together in a self-supporting architecture. The fabric is arranged in the desired shape and the polymer is injected within the fabric. Once impregnated, pressure is applied and the temperature is elevated in order to initiate and maintaining the chemical reaction (in case of a thermoset) which cures the binding polymer [7]. This hardened material made of fabric and cured polymer is called a textile composite. The yarns themselves are composed of an assembly of unidirectional fibres. Thus, once the composite is cured, a yarn is considered as a composite as it contains two types of components: the fibres and a matrix.

The diameter of a fibre is measured in micrometer (typical value for a carbon fibre would be around 7μm). A yarn is composed of thousands of fibres (typically 1K, 3K, 6K or 12K) and the yarns assembly forms a textile reinforcement. The most popular materials for aerospace composites are carbon fibres for the reinforcement and epoxy resin as binding polymer and as a whole are designated as

Carbon Fibre Reinforced Polymers (CFRPs). Some classical textile architectures for composites are the braided, stitched, knitted, 2D woven and 3D woven fabrics [8] (see Fig.2.1), all of which have found applications in the aerospace industry (e.g. woven reinforcements have been used to manufacture rotor blades, fasteners, engine mounts and flaps [8], stiffened panels have been made with knitted and braided reinforcements etc. [9]).

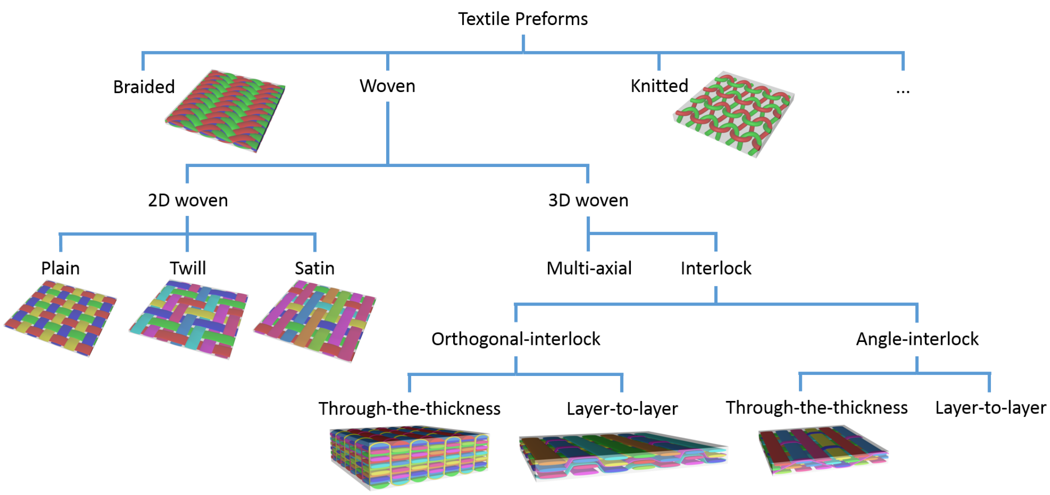

Figure 2.1: Textile patterns adapted from [10] and illustrations generated with TexGen.

These structures are complex at different scale levels and thus the prediction of their dynamic behaviour is complicated. Composite materials scale levels are hierarchical, the nanoscale is the lowest and is the level at which the chemical interface between the matrix and the fibres is studied. It is important as a high-quality interfacing ensures an effective stress transfer from the matrix to the fibres. In order to optimize the interfacial bonding, the fibre manufacturer applies a sizing treatment which enhance the covalent bonding between the fibres and the matrix, but also acts as an antistatic agent and a lubricant to ease textile processing [11]. The higher level is the microscale model which comprises the individual fibres (or filaments) in a matrix (see Fig.2.2). The next modelling scale level is the mesoscale model, and its components are the yarns forming the fabric and the matrix. At last, the highest level is the macroscale model which represents the structure as a whole. Deducing the characteristics of a scale level from its lower or higher scale level model is called a multiscale approach and it has become a standard for composites modelling [12, 13, 14, 15, 16].

Deducing the macroscale characteristics of a model from its lower scales models ('bottom-up' method) is called homogenisation. It presumes substitution of the heterogeneous structure by a homogeneous medium of equivalent mechanical properties. The concept of multiscale modelling is of the upmost importance as it is practically impossible to run a finite element simulation of large-scale structures other than using a macroscale model.

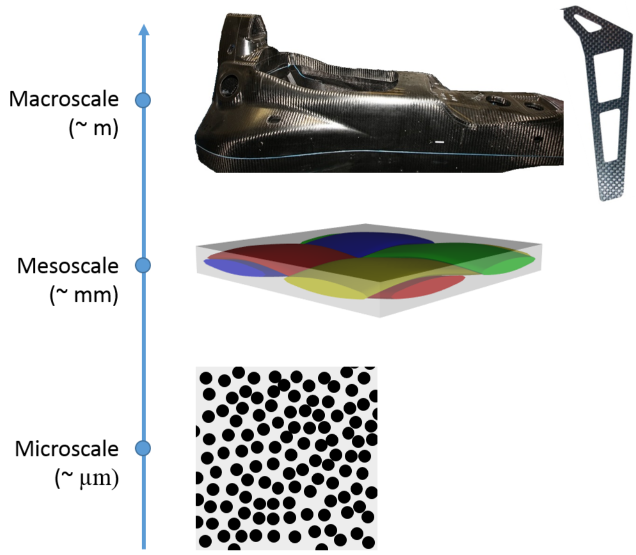

Figure 2.2: 'Bottom-up' multiscale appraoch adapted from [15].

A notion that is a cornerstone of multiscale approach is the Representative Volume Element (RVE). A RVE must feature all the characteristics intrinsic to a scale level so that it can be translated to a higher scale level. It should be large enough to feature all the geometrical specificities and small enough to avoid redundancies. If the medium is periodic, the RVE is called a unit cell and it represents one period of the pattern.

2.1.1 Microscale to mesoscale homogenisation

The microscale model of a composite is used to study the interaction between the numerous fibres and the matrix into which they are bounded. It aims at describing the behaviour of the higher scale level by studying the behaviour of the components. For a textile composite, this scale level is of interest in order to obtain the mechanical characteristics of an individual yarn. It is usually assumed that the fibres are of infinite length, straight, parallel to each other and have a circular cross-section [15]. The fibre material is often categorised as transversely isotropic while the matrix material is assumed to be isotropic. The assembly of fibre bundles oriented in more than one direction and embedded in a matrix material often results in a material that is orthotropic. The relation between stress (σ) and strain (ϵ), commonly known as Hooke's law, defines the compliance matrix S of a material: $\{\epsilon\} = [S]\{\sigma\}$. The compliance matrix of an orthotropic material requires nine independent variables (i.e. elastic constants) as shown in Eq.(2.1). Transversely isotropic materials are orthotropic materials with one axis of symmetry which reduces the number of independent variables necessary to define their constitutive matrices to five [11].

$$\begin{Bmatrix} \epsilon_{11} \\ \epsilon_{22} \\ \epsilon_{33} \\ \epsilon_{23} \\ \epsilon_{31} \\ \epsilon_{12} \end{Bmatrix} = \begin{bmatrix} \frac{1}{E_1} & -\frac{\nu_{21}}{E_2} & -\frac{\nu_{31}}{E_3} & 0 & 0 & 0 \\ -\frac{\nu_{12}}{E_1} & \frac{1}{E_2} & -\frac{\nu_{32}}{E_3} & 0 & 0 & 0 \\ -\frac{\nu_{13}}{E_1} & -\frac{\nu_{23}}{E_2} & \frac{1}{E_3} & 0 & 0 & 0 \\ 0 & 0 & 0 & \frac{1}{G_{23}} & 0 & 0 \\ 0 & 0 & 0 & 0 & \frac{1}{G_{13}} & 0 \\ 0 & 0 & 0 & 0 & 0 & \frac{1}{G_{12}} \end{bmatrix} \begin{Bmatrix} \sigma_{11} \\ \sigma_{22} \\ \sigma_{33} \\ \sigma_{23} \\ \sigma_{31} \\ \sigma_{12} \end{Bmatrix} \quad (2.1)$$

There exist many models for predicting the homogenised mechanical properties of a yarn composed of numerous fibres and a matrix, most of which give a set of five elastic moduli of a transversely isotropic material as result. The first attempts to correlate the mechanical properties of a composite and the properties of its components were named Rule Of Mixtures (ROM) and were developed by Voight [17] and later Reuss [18] in the early 20th centuries. In this approach, a perfect bonding between the fibres and the matrix is assumed and the volume fraction of each component is used as a contribution ratio (see Table 2.1) (the fibre volume fraction of a textile composite is typically situated between 0.5 and 0.6 [14, 19, 20] but is strongly dependent on the compression level). Voigt's model assumes iso-strain situation in the composite (fibres and matrix) along the fibre direction, while Reuss model assumes iso-stress situation in the composite normal to the fibre direction (see Fig.2.3).

However, these formulae do not provide a good agreement with experimental results except for the Young's modulus in the fibre direction (E_{11}). The next

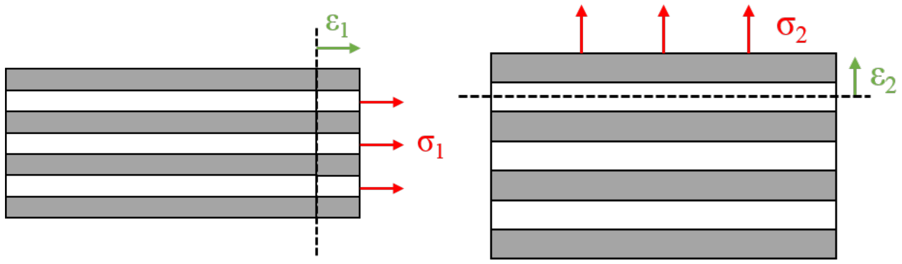

Figure 2.3: Voigt-Reuss ROM hypotheses (a) Isostrain method (b) Isostress method.

attempt was made by Hashin and Rosen in 1964 [21], the fibre and matrix are modelled as a concentric assembly (fibre at the core and matrix around). This two phases model is called the Composite Cylindrical Assemblage Model (CCAM) and it provides an improved formulation for the shear modulus G_{12} while being still distant from the experimental data, Christensen and Lo [22] later developed the Generalised Self Consistent Method (GSCM) which is a three phases model (see Fig.2.4) and gives the same solutions than the CCAM for four of the moduli but gives a better prediction for the transverse shear modulus G_{23}.

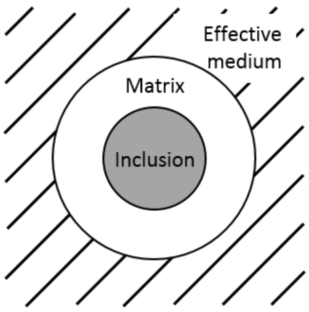

Figure 2.4: Generalized Self Consistent Model.

The Halpin-Tsai model was developed after the CCAM in 1967 [23]. This is a semi-empirical model that tends to correct the transverse Young's modulus E_{22} as well as the shear modulus G_{12} from the Voigt-Reuss model but uses its formulae for Young's modulus E_{11} and Poisson's ratio ν_{12}. Finally, another semi-empirical model was provided by Chamis in 1989 [24]. It uses the Voigt-Reuss formulae for E_{11} and ν_{12} as well but corrected the other moduli formulae in order to fit with experimental results (see Table 2.1). It is still widely used for its simplicity and relative accuracy.

	Voigt	**Reuss**	**Chamis**
E_{11}	$V^f E_{11}^f + V^m E^m$	same	same
ν_{12}	$V^f \nu_{12}^f + V^m \nu^m$	same	same
E_{22}		$\frac{E_{22}^f E^m}{V^f E^m + V^m E_{22}^f}$	$\frac{E^m}{1-\sqrt{V^f}(1-E^m/E_{22}^f)}$
G_{12}		$\frac{G_{12}^f G^m}{V^f G^m + V^m G_{12}^f}$	$\frac{G^m}{1-\sqrt{V^f}(1-G^m/G_{12}^f)}$
G_{23}			$\frac{G^m}{1-\sqrt{V^f}(1-G^m/G_{23}^f)}$
ν_{23}			$V^f \nu_{23}^f + (1-V^f)(2\nu_m - \frac{\nu_{12}}{E_{11}} E_{22})$

Table 2.1: Micromechanical models in the literature.

Another possibility is to use the FE method for the micromechanical analysis. The main advantages are the reliability and accuracy of the method but some disadvantages lie in the time needed for setting up the geometrical dimensions and the meshing in comparison to analytical models. Different idealised fibre arrangements were used in the first models, such as square, hexagonal or square diagonal arrangements [25, 26, 27] (see Fig.2.5). Periodicity of the fibre arrangement allows for micromechanical material characterisation by analysing its unit cell. The analysis simulates the physical experiments that would be performed on a real sample such as applying load cases and measuring the relative displacement field, thus obtaining its effective material properties. This method can also be used for mesoscale to macroscale homogenisation. The analysis requires properly formulated boundary conditions applied to the unit cell as extensively described by Li et al. [28, 29, 30]. This homogenisation method is referred as 'static virtual testing' throughout the thesis and is detailed in Sec.A.1 in Appendix. Idealisation of the fibre arrangement is a trade-off between computational cost and accuracy as in reality the fibres are distributed randomly in the cross-section. However, in 2008, Huang et al. [31] compared the idealised square and hexagonal arrangements with a model of randomly distributed fibres (the moduli are computed for the obtained statistical distribution of stresses) and concluded similar effective material properties prediction for the three models.

2.1.2 Mesoscale to macroscale homogenisation

Textiles observed at a mesoscopic scale are a network of interwoven yarns forming a self-supported architecture. A woven fabric in particular generally consists of

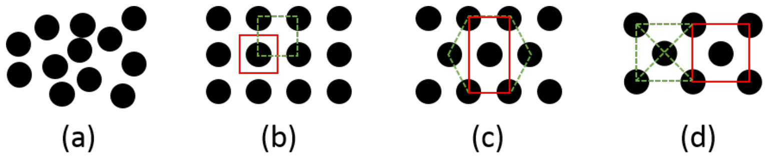

Figure 2.5: Fibre arrangement a) random b) square c) hexagonal d) square diagonal. Green dotted lines are used to justify the arrangement name. The periodic unit cell is displayed within the red boundaries.

two sets of interlaced yarn components called warp and weft yarns and in the case of a 3D weave an additional set of yarns called binder yarns. The different types of yarn are defined by their orientations: warp yarns during the weaving process are positioned longitudinally and held stationary in the weaving device while the weft yarns are transversally threaded through them (see Fig.2.6). Binder yarns are used in 3D weave to hold the layers together, their orientation is mainly out-of-plane as they are threaded through-the-thickness. It is assumed from the lower scale level modelling (microscale modelling described in Sec.2.1.1) that the yarns are homogeneous, transversely isotropic and have known effective properties.

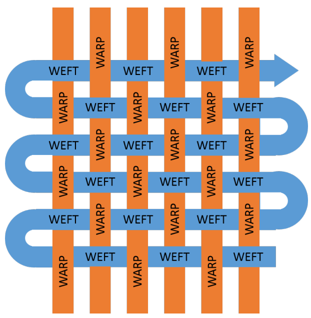

Figure 2.6: Textile warp and weft threading.

A textile is defined by its quantitative parameters (e.g. number of ends per cm, yarn linear density, yarn spacing length) and its qualitative parameters such as the pattern (see Fig.2.1).

A textile reinforcement together with a matrix material form a textile composite. Thus, an accurate mesoscale model of a textile composite relies on the accuracy of the reinforcement geometry modelling. For this reason, the literature survey in this section features both mechanical modelling techniques and geometric description methods. An interesting property of textile preforms and thus textile composites is their periodicity. This means they can be visualised as an assembly of identical unit cells and thus only one has to be modelled in order to obtain the effective mechanical properties of the whole structure.

Most of the models up to now were created for a characterisation of the effective elastic mechanical properties by static loading testing. In that context it was shown that the ability of a model to predict these characteristics lies in the accuracy of the unit cell internal geometry modelling [32, 33] and Lei et al. [34] reported that state-of-the-art modelling of the fabric architecture plays a crucial role in solving dynamic problems as well. Valuable but not exhaustive reviews can be found in [10, 33, 35, 36] on the prediction of the mechanical behaviour of textile composites using various modelling strategies.

Peirce et al. [37] initiated the formalisation of textile geometry in 1937, with idealised assumptions on yarn path and cross-sectional shapes (e.g. assuming that tows had a circular cross-section). Later the first analytical models were created based on the Classical Laminate Theory (CLT) to obtain the effective mechanical characteristics: three of them are presented by Ishikawa et al. [38], the 'Mosaic', 'fibre undulation' and 'bridging' models. 'Mosaic' does not take into account the fibre continuity as the textile composite is considered as an assembly of rectangular cuboids, each being an asymmetrical cross-ply laminate but it still gives a useful rough estimation. This model uses constant strain and stress assumption which gives upper and lower bound solutions for the effective elastic constants of the structure. Later they proposed the 'fibre undulation' model which takes into account the fibres continuity and undulation and thus has better prediction capabilities. The 'bridging model' was specifically developed for satin composites (2D satin woven pattern is shown in Fig.2.1).

In 1986, Yang et al. [39] developed a methodology for predicting elastic properties within 3D textile composites based on the CLT and the fibre inclination (also called orientation averaging (OA)) model. Later, in an article from Whitney et al. [19], a unit cell of a braided composite was divided into micro-cells to define individual yarn position and inclination within it. The CLT and the OA model were also used to predict in-plane properties of 3D angle interlock composites. However, it was concluded that the use of straight segments to model undulating fibres was not suitable and it was shown in the literature a poor agreement with experimental results in particular for satin weave.

After that period, the FE method was gaining in popularity. Indeed some advantages of the method are the possibility for a more accurate geometrical representation of the reinforcement architecture and that the internal stress distributions are computed in detail and thus the iso-strain or iso-stress assumptions described by Reuss and Voight are rendered unnecessary. However, using FE method for homogenisation also means constructing pertinent unit cell models and applying appropriate periodic boundary conditions to it as suggested by the virtual testing method briefly described in Sec.2.1.1. This could be seen as difficulties and the reason why analytical models continued to be developed by researchers.

Cox et al. [40] developed in 1994 the 'binary model' which is a FE model where the yarns are simulated by bar elements and the effective matrix by brick elements. The following year, Whitcomb et al. [41] developed a new method using FE based on the 'global/local methodology'. The local model consists of a refined mesh of a unit cell and is used to compute homogenised engineering properties to obtain global solutions. Periodic boundary conditions were applied to the local model so that its behaviour is similar as if it was embedded in an infinite array. The authors stated that this was a preliminary study and that more realistic configurations needed to be studied.

In 1995, Naik [42] developed a code called TEXCAD to predict amongst other things mechanical properties in 2D woven and triaxial braided composites. This code uses an analytical method in which each yarn of the unit cell of the composite is discretised in slices and the stiffness matrix is computed for each slice, transformed to the global coordinates, multiplied by the slice volume fraction (volume averaging technique) and assembled all together to form the overall effective stiffness matrix. Although it is based on restrictive assumptions, the model provided good approximation of the stress-strain relation for plain weave composites under axial tension.

In 1996, in Glaessgen et al. [32], a FE modelling is carried out at the unit cell level. A Bezier curve (i.e. a parametric curve using Bernstein polynomials as a basis [43]) represents the centre line of each yarn and allows for a realistic modelling of the textile. Their cross-sectional shapes are elliptical and the constituent materials are defined as transversely isotropic for the yarns and isotropic for the matrix.

In 1997, Kuo et al. [44] thought that FE methods, even though useful to describe complex geometry and multi-material problems, are computationally too expensive to obtain satisfactory results. Thus they developed the 'iso-phase model', originally developed by the same authors for 2D woven composites, it is extended to 3D woven composites in [44], in which the yarns are assumed transversely isotropic, are spatially oriented and their undulation is described using sinusoidal functions.

The following year, Tan et al. [45] compared two FE models of a 3D orthogonal woven composite (respectively with rectangular and elliptical cross-sectional shapes for the yarns) with four theoretical models in which the same unit cell is divided by rectangular blocks of one or two homogeneous materials in four different ways, all have rectangular cross-sectional shapes for the yarns. The whole set of effective mechanical properties is deduced for each of the four theoretical models using a mixed iso-stress and iso-strain based analytical theory. The so-called 'XYZ model' provided results closer to those predicted by the FE models than the three others. A comparison between the FE models, the theoretical method and experimental results from the literature was carried out and a good agreement is observed for the in-plane Young's moduli.

In 2000, Lomov et al. [46] stated that a good model relies on an accurate geometric description and thus on cross-sectional observations under the microscope. The same authors later developed a textile geometry pre-processor named 'WiseTex' [47]. It provides opportunity to use manufacturer's fabric and yarns data as a starting point for modelling composite materials. It also gives solid foundation for mechanical properties prediction of composite material. It is based on an energy minimisation algorithm (i.e. minimise the bending and tension energy of the yarns [48]) to determine the precise geometry of a textile in its relaxed state, thus the geometry is based on physical properties.

In parallel, Robitaille et al. [49] developed an algorithm generating the geometric definition of a repeated unit cell of a textile composite, following previous works on the formalisation of the description of interlacing patterns by vectors

[50] named 'TexGen'. In this pre-processor, no energy minimisation algorithm is involved so it has less geometrical restrictions and thus more flexibility. It is also free and open source with a powerful Python scripting interface [51].

Nowadays most mesoscale modelling use these pre-processors to create a geometry to be exported on a FE software. This allows for creating still idealised yet more realistic models. For example, Green et al. in [52] used Python scripting to create a more realistic geometry of a complex orthogonal 3D woven composite within TexGen. Nevertheless, even if one period of the textile is modelled according to microscopic observations of the yarns cross-sectional shapes or the yarns nesting for example, in reality there will be variations as the period is repeated to form the textile. This can have a significant effect on the prediction of the mechanical properties of the material and models incorporating these natural internal variabilities are developed [53].

2.2 Numerical determination of the dispersion characteristics of periodic media

In this section, a non exhaustive review on wave propagation modelling in continuous and periodic media is proposed. Thin structures are of interest as they guide waves with minimal loss in one or two directions. Structures that guide waves in one or two directions are respectively called one- or two-dimensional waveguides. The relation between the wavelength or wavenumber of a wave and its frequency in a particular medium is called a dispersion relation. From that relation can be derived the phase and group velocities. The phase velocity represents the rate at which the phase of a wave propagates and the group velocity represents the speed at which the amplitude envelop of a wave propagates.

2.2.1 Analytical models for wave propagation in isotropic media

Wave propagation in simple waveguides can be investigated through analytical models allowing for computing their dispersion characteristics [54, 55]. The analytical solutions of the wavenumber, the phase velocity, the group velocity etc. for some simple structures such as rod or beam have been available for decades. However, those analytical models often involve assumptions and/or approximations concerning the mechanical properties of the structure, and refined models are required in the high frequency regime.

Analytical models for a thin isotropic beam

Longitudinal wave The governing equation of motion for a free longitudinal wave is derived and given in [54] as

$$E\frac{\partial^2 u(x,t)}{\partial x^2} - \rho\frac{\partial^2 u(x,t)}{\partial t^2} = 0, \tag{2.2}$$

where $u(x,t)$ is the longitudinal displacement, x the position along the beam axis, t the time, E the elastic modulus (or Young's modulus) and ρ the density.

The wavenumber k is easily deduced from Eq.(2.2)

$$k = \sqrt{\frac{\rho}{E}}\omega. \tag{2.3}$$

Torsional wave The governing equation of motion for a free torsional wave is identical in form to that of longitudinal wave as shown in [54]

$$\frac{\partial^2 \Theta(x,t)}{\partial x^2} - \frac{\rho}{C}\frac{\partial^2 \Theta(x,t)}{\partial t^2} = 0, \tag{2.4}$$

where $\Theta(x,t)$ is the angular rotation (around Ox), $C = \frac{G\gamma}{J}$ the torsional rigidity, G the modulus of rigidity, J the polar moment of inertia and γ the torsional constant estimated by Roark in [56].The wavenumber is deduced from Eq.(2.4)

$$k = \sqrt{\frac{\rho}{C}}\omega. \tag{2.5}$$

Bending waves Free bending waves propagation in thin beams were firstly described by the Euler-Bernoulli beam theory and by the Euler-Lagrange equation in dynamics. By deriving this Euler-Lagrange equation, the following governing equation for free transverse vibration can easily be obtained [57, 58] (for a beam of uniform cross-section):

$$EI\frac{\partial^4 v(x,t)}{\partial x^4} + \rho A\frac{\partial^2 v(x,t)}{\partial t^2} = 0, \tag{2.6}$$

where $v(x,t)$ is the transverse displacement, x the position along the beam axis, t the time, E the elastic modulus, ρ the density, A the cross sectional area, and I the second moment of inertia of the cross section.

Assuming a time and space harmonic motion:

$$v(x,t) = V(x)\sin(\omega t + \alpha). \tag{2.7}$$

where V is the amplitude, x the position along the beam axis, ω the angular frequency, t the time and α the phase.

The dispersion equation for the bending waves is given by

$$k = \sqrt[4]{m\omega^2/EI}. \tag{2.8}$$

The equation has four roots. Each wavenumber describes a wave, two describe the propagating ones and two describe the nearfield waves, whose amplitudes decay rapidly with distance.

The Euler-Bernoulli theory only considers the effect of bending moment. While this is sufficient to describe the behaviour of thin beams at low frequencies, this theory oversimplifies the problem and thus provides wrong predictions for thicker beams and higher frequencies. The Timoshenko beam theory was formulated in 1921 [59, 60] to overcome these restrictions. It extends the Euler-Bernoulli theory by taking account of shear deformation and rotatory inertia. The Lagrangian equations of motion yield

$$\rho I\frac{\partial^2 \Theta(x,t)}{\partial x^2} - EI\frac{\partial^2 \Theta(x,t)}{\partial x^2} - KGA\left(\frac{\partial v(x,t)}{\partial x} - \Theta(x,t)\right) = 0, \tag{2.9}$$

where $\Theta(x,t)$ is the angular rotation (around Oy for one bending mode and around Oz for the other, given that Ox is the axis of the beam length), G the modulus of rigidity and K a dimensionless quantity dependent on the shape of the cross section used as a correction factor to account for the non-uniform distribution of the shear stress and strain over the cross section. Cowper [61] later defined K for a beam of rectangular cross-section as independent of the aspect ratio of the rectangle and dependent of the material Poisson's ratio only (ν):

$$K = \frac{10(1+\nu)}{12+11\nu}. \tag{2.10}$$

The dispersion relation for the bending waves is then given as

$$k = \sqrt{\left(\frac{\rho}{2E} + \frac{\rho}{2GK}\right)\omega^2 + \sqrt{\left(\frac{\rho}{2E} - \frac{\rho}{2GK}\right)^2 \omega^4 + \frac{\rho A}{EI}\omega^2}}, \tag{2.11}$$

and has four roots again.

Analytical models for a thin isotropic plate

Wave propagation in infinite plates was firstly studied by Rayleigh and Lamb [62]. A number of authors have worked on the Classical Plate Theory (CPT) after that [54, 63] for various material categories. In isotropic plates, guided waves propagating at low frequency are classified into three types: longitudinal (or extensional), shear (or transverse) and bending (or flexural) and their governing equations are given in the following paragraphs.

Longitudinal and shear waves Combining once again Newton's second law and the generalised Hooke's law relations, one can establish the governing equation for in-plane motion [64]

$$\frac{E}{(1-\nu^2)}\left(\frac{\partial^2 u}{\partial x^2} + (1+\nu)\frac{\partial^2 v}{\partial x \partial y} + \left(\frac{1-\nu}{2}\right)\frac{\partial^2 u}{\partial y^2}\right) = \rho\frac{\partial^2 u}{\partial t^2}, \tag{2.12}$$

and

$$\frac{E}{(1-\nu^2)}\left(\frac{\partial^2 v}{\partial y^2} + (1+\nu)\frac{\partial^2 u}{\partial x \partial y} + \left(\frac{1-\nu}{2}\right)\frac{\partial^2 v}{\partial x^2}\right) = \rho\frac{\partial^2 v}{\partial t^2}. \tag{2.13}$$

The dispersion relation for the longitudinal wave is then given as

$$k = \sqrt{\frac{\rho(1-\nu^2)}{E}}\omega, \tag{2.14}$$

and the shear wave as

$$k = \sqrt{\frac{\rho}{G}}\omega. \tag{2.15}$$

Bending wave For a plate whose thickness/wavelength ratio is smaller than 1/10, the bending wave equation in a plate of thickness h is

$$D\left(\frac{\partial^4 w(x,y,t)}{\partial x^4} + 2\frac{\partial^4 w(x,y,t)}{\partial x^2 \partial y^2} + \frac{\partial^4 w(x,y,t)}{\partial y^4}\right) = -\rho h \frac{\partial^2 w(x,y,t)}{\partial t^2}, \tag{2.16}$$

where $D = \frac{Eh^3}{12(1-\nu^2)}$ is the flexural rigidity and $w(x,y,t)$ is the out-of-plane displacement.

The dispersion relation is written as [58]

$$k = \sqrt[4]{\left(\frac{\rho h}{D}\right)}\sqrt{\omega}. \tag{2.17}$$

At higher frequency ranges, these guided waves are called Lamb waves. They are classified according to their modeshapes as symmetrical (S) and antisymmetric (A) modes and involve motion of the medium in the x-z plane only. The modes that are nascent at a frequency of zero are the zero-order modes and are written A_0 and S_0. A_0 is equivalent to the bending mode at low frequency, and S_0 to the longitudinal one. The shear-horizontal wave modes involve motion of the medium in the y direction only. They are complementary to the Lamb wave modes classification and are written SH. These three modes (A_0, SH_0 and S_0) are commonly used for wave based damage detection methods in composite structures [65].

With the dispersion relations $k(\omega)$ known, other characteristics of a wave can be computed such as the phase or group velocity. The phase velocity is given by the proportionality between the angular frequency ω and the wavenumber k:

$$c_p = \frac{\omega}{k}. \tag{2.18}$$

The slowness is another characteristic that is often used and is the inverse of the phase velocity

$$s = \frac{1}{v_p}. \tag{2.19}$$

The group velocity is given as

$$c_g = \frac{\partial \omega}{\partial k}. \tag{2.20}$$

2.2.2 Wave propagation in periodic structures

A periodic structure can be seen as an infinite assembly of identical elements joined end-to-end in the case of a one-dimensional periodic structure (e.g. a railway or a unidirectional composite) and also side-by-side when considering a two-dimensional periodic structure (e.g. an aircraft fuselage or a textile composite structure). Textile composites are two-dimensional periodic structures whose representative period is called unit cell.

Floquet in 1883 [66] gives the first modern mathematical description of one-dimensional periodic structures and proved a theorem that reveals itself to be crucial for the study of infinite periodic media. Bloch [67] generalised the results of Floquet by extending his theorem to multidimensional periodic structures, showing that the wave field in those structures is also periodic up to a phase multiplier. The Bloch-Floquet theorem thus allows for considerable analysis savings as only a single unit cell needs to be considered to simulate wave propagation through the entire periodic structure. The Bloch-Floquet theorem, also called PST, is the foundation of modern research on wave propagation in periodic structures as stated in two review publications [68, 69].

In 1946, Brillouin [70] traced the historical background of the mathematics of wave propagation and diffraction in periodic structures. He also applied the Bloch-Floquet theorem to analyse the elastic wave propagation in periodic networks and defined the reduced zones named the Brillouin zones in which the dispersion behaviour is fully described. Indeed, in a periodic structure of period Δ, the dispersion relation $k(\omega)$ is periodic with a period of $\frac{2\pi}{\Delta}$ and the dispersion behaviour is fully described in the fundamental period $k \in [-\frac{\pi}{\Delta}, +\frac{\pi}{\Delta}]$. This wavenumber range is called the first Brillouin Zone (BZ). The dispersion relations being symmetric about $k = 0$ it can be fully characterised in half on the first BZ, i.e. $k \in [0, +\frac{\pi}{\Delta}]$. This further reduced wavenumber range is named the Irreducible Brillouin Zone (IBZ).

Another interesting feature of dispersion relations of periodic structures is that they can exhibit wave filtering behaviours called 'stop-bands' or 'band-gaps'. Lord Rayleigh was the first to demonstrate their existence in 1887 [71] by considering a string with a periodic variation of density along its length. Those special wave phenomenon are generated by periodic impedance mismatch in the unit cells. Indeed, a unit cell of a periodic structure can be a very heterogeneous medium both in geometry and in material properties (see Fig.2.1 for examples) and thus the assembly of these periodic elements can be seen as a set of periodic discontinuities. Two types of stop-bands can be distinguished by their origin mechanism. The Bragg stop-bands are due to the interactions between incident and reflected waves that create destructive interference and are linked to the length scale of periodicity (i.e. occurring at BZ limits, when the wavelength is a multiple of the unit cell's length), while the local resonant stop-bands usually appear when the unit cell displays one or more resonant unit [72, 73, 74]. By opposition are called pass-bands the remaining frequency ranges in which the waves are allowed to propagate. While these phenomenon can be used to generate frequency filters [72, 73, 75, 76, 77], waveguiding features [75] and other innovative applications [69], they often cause complication to guided wave inspection as they prevent the use of bandwidths for this application (i.e. the excitation frequency should be selected in the frequency range of pass-bands) [78, 79] and thus it emphasises the need for an accurate characterisation of the dispersion.

2.2.3 Analytical and semi-analytical methods for wave propagation in composite structures

Analytical methods

Wave propagation in composite structures is highly dispersive due to the complexity of the medium, and traditional analytical models such as the ones presented in Sec.2.2.1 are too simplistic to accurately describe the dispersive behaviour of such structures [80, 81] and thus more complex, often matrix based, methods were developed.

One of the first analytical method is the Dynamic Stiffness Method (DSM) widely developed by Banerjee [82] and applied on laminated composites in [83, 84].

The section is divided into a number of elements whose differential equations exact solution give the exact shape functions. The results of this method are mostly independent from the number of elements chosen to describe the section. The accuracy of the method depends on the analytical models used to define the governing equations. In 1950, Thompson [85] proposed the Transfer Matrix Method (TMM) which allowed the analysis of laminated structures, by creating transfer matrices that account for the stress and strain continuity between two adjacent layers and multiplying them altogether to obtain the dispersion relations of the laminate, but had the disadvantage of being computationally instable as poor conditioning occurred at high frequencies. The Global Matrix Method (GMM) uses a similar approach but concatenates the matrices instead of multiplying them, hence forming a global matrix. Unlike the TMM where the equations for the intermediate interfaces are eliminated (the fields in all layers are described only in terms of the external boundary conditions), the GMM imposes boundary conditions at the layers interfaces. Thus, in the GMM the equations at an interface are influenced by the arrival of waves from the neighboring interfaces [86]. This technique is robust and easy to implement and is the basis of the Disperse software developed at the Imperial College of London. However, a drawback of that method is an expensive computation time for media with many layers.

It seems, however, that each of these analytical methods either came with computational limitations or were not ideal for complex structures applications such as composites. On the other hand, FE methods even though able to deal with very complex geometry, often lead to prohibitive computational costs. To counteract both these issues, semi-analytical methods were developed. It often consists in describing the out-of-plan strain in a unit cell with a FE approach while the in-plane wave propagation is described analytically.

Semi-analytical methods

There are many significant semi-analytical methods for computing wave dispersion characteristics of composites. The Semi-Analytical Finite Element (SAFE) method and the WFE method are two semi-analytical methods that are widely used for NDE and SHM applications on composites.

SAFE The SAFE method was proposed by Dong and Nelson [87] in 1972 for cylinders and plate structures and applied to laminates by Liu [88, 89]. Jezzine [90] extended the SAFE method to compute the modal solution for waveguides of any shape. Bartoli [91] extended the method to introduce wave propagation damping in laminates. The SAFE method uses a FE discretisation of the waveguide cross-section (two-dimensional elements for beam-like structures) or through-the-thickness of the waveguide (one-dimensional elements for plate-like structures) as shown in Fig.2.7.a and thus is really efficient to describe wave propagation in a laminate for example.

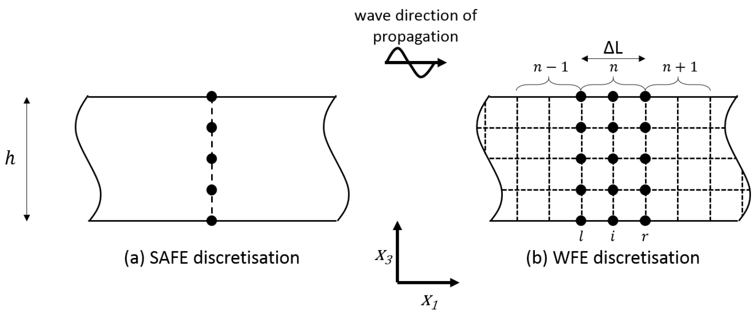

Figure 2.7: Cross-sectional view of a waveguide enhancing the model discretisation for (a) the SAFE method (b) the WFE method.

Assuming a plate-like structure as waveguide, a Cartesian system with x_1 and x_2 two normal axis in the plan and x_1 the considered direction of propagation. x_3 is the axis normal to the plate and h the thickness of the structure. The FE discretisation is realised through-the-thickness as displayed in Fig.2.7.a. The approximate time-dependent displacement of a point within the e^{th} element $u^{(e)}$ is described as:

$$u^{(e)}(x_1, x_2, x_3, t) = \mathbf{N}(x_2, x_3)\mathbf{q}^{(e)}\mathrm{e}^{\mathrm{i}(\omega t - kx_1)}, \tag{2.21}$$

with $\mathbf{N}$ the matrix of the shape functions and $\mathbf{q}^{(e)}$ the vector of nodal displacements. Applying Hamilton's principle, the SAFE governing equation for a plate is written as follows:

$$[k^2\mathbf{K}_1 + k\mathbf{K}_2 + \mathbf{K}_3 - \omega^2\mathbf{M}]\mathbf{U} = 0, \tag{2.22}$$

with k the wavenumber, ω the angular frequency, $\mathbf{M}$ the global mass matrix, $\mathbf{U}$

the global nodal displacement vector and $\mathbf{K}_1$, $\mathbf{K}_2$ and $\mathbf{K}_3$ are the global stiffness matrices as shown in [78, 91, 92, 6]. For a given frequency, the equation forms a quadratic problem, and the eigenvalue k and eigenvector $\mathbf{U}$ can be extracted. This method is used in the CIVA software developed at the CEA List. While the SAFE method is very time efficient when investigating a material that is inhomogeneous in its thickness but homogeneous in the direction of propagation (such as composite laminates), it encounters severe limitations when it comes to materials that are periodic in the directions of propagation (such as metamaterial or textile composites) [6].

WFE The WFE method was firstly introduced by Orris and Petyt in [93, 94]. In [95], Abdel-Rahman extended the method to different periodic structures. The WFE method has been applied to various types of one-dimensional waveguides such as beam-like structures [96, 97]. Since then, the method was extended to two-dimensional waveguides by Manconi [98] and applied to various type of structures such as plates [99, 100], thin-walled structures [101], curved layered shells [102] and more recently periodically ribbed panels [103]. The WFE combines the Bloch-Floquet theorem (or PST) with the FE method. The finite element discretisation is applied to a period of the structure (e.g. the period n of length ΔL in Fig.2.7.b), using three-dimensional elements, and thus is an efficient tool to study wave propagation in periodic structures whose complex period can be modelled with a commercial FE software. The method is further described in Sec.2.3.

To fully understand the advantages and drawbacks of both the SAFE and the WFE methods, some applications are detailed. Firstly, when considering a plate-like waveguide whose material varies through-the-thickness (x_3 direction in Fig.2.7) but is continuous in the two other principal directions (x_1 and x_2) e.g. a laminate, the WFE and SAFE methods both provide the same outputs (dispersion relations and modeshapes) for a similar nodal discretisation in the thickness. However, the SAFE method uses one-dimensional elements while the WFE method uses three-dimensional elements, thus computational time is reduced in comparison to the WFE. Secondly, if the material is periodic in the

x_1 and x_2 directions, the SAFE method cannot be used while the WFE method is adequate. To summarise, the main advantage of the SAFE method over the WFE method is its reduced computational time, while the main advantage of the WFE method over the SAFE method is its wider range of application.

2.2.4 Wave-based homogenisation techniques

Inverting material constants from wave-based data using optimisation algorithms is a popular technique as the dispersive characteristics of a material are directly dependent on its elastic constants. Bulk [104, 105, 106, 107, 108] and Lamb [92, 108, 109, 110, 111, 112] wave data are both of interest and many different optimisation algorithm have been proposed in that context, such as the least-square method [104, 105, 106], simulated annealing [112] or Genetic Algorithms (GAs) [107, 109, 92, 110, 111, 108]. Balasubramaniam [107] was the first to employ GAs for inverting unidirectional composite material elastic moduli with great success. The advantages of GAs over other search algorithms are that they do not need an initial guess but rather a valid search space, it is also robust and avoid entrapment at local minima. Using Lamb wave data rather than bulk wave data is getting more popular nowadays for its numerous advantages such as no need to immerse the sample, direct applications for SHM work etc. [109]. The combination of Lamb wave data and GA has been used for material characterisation in previous research for isotropic [92, 110], transverse isotropic [108, 111] and orthotropic materials [109, 110].

2.2.5 Damping characterisation of composite materials

Damping is an important parameter in the design and analysis of composite materials, especially for engineering applications in which the dynamic response often needs to be controlled. The attenuation of a propagating wave in a thin structure can be caused by many factors, nonetheless this subsection focuses on the material damping only.

Damping characteristics of composite materials

Numerous analytical models have been developed throughout the years, at both macro- and mesoscales. At macromechanical scale, the effect of the stacking sequence of the composites on the damping are studied, while at mesoscale, the yarns arrangements are of concern. The damping capacity in composite structures is generally higher than in a traditional material, mostly because of the viscoelastic properties of the matrix [113]. A viscoelastic material is a material which has both viscous and elastic characteristics. Thus, its behaviour is defined both by Hooke's law of perfect elasticity whose component can be represented by springs that store energy and by Newton's law of viscosity whose component can be represented by dashpots that dissipate energy [114].

This capacity can be used to enhance the uses of composite materials. Indeed it is well known that composites can be tuned to fit particular stiffness and strength properties, but damping properties can be tuned as well modifying constitutive parameters such as the periodic sequence, the mesoscale arrangement of the fibre etc. [113]. It is also known that the inherent damping of the components of a composite is the main source of damping. Increasing the matrix proportion (i.e. decreasing the fibre volume fraction) often results in a higher damping [113, 115]. Damping of a propagating guided wave can result in a decreased propagation distance, thus a reduced inspection range. Therefore, it is of the upmost importance to know these properties for NDE and SHM purposes [116].

Numerous studies have been carried out on the effect of fibre properties on the damping. Early work was performed experimentally: in [117], Wright compares the loss factors of different fibre/resin combinations by a resonant beam method, for glass and carbon fibres. Crane [118] investigated the effect of fibre and matrix properties as a function of frequency on the damping of composites for glass and graphite fibre composites. Ply orientation and stacking sequence are some other fundamental factors and thus their effect on the damping have been thoroughly investigated. At first, those investigations were mostly involving analytical and experimental work. Adams and Bacon [119] studied the effect of fibre orientation and laminate geometry on the dynamic properties of CFRP. They also stated, by separating the energy dissipations associated to the individual stress components, that shear is the factor that can give high damping. Using this concept of energy dispersion separation, Adams and Maheri studied the effect of stress level on the damping variation in CFRP [120] and showed that the fibre orientation and stacking has an effect on the damping in [121]. Berthelot [122] did a similar study, comparing the effect of fibre orientation in glass and Kevlar fibre composites on the damping. This subject has drawn a lot of experimental work since [123].

Thanks to the early work of Adams and Bacon and their damping criterion, some theoretical models for predicting damping emerged. Ni and Adams [124] developed a model both useful and accurate for predicting damping in composite laminates. Yim compared some damping prediction models (including Ni and Adams') in [125] for laminated composite beams and stated that the fibre orientation has a strong effect on the damping. Berthelot et al. [126] developed a synthesis of damping analysis of laminate material, comparing analytic method with experimental results. In [127] Maheri compared the damping in layered FRP panel under different boundary conditions and using various stacking sequences. It showed that yarn orientation has an influence on the modal damping.

Thanks to the enhancement of numerical methods in the last decades, the effect of the fibre micromechanical arrangement could be thoroughly investigated, using FEM for example. Hwang and Gibson [128, 129] utilised a FE approach for characterising the effects of stress on damping in laminated composites. Tsai and Chi [130] compared different fibre micromechanical arrangements in composites with Finite Element Analysis (FEA). Chandra et al. [131] have investigated the effect of fibre cross-section and fibre volume fraction on damping. FEM was used as well for establishing damping model at macroscale. Mahi in [132] evaluates the energy dissipation for different fibre orientations, for composite materials. Guan and Gibson [133] used FEM to study the damping characteristics of woven fabric-reinforced for the first time. The method was compared with a closed-form solution and experiments in order to assess the validity of the method. However, the effect of undulate fibre bundles on the damping properties is not considered in that study. In [134], Yu and Zhou established a damping prediction approach for woven composites, taking the undulation of the fibres into account. This study shows once again a correlation between the decreasing of the loss factor with an increasing fibre volume fraction.

Damping modelling in FEA

There are several ways of modelling the damping using FE. The complex modulus model is an approach which consists of allowing complex frequency independent components in the material stiffness matrix. This approach is widely used for modelling the damping in FE codes [91, 135, 136, 137] or within semi-analytical models as well [138]. The stiffness matrix $\mathbf{K}$ is treated as complex [139] to make up for the damping term in the equation of motion. This complex matrix is composed of a real part that represents the storage modulus referring to the elastic behaviour, while the imaginary part represents the loss modulus referring to the dissipative behaviour of the material. The accuracy of this method was discussed by Crandall in [140, 141] and it was pointed out that this representation does not satisfy the causality requirement thus has serious physical limitations. Viscoelastic behaviour of the constituent elements is not the only damping mechanism occuring in composite materials: thermoplastic damping and Coulomb friction damping in the fibre/matrix interface regions are two other mechanisms to name a few. However, it has been identified as the dominant damping mechanism [142] and thus is the one studied here. In this modelling method, the global stiffness matrix K is given as in Eq.(2.23):

$$\mathbf{K} = \mathbf{K}' + \mathrm{i}\mathbf{K}'' = \sum_{k=1}^{n} (\mathbf{K}'_k + \mathrm{i}\mathbf{K}''_k), \tag{2.23}$$

where n is the total number of solid elements used in the FE discretisation. $\mathbf{K}'_k$ and $\mathbf{K}''_k$ are respectively the real and imaginary stiffness matrix contributions to the k^{th} finite element of the global stiffness matrix $\mathbf{K}$.

Another viscoelastic model is named Kelvin-Voigt [143, 144] and has been widely used in the literature [138, 145]. It is similar to the complex modulus model except that the added term is frequency dependent:

$$\mathbf{K} = \mathbf{K}'(1 + \mathrm{i}\omega\eta). \tag{2.24}$$

The Kelvin-Voigt model has been compared along the complex modulus approach to experimental results for laminated composite samples in [138] and it was concluded that the Kelvin-Voigt model provides more accurate predictions.

At last, the proportional damping model (also called Rayleigh) is the most commonly used viscous damping model in FE methods [146, 147]. The damping matrix $\mathbf{C}$ is expressed as a linear function of the mass $\mathbf{M}$ and stiffness $\mathbf{K}$ matrices:

$$\mathbf{C} = \alpha\mathbf{M} + \beta\mathbf{K}. \tag{2.25}$$

where α and β are respectively the mass and stiffness proportionality coefficients.

Loss factor determination

A method for computing the loss factor is the strain energy method, which is an approach proposed by Ungar and Kerwin in [148] in which they gave a formulation for the loss factor in terms of energy. Using the fact that the dissipated energy is the result of each component contribution (fibres and matrix in the case of composite materials). They defined the loss factor as follows:

$$\eta = \frac{\sum_{k=1}^{n} \eta_k W_k}{\sum W_k}, \tag{2.26}$$

where n is the total number of solid elements used in the FE discretisation. η is the loss factor of the system, η_i is the loss factor of the i^{th} finite element in the system. W_i denotes the strain energy stored in the i^{th} element at maximum amplitude. Which would give for a composite composed of only two materials:

$$\eta = \frac{\eta_f W_f + \eta_m W_m}{W}. \tag{2.27}$$

η_f and η_m being respectively the loss factor of the fibre and matrix materials, and W_f and W_m the strain energy of the fibres and matrix. This method has been used in many studies [139, 142, 149]. In 1982, Johnson et al. [139] identified the modal strain energy method as the most promising for large-scale applications. Hwang et al. [142] stated that the method provides a convenient and efficient approach for damping characterisation of composites. A drawback, however, lies in the need for a pre-determined loss factor for the constituent materials. In [149], the strain energy method was used to predict the damping at microscale of fibre reinforced polymers and reasonable agreement with experimental results was observed.

2.3 The Wave and Finite Element method

The Wave Finite Element (WFE) method is used to study the dispersion characteristics of continuous waveguides or periodic structures. In this method, only a small segment of the waveguide or a unit cell of the periodic structure needs to be modelled to obtain the dispersion characteristics of the whole structure using the PST (also called Bloch-Floquet theorem). A great advantage of this method is that a complex unit cell can be modelled with a commercial FE package, and its stiffness and mass matrices can easily be obtained to solve the equation of motion written as

$$\mathbf{M}\ddot{\mathbf{q}}(t) + \mathbf{C}\dot{\mathbf{q}}(t) + \mathbf{K}\mathbf{q}(t) = \mathbf{f}(t), \tag{2.28}$$

where $\mathbf{M}$, $\mathbf{C}$ and $\mathbf{K}$ are the mass, damping and stiffness matrices and $\mathbf{q}$ and $\mathbf{f}$ represent a vector of respectively the nodal DoFs and forces in the unit cell. Free wave motion is considered so $\mathbf{f}$ only represents the nodal forces responsible for transmitting the wave motion from one element to the next. When no damping and time-harmonic behaviour (leading to $\ddot{\mathbf{q}} = -\omega^{\mathbf{2}}\mathbf{q}$) is assumed, Eq.(2.28) is rewritten as

$$\left[\mathbf{K} - \omega^{\mathbf{2}}\mathbf{M}\right]\mathbf{q} = \mathbf{f}. \tag{2.29}$$

According to the PST [58, 70], when a free wave travels along a periodic waveguide, the displacements between two opposite boundary sides of a unit cell differ only by a propagation factor

$$\mathbf{q_B} = \lambda\mathbf{q_A} \quad \text{and} \quad \mathbf{f_B} = -\lambda\mathbf{f_A}, \tag{2.30}$$

with $\mathbf{q_A}$ and $\mathbf{q_B}$ the nodal displacement on respectively a face named A of the considered unit cell and B its opposite face, separated by the distance Δ. λ is the propagation factor such as

$$\lambda = \mathbf{e}^{-\mu\boldsymbol{\Delta}}\mathbf{e}^{-\mathrm{i}k\boldsymbol{\Delta}}, \tag{2.31}$$

in which μ represents the change in amplitude and k represents the change in phase. For models in which no damping is considered, the amplitude of a propagating wave remains constant, which is given by $\mu = 0$. The propagation factor depends only of the wavenumber k and the length between opposite faces Δ:

$$\lambda = \mathbf{e}^{-\mathrm{i}k\boldsymbol{\Delta}}. \tag{2.32}$$

Combining Eq.(2.29) with Eq.(2.30) and Eq.(2.32) gives an eigenvalue problem whose form depends on the nature of the solution sought. The two following subsections explore the different eigenproblem formulations for one-dimensional and two-dimensional waveguides (meaning waveguides in which waves propagate along one or two directions respectively). The third subsection introduces the Craig-Bampton method for a further reduction of the problem size.

2.3.1 One-dimensional WFE

A one-dimensional waveguide is a medium in which a wave propagates in one main direction of propagation (e.g. a beam or a rod). In 1D WFE, it is almost a convention to consider the wave motion to be along the x direction, so Eq.(2.30) can be written as [58]

$$\mathbf{q_R} = \lambda_x \mathbf{q_L} \quad \text{and} \quad \mathbf{f_R} = -\lambda_x \mathbf{f_L}, \tag{2.33}$$

with q_R and f_R respectively the displacement and force on the right side of the considered unit cell and q_L and f_L respectively the displacement and force on the left side.

The nodal DoFs of the unit cell are partitioned in the following way: left, right and internal DoFs, which gives $\mathbf{q} = \begin{bmatrix} \mathbf{q_L^T} & \mathbf{q_R^T} & \mathbf{q_I^T} \end{bmatrix}^T$. In order to use the PST, it is important to note that the considered unit cell needs to be meshed in a similar way on its opposite boundaries (left and right sides for a one-dimensional waveguide), so that continuity in displacements and forces equilibrium is respected.

Different formulations of the problem exist, all leading to a different eigenvalue problem. These are presented in the following subsections.

The wavenumber k is specified, $\mu = 0$ and the angular frequency ω is sought

In this first formulation, abbreviated $\omega(k)$, the frequency of a wave propagating in the structure can be calculated from the standard linear eigenvalue problem for a specified wavenumber. Using the PST (Eq.(2.33)), the nodal DoFs are rewritten as [150, 151]

$$\begin{pmatrix} \mathbf{q_L} \\ \mathbf{q_R} \\ \mathbf{q_I} \end{pmatrix} = \begin{bmatrix} \mathbf{I} & \mathbf{0} \\ \mathbf{I}\lambda_x & \mathbf{0} \\ \mathbf{0} & \mathbf{I} \end{bmatrix} \begin{pmatrix} \mathbf{q_L} \\ \mathbf{q_I} \end{pmatrix} = \mathbf{\Lambda_R}(\lambda_x) \begin{pmatrix} \mathbf{q_L} \\ \mathbf{q_I} \end{pmatrix}. \tag{2.34}$$

Equilibrium at the left side nodes gives:

$$\mathbf{\Lambda_L}(\lambda_x) \begin{pmatrix} \mathbf{f_L} \\ \mathbf{f_R} \\ \mathbf{0} \end{pmatrix} = \mathbf{0}, \tag{2.35}$$

with

$$\mathbf{\Lambda_L}(\lambda_x) = \begin{bmatrix} \mathbf{I} & \mathbf{I}{\lambda_x}^{\mathbf{-1}} & \mathbf{0} \\ \mathbf{0} & \mathbf{0} & \mathbf{I} \end{bmatrix}. \tag{2.36}$$

Combining Eq.(2.29), Eq.(2.34) and Eq.(2.35), the following eigenvalue problem appears

$$\mathbf{\Lambda_L}(\mathbf{K} - \omega^2\mathbf{M})\mathbf{\Lambda_R} \begin{pmatrix} \mathbf{q_L} \\ \mathbf{q_I} \end{pmatrix} = 0, \tag{2.37}$$

with Λ_L and Λ_R depending on the specified wavenumber k_x. The angular frequency ω and its corresponding modeshape q are sought. Iterating the calculation for a set of specified wavenumbers gives a set of angular frequencies and their corresponding modeshapes. An advantage of that formulation is that it keeps the full set of nodal DoFs, its main disadvantage however relies in the assumption of no attenuation [150, 152].

The angular frequency ω is assigned, complex wavenumber k is sought

This formulation is abbreviated $k(\omega)$. The eigenvalue problem is polynomial, a dynamic stiffness matrix $\widetilde{\mathbf{D}}$ needs to be constructed

$$\widetilde{\mathbf{D}} = \mathbf{K} - \omega^2\mathbf{M}. \tag{2.38}$$

Decomposing the matrix into left, right and internal DoFs and combining it with Eq.(2.29) results in the following equation

$$\begin{bmatrix} \widetilde{\mathbf{D}}_{\mathbf{LL}} & \widetilde{\mathbf{D}}_{\mathbf{LR}} & \widetilde{\mathbf{D}}_{\mathbf{LI}} \\ \widetilde{\mathbf{D}}_{\mathbf{RL}} & \widetilde{\mathbf{D}}_{\mathbf{RR}} & \widetilde{\mathbf{D}}_{\mathbf{RI}} \\ \widetilde{\mathbf{D}}_{\mathbf{IL}} & \widetilde{\mathbf{D}}_{\mathbf{IR}} & \widetilde{\mathbf{D}}_{\mathbf{II}} \end{bmatrix} \begin{pmatrix} \mathbf{q_L} \\ \mathbf{q_R} \\ \mathbf{q_I} \end{pmatrix} = \begin{pmatrix} \mathbf{f_L} \\ \mathbf{f_R} \\ \mathbf{0} \end{pmatrix}. \tag{2.39}$$

Using the third row of Eq. 2.39, the internal DoFs are eliminated [153]

$$\mathbf{q_I} = -\widetilde{\mathbf{D}}_{\mathbf{II}}^{-1}(\widetilde{\mathbf{D}}_{\mathbf{IL}}\mathbf{q_L} + \widetilde{\mathbf{D}}_{\mathbf{IR}}\mathbf{q_R}). \tag{2.40}$$

This leads to

$$\begin{bmatrix} \widetilde{\mathbf{D}}_{\mathbf{LL}} - \widetilde{\mathbf{D}}_{\mathbf{LI}}\widetilde{\mathbf{D}}_{\mathbf{II}}^{-1}\widetilde{\mathbf{D}}_{\mathbf{IL}} & \widetilde{\mathbf{D}}_{\mathbf{LR}} - \widetilde{\mathbf{D}}_{\mathbf{LI}}\widetilde{\mathbf{D}}_{\mathbf{II}}^{-1}\widetilde{\mathbf{D}}_{\mathbf{IR}} \\ \widetilde{\mathbf{D}}_{\mathbf{RL}} - \widetilde{\mathbf{D}}_{\mathbf{RI}}\widetilde{\mathbf{D}}_{\mathbf{II}}^{-1}\widetilde{\mathbf{D}}_{\mathbf{IL}} & \widetilde{\mathbf{D}}_{\mathbf{RR}} - \widetilde{\mathbf{D}}_{\mathbf{RI}}\widetilde{\mathbf{D}}_{\mathbf{II}}^{-1}\widetilde{\mathbf{D}}_{\mathbf{IR}} \end{bmatrix} \begin{pmatrix} \mathbf{q_L} \\ \mathbf{q_R} \end{pmatrix} = \begin{pmatrix} \mathbf{f_L} \\ \mathbf{f_R} \end{pmatrix}, \tag{2.41}$$

which can be written

$$\begin{bmatrix} \mathbf{D_{LL}} & \mathbf{D_{LR}} \\ \mathbf{D_{RL}} & \mathbf{D_{RR}} \end{bmatrix} \begin{pmatrix} \mathbf{q_L} \\ \mathbf{q_R} \end{pmatrix} = \begin{pmatrix} \mathbf{f_L} \\ \mathbf{f_R} \end{pmatrix}. \tag{2.42}$$

The transfer matrix that depends only on the dynamic stiffness matrix of the cell is sought [58, 154] as

$$\mathbf{T} \begin{pmatrix} \mathbf{q_L} \\ \mathbf{f_L} \end{pmatrix} = \lambda_x \begin{pmatrix} \mathbf{q_L} \\ \mathbf{f_L} \end{pmatrix}, \tag{2.43}$$

it follows from Eq.(2.42) that

$$\mathbf{T} = \begin{bmatrix} -\mathbf{D_{LR}^{-1}D_{LL}} & \mathbf{D_{LR}^{-1}} \\ -\mathbf{D_{RL}} + \mathbf{D_{RR}D_{LR}^{-1}D_{LL}} & -\mathbf{D_{RR}D_{LR}^{-1}} \end{bmatrix}. \tag{2.44}$$

Solving the eigenvalue problem presented in Eq.(2.43) gives a relation between the wavenumber and the angular frequency and the associated modeshapes $[\ \mathbf{q_L} \quad \mathbf{f_L}\ ]^{\mathbf{T}}$. The main disadvantage of this formulation is the condensation of the internal D-oFs to the boundary.

Both formulations provide the same results as long as the medium is homogeneous in the direction of propagation. For a periodic medium, the condensation of the internal DoFs performed in the second formulation alters the results.

2.3.2 Two-dimensional WFE

This method has been extended by Manconi and Mace in [98] for free wave propagation in homogeneous structures in both the x and y directions but whose properties may vary in the through-the-thickness (z) direction. The authors applied this method in particular to isotropic, orthotropic and composite laminated plates and cylinders [98, 155]. In order to use the PST, it is important to note that the considered unit cell needs to be meshed in a similar way on its opposite boundaries (i.e. left and right sides; bottom and top sides; and every edges along the z direction for a two-dimensional waveguide as seen in Fig.2.8), so that continuity in displacements and forces equilibrium is respected (i.e. $q_B^{k,m+1} = q_T^{k,m}$ and $f_B^{k,m+1} = -f_T^{k,m}$) as shown in Fig.2.9.

As for the 1D WFE method, using the PST allows for reducing considerably the number of variables [150]:

$$\begin{gathered}\mathbf{q_R} = \lambda_x \mathbf{q_L}; \qquad \mathbf{q_T} = \lambda_y \mathbf{q_B} \\ \mathbf{q_{RB}} = \lambda_x \mathbf{q_{LB}}; \quad \mathbf{q_{LT}} = \lambda_y \mathbf{q_{LB}}; \quad \mathbf{q_{RT}} = \lambda_x \lambda_y \mathbf{q_{LB}}.\end{gathered} \tag{2.45}$$

The nodal DoFs of the unit cell are partitioned in the following way: bottom, top, left, right, left bottom corner, right bottom corner, left top corner, right top corner and internal DoFs, which gives Eq.(2.46) (bd subscript stands for boundary).

$$\mathbf{q} = \begin{bmatrix}\mathbf{q_B^T} & \mathbf{q_T^T} & \mathbf{q_L^T} & \mathbf{q_R^T} & \mathbf{q_{LB}^T} & \mathbf{q_{RB}^T} & \mathbf{q_{LT}^T} & \mathbf{q_{RT}^T} & \mathbf{q_I^T}\end{bmatrix}^T = \begin{bmatrix}\mathbf{q_{bd}^T} & \mathbf{q_I^T}\end{bmatrix}^T. \tag{2.46}$$

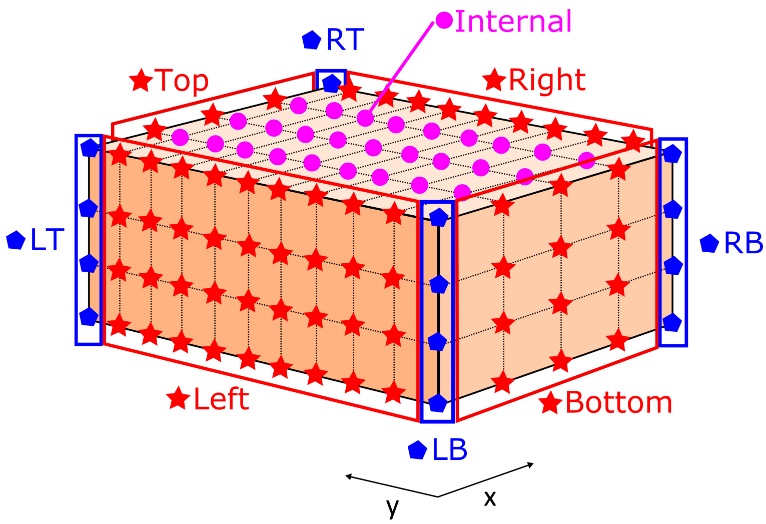

Figure 2.8: Partitioning of the degrees of freedom of a unit cell; '*' side nodes: bottom, top, left, right; 'diamond' corner nodes: LT (left-bottom), RB (right-bottom), LT (left-top), RT (right-top); 'o' internal nodes. Adapted from [150].

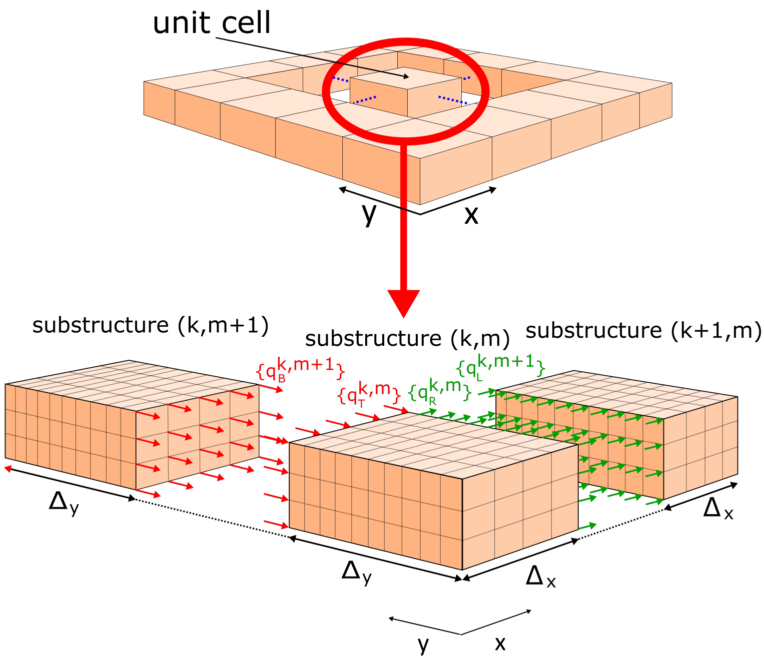

Figure 2.9: Decomposition of a two-dimensional periodic structure in an assembly of unit cells and presentation of the PST adapted from [96, 151].

In 2D WFE, the wavenumber k is expressed as follows:

$$k_x = k\cos(\theta), \quad k_y = k\sin(\theta),$$
$$k = \sqrt{k_x^2 + k_y^2}, \tag{2.47}$$

and the direction of propagation is written: $\theta = \tan^{-1}(k_y/k_x)$. The form of the eigenproblem depends once again on the problem type [152].

The wavenumber $k(k_x, k_y)$ is specified, $\mu = 0$ and ω is sought

The frequencies of the waves that propagate in the structure can be calculated from the standard linear eigenvalue problem [156, 157]. Using Eq. 2.45, the nodal DoFs can be rearranged as [150, 151]

$$\begin{pmatrix} \mathbf{q_B} \\ \mathbf{q_T} \\ \mathbf{q_L} \\ \mathbf{q_R} \\ \mathbf{q_{LB}} \\ \mathbf{q_{RB}} \\ \mathbf{q_{LT}} \\ \mathbf{q_{RT}} \\ \mathbf{q_I} \end{pmatrix} = \begin{bmatrix} \mathbf{I} & \mathbf{0} & \mathbf{0} & \mathbf{0} \\ \mathbf{I}\lambda_y & \mathbf{0} & \mathbf{0} & \mathbf{0} \\ \mathbf{0} & \mathbf{I} & \mathbf{0} & \mathbf{0} \\ \mathbf{0} & \mathbf{I}\lambda_x & \mathbf{0} & \mathbf{0} \\ \mathbf{0} & \mathbf{0} & \mathbf{I} & \mathbf{0} \\ \mathbf{0} & \mathbf{0} & \mathbf{I}\lambda_x & \mathbf{0} \\ \mathbf{0} & \mathbf{0} & \mathbf{I}\lambda_y & \mathbf{0} \\ \mathbf{0} & \mathbf{0} & \mathbf{I}\lambda_x\lambda_y & \mathbf{0} \\ \mathbf{0} & \mathbf{0} & \mathbf{0} & \mathbf{I} \end{bmatrix} \begin{pmatrix} \mathbf{q_B} \\ \mathbf{q_L} \\ \mathbf{q_{LB}} \\ \mathbf{q_I} \end{pmatrix} = \mathbf{\Lambda_R}(\mathbf{\lambda_x}, \mathbf{\lambda_y}) \begin{pmatrix} \mathbf{q_B} \\ \mathbf{q_L} \\ \mathbf{q_{LB}} \\ \mathbf{q_I} \end{pmatrix}. \tag{2.48}$$

Equilibrium at the right top corner nodes gives:

$$\mathbf{\Lambda_L}(\lambda_x, \lambda_y) \begin{pmatrix} \mathbf{f_{bd}} \\ \mathbf{0} \end{pmatrix} = \mathbf{0}, \tag{2.49}$$

with

$$\mathbf{\Lambda_L}(\lambda_x, \lambda_y) = \begin{bmatrix} \mathbf{I} & \mathbf{I}{\lambda_y}^{-1} & \mathbf{0} & \mathbf{0} & \mathbf{0} & \mathbf{0} & \mathbf{0} & \mathbf{0} & \mathbf{0} \\ \mathbf{0} & \mathbf{0} & \mathbf{I} & \mathbf{I}{\lambda_x}^{-1} & \mathbf{0} & \mathbf{0} & \mathbf{0} & \mathbf{0} & \mathbf{0} \\ \mathbf{0} & \mathbf{0} & \mathbf{0} & \mathbf{0} & \mathbf{I} & \mathbf{I}{\lambda_x}^{-1} & \mathbf{I}{\lambda_y}^{-1} & \mathbf{I}\lambda_x^{-1}\lambda_y^{-1} & \mathbf{0} \\ \mathbf{0} & \mathbf{0} & \mathbf{0} & \mathbf{0} & \mathbf{0} & \mathbf{0} & \mathbf{0} & \mathbf{0} & \mathbf{I} \end{bmatrix}. \tag{2.50}$$

The following eigenvalue problem appears

$$\mathbf{\Lambda_L}(\mathbf{K} - \omega^2\mathbf{M})\mathbf{\Lambda_R} \begin{pmatrix} \mathbf{q_B} \\ \mathbf{q_L} \\ \mathbf{q_{LB}} \\ \mathbf{q_I} \end{pmatrix} = 0. \tag{2.51}$$

The frequency and one wavenumber, say k_x, is specified. k_y is sought

The eigenvalue problem is quadratic in λ_y [156, 157]. The inner DoFs are condensed, the explicit coefficients $\mathbf{X}(\omega, \lambda_x), \mathbf{Y}(\omega, \lambda_x), \mathbf{Z}(\omega, \lambda_x)$ are given such that the equation of motion is written as:

$$(\lambda_y^2 \mathbf{X} + \lambda_y \mathbf{Y} + \mathbf{Z}) \begin{pmatrix} \mathbf{q_B} \\ \mathbf{q_L} \\ \mathbf{q_{LB}} \end{pmatrix} = \mathbf{0}. \tag{2.52}$$

The frequency and the direction of propagation are specified, k is sought

The eigenvalue problem is polynomial or transcendental [98].

2.3.3 The Craig-Bampton method

Applying the WFE method to large models implies large computational cost. Component Mode Synthesis (CMS) are standard methods to reduce the complexity of structural dynamics models leading to reduced CPU cost. The Craig-Bampton method introduced in [158] is one of them. This method has been widely used in the literature and in particular alongside the WFE method [103, 157, 150, 151, 159, 160].

For free wave propagation, no external force acts on the internal nodes of the structure, this leads to $\mathbf{f_I} = \mathbf{0}$. The equation of motion (Eq.(2.29)) of the unit cell becomes:

$$\left(\begin{bmatrix} \mathbf{K_{bdbd}} & \mathbf{K_{bdI}} \\ \mathbf{K_{Ibd}} & \mathbf{K_{II}} \end{bmatrix} - \omega^2 \begin{bmatrix} \mathbf{M_{bdbd}} & \mathbf{M_{bdI}} \\ \mathbf{M_{Ibd}} & \mathbf{M_{II}} \end{bmatrix} \right) \begin{Bmatrix} \mathbf{q_{bd}} \\ \mathbf{q_I} \end{Bmatrix} = \begin{Bmatrix} \mathbf{f_{bd}} \\ \mathbf{0} \end{Bmatrix}. \tag{2.53}$$

with $\mathbf{q_{bd}}$ the boundary nodal DoFs, which vary according to the type of problem (i.e. 1D WFE or 2D WFE).

The key to this method is the reduction of the internal nodal DoFs. $\mathbf{q_\Phi}$ is the reduced set of the physical internal DoFs $\mathbf{q_I}$, whereas the boundary DoFs $\mathbf{q_{bd}}$ are kept as physical coordinates [158, 161]. Hence, a set of ‘fixed boundary’ modes, also called ‘component’ modes $\mathbf{\Phi_C}$ are selected amongst a subset $\mathbf{\Phi_I}$ of the local modes of the unit cell when the boundary DoFs are fixed and no force is acting on the internal nodes. $\mathbf{\Phi_I}$ is obtained by solving the following eigenvalue problem:

$$\left[\mathbf{K_{II}} - \omega^2\mathbf{M_{II}}\right]\mathbf{\Phi_I} = \mathbf{0}, \tag{2.54}$$

The modal selection is based on the lowest resonance frequencies of the clamped model. A rule-of-thumb is to select all modes in $\mathbf{\Phi_I}$ whose resonance frequency is situated within $[0, 3f_{max}]$ to form the modal basis $\mathbf{\Phi_C}$, with f_{max} the maximum frequency of interest for the wave dispersion analysis [157, 151, 159].

$\mathbf{\Phi_{bd}}$ represents the static boundary modes. It is called 'static' as it uses the system equation describing the unit cell behaviour for a static analysis [158]:

$$\mathbf{Kq} = \mathbf{F}. \tag{2.55}$$

This gives

$$\begin{bmatrix} \mathbf{K_{bdbd}} & \mathbf{K_{bdI}} \\ \mathbf{K_{Ibd}} & \mathbf{K_{II}} \end{bmatrix} \begin{Bmatrix} \mathbf{q_{bd}} \\ \mathbf{q_I} \end{Bmatrix} = \begin{Bmatrix} \mathbf{f_{bd}} \\ \mathbf{0} \end{Bmatrix}. \tag{2.56}$$

And from the second row of Eq.(2.56), it can be written

$$\mathbf{K_{Ibd}q_{bd}} + \mathbf{K_{II}q_I} = \mathbf{0}, \tag{2.57}$$

or

$$\mathbf{q_I} = -\mathbf{K_{II}}^{-1}\mathbf{K_{Ibd}q_{bd}} = \mathbf{\Phi_{bd}q_{bd}}. \tag{2.58}$$

Thus, the matrix of static boundary modes $\mathbf{\Phi_{bd}}$ is written as proposed in [157, 158, 150, 151, 159] and displayed in Eq.(2.59):

$$\mathbf{\Phi_{bd}} = -\mathbf{K_{II}^{-1}K_{Ibd}}. \tag{2.59}$$

Matrix inversion can be very costly when considering extra large problems. Using the preconditioned conjugate gradients method allows for solving $-\mathbf{K_{II}\Phi_{bd}} = \mathbf{K_{Ibd}}$ without inversion and is used in our methodology. The Craig-Bampton transformation matrix $\mathbf{B}$ uses both $\mathbf{\Phi_C}$ and $\mathbf{\Phi_{bd}}$ to reduce the internal nodal

DoFs and keeps the boundary nodal DoFs identical as follows:

$$\left\{ \begin{array}{c} \mathbf{q_{bd}} \\ \mathbf{q_I} \end{array} \right\} = \left[\begin{array}{cc} \mathbf{I} & \mathbf{0} \\ \mathbf{\Phi_{bd}} & \mathbf{\Phi_C} \end{array} \right] \left\{ \begin{array}{c} \mathbf{q_{bd}} \\ \mathbf{q_\Phi} \end{array} \right\} = \mathbf{B} \left\{ \begin{array}{c} \mathbf{q_{bd}} \\ \mathbf{q_\Phi} \end{array} \right\}. \tag{2.60}$$

The $\mathbf{B}$ matrix is the link between the physical coordinates and reduced ones. The mass and stiffness matrix $\mathbf{M}$ and $\mathbf{K}$ are projected on this basis [157, 158, 150, 151, 159].

$$\tilde{\mathbf{K}} = \mathbf{B^T K B}, \qquad \tilde{\mathbf{M}} = \mathbf{B^T M B}. \tag{2.61}$$

This provides an efficient and reduced basis allowing for describing the response of the internal DoFs.

The WFE formulation (1D or 2D) dictates the boundary nodal DoFs that need to be 'clamped' in order to obtain the appopriate $\mathbf{\Phi_C}$. Combining the CMS reduction method (Eq.(2.61)) and the 1D WFE method (Eq.(2.37)) gives

$$\mathbf{\Lambda_L B^T}(\mathbf{K} - \omega^2 \mathbf{M})\mathbf{B \Lambda_R} \begin{pmatrix} \mathbf{q_L} \\ \mathbf{q_\Phi} \end{pmatrix} = 0. \tag{2.62}$$

When combined with the 2D WFE method (Eq.(2.51)), the eigenproblem to be solved is given as follows

$$\mathbf{\Lambda_L B^T}(\mathbf{K} - \omega^2 \mathbf{M})\mathbf{B \Lambda_R} \begin{pmatrix} \mathbf{q_B} \\ \mathbf{q_L} \\ \mathbf{q_{LB}} \\ \mathbf{q_\Phi} \end{pmatrix} = 0. \tag{2.63}$$

2.4 Conclusions

Textile composite materials are increasingly used in the aerospace industry. They are composed of a fabric used as reinforcement and a binding polymer used as a matrix. These materials are complex at different level and thus the prediction of their dynamic behaviour is complicated. For these reasons, multiscale modelling needs to be considered for simulations involving these materials.

For SHM and NDE purposes, being able to predict wave propagation characteristics in these materials is of the upmost importance. Various methods for dispersion characterisation of homogeneous, layered or periodic structures have been presented. WFE and in particular the formulation where the wavenumber is specified and the frequency sought is the most adequate method to be applied to a detailed model. Thus, attempts should be made to combine this method with detailed mesoscale models of textile composites for dispersion characterisation. A drawback of this formulation, however, lies in the assumption of no attenuation. Therefore, an effort to formulate a damping model within this method is to be made.

Chapter 3

Methodology for numerical dispersion characterisation of textile composites

In this chapter, a novel methodology for dispersion characteristics prediction of textile composites is presented. The methodology combines mesoscale modelling of the material with the WFE and CMS methods. In the first two sections, the one- and two-dimensional WFE methods are used to compute the dispersion characteristics for structures made of isotropic and laminated composite materials, and are compared with other analytical, semi-analytical and numerical methods. The aim is to display the wide range of application of the WFE method and to verify its validity in comparison with other existing methods. The third section presents the whole methodology developed to obtain the dispersion characteristics of textile composites.

3.1 One-dimensional WFE: examples and comparisons

Comparisons involving the 1D WFE method are presented in this section. Analytical models are compared against the WFE method for a homogeneous isotropic beam. Then, the WFE method is compared to a transient FEA for a laminated composite beam.

3.1.1 Comparison of analytical models and the WFE method

The dispersion characteristics are computed for a homogeneous beam made of an isotropic material. Different methods are used: the analytical method whose models are described in Sec.2.2.1 and the WFE method whose formulations are described in Sec.2.3.1. Even though the WFE method is suited for layered or periodic media, it can be applied to continuous media as well by introducing a virtual periodicity. An example of a period of a homogeneous isotropic beam modelled with Abaqus is displayed in Fig.3.1. Linear brick elements (C3D8) are used and no boundary conditions are applied. The model dimensions are of $0.02 \times 0.1 \times 0.5$ mm and the beam is assumed to be of infinite length in the x direction. Its mechanical properties are as follow: E=70 GPa, $\nu = 0.1$ and $\rho = 1600 kg/m^3$.

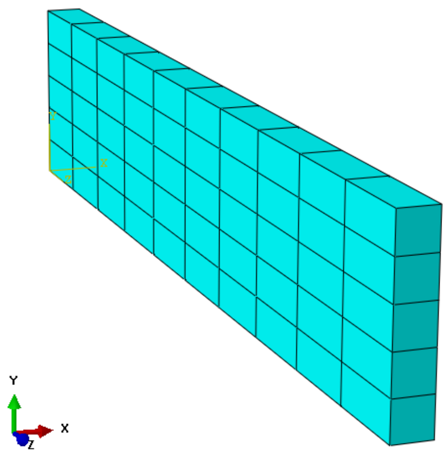

Figure 3.1: Meshed unit cell model used to compute the dispersion characteristics of the described beam structure by WFE.

Figure 3.2 displays the dispersion characteristics obtained with the analytical models presented in Sec.2.2.1 as well as the results obtained with both eigenproblem formulations of the 1D WFE presented in Sec.2.3.1 for relatively low frequencies. A perfect agreement is observed between the dispersion curves obtained through the three different methods as expected.

Figure 3.3 shows the dispersion characteristics of the two bending modes obtained with the Euler-Bernoulli and Timoshenko analytical models presented in Sec.2.2.1 as well as all modes obtained with the WFE method for a middle to high frequency range. From around 0.2 MHz, the predictions from the Euler-Bernoulli

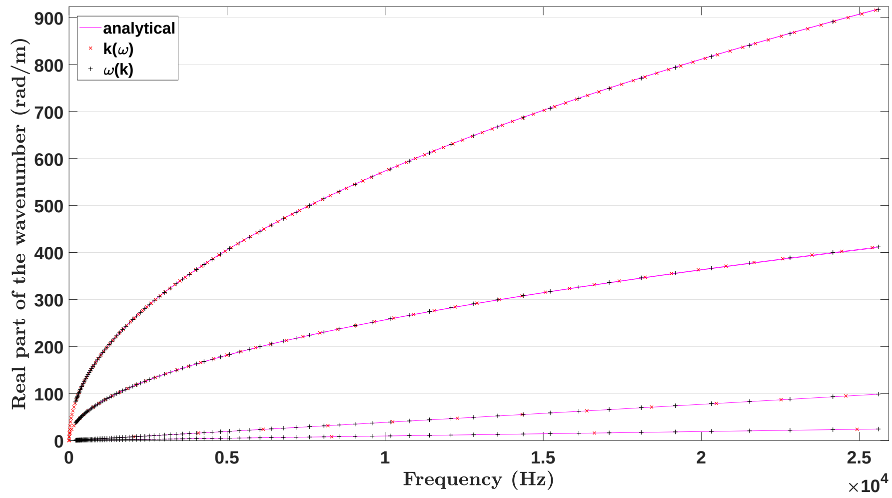

Figure 3.2: Dispersion curves of the first four modes of a thin isotropic beam using three different methods at low frequency: the analytical method whose models are found in Sec.2.2.1 (–), the k(ω) WFE formulation (*) (see Eq.(2.37)), and the ω(k) WFE formulation (+) (see Eq.(2.43)). From the lowest part of the figure to the highest: the longitudinal mode, the torsional mode and the two bending modes.

model start diverging from the two other methods. The Timoshenko model and the WFE method, however, are showing a good agreement. These results were expected as stated in Sec.2.2.1.

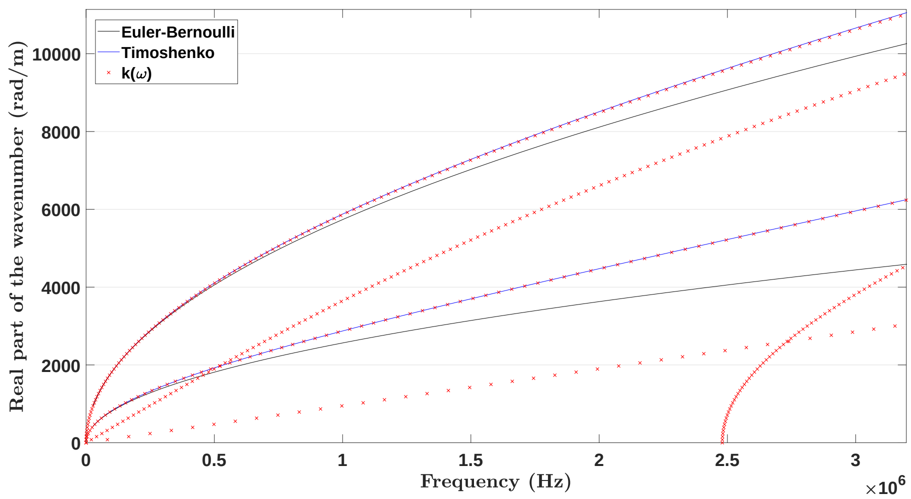

Figure 3.3: Dispersion curves of the two bending modes of a thin isotropic beam using three different methods at higher frequency: the Euler-Bernoulli analytical model (black –), the Timoshenko analytical model(blue –) and the k(ω) WFE formulation (*) for which all modes are plotted.

Comparing the WFE method with analytical models for validation shows limitations as the analytical models lack in robustness for inhomogeneous materials and high frequencies.

3.1.2 Comparison of transient FEA and the WFE method

To ensure the numerical validity of the WFE method, a transient FEA is performed for a laminated composite beam as an alternative to obtain the dispersion relations using Abaqus. The beam is composed of five orthotropic layers of different moduli and a period is displayed in Fig.3.4. The mechanical properties of the five layers can be found in Tables B.1-B.5 in Appendix.

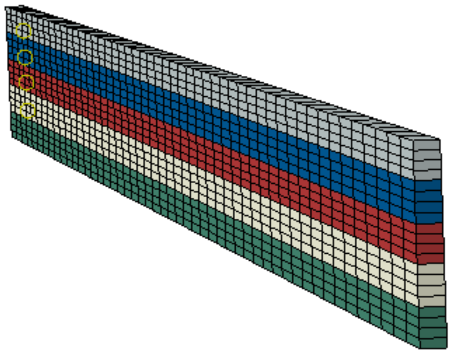

Figure 3.4: Meshed unit cell model used to compute the dispersion characteristics of the described laminated composite beam structure by WFE. The dimensions of the modelled unit cell are $0.20 \times 20 \times 1.97$ mm.

The modelled beam is 20 mm wide, 2750 mm long and has a thickness of 1.97 mm. No boundary conditions are applied, the elements are C3D8 and Abaqus/Explicit solver is used. A signal is generated at one end side of the beam and the displacements induced by the wave propagation along the beam are measured and recorded over time at a set of discrete positions. The input excitation signal is sinusoidal periodic and carries a wide frequency band. Two cycles of the sinusoidal function (Eq.(3.1)) are modulated by a window function (Hanning window here: Eq.(3.2)).

The equation for the sinusoidal function is as follows

$$f(t) = sin(\omega t), \tag{3.1}$$

with ω the angular frequency and t the time. The Hanning window is written as

$$w(n) = sin^2\left(\frac{\pi n}{N}\right), 0 \leq n \leq N, \tag{3.2}$$

$L = N + 1$ is the window length. N is calculated as follows

$$N = No._{cycles}\frac{2\pi f_s}{\omega}, \tag{3.3}$$

with $No._{cycles}$ the number of cycles and f_s the sampling frequency.

These two functions as well as the result of the modulation are shown in Fig.3.5. The discrete Fourier transform of the signal is plotted in Fig.3.6. It can be observed that the signal has a wide frequency band around the central frequency of 300 kHz. The interest in having a wide frequency band in the excitation signal is that only one simulation is needed to obtain the dispersion relations for a large frequency band.

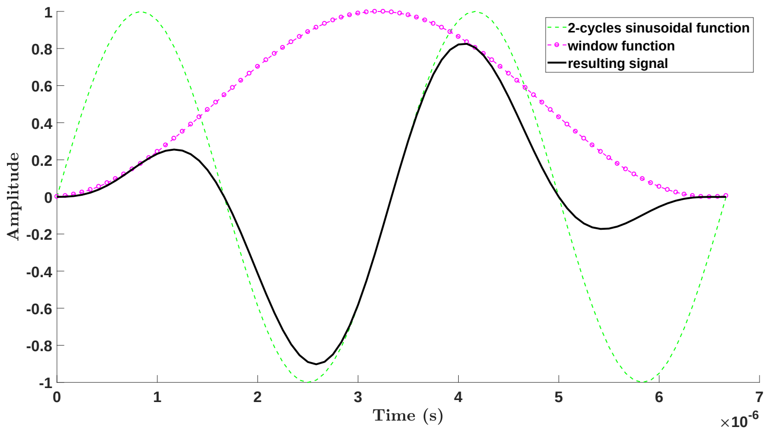

Figure 3.5: Example of an input signal (–) created using a 2-cycles sinusoidal function with a central frequency of 300 kHz (- -), modulated by a Hanning window (- o -).

The two-dimensional Fast Fourier Transform (FFT) [162, 163] is applied on the displacements amplitude over time extracted at a set of discrete positions along the beam to obtain the dispersion curves. These dispersion characteristics are plotted in Fig.3.7 and a perfect agreement between this method and the WFE method is observed.

A drawback of using the first formulation presented in Sec.2.3.1 comes from the periodicity of the propagation constant function ($\lambda = e^{-ik\Delta}$) which restricts

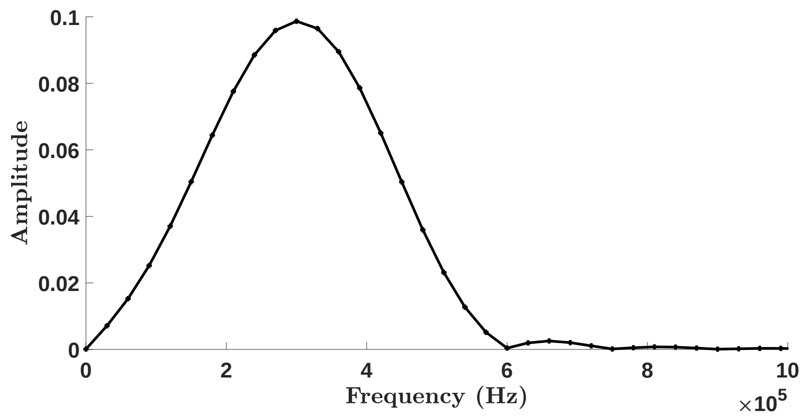

Figure 3.6: Discrete Fourier transform of the input signal presented in Fig.3.5.

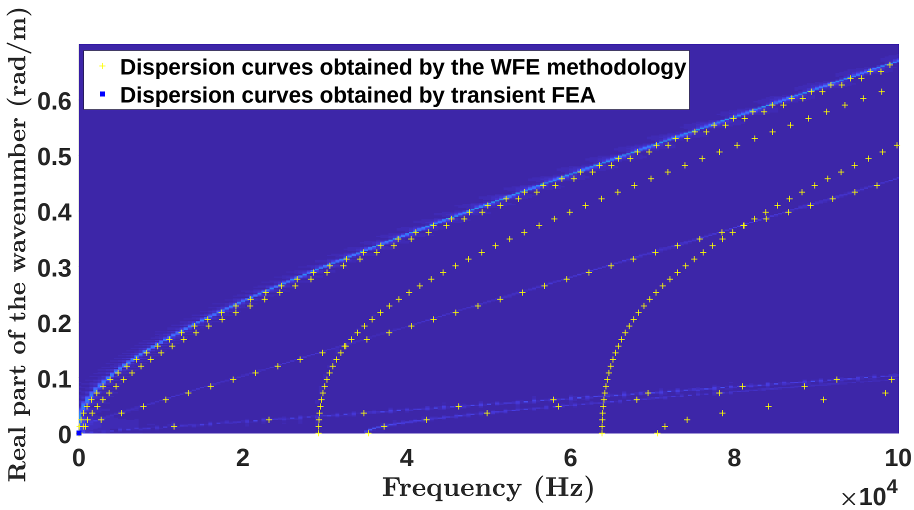

Figure 3.7: Dispersion characteristics of a laminated composite beam, whose layers each are a different homogeneous orthotropic material. In the background are the results from the transient FEA, the WFE results are plotted as yellow +. A perfect agreement is observed. In this transient FEA, only the longitudinal and out-of-plane displacements (respectively U_1 and U_3) were captured, thus the flexural mode, whose principal displacement component is U_2, is not observed.

the wavenumber study in the $[-\pi/\Delta, \pi/\Delta]$ interval (called the BZ as detailed in Sec.2.2.2) and when applied to a continuous medium, artificial aspects are introduced due to this periodicity: the branches of the dispersion curves are reflected at the limits of the BZ creating a confusing representation. In order to obtain a clear dispersion curves representation, the aspect ratio of the unit cell $Ra = \Delta/2b$ has to be chosen wisely (2b represents the thickness and Δ the cell length). Figure 3.8 shows the results obtained for a unit cell of aspect ratio $Ra = 0.1$ and of $Ra = 4$. In the case of a continuous medium, the reflected branches do not have a physical meaning as the periodicity of the material is only virtual and cannot be observed using transient FEA as seen in Fig.3.7. In [164], the authors state that the aspect ratio should be below 0.2 to provide a clear representation. While it is possible to wield the length of the unit cell to provide a good aspect ratio in the case of a continuous medium, this is not an option when considering a periodic medium as its period is definite and its thickness cannot be changed either without altering the properties of the model.

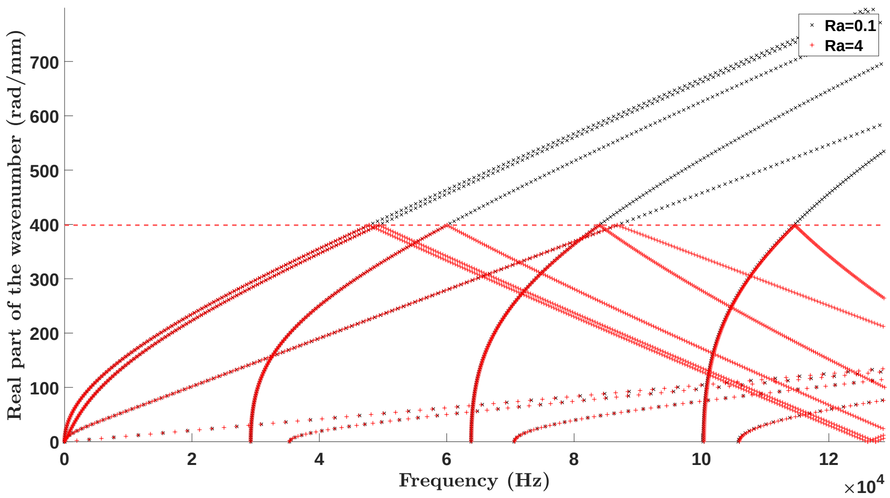

Figure 3.8: Dispersion characteristics of a laminated composite beam, whose layers each are a different homogeneous orthotropic material, for two different aspect ratios. $Ra = 0.1$ (+) and $Ra = 4$ (*). The horizontal red dotted line defines the limit of the IBZ.

A method based on the computation of the correlation level between mode-shapes allows for recovering results in a clear form (similarly to the results obtained for $Ra = 0.1$ in Fig.3.8) from results obtained with a large Ra (similarly to the results obtained for $Ra = 4$) by 'unwrapping' the modes branches. The Modal Assurance Criterion (MAC) as defined in [165] is used to quantify the correlation.

3.2 Two-dimensional WFE: examples and comparisons

Comparisons involving the 2D WFE method are presented in this section. The analytical models are compared against the WFE method for a homogeneous isotropic plate. Then, the SAFE and WFE methods are compared for a laminated composite plate.

3.2.1 Comparison of analytical models and the WFE method

The dispersion characteristics are computed for a homogeneous plate made of an isotropic material. Different methods are used: the analytical method whose models are described in Sec.2.2.1 and the WFE method whose formulations are described in Sec.2.3.2. Even though the WFE method is suited for periodic media, it can be applied to continuous media as well by introducing a virtual periodicity. An example of a period of a homogeneous plate modelled with Abaqus is displayed in Fig.3.9. No boundary conditions are applied and the elements are C3D8. A convergence study was performed to ensure sufficient elements in the thickness. Its dimensions are of 0.02 $\times$ 0.02 $\times$ 0.5 mm and the plate is assumed to be of infinite length in both the x and y directions. Its mechanical properties are as follow: E=70 GPa, $\nu = 0.1$ and $\rho = 1600 kg/m^3$.

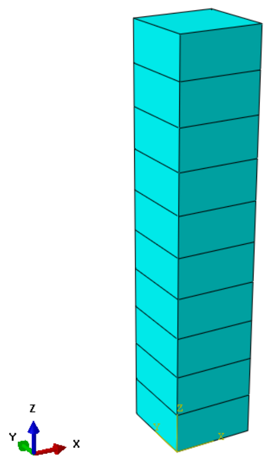

Figure 3.9: Meshed unit cell model used to compute the dispersion characteristics of the described plate structure by WFE.

Figure 3.10 displays the dispersion characteristics obtained with the analytical model presented in Sec.2.2.1 as well as the results obtained with the 2D WFE method for two of the eigenproblem formulations presented in Sec.2.3.2 for relatively low frequencies. A perfect agreement is observed between the dispersion curves obtained through all three different methods as expected.

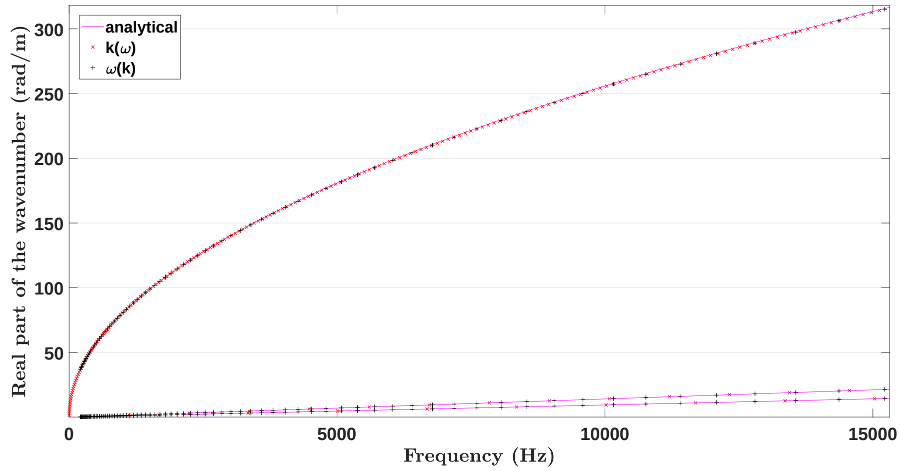

Figure 3.10: Dispersion curves of the first three modes of a thin isotropic plate using three different methods at low frequency: the analytical method whose models are found in Sec.2.2.1 (–), the k(ω) WFE formulation (*), and the ω(k) WFE formulation (+).

Figure 3.11 shows the dispersion characteristics of the three first modes obtained with the analytical model presented in Sec.2.2.1 as well as the dispersion curves obtained with the WFE method for a middle to high frequency range. It shows a divergence between the two models starting at around 50 kHz. There exist analytical models that provide better predictions for a higher frequency range but this is not the topic of the thesis.

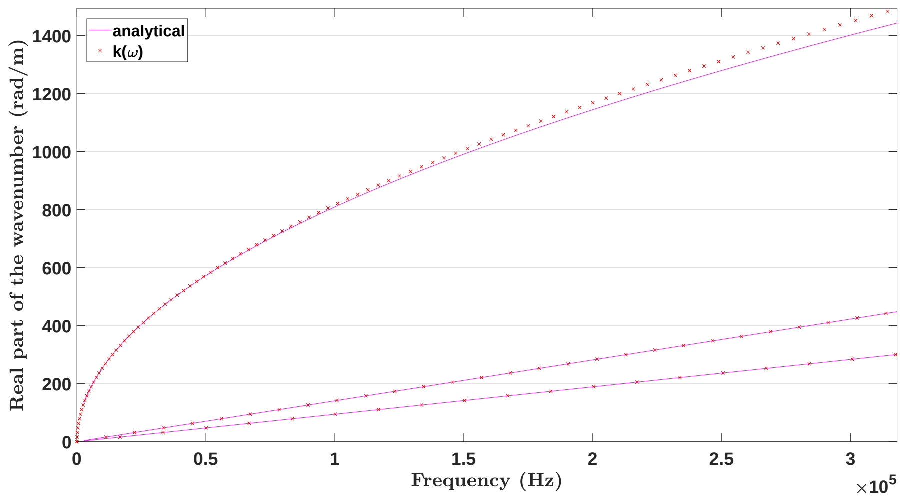

Figure 3.11: Dispersion curves of the first three modes of a thin isotropic plate using two different methods at higher frequency: the analytical method whose models are found in Sec.2.2.1 (–), and the k(ω) WFE formulation (*).

Once again, comparing the WFE method with analytical models shows limitations as they lack in robustness for inhomogeneous materials and high frequencies. Indeed, in the CPT, the displacement field is based on the three Kirchhoff hypothesis [166] which encounter limitations for high frequencies.

3.2.2 Comparison of the SAFE and WFE methods

SAFE just like WFE is a semi-analytical method that is used in industry for simulating Lamb waves in inhomogeneous media such as laminated composites. The output from the SAFE method (briefly presented in Sec.2.2.3) are the wavenumbers and the modeshapes similarly to one of the WFE formulations. The SAFE method, however, has the advantage of being faster than the WFE method. Nonetheless it bears a significant disadvantage over the WFE method in its limited range of application. Indeed while the WFE can deal both with periodic and continuous laminated structures, the SAFE method only handles the latter.

Both methods are used to compute the dispersion relations of a laminated composite plate, whose layer properties are orthotropic and of infinite dimensions, for propagation in the x and y directions and displayed in Fig.3.12-3.13. An excellent agreement between the two methods is observed for a wide frequency band.

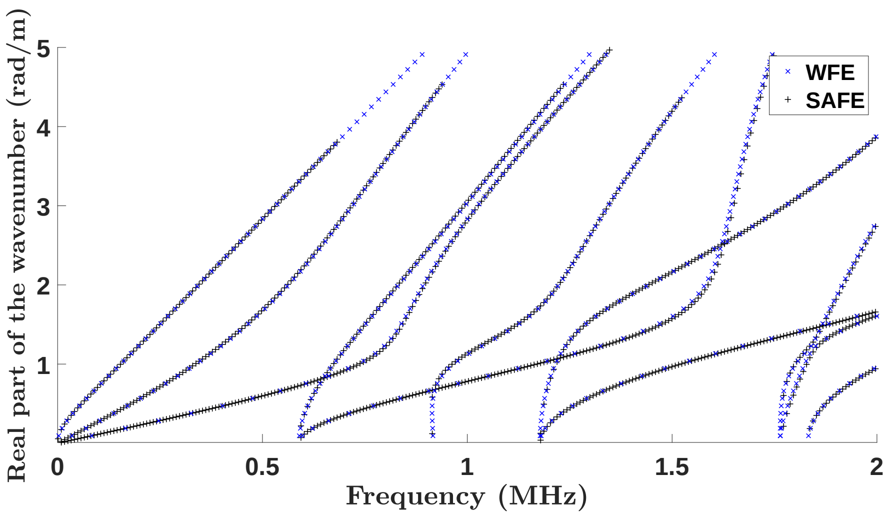

Figure 3.12: Dispersion characteristics of a laminated composite plate composed of five orthotropic layers in the x direction of propagation. Using the WFE method ($\times$) and the SAFE method ($+$). Excellent agreement is observed.

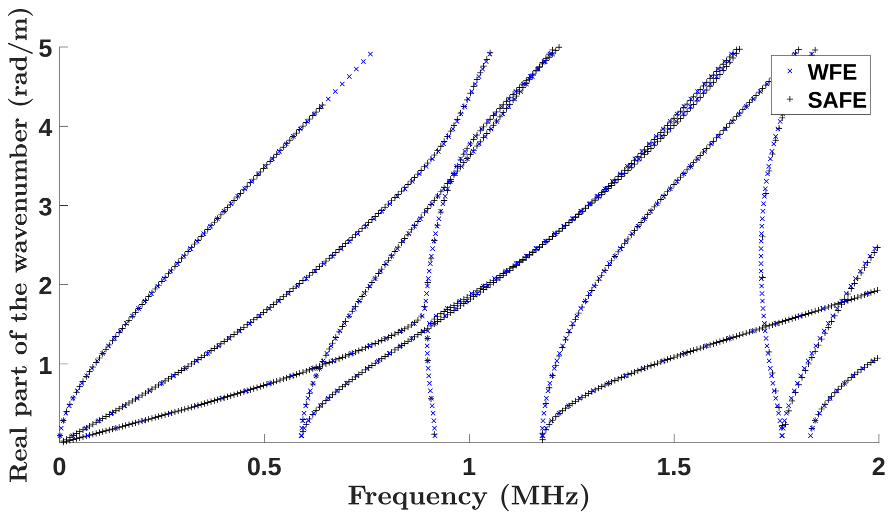

Figure 3.13: Dispersion characteristics of a laminated composite plate composed of five orthotropic layers in the y direction of propagation.Using the WFE method ($\times$) and the SAFE method ($+$). Excellent agreement is observed.

3.3 Dispersion characterisation of textile composites

Numerical characterisation of the dispersion properties of a textile composite structure begins with the mesoscale modelling of its unit cell. Firstly, the definition of the textile unit cell geometry is performed using a specialist pre-processor such as Texgen [51, 167, 168, 169, 170] (see Sec.B.2 in Appendix). This open source software is developed by the Composites Research Group at the University of Nottingham and is used for modelling the geometry of textile structures such as 2D or 3D fabrics (see Fig.2.1). The mechanical properties are added to the yarns and the matrix during the model definition process. Once the model has been generated, it can be exported to a FE software, and finally the mass and stiffness matrices $\mathbf{M}$ and $\mathbf{K}$ of the unit cell can be extracted, as shown in Fig.3.14. The matrices are inserted in the equation of motion (see Eq.(2.29)), the Craig-Bampton method (see Sec.2.3.3) is applied to reduce the size of the problem and finally the WFE method is applied to obtain the dispersion relations for a one-dimensional or two-dimensional waveguide as presented respectively in Sec.2.3.1 and Sec.2.3.2. In order to avoid a condensation of the internal DoFs to the boundary of the unit cell, the eigenproblem formulation of choice is the one where the wavenumber k is specified, $\mu = 0$ and the frequency is sought.

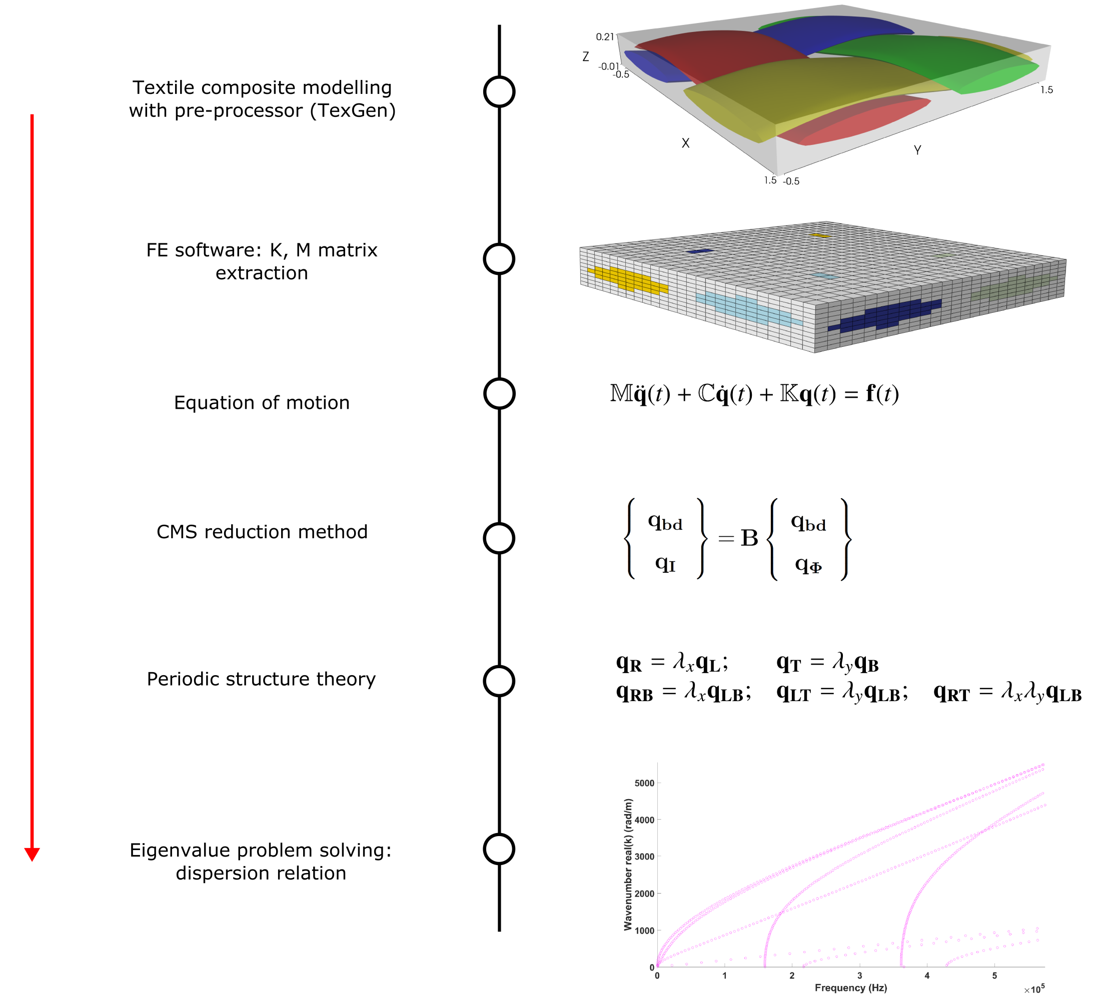

Figure 3.14: Step-by-step methodology of the mesoscale formulation for dispersion characterisation of composites.

This section focuses on the compatibility and interfacing between the textile composite mesoscale modelling and the WFE and CMS methods as well as the different issues it raises. The textile composite of choice for most case studies in this section is a one layer 2D plain woven composite (whose unit cell is shown in Fig.3.14) as it requires only a simple modelling while exhibiting characteristics of textile composites such as yarn undulation and interlacing.

3.3.1 Element types

The FE software used in the study is Abaqus whose choices of 3D solid elements are hexahedral, wedge or tetrahedral elements. TexGen on the other side offers two types of discretisation that are compatible with Abaqus: either a voxel discretisation with a hexahedral mesh or a conformal discretisation with a tetrahedral mesh [167]. The voxel mesh proposes a coarse but robust discretisation of the geometry and greatly simplifies the automated mesh generation while a tetrahedral mesh provides much better geometrical description but possibly degenerated elements (e.g. disproportionate elements with one edge considerably larger than another).

When considering a linear brick element (e.g. C3D8 in Abaqus) and a linear tetrahedral element (e.g. C3D4 in Abaqus), the linear brick element is of better quality. The use of linear tetrahedral elements is often discouraged unless used in great quantity for an extremely fine mesh as they are overly stiff. Another possibility is to use quadratic tetrahedral elements (e.g. C3D10 in Abaqus), however, these greatly increase the number of nodes without increasing the quality of the geometrical discretisation.

It is important to note that in order to obtain accurate results, a requirement of using at least six to ten elements per wavelength [58] has to be applied. Also in the cross-sectional plan, the number of elements has to be high enough to describe the geometrical and mechanical properties of the material but also to characterise the modeshapes. Finally the shape of the elements should comply with requirements of conventional FE modelling.

Three mesh convergence studies are performed on a 2D plain woven composite model, whose unit cell is displayed in Fig.3.15. One uses linear hexahedral elements (i.e. C3D8), the second uses linear tetrahedral elements (i.e. C3D4) and the last uses quadratic tetrahedral elements (i.e. C3D10). An example of each mesh with approximately the same number of nodes is displayed in Fig.3.16 for comparison. The materials properties are given in Tables B.6 and B.7 in Appendix.

A convergence study is performed by comparing the effective mechanical properties obtained by static virtual testing (see Sec.A.1 in Appendix). For simplicity, this type of convergence study is named ‘static convergence study’ in the manuscript. The mesh is gradually refined and each new mesh is composed of around twice as many nodes as the previous mesh. The relative error for a mesh is computed relatively to the next finer mesh. Detailed illustrations displaying the mesh refinement of the models are shown in Fig.B.4-B.6 and their effective

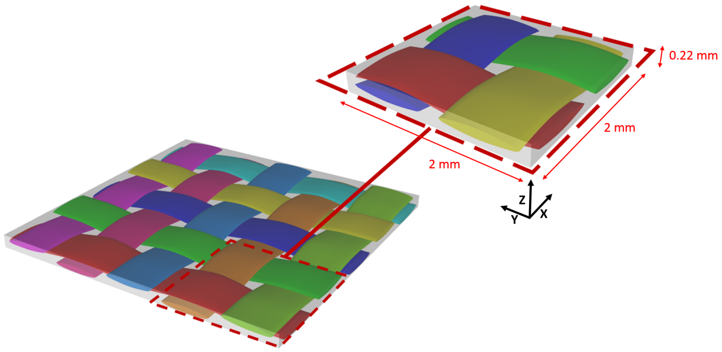

Figure 3.15: 2D plain woven composite and its unit cell.

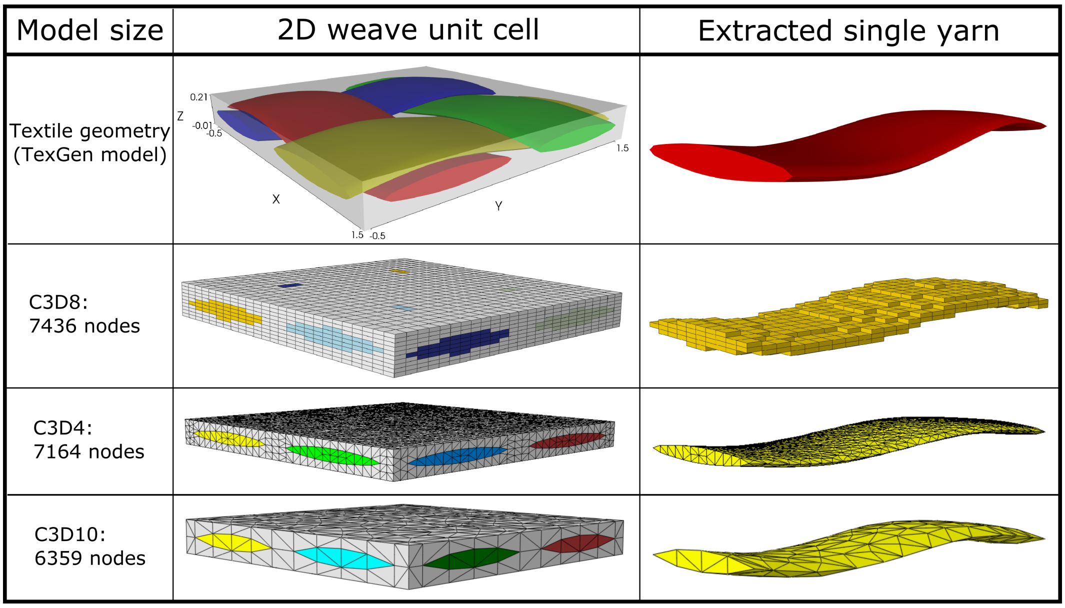

Figure 3.16: C3D8, C3D4 and C3D10 mesh models comparison for the same unit cell of a 2D plain woven composite. All three models contain approximatively the same number of nodes.

mechanical properties in Tables B.8-B.10 in Appendix.

Figure 3.17 displays the results for a static convergence study performed for the linear hexahedral mesh models. It is observed that the effective material properties tend to converge only for very a fine mesh (see Fig.B.6 in Appendix) when using a voxel discretisation and linear hexahedral elements. This can easily be justified by the lack of accuracy in the geometry representation induced by the voxel discretisation and can be quantified by observing the matrix and yarn volume fraction in the model (see Fig.3.18).

On the other hand, a standard discretisation using tetrahedral elements provides an accurate geometrical representation and thus a steady yarn volume frac-

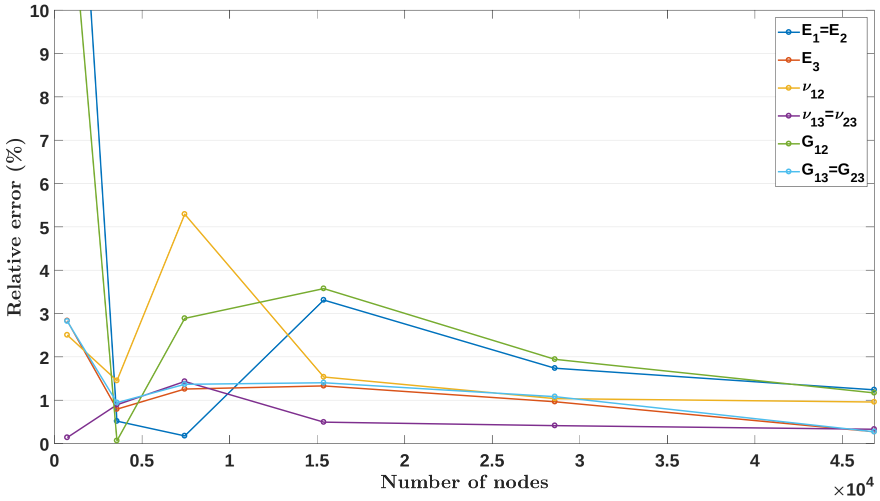

Figure 3.17: Convergence study, using the engineering constants as comparing parameters for the models discretised using a linear hexahedral mesh.

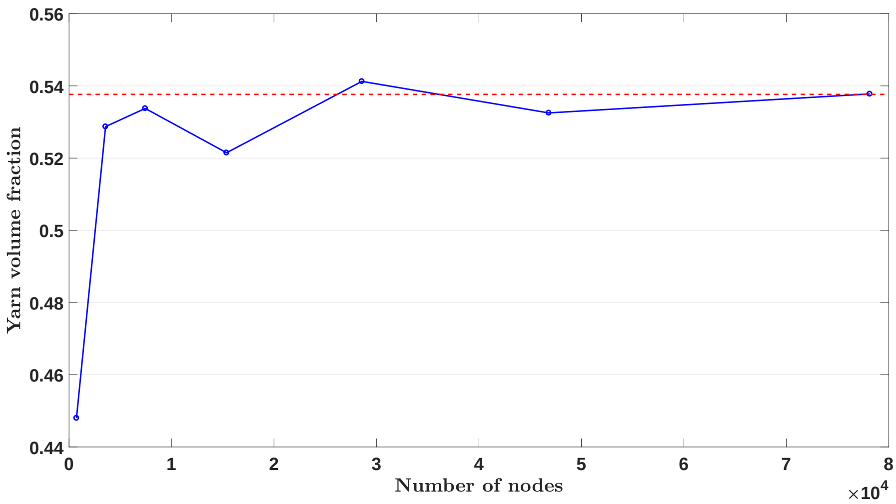

Figure 3.18: Yarn volume fraction within the different models discretised using voxel elements (in blue). The red horizontal line gives the theoretical TexGen value.

tion and a 'fast' convergence of the effective material properties as observed in Fig.3.19 and in [171].

A technique to correct the inaccurate yarn volume fraction in the voxel models is to reflect the error on the fibre volume fraction contained in a yarn, e.g. if the effective yarn volume fraction in the FE model is lower than the theoretical yarn volume fraction, increasing the fibre volume fraction within the yarn increases the actual fibre volume fraction in the whole composite and thus provides a faster convergence as shown in Fig.3.20.

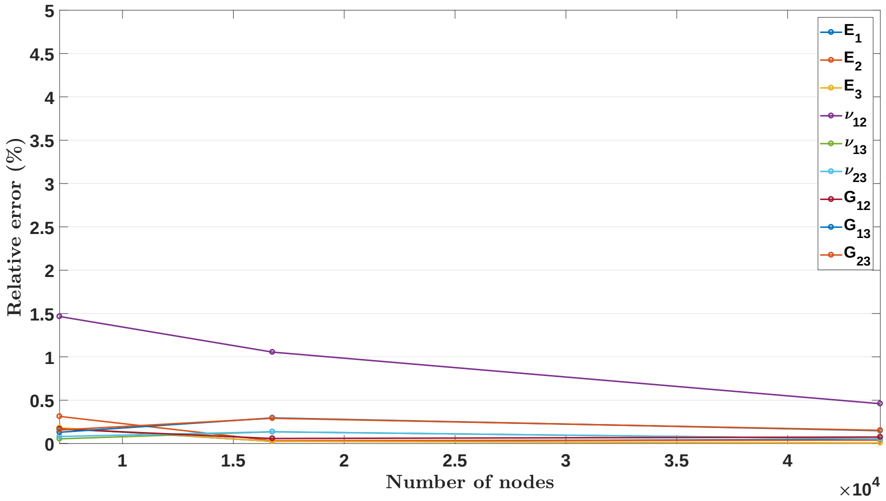

Figure 3.19: Convergence study, using the engineering constants as comparing parameters for the models discretised using a linear tetrahedral mesh.

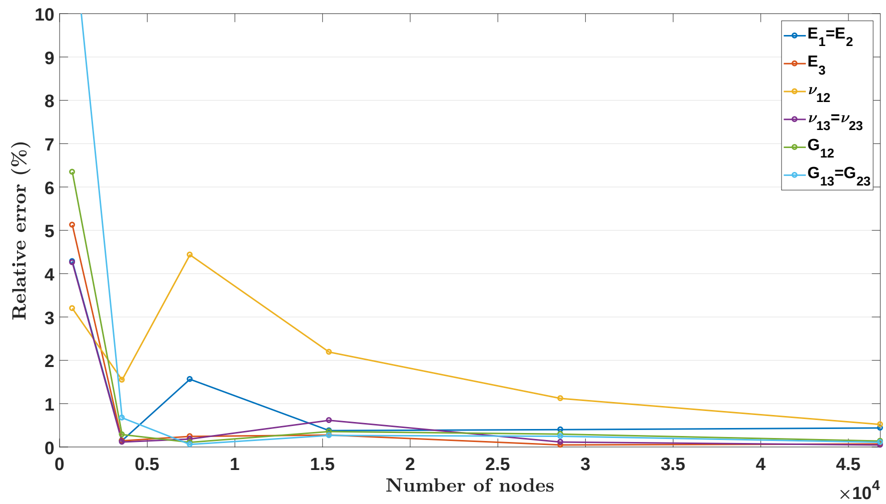

Figure 3.20: Convergence study, using the engineering constants as comparing parameters for the models discretised using a linear hexahedral mesh and adjusted volume fractions.

However, since the dispersion characteristics are of interest, a second convergence study is performed by comparison of the dispersion curves obtained using the different meshes. It should be noted that most studied mesoscopic structures in the thesis are complex composite plates whose cross-sections are non-homogeneous, thus the propagating modes are not pure Lamb modes but rather quasi Lamb modes. For the sake of briefness, the quasi Lamb modes will simply be referred as Lamb modes throughout the thesis. In Fig.3.21.a are displayed the flexural modes obtained for linear tetrahedral meshes of the 2D plain

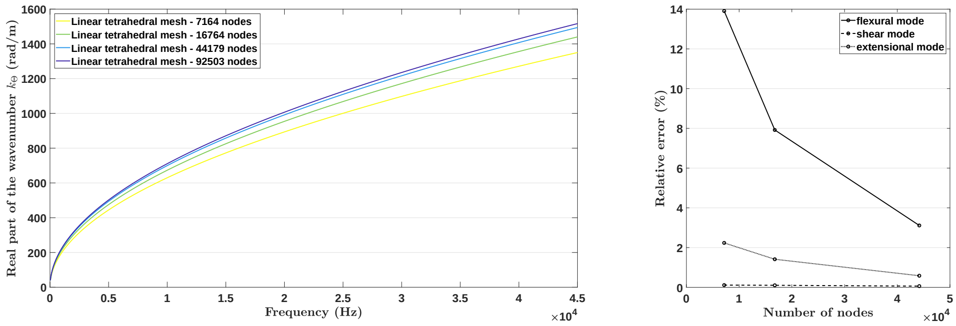

(a) (b)

Figure 3.21: Convergence study based on the dispersion characteristics of the linear tetrahedral mesh models. (a) flexural mode dispersion curve for models with different number of nodes (b) convergence of the wavenumber parameter.

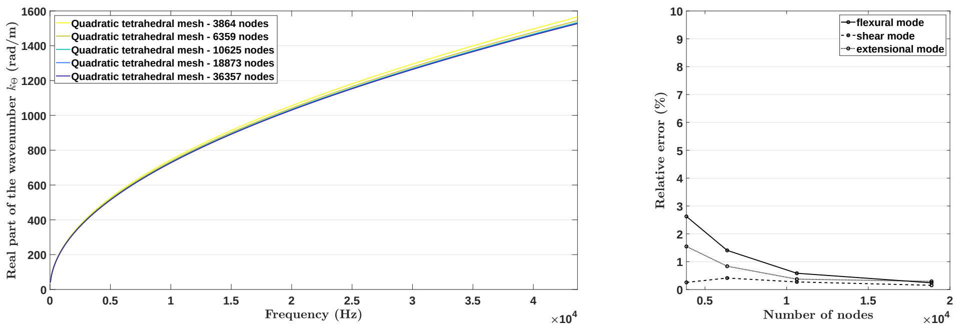

(a) (b)

Figure 3.22: Convergence study based on the dispersion characteristics of the quadratic tetrahedral mesh models. (a) flexural mode dispersion curve for models with different number of nodes (b) convergence of the wavenumber parameter.

woven composite model and in Fig.3.21.b the relative error for the three first modes dispersion curves. It is deduced that a great number of elements would be needed for a linear tetrahedral mesh to converge to a solution. As it was stated before, the C3D4 elements are overly stiff and do not converge unless using a very fine mesh.

The following two figures (Fig.3.22.a and 3.22.b) display the results from the same study using quadratic tetrahedral elements. The convergence in that case is very fast as the model with 10625 nodes is converged. While performing this convergence study, it occurred that meshing using tetrahedral elements is not robust as many degenerated elements were created and in many cases it prevented the dispersion characterisation of the model to be performed.

The following two figures (Fig.3.23.a and 3.23.b) are showing results from the

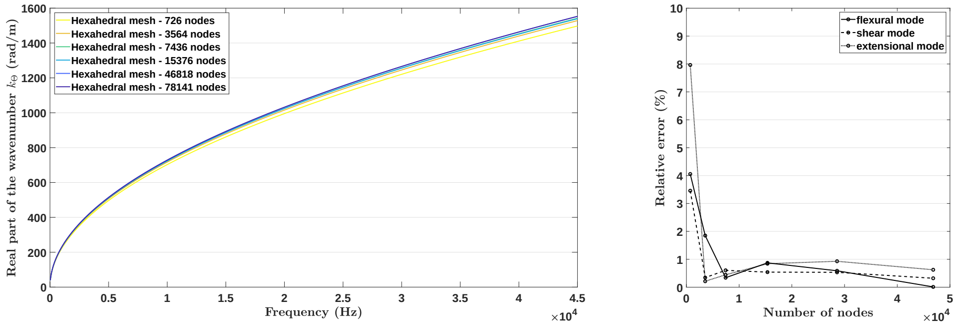

(a) (b)

Figure 3.23: Convergence study based on the dispersion characteristics of the linear hexahedral mesh models. (a) flexural mode dispersion curve for models with different number of nodes (b) convergence of the wavenumber parameter.

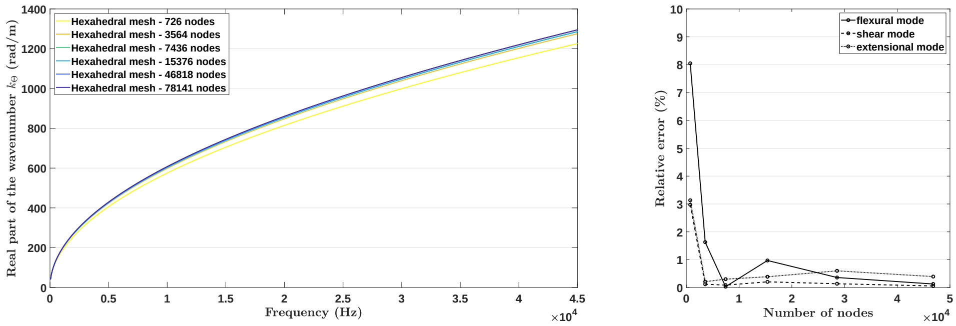

(a) (b)

Figure 3.24: Convergence study based on the dispersion characteristics of the linear hexahedral mesh with adjusted volume fraction models. (a) flexural mode dispersion curve for models with different number of nodes (b) convergence of the wavenumber parameter.

same convergence study. However, in that case a voxel discretisation with a mesh made of linear hexahedral elements is studied. The meshing process is robust and the convergence is fast as well. The model with 7436 nodes is converged, while using quadratic tetrahedral elements, 10625 nodes were needed. It can be concluded that using a voxel discretisation and linear hexahedral elements means a more robust discretisation process at lower CPU cost for obtaining converged dispersion characteristics.

Finally, this study is performed once again with the same models (i.e. voxel discretisation and C3D8 elements) but with adjusted fibre volume fractions. The results are displayed in Fig.3.24 and it occurs that adjusting the fibre volume fraction has little effect on this dispersion characteristics based convergence study.

From this subsection, it is concluded that a hexahedral mesh is robust and accurate for obtaining dispersion characteristics in textile composites. Also re-calculating the fibre volume fraction according to the yarn volume fraction in the model helps for a faster convergence of the static effective material characteristics but has no incidence on the convergence of the dispersion characteristics. Thus this meshing methodology will be used for the next case studies in this thesis.

3.3.2 Choice of the representative period

The choice of the unit cell to study in order to obtain the dispersion characteristics of a textile composite is of importance. One wants to have a cell with the smallest dimensions while still containing all of the features that defines the textile composite, that is per definition of the unit cell. However, the fact that the unit cell needs to be discretised has to be taken into consideration when choosing it.

A voxel discretisation infers brick elements whose edges are directed towards the x, y and z directions. A textile composite on the other hand often has two main fibre orientations, perpendicular to each other. In that case it is advantageous to choose the unit cell accordingly, e.g. choosing the unit cell number one instead of number two on Fig.3.25 allows for avoiding a sawtooth mesh pattern on the edge on the yarns while increasing its dimensions by only a small factor. Another rule-of-thumb is to try to keep each yarn as one piece instead of two as shown on Fig.3.25 with unit cell number three as it creates undesirable discretisation effects.

These rules-of-thumb should be respected in order to provide a faster and more robust mesh convergence for the models. However, any of these choices, given that the mesh is converged should provide the exact same results. In Fig.3.26 the dispersion curves for waves propagating in the x direction computed for the three unit cells highlighted in Fig.3.25 can be observed. The figure shows indeed that the dispersion curves are similar for all models with some slight differences at relatively high frequencies originating from the use of non-converged meshes.

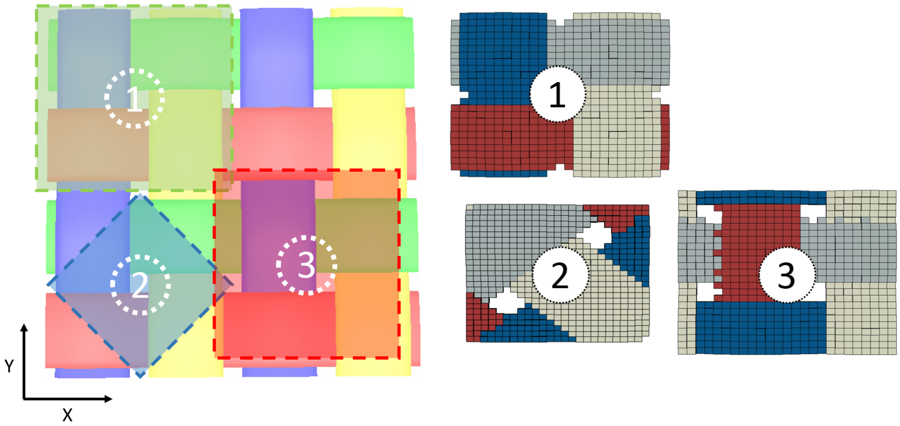

Figure 3.25: Different choice of unit cell for a 2D plain woven composite on the left, the yarns discretisation with the same number of total elements in each representations.

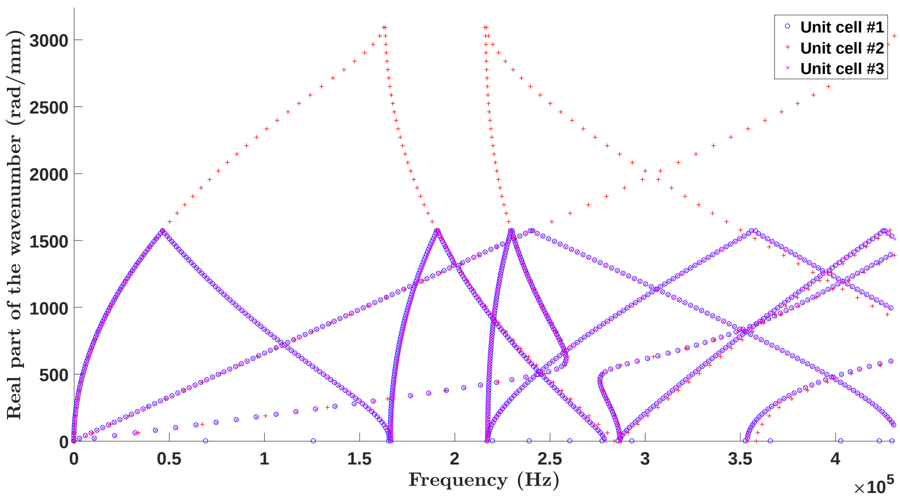

Figure 3.26: Dispersion curves for different unit cells of the same 2D plain woven composite for waves propagating in the x direction.

3.3.3 Influence of the CMS reduction method

In order to apply the WFE method to textile composites, a fine mesh is needed for an accurate mesoscale description. This implies a large number of DoFs and therefore large computational cost. Thus the Craig-Bampton method detailed in Sec.2.3.3 is used to reduce the complexity of the textile composite models. In this short subsection, the impact of the CMS reduction method on the results is studied. Two methodologies are compared, the 'classical' one shown in Fig.3.14, and the same one omitting the CMS reduction step, both applied on the same model of a 2D plain woven composite. The comparison is performed in the frequency range $[0, 0.4MHz]$ as displayed in Fig.3.27. Thus, to apply the CMS method, a reduced set q_{Φ} of modes has to be selected based on the lower resonance frequencies of the clamped model in the range $[0, 3f_{max}]$ as a rule-of-thumb. In this case, it means that at least all the modes situated in $[0, 1.2MHz]$ are selected.

The results are displayed in Fig.3.27. It can be seen that the CMS reduction method shows negligible error (mean relative difference of 0.06% for the flexural mode, 0.27% for the shear mode and 0.13% for the extensional mode). Moreover, a Bragg stop-band is present around 200 kHz in the flexural mode and is predicted by both models.

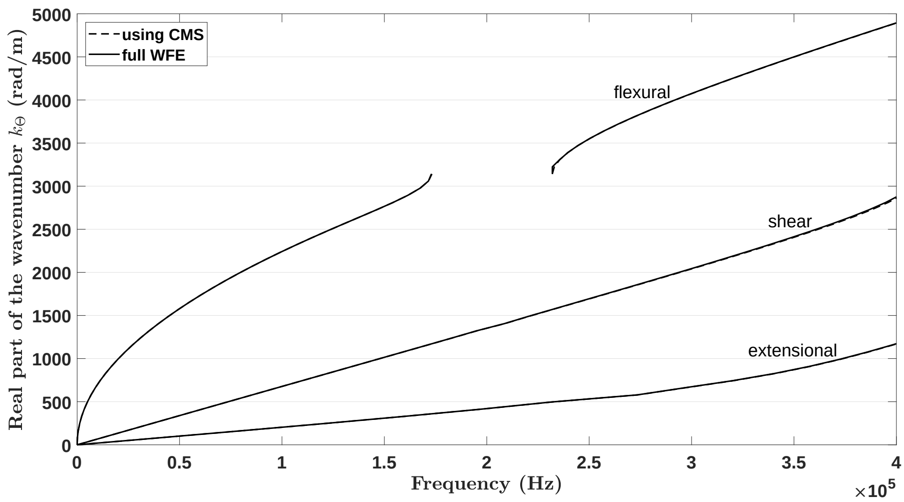

Figure 3.27: Dispersion curves of the flexural, shear and extensional modes for a same model but different reduction methods; (- -) using both the CMS and WFE methods and (–) using only the WFE method. The complete overlapping of the curves shows a great agreement.

3.3.4 Mesoscale and macroscale methodologies comparison

In this subsection, dispersion curves computed for two different textile composites considered at mesoscopic scale and their equivalent macroscale models are compared. Mechanical parameters of the macroscale models are obtained by static virtual testing of the mesoscale model as described in Sec.A.1 in Appendix. Using a macroscale instead of a mesoscale model allows for reducing the complexity of the problem. An advantage is the enhancing of the calculations speed, a drawback, however, lies in the possible oversimplification of the problem and thus a lack of accuracy in the results. A laminate composite usually is homogenised with each layer considered independently, resulting in an assembly of orthotropic layers (each modelled at a macroscopic scale), whereas a textile composite cannot be divided into individual layers in a straightforward way as the yarn assembly is more complex (e.g. through-the-thickness binder yarns, interwoven yarns etc.). To solve this issue, textile composites with many yarns in the thickness direction are homogenised following two distinct methods. Both methods are shown in Fig.3.28 and involve static virtual testing. The first tests the unit cell as a whole, this gives a model made of a single material considered at a macroscopic scale. The second gives a model that is similar to a laminate composite, with a single homogenised material per layer and where each layer is considered at a macroscopic scale. Throughout the thesis, these two homogenisation methods are respectively denoted 'static macroscale' and 'static macroscale per layer' for simplicity.

It is clearly observed in Fig.3.28 that using the static macroscale per layer method threatens the integrity of some yarns that are 'chopped down' and this justifies why both macroscale methods are employed, whereas textile composites with only a little number of yarns in the thickness direction (such as 2D woven composites) are homogenised using only the static macroscale method.

A detailed example is provided in Fig.B.8-B.9 in Appendix for a 3D woven composite model for more clarity. Figure B.8 shows that the homogenised properties are extracted for the unit cell as a whole, thus only one set of orthotropic moduli is obtained. Figure B.9 displays the decomposition in layers and their homogenised properties. In this case, the 3D woven composite is decomposed in five layers, resulting in five sets of orthotropic moduli.

Case study: 2D plain woven composite

The first comparison is made for a 2D plain woven composite plate model, also used in the previous subsections (see Fig.3.15). The dimensions of the unit cell are $2 \times 2 \times 0.2$ mm. The FE model is composed of 6250 elements ($25 \times 25 \times 10$). The materials properties are given in Tables B.6 and B.7 in Appendix. The dispersion curves for the flexural mode of both the mesoscale and the stat-

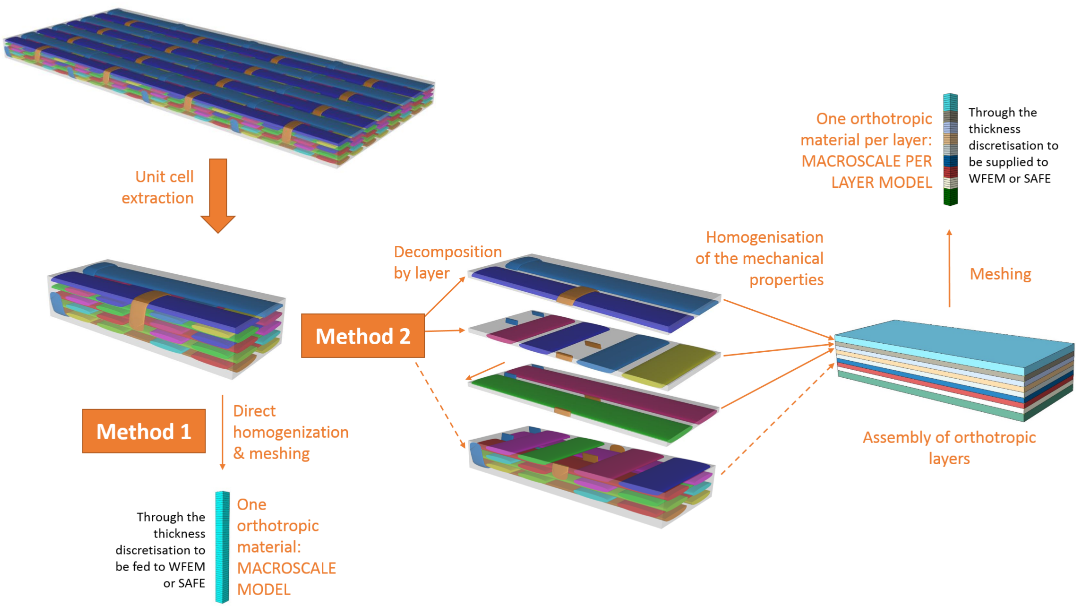

Figure 3.28: Unit cell homogenisation: two methods are presented. One is the homogenisation of the unit cell as a whole, which results in one set of orthotropic properties (named 'static macroscale'). The second considers an independent homogenisation for each layer of the unit cell, resulting in as many sets of orthotropic properties as the number of layers (named 'static macroscale per layer').

ic macroscale models are displayed in Fig.3.29. The first important difference between both curves is the Bragg stop-band exhibited by the mesoscale modelling while the dispersion curve from the macroscale model shows none. The stop-band occurs when the curve reaches a limit of the BZ. It is an effect of the periodicity of the structure thus is not predicted by the macroscale model. The second important difference lies in the strong mismatching of both curves. Using the static macroscale method to describe the dispersion characteristics of a textile composite not only overlooks the stop-bands but also predicts different dispersion relations.

Case study: 3D woven composite

The second comparison is made for a plate structure made of the 3D woven composite represented on Fig.3.30 using the presented mesoscale methodology and both its static macroscale and macroscale per layer models. The materials properties are given in Tables B.6 and B.7 in Appendix for the mesoscale model and the discretised model is shown in Fig.B.7 in Appendix. The dimensions of the unit cell are $2 \times 1.5 \times 0.6$ mm. This FE model is composed of 15625 elements (25

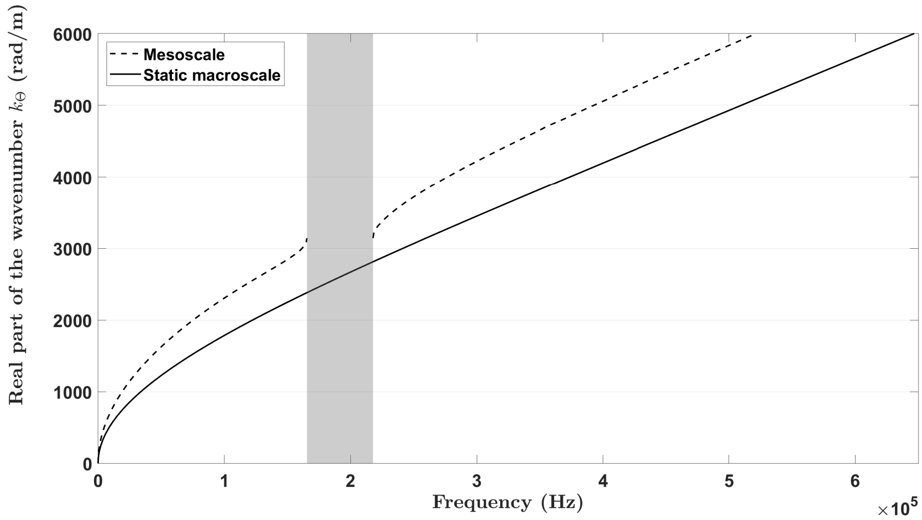

Figure 3.29: Dispersion curve of the flexural mode of the 2D plain woven composite mesoscale model and the static macroscale model; presenting a stop-band (grayed area) for the the mesoscale model; (- -) mesoscale model and (–) static macroscale model.

$\times$ 25 $\times$ 25). The homogenised properties obtained for both macroscale models are displayed in Fig.B.8-B.9 in Appendix.

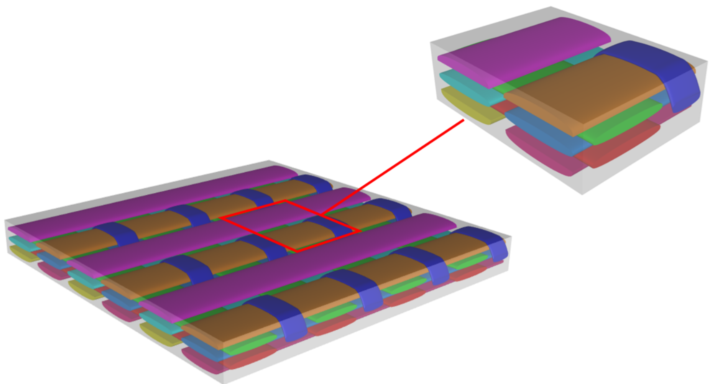

Figure 3.30: 3D woven composite model and its unit cell.

The dispersion curves of the first two modes are displayed in Fig.3.31-3.32. Similar observations to the 2D plain woven composite can be made for the flexural mode comparison (see Fig.3.31) with again a strong mismatch between the static macroscale and mesoscale models and a Bragg stop-band is predicted by the mesoscale model at a BZ limit. The results from the static macroscale per layer and mesoscale models are, however, very similar. The main difference being again the lack of stop-band prediction by the static macroscale per layer model.

However, the dispersion curves of the shear mode (see Fig.3.32) for the mesoscale and static macroscale models are in agreement for low frequency range until the mesoscale model predicts a Bragg stop-band, then a mismatch between the curves appears. The mesoscale and static macroscale per layer models provide different results for the shear mode for any frequency range.

Both the static macroscale and static macroscale per layer models provide wrong dispersion characteristics predictions in comparison to the mesoscale model for the 3D woven composite.

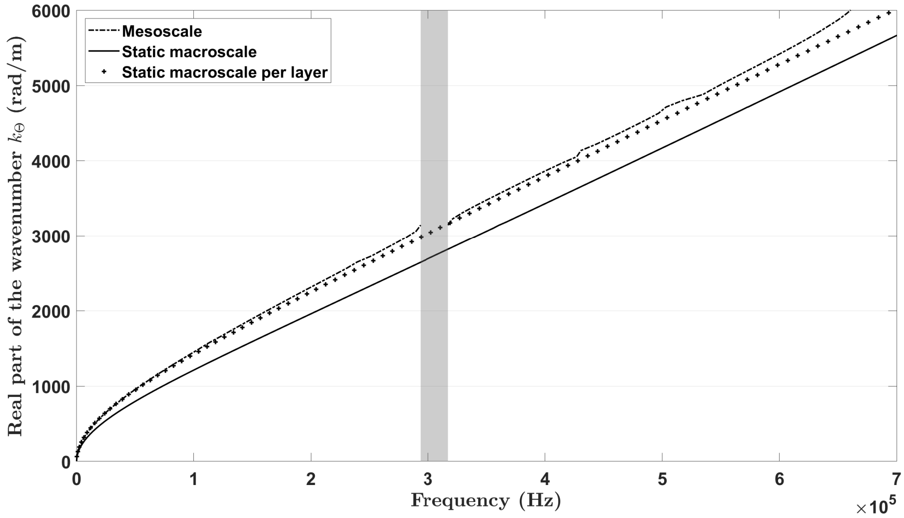

Figure 3.31: Dispersion curve of the flexural mode of the 3D woven composite mesoscale model and static macroscale model; presenting a stop-band (grayed area) for the the mesoscale model; (- -) mesoscale model, (–) static macroscale model and (+) static macroscale per layer model.

3.3.5 Numerical comparison of the 1D WFE mesoscale methodology with transient FEA

The dispersion relations of a textile composite structure can be obtained by transient FEA as detailed in Sec.3.1.2. Due to the high computational costs induced by mesoscale modelling, the numerical comparison is performed only for the 1D formulation (beam-like structure). In this subsection, this method is used to provide for comparison with the WFE/CMS mesoscale methodology. The comparison is performed for two textile composites.

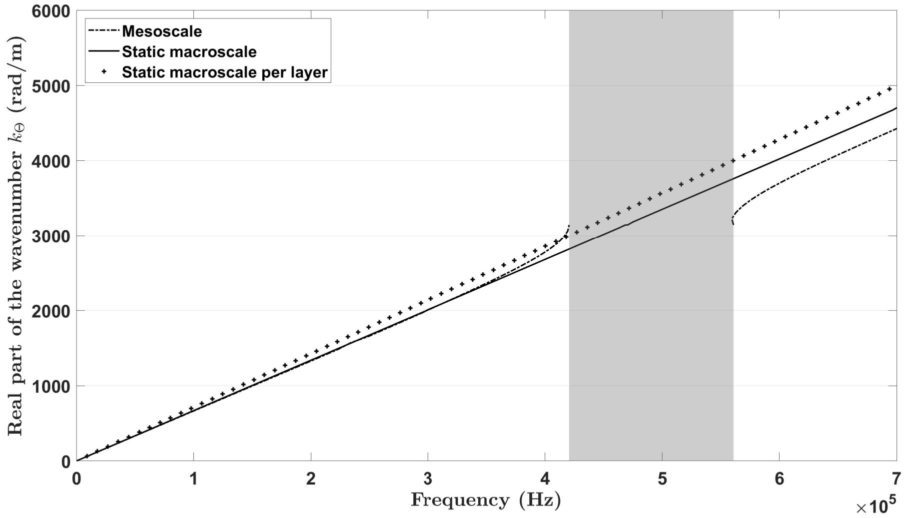

Figure 3.32: Dispersion curve of the shear mode of the 3D woven composite mesoscale model and static macroscale model; presenting a stop-band (grayed area) for the the mesoscale model; (- -) mesoscale model, (–) static macroscale model and (+) static macroscale per layer model.

Case study: triaxial braided composite

The first comparison is performed on a beam made of a triaxial braided composite, whose unit cell is displayed in Fig.3.33. The dimensions of the beam modelled for the transient FEA are of 100 $\times$ 0.6 $\times$ 0.4 mm while the period modelled for the WFE analysis is of 2 $\times$ 0.6 $\times$ 0.4 mm. A similar discretisation is used for both models, leading to 600 000 elements for the transient analysis and to 12 000 elements (40 $\times$ 20 $\times$ 15) for the WFE. The results from the WFE/CMS mesoscale model (plotted in red in Fig.3.34) are only computed over the IBZ and mirrored over its boundary to provide the results for the next BZ and so on. The dispersion relations obtained by transient FEA are shown in the background of Fig.3.34. A perfect agreement between the main branches of the modes for both the WFE/CMS mesoscale and the transient FEA models is observed.

An effect of the textile composite periodicity is observed in the transient FEA results and is highlighted in Fig.3.34 (circled in yellow). Indeed, for a periodic material, any point outside the first BZ can also be expressed as a point inside the zone. These effects are predicted by the WFE/CMS mesoscale model too. In Sec.3.1.2 it was shown that the WFE method induced artificial aspects due to the continuous material being considered as virtually periodic. On a real peri-

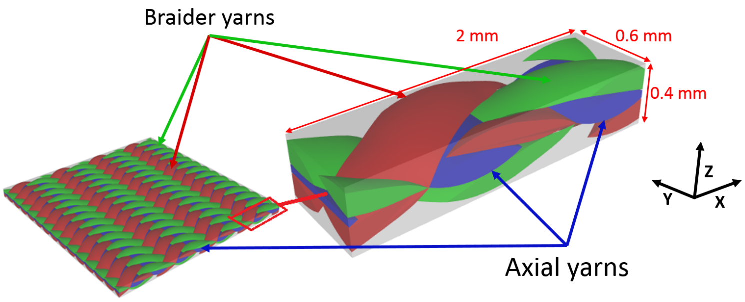

Figure 3.33: Triaxial braided composite model.

odic medium, however, the repetition of the main branches into less discernable branches over the different BZs has been observed for periodic photonic crystals [172, 173] and is observed in this model (repetition of period $2\pi/\Delta$ as well). It is interesting to note that for the first modes the maximal intensity of their first branch lies within the first BZ, and likewise their second, third, forth and fifth branches attain their maximal intensity in the second, third, forth and fifth BZs respectively, while their intensity is lesser outside of their respective BZs, as highlighted by the yellow circles in Fig.3.34. The same phenomenon was observed in photonic crystals in [174, 173] as a consequence of the Umklapp scattering. This scattering process happens when two ingoing phonons result in a phonon whose wave vector falls outside the first BZ.

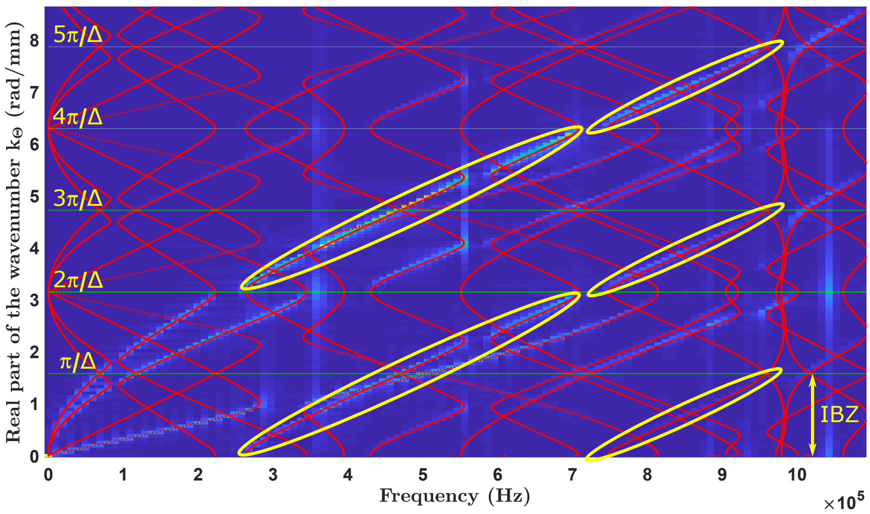

Figure 3.34: Dispersion curves computed for a beam made of a triaxial braided composite using the WFE/CMS mesoscale methodology (red dots) and transient FEA (results in the background). The IBZ and the limit of the higher order BZs (green horizontal lines) are displayed. Periodic effects are highlighted (circled in yellow).

The dispersion characteristics are computed by the static macroscale method as well and are plotted in yellow in Fig.3.35. A strong mismatch with the dispersion relations obtained by transient FEA is observed. The results obtained by transient FEA also display stop-bands that are circled on the figure for emphasis. It is observed once again that the mesoscale modelling can predict them while the macroscale model cannot. As detailed in Sec.2.2.2 there are two types of stop-bands, the Bragg stop-bands are circled in green and the local stop-bands in yellow in Fig.3.35. Using a mode sorting algorithm based on the MAC, the dispersion characteristics obtained by the WFE/CMS mesoscale methodology are unwrapped and plotted in Fig.3.36 for a clearer overview.

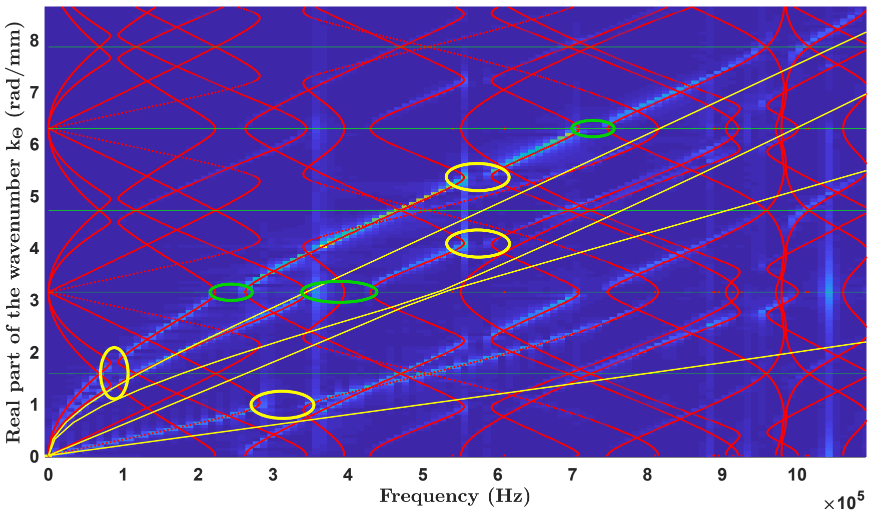

Figure 3.35: Dispersion curves computed for a beam made of a triaxial braided composite using the WFE/CMS mesoscale methodology (red dots), the static macroscale methods (yellow –) and transient FEA (results in the background). The IBZ and the limit of the higher order BZs (green horizontal lines) are displayed. The stop-bands are highlighted (Bragg stop-bands circled in green, local stop-bands circled in yellow).

The computational cost for the transient FEA (whole textile composite beam structure modelled at a mesoscopic scale) is situated around twenty hours on a standard desktop computer (4 cores and 8 GB of RAM). In the case of a plate structure, the computational cost would be utterly expensive. However, using the WFE/CMS mesoscale methodology allows for obtaining the dispersion characteristics in less than an hour for both a beam or plate structure.

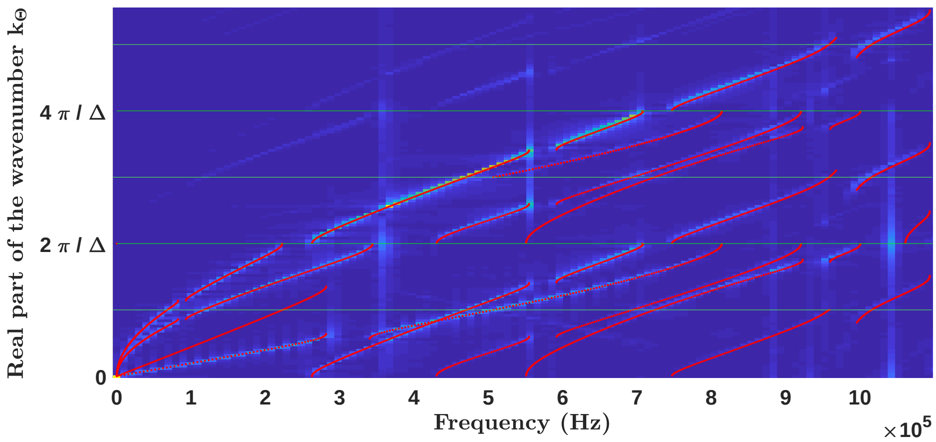

Figure 3.36: Dispersion curves computed for a beam made of a triaxial braided composite using the WFE/CMS mesoscale methodology and mode sorting algorithm based on the MAC criterion (+) and transient FEA (results in the background).

Case study: 2D plain woven composite

Similarly to the comparison provided in the previous subsection, a second comparison is performed on a beam made of the 2D plain woven composite, presented in Fig.3.15, modelled both with the mesoscale and the static macroscale methods. The dimensions of the beam modelled for the transient FEA are of $100 \times 2 \times 0.22$ mm while the period modelled for the WFE analysis is of $2 \times 2 \times 0.22$ mm. A similar discretisation is used for both models. The resulting dispersion curves are plotted for the mesoscale and static macroscale models in red and yellow respectively in Fig.3.37. The dispersion relations obtained by transient FEA are shown in the background of the figure. A strong mismatch between the dispersion relations obtained for the mesoscale and macroscale models is observed once again. A great agreement, however, is provided using the WFE/CMS mesoscale methodology and the transient FEA. Stop-bands are observed once again in the dispersion curves obtained by mesoscale modelling.

3.3.6 Artefacts induced by the presented mesoscale methodology

It is stated in Sec.3.1.2 that the RVE must be chosen carefully so that its aspect ratio ($Ra = \Delta/2b$) is small enough to provide clear results. However, when

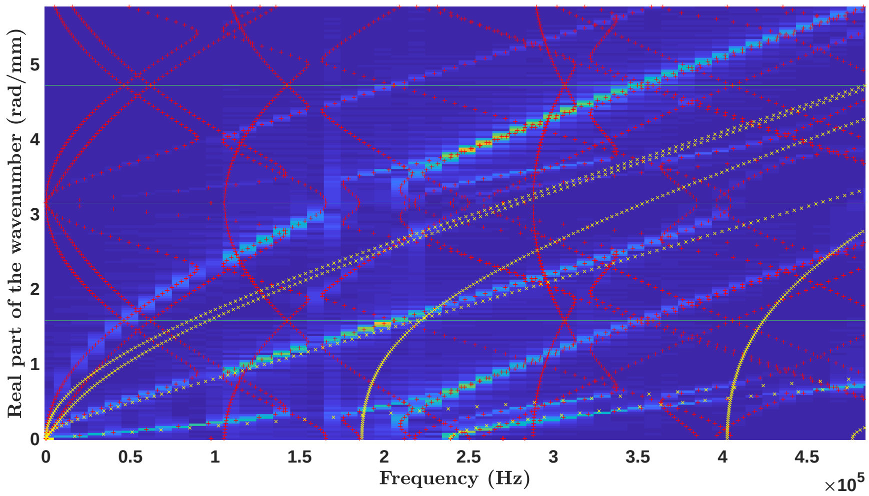

Figure 3.37: Dispersion curves computed for a beam made of a 2D plain woven composite using the WFE/CMS mesoscale methodology (red +), the static macroscale methods (yellow ×) and transient FEA (results in the background).

having a small aspect ratio is not an option, the high aspect ratio can generate some branches in the dispersion curves that are artefacts. This phenomenon is studied in the section.

Case study: homogeneous orthotropic material

As an example, Fig.3.38 shows the dispersion curves for a homogeneous orthotropic plate structure for a set of different aspect ratios. The thickness ($2b$) is the same in all cases so that it does not change the properties of the structure of interest, only the length of the unit cell (Δ) can vary. The horizontal dotted lines represent the limit of the IBZ for each model. For the smallest aspect ratio ($Ra = 0.4$) used as a reference, the IBZ limit is too high to be represented on the figure and thus no folding of the branches is observed, thus providing a clear set of five dispersion curves (three zero-order modes and two first-order modes whose cut-off frequencies are around 2.1MHz). It can be observed from the figure for the three other aspect ratios dispersion curves that once their branches are unfolded over the IBZ, they would overlap each other to form the flexural, shear and longitudinal modes and the two first order modes are observed as well, overlapped to each others. However, once these branches unfolded, it is observed that 'uncategorised' modes remain. These modes are designated by arrows in the lower part of Fig.3.38. These modes do not have a physical meaning and thus are categorised as 'artefacts'.

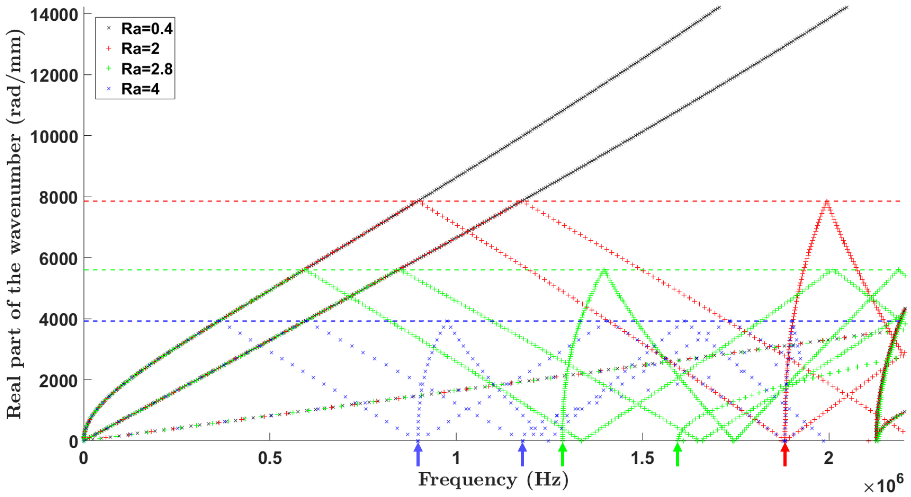

Figure 3.38: Dispersion curves computed for a homogeneous orthotropic plate structure using different aspect ratios. Artefacts modes are shown using arrows pointing at their cut-off frequency.

Case study: 2D plain woven composite

The aspect ratio cannot be controlled when considering a textile composite as it is directly linked to the period of the textile composite and therefore can be way over the recommended value of 0.2. In the case of the unit cell of a 2D plain woven composite, the smallest aspect ratio is of $Ra = \Delta/2b = 6.4$ for the unit cell displayed in Fig.3.39 and cannot be reduced and thus it is difficult to uncover which branches amongst the dispersion curves are artefacts. The aspect ratio, however, can be augmented using a larger period of the textile composite ($Ra = 9.1$) or by considering multiple periods ($Ra = 18.2$) as displayed in Fig.3.39.

Figure 3.40 shows the dispersion curves for these three different aspect ratios. It is clear that the green curve representing a mode whose cut-off frequency is around 47 kHz for a model whose aspect ratio is very large ($Ra = 18.2$) is an artefact as it does not appear in the results from the two other models. Another mode appears at a the cut-off frequency of 165 kHz and is visible for all models. Even though it might be an artefact, it is not possible to conclude, and thus one must be aware of these effects when using this methodology.

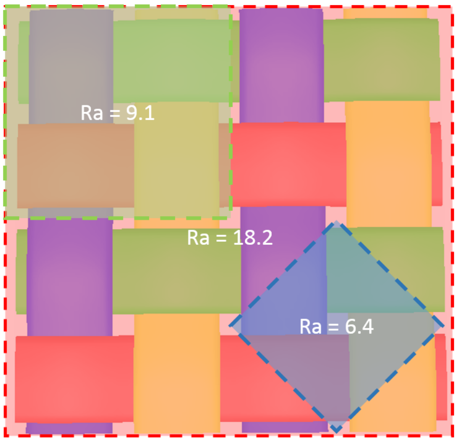

Figure 3.39: Different representative periods of the same textile composite and their aspect ratios.

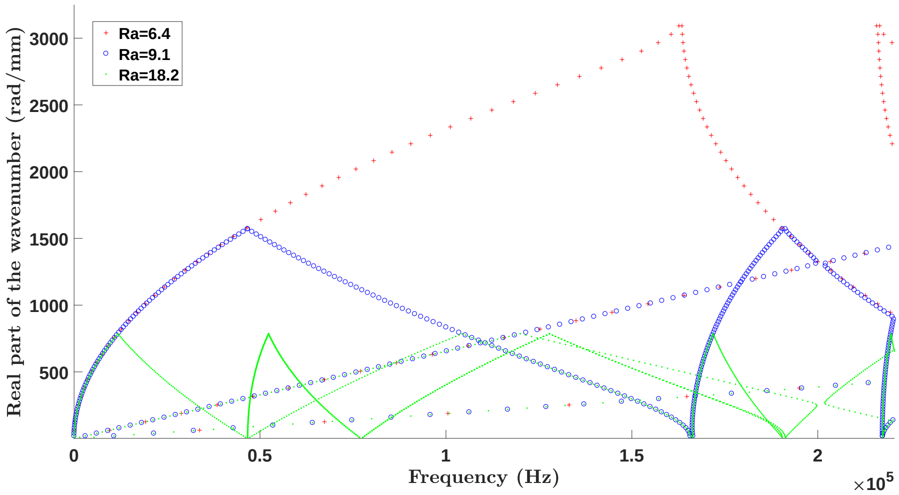

Figure 3.40: Dispersion curves computed for a 2D plain woven composite plate structure using different aspect ratios. Artefacts modes are observed.

3.4 Conclusions

In this chapter, a methodology that allows for dispersion characterisation of periodic textile composites is presented. It combines the computational advantages of both the CMS reduction method and the WFE method with the accuracy of a mesoscale modelling.

Different modelling options such as the choice of the representative period, the meshing options etc., are considered and compared. The methodology is applied to three different textile composites: a 2D plain woven, a 3D woven and a triaxial braided composites and the 1D WFE/CMS mesoscale formulation is compared to transient FEA with great success. The complex dispersion phenomenon induced by the periodicity and the strong anisotropy of textile composites are identified and discussed. It is shown that the presented methodology is needed for increased prediction accuracy in comparison to macroscale modelling used traditionally.

It can be concluded that:

- Discretisation of textile composite mesoscale models using linear hexahedral voxel mesh provides very robust results for a relatively low number of nodes.
- Any representative period of a unique textile composite provides the same dispersion predictions. However, some rules-of-thumb should be followed for its selection.
- There are significant differences in the dispersion relations predictions resulting from the presented mesoscale methodology and macroscale modelling.
- Complex phenomenon such as stop-bands cannot be predicted by macroscale modelling and the mesoscale methodology is needed.
- Numerical comparison between the WFE/CMS mesoscale methodology and transient FEA at a mesoscale level shows perfect agreement. The presented methodology is verified.
- Computational times for the presented textile composite models are reasonable while obtaining the dispersion relations for a textile composite plate structure by transient FEA would be very costly.

Chapter 4

Experimental and numerical schemes comparison

In the previous chapter, the mesoscale methodology has been introduced and compared with results obtained by transient FEA for validation. This chapter aims at comparing the numerical mesoscale methodology to experimental results. For this study, 3D woven composite samples have been manufactured and tested. The first section gives details on their architectures and on the manufacturing process used. The subsequent section explains how the samples were tested to obtain the dispersion characteristics. The next section details the realistic modelling of the composite samples. Finally, a section is dedicated to the comparison between numerical and experimental approaches for all 3D woven composite samples.

4.1 Manufacturing of the 3D woven composite samples

Six samples composed of a total of three different architecture reinforcements (from Carr Reinforcements Ltd.) [20] were manufactured for this study. Their architectures are briefly described here, and further illustrated in Fig.4.1 as the details are of the utmost importance when it comes to geometrical modelling (definitions of the nomenclature relative to 3D woven fabric can be found in Sec.2.1 and in [175]).

- Three 250 × 250 × 1.97 mm plates using a classic (off the shelf) through-the-thickness angle interlock ($\gamma = 25.6°$) weave architecture reinforcement (Fabric 1), all of them infused with IN2 epoxy resin from easycomposites™. Fabric 1 comprises two layers of 2 × 12K tows in the warp direction; three layers of 12K tows in the weft direction and 6K binder tows, alternating with the warp tows.

- Two 250 × 250 × 1.95 mm plates using a less conventional (custom experimental architecture [20]) angle interlock ($\gamma = 23.9°$) weave architecture reinforcement (Fabric 2), all of them infused with the PRIME™20LV epoxy resin from Gurit. Fabric 2 comprises two layers of 4 × 12K tows in the warp direction; three layers of 12K tows in the weft direction; 6K binder tows, alternating with the warp tows and 6K tows in the warp direction, interwoven with weft layers on the surfaces of the fabric.

- One 250 × 250 × 4.98 mm plate using an orthogonal weave architecture reinforcement (Fabric 3), infused with the IN2 epoxy resin for the matrix. Fabric 3 comprises six layers of 12K tows in the warp direction; seven layers of 2 × 6K tows in the weft direction; 1K binder tows, alternating with the warp tows.

A through-the-thickness angle interlock weave architecture reinforcement means the binder yarns travel in a fixed pattern (at a certain angle) from top to bottom. An orthogonal weave architecture reinforcement means the binder yarns are either at top or bottom travelling vertically through layers (classical reinforcements are illustrated in Fig.2.1).

Liquid Composite Moulding (LCM) comprises all the composite manufacturing processes that involves the injection of a liquid resin into a dry fibre preform. There exist various LCM technologies, amongst them the Resin Transfer Moulding (RTM), Vacuum-Assisted RTM (VARTM), Vacuum Infusion (VI) etc. The VARTM technique was chosen because it is consistent, easy to control, it allows for a high rate of production and most importantly for having two smooth surfaces. The VI and VARTM techniques respectively create a sample with one or two smooth and glossy sides. At least one smooth surface is necessary as it will

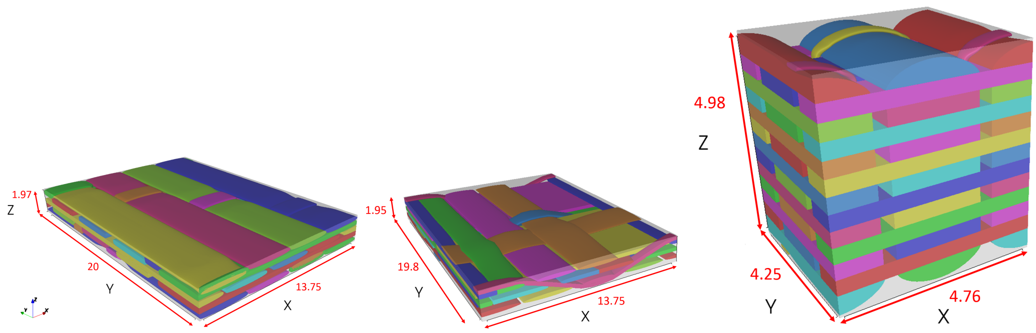

(a) Material 1 (b) Material 2 (c) Material 3

Figure 4.1: Unit cells of the three studied textile composites, (a) Material 1 is a classic 3D through-the-thickness angle interlock composite, (b) Material 2 is a less conventional 3D through-the-thickness angle interlock composite, (c) Material 3 is a classic 3D through-the-thickness orthogonal interlock composite - the dimensions are in mm.

be the surface of reflection for the laser vibrometer used for the experimental measurements. Two smooth surfaces are preferred as it simplifies the geometry of the composite and thus the geometrical modelling. VARTM uses a closed metallic mould. A metallic frame, whose thickness gives the final thickness of the samples (2 mm and 5 mm in our cases), is placed in between the two sealing parts of the mould, each having a flat surface on one side. The 250 $\times$ 250 mm piece of the preform is placed in the frame as depicted in Fig.4.2. A limitation of this manufacturing technique is that the dimension of the plates is defined by the frame and mould sizes which in our case are rather modest.

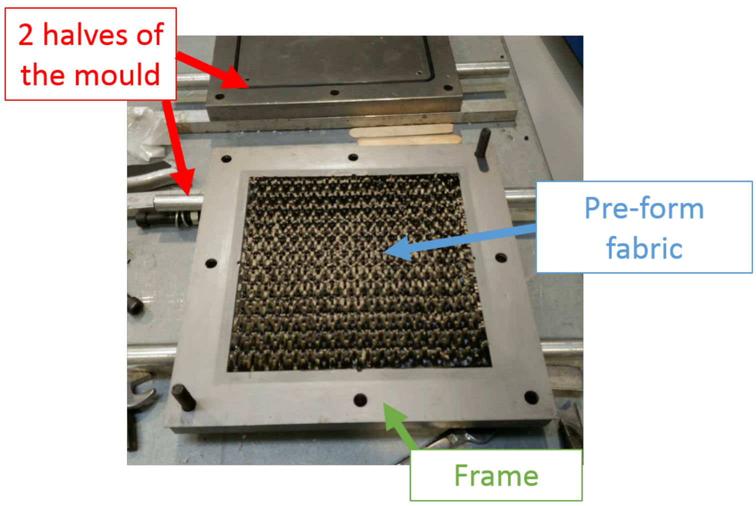

Figure 4.2: Photography showing the two halves of the mould, with the frame placed on one half and the pre-form fabric sheet fitted inside the frame.

The mould is closed, sealed and four outlets located at each corner of the square mould are placed under vacuum as depicted in Fig.4.3. The homogeneous resin mixture is degassed by a vacuum pump and placed inside the resin injector. The resin is then transferred from the resin injector to the mould through the central inlet. The resin will flow from the centre of the mould to the four corner outlets, filling the internal void space of the mould. It takes about 30 minutes for the resin to fill all the free spaces and to impregnate the fibres deeply. The four outlets are connected to a vacuum pot to make sure all the air is sucked out of the mould. At 25°C, the resin pot life is of 80 to 100 minutes for the IN2 resin and of 1 hour for the PRIME LV20 resin. The plates made of IN2 resin are left to cure at 25°C for 24 hours and then post-cured in an oven at 60°C for about 6 hours. The plates using PRIME LV20 resin are left to cure at 50°C for 24 hours.

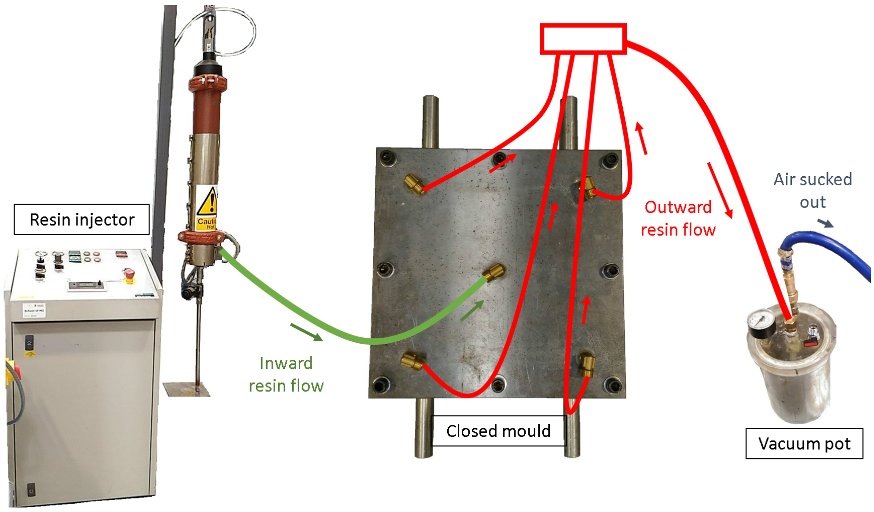

Figure 4.3: Picture depicting the resin flow from the injector to the sealed mould. The resin is injected from the resin injector to the closed mould through the central inlet. A vacuum is created in the vacuum pot. As the air is sucked out from the mould through the four corner outlets, the resin flows from the centre of the mould to the corner exits and fills the mould's free space with resin.

Figure 4.4 shows a photography of the setup. However on this picture the inlet is connected to a barometer as the leak proofing was taking place. It is then disconnected from the barometer and connected to the infusion pot where the resin is situated and from where it will be flowing.

In order to proceed to a validation of the methodology, several samples composed of the same preform and same resin were manufactured and tested to ensure repeatability.

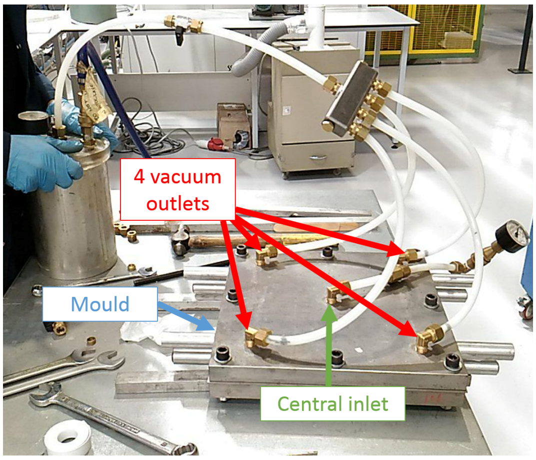

Figure 4.4: Photography depicting the sealed mould with the different connected in- and outlets.

4.2 Experimental determination of the dispersion curves

Three steps are necessary in order to experimentally obtain the dispersion curves in the plate samples. Firstly, a disk Piezoeletric Transducer (PZT) ceramic is glued to the plate. It is used to generate the guided waves in the plate. Secondly, a laser scan is performed on the plate to measure the displacement as a function of time at different discrete positions on the plate. At last, these measurements are post-processed to obtain the results in the frequency-wavenumber domain corresponding to the dispersion curves. These steps are further described in the next paragraphs. To visualise the guided wave propagation, a laser scan of a 2D surface (C-scan) of a plate sample can be performed to obtain the time-dependant displacement of a signal generated by a transducer.

For the dispersion characterisation, a broadband excitation signal is transmitted to the studied structure (simply supported woven composite plate samples in our case) by means of a PZT bounded to it. The input excitation signal is sinusoidal, its central frequency is of 100kHz but it carries a wide frequency band as detailed in Sec.3.1.2. Two cycles of the sinusoidal function are modulated by a window function (Hanning window here) as shown in Fig.3.5. The interest in having a wide frequency band in the excitation signal, is to obtain the dispersion relations for a large frequency band, performing only one linear scan per direction of interest.

The set-up (displayed in Fig.4.5) is composed of a waveform generator that is used to generate the electrical waveform transmitted to the PZT. Before it is transmitted to the PZT, the signal is amplified as the waveform generator can only provide a tension of 10Vpp maximum. The high speed bipolar amplifier allows for reaching a higher tension (70Vpp) which then allows the signal to propagate further and with a higher amplitude.

The transducer (13 mm diameter) is glued on the surface of the tested textile composite sample. The Laser Doppler Vibrometer (LDV) is programmed to measure the displacement at a set of discrete positions on a straight line (B-scan) originated at the PZT. The PZT element has to be placed in the continuity of that line. One B-scan provides the dispersion relations in one direction, therefore multiple B-scans of various orientations are required to capture the anisotropic behaviour of the materials. In our study, five directions of propagation are investigated (0°, 30°, 45°, 60°, 90°). The laser vibrometer measures the out-of-plane displacement (U_3) or velocity component which greatly limits the ability to measure the S_0 mode.

For each position, the amplitude over time is measured with a sampling frequency of 10 Msamples/s for a duration of 0.5 ms (thus sample size is of 5000 time points). This relation is measured every 20 ms for two hundred times and then is averaged and recorded by the oscilloscope. The scanning head is then moved to the next discrete position (step of 0.5 mm) and is connected to a pass band filter which filters out high frequency noise and low frequency vibrations.
For illustration purposes, the results of a B-scan, i.e. the out-of-plane displacements measured by the laser as a function of time and for a set of discrete positions, are shown in Fig.4.6.a. The progress and dispersion of the forward going wavepacket can be observed as well as some reflected waves. The almost vertical line, whose magnitude is weak, on the left-hand side of the figure shows the pressure mode (S_0) that is the fastest to propagate, while the second line with a smaller slope and a higher magnitude shows the flexural mode (A_0). The flexural mode is more clearly observed as the laser measures the out-of-plane component which is strongly solicited by this mode.

One of the difficulties associated with the measurement of the dispersion re-

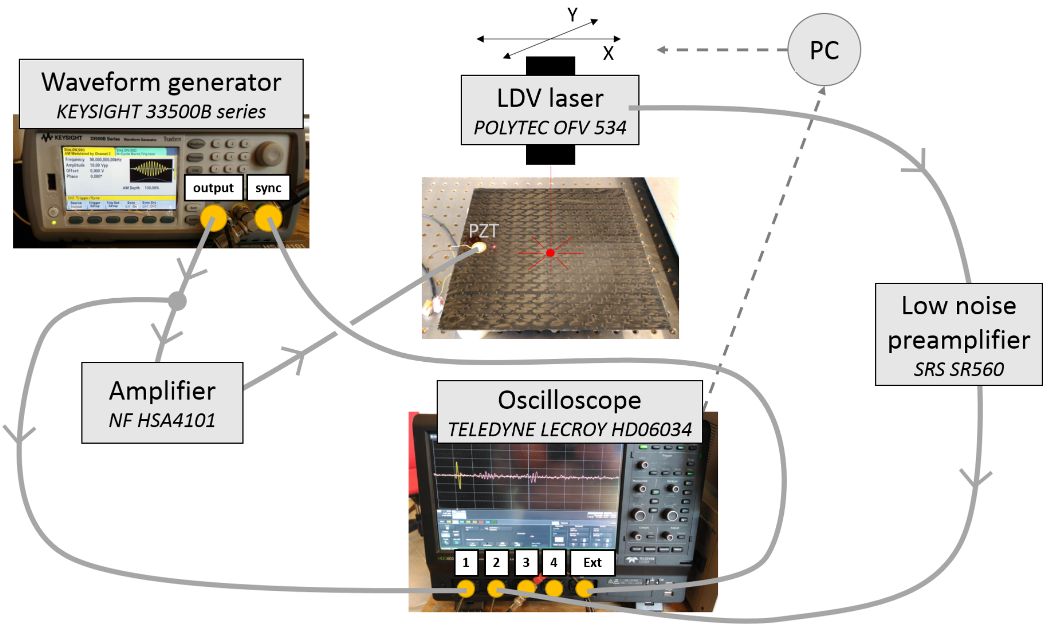

Figure 4.5: Experimental set-up for B-scan measurements. A signal is generated by the waveform generator, amplified and transmitted to the PZT. The PZT transmits the vibrations to the composite plate. The LDV measures the out-of-plane displacements which are filtered by the low noise preamplifier. The input and measured signals are recorder by the oscilloscope.

lations in a thin structure (beam or plate for example) is that at least two modes can exist and propagate for any given frequency. Thus the 2D FFT [162, 163] is applied to obtain the dispersion curves.

In the dispersion curves displayed in Fig.4.6.b, the A_0 mode can be clearly observed, while the S_0 mode is barely visible. To highlight the visibility of the S_0 mode, a 15° angle (with the z axis normal to the plate, and x the axis of laser inspection, the 15° angle is given relatively to z and around the y axis) was given to the laser beam so that a small portion of the U_1 component could be captured as well, and S_0 observed. Also, the resolution on the figure is of poor quality, this is explained by the rather small size of the sample plates limited by the manufacturing equipment used. Indeed, a pixel height (in the wavenumber direction) is inversely proportional to the scanned length. In our case, the small plate length (250 × 250 mm) results in large pixels and thus a low wavenumber resolution.

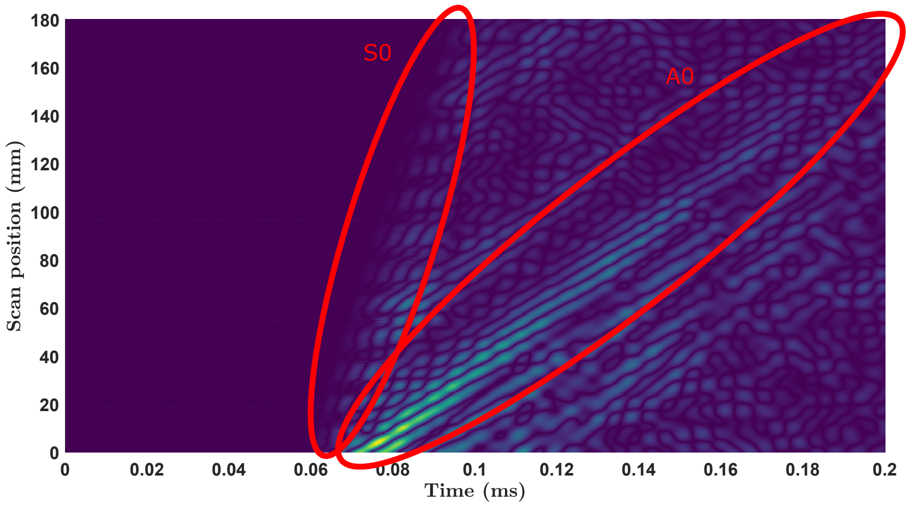

(a)

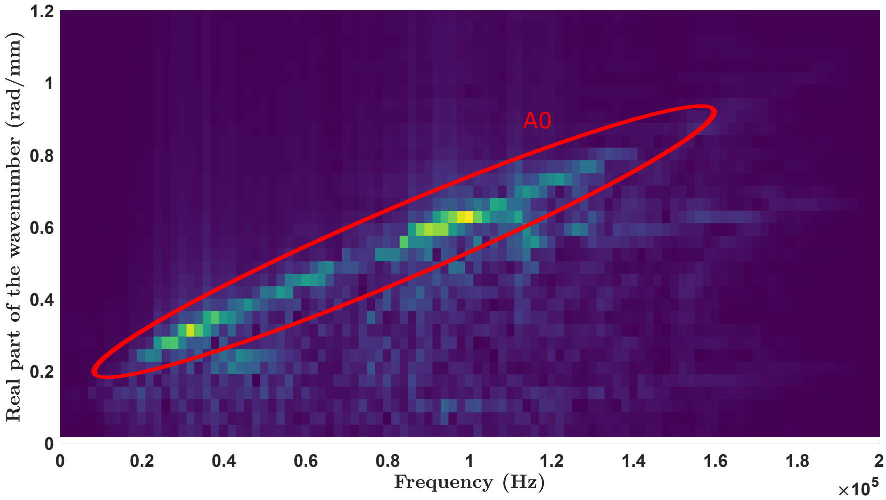

(b)

Figure 4.6: Type of results that can be obtained from measurements from the Laser Doppler Vibrometer performed on a textile composite plate.(a) Out-of-plane displacement magnitude (U_3) measured by the scanning laser Doppler vibrometer as a function of space x and time t. Two propagating modes (circled in red) can be observed (S_0 and A_0). (b) Dispersion curves obtained by 2D FFT of the experimental data. A_0 can be observed. The central frequency of the sinusoidal signal is of 100kHz thus it is hard to observe the mode for frequencies higher than 200kHz.

4.3 Realistic modelling of a textile composite

This section describes how the actual composites presented in Sec.4.1 are modelled. The mechanical characteristics of the components (i.e. matrix and yarns) as well as the geometrical properties of the woven composites are sought (process described in Fig.4.7). Their wave dispersion properties are then computed using the WFE/CMS methodology.

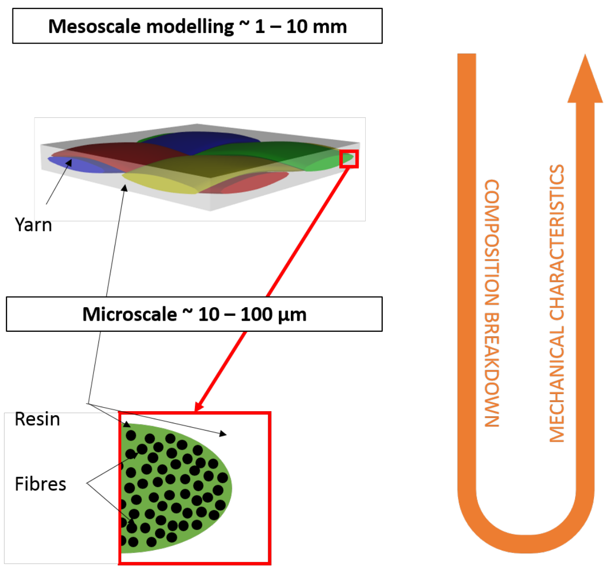

Yarns properties

Yarn:	+ =
Given by manufacturer	Filaments number, filament's cross-sectional area
Observed from cross-sections	Yarns cross-sectional area
Calculated with Eq.(4.2)-(4.3)	V_f, ρ
Computed by virtual static testing	E_1, $E_{2,3}$, $\nu_{12,13}$, ν_{23}, $G_{12,13}$

Fibres & matrix properties

	Fibres:	Matrix:
Given by manufacturer	E_1, ρ	E, ρ
Assumed from literature	$E_{2,3}$, $\nu_{12,13}$, ν_{23}, $G_{12,13}$	ν

Figure 4.7: Determination of the mechanical properties with a multiscale approach. The textile is modelled at a mesoscopic scale. A microscale model is used to calculate the yarns effective mechanical properties. These properties are used in the mesoscale model alongside the matrix properties.

4.3.1 Mechanical characteristics determination

As thoroughly described in Sec.2.1, a yarn is a bundle of aligned fibres (also called filaments) and once the resin is infused, the yarns are composed of fibres packed in a matrix of cured resin (see Fig.4.7 under microscale). In reality the fibres are randomly distributed in the cross-sectional view but the distribution is considered regular and periodic as the elastic moduli predictions are similar [31]. To determine the yarn properties, a mechanical analysis based on idealised hexagonal fibre arrangement model can be performed [31, 10, 176].

In the following subsection, the mechanical characteristics of the individual matrix and fibres materials composing a yarn are described. A second subsection explains how the mechanical properties of a yarn are obtained from the ones of the matrix and fibres materials.

Microscale: Matrix and filaments materials

The tensile modulus, the density and the average superficial density of the fabric are provided by the supplier, as well as for the resin tensile modulus and density. These mechanical properties are displayed in Table C.1 in Appendix. While it is quite straightforward for the manufacturer to establish the static mechanical properties for an isotropic thermoset material such as epoxy, it is hard to provide the full set of transverse isotropic moduli for a bundle of fibres. Indeed, tensile properties of the yarn, are tested using a tensile testing machine [177] and thus only in the direction of the fibre. The transverse elastic modulus of the fibres can be measured by Raman spectroscopy or, for example, by nanoindentation. However, these methods are difficult to apply and the convergence is not assured [178, 179, 180]. This is not the only property that is neither given by the supplier, nor straightforward to measure, e.g. $G_{12,13}$ is measured via the torsional pendulum test [179, 181]. For these reasons, some hypothesis need to be done for the other parameters. Firstly, the matrix material is considered isotropic, while the fibres and thus the yarns are considered transverse isotropic materials. For the matrix material, the missing engineering constant is the Poisson ratio, while for the filaments, the transverse modulus $E_{2,3}$, the in-plane shear modulus $G_{12,13}$ and the Poisson ratios $\nu_{12,13}$ and ν_{23} are missing. All these missing properties are selected from the literature (Table C.2 in Appendix), and a sensitivity study is performed to observe the impact of these constants on the final result.

From the literature, it is observed that $E_{2,3}$ ranges from 10 to 17 GPa, $G_{12,13}$ from 9 to 28 GPa, $\nu_{12,13}$ and ν_{23} from 0.2 to 0.25 for carbon fibres, while ν is around 0.35 for epoxy resin. For our study, $E_{2,3}$ is set to 15 GPa, $G_{12,13}$ to 18 GPa, $\nu_{12,13}$ to 0.2 and ν_{23} to 0.25 for the filaments. As a filament is considered a transverse isotropic material, G_{23} can be calculated using Eq.(4.1).

$$G_{23} = \frac{E_{2,3}}{2(1+\nu_{23})}, \tag{4.1}$$

ν is set to 0.35 for the matrix material.

From microscale to mesoscale: Yarn mechanical properties

A mesoscale model of a yarn considers it as a homogeneous component made of an orthotropic material. Its properties are derived from the microscale model characteristics as explained in Sec.2.1.1. For a yarn of aligned filaments, the fibre volume fraction V_f^{yarn} is calculated using [20]:

$$V_f^{yarn} = \frac{n_{fil} A_{fil}}{A_{yarn}} = \frac{n_{fil} \pi R_{fil}^2}{A_{yarn}}, \tag{4.2}$$

with n_{fil} the number of filaments in the yarn, A_{fil} the cross-sectional area of a filament, R_{fil} the radius of a filament and A_{yarn} the cross-sectional area of the considered yarn.

The density is calculated using:

$$\rho_{yarn} = \rho_f V_f^{yarn} + \rho_m (1 - V_f^{yarn}), \tag{4.3}$$

with ρ_f the density of the fibre material, ρ_m the density of the matrix material.

The homogenisation by virtual testing from microscale (fibres & resin) to mesoscale (yarn) gives us the properties for the different yarns of each material (Table C.3 in Appendix). It is important to note that, since a voxel mesh is coarse, the yarn and matrix volume fractions in the models are slightly different from their theoretical values and thus the overall fibre volume fraction is inexact. An inexact fibre volume fraction in the model has an effect on the elastic properties of the entire textile. In order to avoid that, the error on a yarn volume fraction is reflected on the fibre volume fraction in this yarn, as detailed in Sec.3.3.1.

As the homogenisation is performed by virtual testing, it implies that the microstructure has no effect on the dispersion properties of the mesostructure for low to middle range frequencies. A quick calculation is realised on a unit cell of a bundle made of an hexagonal arrangement of filaments to confirm the hypothesis. The unit cell is displayed in Fig.4.8.a.

The dispersion curves are computed for this unit cell using the method presented in Sec.3.3 and compared with a unit cell made of a homogeneous material whose properties are acquired by virtual static testing homogenisation. The results are displayed in Fig.4.8.b for one direction of propagation. It is observed

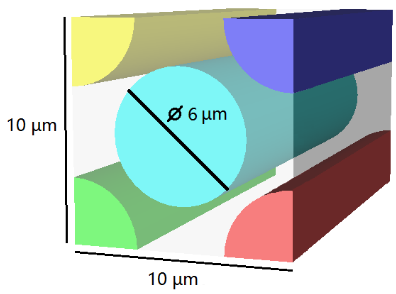

(a)

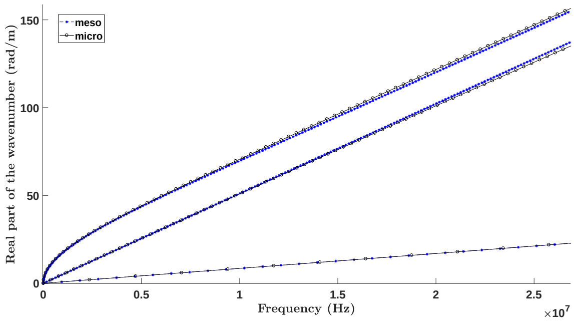

(b)

Figure 4.8: (a) Unit cell of the microscale structure of an hexagonal arrangement (b) Dispersion curves comparison between micro and mesoscale models of a unit cell of a fibre bundle.

that for low to middle frequency ranges, the internal architecture of the bundle has little effect on the dispersion properties. The hypothesis is considered valid for these applications.

Sensitivity analysis of the unknown microscale mechanical properties

In Sec.4.3.1, the 'unknown' mechanical properties of the fibres and the matrix are chosen from the literature (see Table C.2 in Appendix). To ensure that the selection of the properties from the literature does not have a strong impact on the final results, a sensitivity study is performed on a simple 2D plain woven composite model composed of four yarns as displayed in Fig.4.7. Its fibre volume fraction is of 0.5, similarly to the studied experimental materials.

One by one all the parameters are set to a minimum and a maximum [min, max] (inspired from the literature) while the others remain constant (for the fibre material, $E_{2,3}$ are set to [10,20] GPa, $G_{12,13}$ are set to [8,28] GPa, $\nu_{12,13,23}$ are set to [0.2,0.3] and for the matrix material ν_{matrix} is set to [0.3,0.35]), and the dispersion curves are computed using the WFEM/CMS methodology. The value from the [min, max] couple that gives the lowest and highest wavenumbers function of the frequency for a mode are respectively indexed. All indexed parameters are then used to form respectively the lowest and highest dispersion curves possible (the extreme opposite scenarii). The curves that have the lowest wavenumbers are obtained for the following set of parameters: $E_{2,3} = 20$ GPa, $G_{12,13} = 28$ GPa, $\nu_{12,13,23} = 0.2$ and $\nu_{matrix} = 0.35$. The highest curves are obtained for

$E_{2,3} = 10$ GPa, $G_{12,13} = 8$ GPa, $\nu_{12,13,23} = 0.3$ and $\nu_{matrix} = 0.3$. The difference between the dispersion curves obtained with these two extreme sets of parameters is of 4.15% for the flexural mode, 4.46% for the shear mode and of 4.38% for the pressure mode. These two extreme opposite scenarios do not provide considerable differences in the dispersion curves. Thus by choosing intermediate values for the missing parameters, the error is limited to a few percents.

4.3.2 Geometric modelling of the yarns arrangement

The geometric modelling of a unit cell is done using TexGen, which allows for modelling complex internal geometry enabling to describe even the nesting of the yarns for example [10, 176, 169, 182, 183]. However, an accurate modelling of the geometric shapes requires to make observations from optical microscopy scans of the material [183, 184] such as the ones shown in Fig.4.9. In this figure, it can be observed the effort made toward an accurate geometric modelling of the textile composite as a good agreement between the photo/micro-graphies and the TexGen models captures is noted. The unit cells defining the geometry of the three studied textile composites are displayed in Fig.4.1.

Knowing the number of fibres and thus the fibre volume fraction in each yarn, the total fibre volume fraction can be calculated for the three numerical models as shown in Table 4.1. This is in adequation with the results from [20].

Material	Material 1	Material 2	Material 3
Fibre volume fraction	0.41	0.42	0.55

Table 4.1: Fibre volume fraction in each of the three materials, in adequation with [20].

A trade-off needs to be found between the sufficient number of elements to represent the geometrical features of the unit cell and a low enough number of nodes to facilitate the computation. This will be further discussed in Sec.4.4.1.

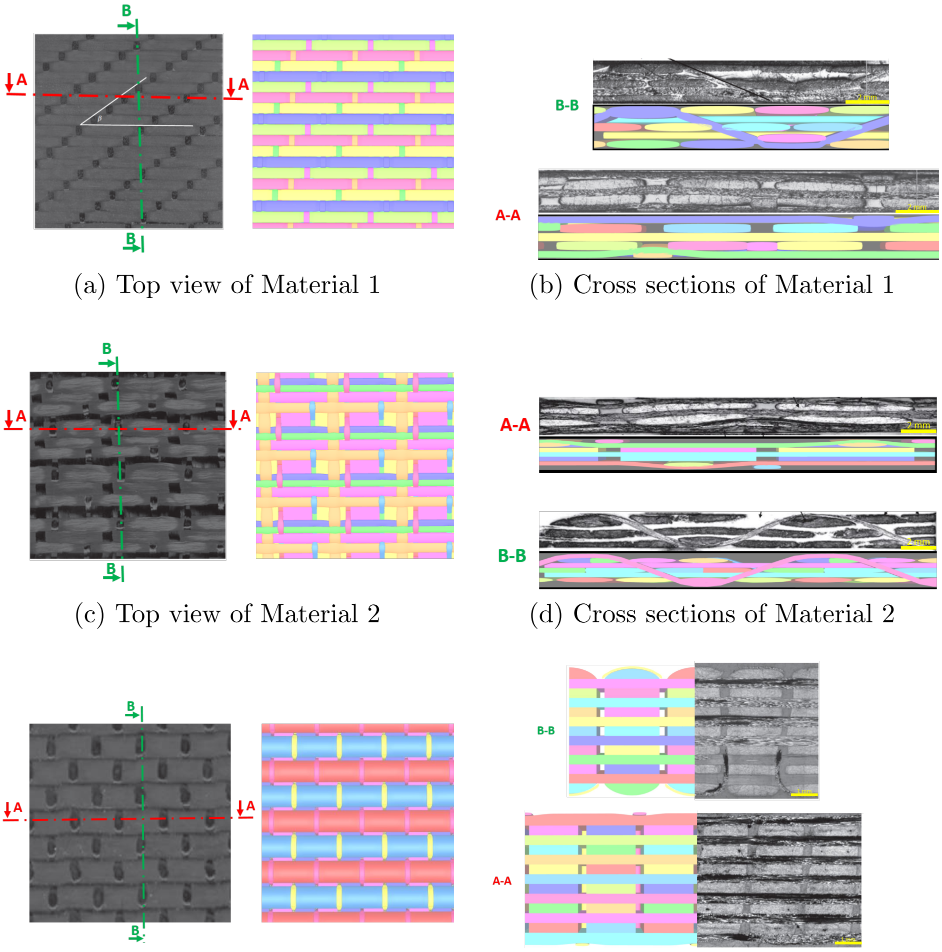

(a) Top view of Material 1 (b) Cross sections of Material 1

(c) Top view of Material 2 (d) Cross sections of Material 2

(e) Top view of Material 3 (f) Cross sections of Material 3

Figure 4.9: Left: photography of the actual composite [20] and the geometrical TexGen [167] model are compared - Right: micrographic scans of the actual composite [20] and the geometrical TexGen [167] model are compared.

4.4 Schemes comparison for 3D woven composites

This section aims to compare the dispersion characteristics obtained experimentally (see Sec.4.2) and numerically using the WFE/CMS mesoscale methodology (see Sec.3.3) for the three different studied textile composites. The results for each of the three materials are presented in separate subsections.

4.4.1 Material 1: classic 3D through-the-thickness angle interlock composite

The tested plate samples are made of Material 1 which is a classic 3D through-the-thickness angle interlock fabric infused with epoxy resin. The geometrical attributes of Material 1 can be visualised in Fig.4.9.a-.b. The plates measure 250 $\times$ 250 $\times$ 1.97 mm as presented in Sec.4.1. A unit cell of this composite as been modelled in Sec.4.3.2 and is shown in Fig.4.1.a.

Mesh convergence study

A quick convergence study is performed on the unit cell of Material 1 to ensure the validity of the mesh used. Five models, each with a different number of elements are created (40 $\times$ 22 $\times$ 10: 8800 elements; 50 $\times$ 30 $\times$ 12: 18000 elements; 60 $\times$ 40 $\times$ 15: 36000 elements; 70 $\times$ 50 $\times$ 20: 70000 elements; 80 $\times$ 60 $\times$ 30: 144000 elements). The convergence is obtained for the model 70 $\times$ 50 $\times$ 20 which displays less than 1% of relative difference with the next model, containing twice as many elements, for any mode in the five studied directions of propagation.

Experimental validation

In Fig.4.10.a, it can be observed the experimental and numerical dispersion curves for the first modes propagating in the x direction. The picture resulting from the 2D FFT applied on the experimental data has a low resolution due to the length of the composite samples used (250 $\times$ 250 mm) as explained in Sec.4.2. Three types of numerically obtained dispersion curves are also displayed. One is a result of the mesoscale methodology presented in Sec.4.3.2, while the last two are results of the two static macroscale modelling approaches as depicted in Fig.3.28.

It has to be noted that only the A_0 and S_0 can be observed on the dispersion curves obtained through experimental data. The first reason is that the studied frequency range is below the first cut-off frequency, so only the A_0, S_0 and SH_0 could be observed. The SH_0 mode is not measured by the laser vibrometer used for that study as it measures displacements in the direction normal to the surface (U_3 direction). Thanks to the 15° angle (relatively to the normal and around the y axis) given to the laser beam, U_1 can be captured and S_0 can be observed.

The mesoscale model provides a really good agreement with the experimental results for both the S_0 and A_0 modes, while the A_0 mode given by the static macroscale model has a relative difference of 11.6% when compared to the experimental results (in the x direction of propagation). It is however hard to conclude whether the mesoscale model or the static macroscale per layer gives more accurate results as the picture resolution is low. Similarly to Fig.4.10.a, Fig.4.10.b-d. and 4.12.a display dispersion curves of Material 1, only this time different directions of propagation are studied.

In directions other than x and y (Fig.4.10.b-.d), the S_0 mode is not seen. This phenomenon can be explained by the energy focusing of Lamb waves. It is analog to the phonon focusing effect unveiled by Maris in [185], in which the energy flux is more intense in some directions. It can be predicted using the focusing (or Maris) factor [186, 187]

$$A(\theta) = \left[s^2 + \frac{\partial s}{\partial \theta}^2\right]^{-\frac{1}{2}} |K_s|^{-1}, \tag{4.4}$$

where s is the slowness surface and K_s its curvature and θ the propagation angle.

Figure 4.11.a shows the slowness curve in Material 1 for the S_0 mode for a propagation angle (θ) ranging from 0° to 90°. At low frequency-thickness products, the S_0 mode is non dispersive and for that reason no frequency is given here. From the slowness curve, the focusing factor is computed and shown in Fig.4.11.b. It can be seen that the focusing is very intense in the fibre directions (x and y directions) and is very low in the other directions, especially at a 45° direction of propagation. This was observed in [186, 188] as well and it indicates

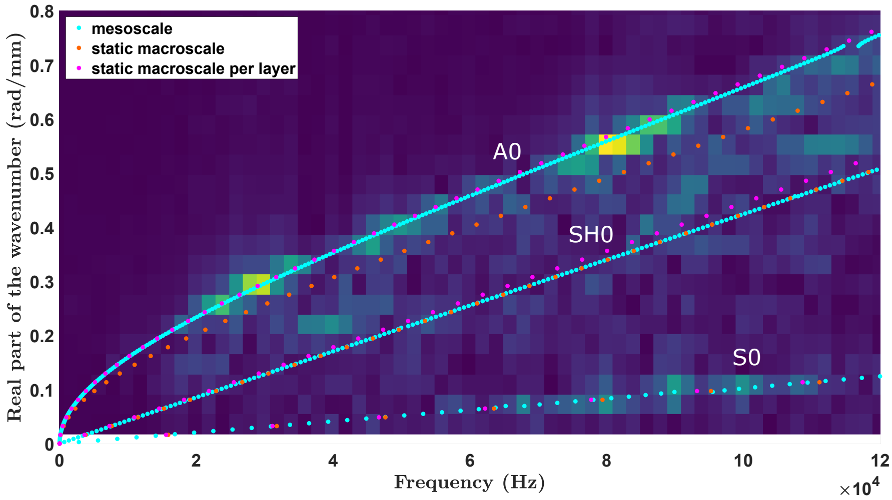

(a) x direction

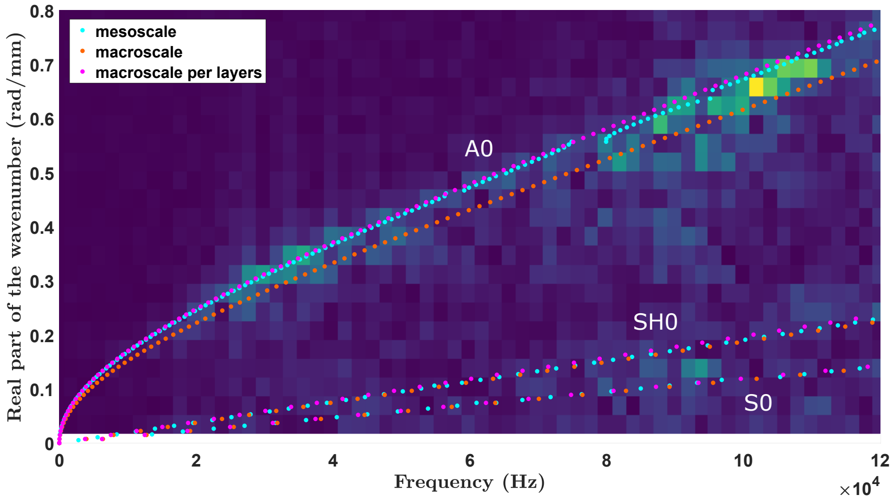

(b) 30° angle

Figure 4.10: Dispersion relations for Material 1: (results in the background) experimentally obtained, (×) obtained with the mesoscale method, (magenta dots) obtained with the static macroscale per layer method and (yellow dots) obtained with the static macroscale method. (a) Waves propagating in the x direction. (b) Waves propagating at a 30° angle to the x direction. (c) Waves propagating at a 45° angle to the x direction. (d) Waves propagating at a 60° angle to the x direction.

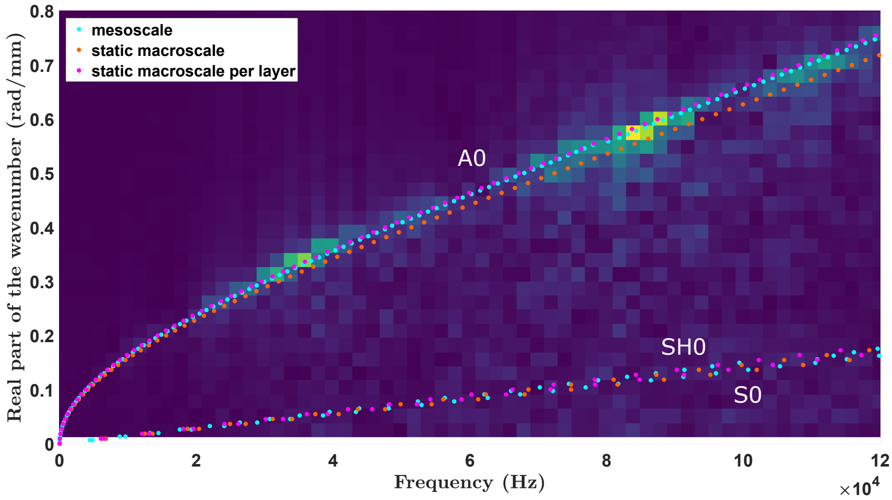

(c) 45° angle

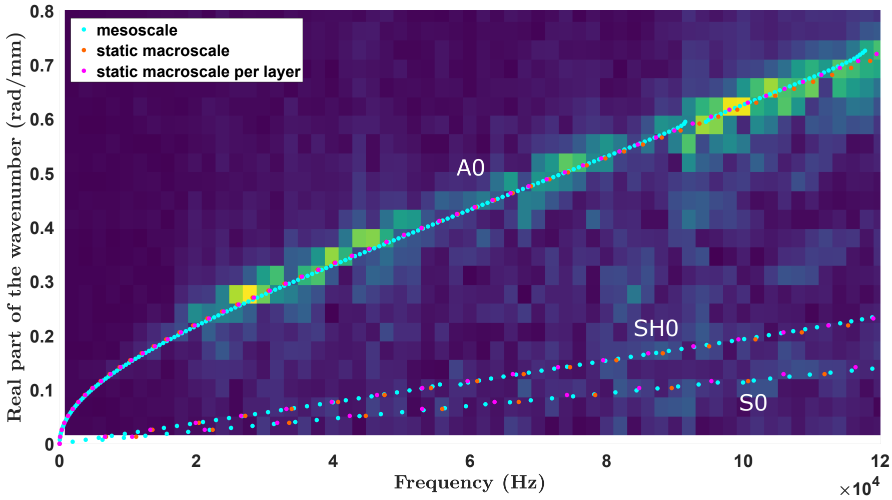

(d) 60° angle

Figure 4.10: Dispersion relations for Material 1: (results in the background) experimentally obtained, (×) obtained with the mesoscale method, (magenta dots) obtained with the static macroscale per layer method and (yellow dots) obtained with the static macroscale method. (a) Waves propagating in the x direction. (b) Waves propagating at a 30° angle to the x direction. (c) Waves propagating at a 45° angle to the x direction. (d) Waves propagating at a 60° angle to the x direction.

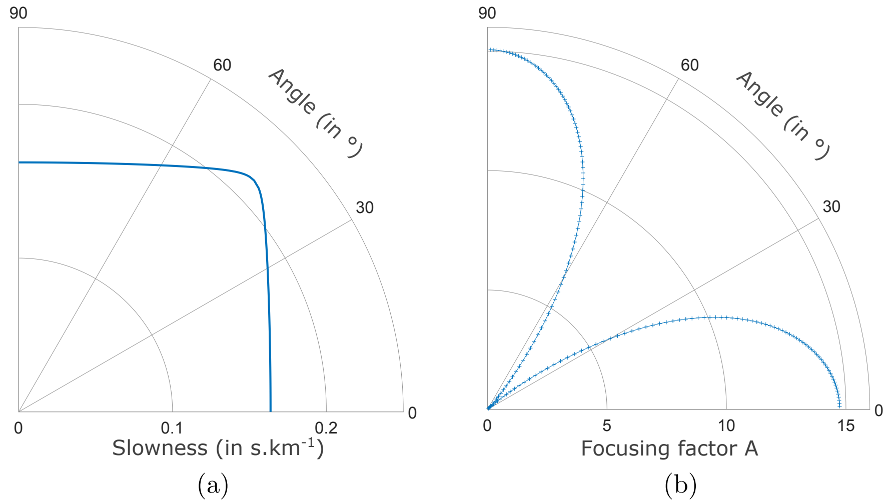

Figure 4.11: (a) Slowness curve in s.km^{-1} in Material 1 for S_0 mode (b) Focusing factor A for the S_0 mode computed using Eq.(4.4).

the difficulty of energy propagation in non-fibre directions.

In Fig.4.12.a, which displays the experimental and numerical dispersion curves for the modes propagating in the y direction, A_0 and S_0 modes are observed as usual, but another less conventional mode can be seen. Displaying the green horizontal lines indicating the BZ boundaries $k = n\pi/\Delta$, an hypothesis can be formulated. This material being periodic, we could be observing the same phenomenon as seen in Fig.3.34. The S_0 mode is plotted again but in a different colour (white) for $k = k + 2\pi/\Delta$ and it shows a good agreement with this 'third' experimentally observed mode. However, it is hard to explain why this mode does not appear in the other directions of propagation. In the numerical transient FEA performed for another textile composite (Fig.3.34) only a few modes are indeed repeated at $k = 2\pi/\Delta$, it is not clear either why these ones are and not the others.

Another phenomenon is observed in all experimental dispersion relations: the curves are discontinuous. These discontinuities are mainly justified by PZT frequency transduction effects and other experimental choices. Indeed, a simple equation gives the ability of a PZT to detect a wave according to the PZT diameter ($\varnothing_{PZT}$), the frequency and the wave dispersion characteristics. This ability is called frequency filtering or tuning (written f_{PZT}) and expressed as a normalised

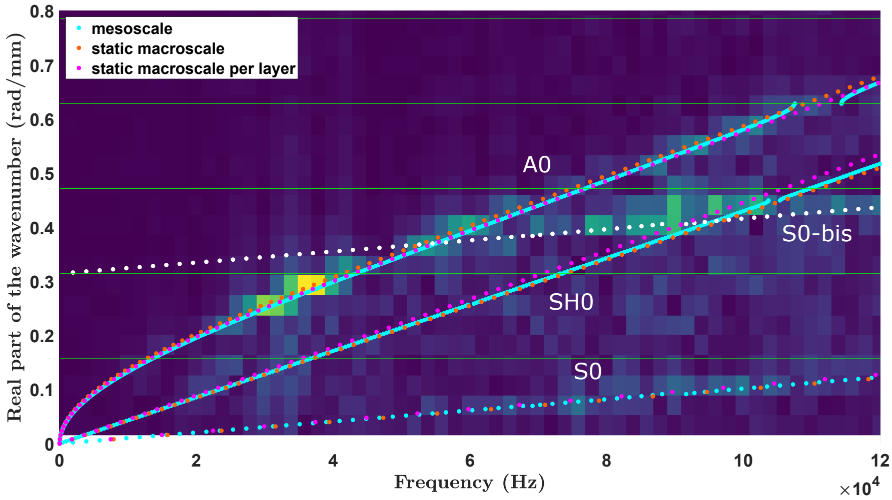

(a)

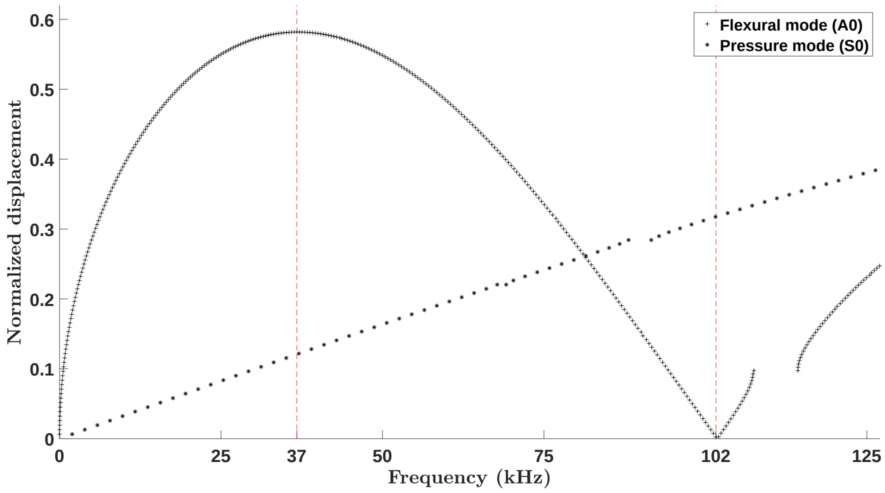

(b)

Figure 4.12: (a) Dispersion relations obtained for Material 1 for waves propagating in the y direction; (results in the background) experimentally obtained, ($\times$) obtained with the mesoscale method, (magenta dots) obtained with the static macroscale per layer method and (yellow dots) obtained with the static macroscale method. The green lines indicate the BZ boundaries $k = n\pi/\Delta$ (b) Frequency filtering operated by the PZT for the A_0 and S_0 modes in the y direction (PZT diameter of 13 mm) computed using Eq.(4.5).

displacement [2, 189, 190]

$$f_{PZT} = \left| J_1 \left(\pi \frac{\varnothing_{PZT}}{\lambda(\omega)} \right) \right|, \tag{4.5}$$

where $\lambda(\omega)$ is the wavelength as a function of the angular frequency and J_1 the Bessel function of the first kind and first order.

It is observed in the flexural mode in Fig.4.12.a a very low magnitude at 100 kHz, that is an effect of the frequency filtering operated by the PZT (see Fig.4.12.b) in the y direction. The high magnitude captured for the same mode at 37 kHz is an effect of the frequency filtering again, it corresponds to the frequency at which the PZT transmits the most energy for that mode [1, 190]. Even though this model is valid for predictions in isotropic media only, it provides some hints of explanation on the observed amplitude.

4.4.2 Material 2: less conventional 3D through-the-thickness angle interlock composite

The tested plate samples are made of Material 2 which is a less conventional 3D through-the-thickness angle interlock fabric infused with epoxy resin. The geometrical attributes of Material 2 can be visualised in Fig.4.9.c-d. The plates measure 250 $\times$ 250 $\times$ 1.95 mm as presented in Sec.4.1. A unit cell of this composite has been modelled in Sec.4.3.2 and is shown in Fig.4.1.b.

The same study is performed on this material. This model unit cell is discretised in 70 $\times$ 50 $\times$ 25 elements, totalising 87500 elements. In Fig.4.13 can be observed the comparison between the experimental and numerical dispersion curves for different directions of propagation. The mesoscale results are in good agreement with the experimental results, except for A_0 in the y direction (Fig.4.13.d) where the predictions are slightly higher from 80 kHz. The predictions from the macroscale per layer model for A_0 in the same direction of propagation are slightly lower in comparison to the experimental curve as well. In this case, it seems that the macroscale model is the only one to provide an accurate prediction of the A_0 dispersion curve in the y direction. This, however, does not make it a better prediction model as it is strongly off for at least two other directions of propagation (x and 45°).

For the first time, it is observed in Fig.4.13.c that the mesoscale and static macroscale per layer models provide dispersion curves of the flexural mode that are significantly different. The mesoscale model gives results that are in good agreement with the experimental ones while the flexural modes given by both static macroscale models are lower. In Fig.4.13.d, the same phenomenon as in

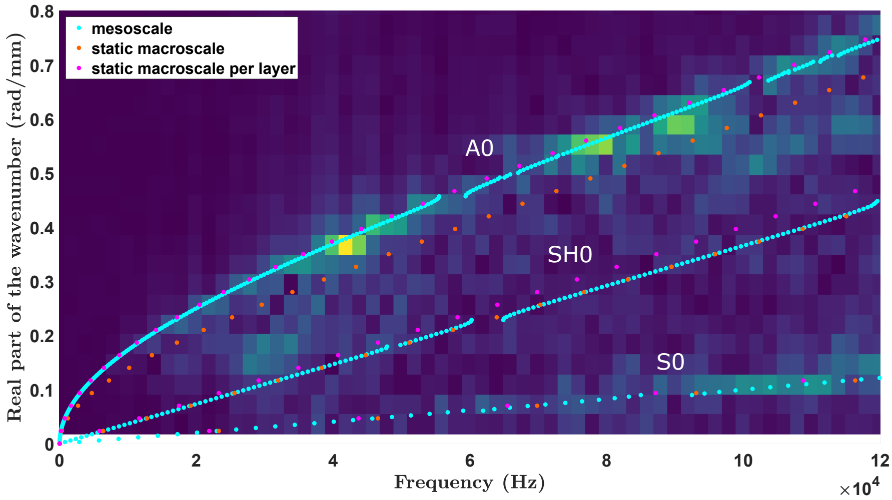

(a) x direction

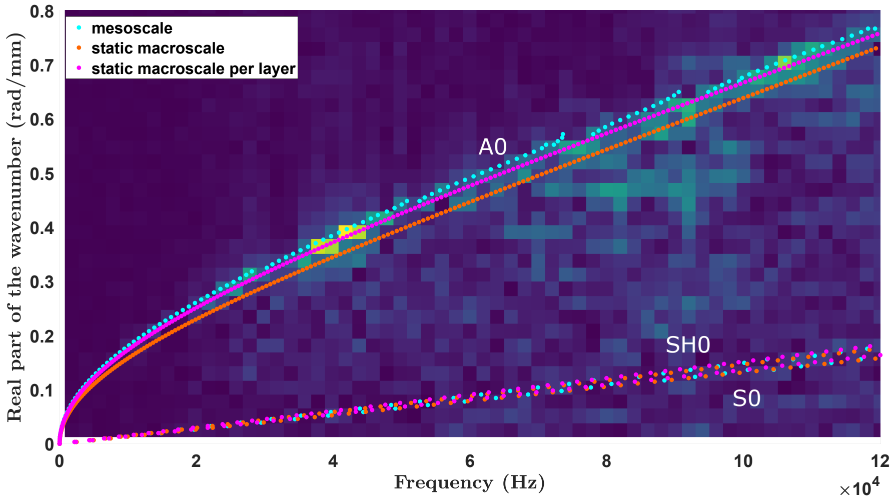

(b) 45° angle

Figure 4.13: Dispersion relations for Material 2: (results in the background) experimentally obtained, (×) obtained with the mesoscale method, (magenta dots) obtained with the static macroscale per layer method and (yellow dots) obtained with the static macroscale method. (a) Waves propagating in the x direction. (b) Waves propagating at a 45° angle to the x direction. (c) Waves propagating at a 60° angle to the x direction. (d) Waves propagating in the y direction.

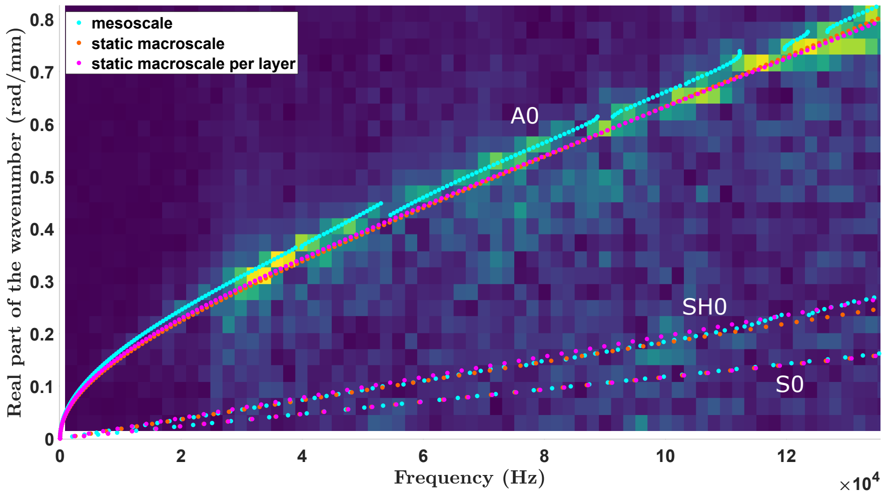

(c) 60° angle

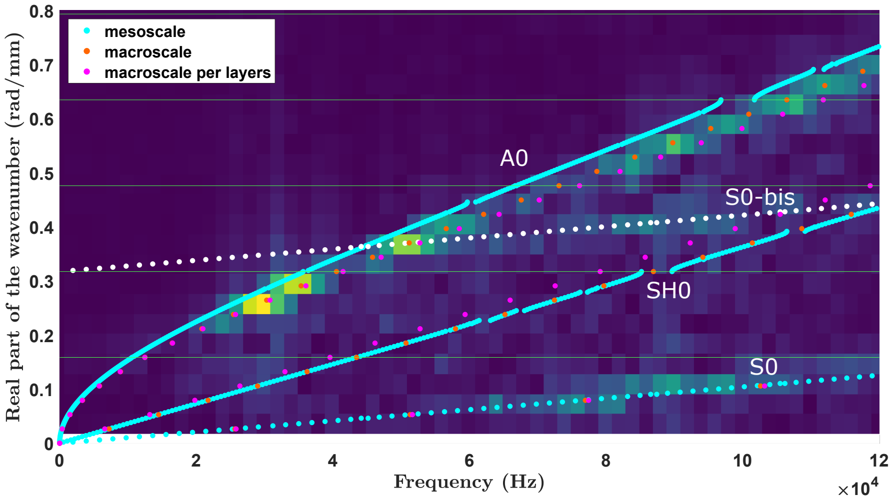

(d) y direction

Figure 4.13: Dispersion relations for Material 2: (results in the background) experimentally obtained, ($\times$) obtained with the mesoscale method, (magenta dots) obtained with the static macroscale per layer method and (yellow dots) obtained with the static macroscale method. (a) Waves propagating in the x direction. (b) Waves propagating at a 45° angle to the x direction. (c) Waves propagating at a 60° angle to the x direction. (d) Waves propagating in the y direction.

Fig.4.12.a is observed: the A_0 and S_0 modes are seen as usual, but another less conventional mode can be observed. Displaying the BZ boundaries $k = n\pi/\Delta$ (in green) and plotting the predicted S_0 mode for $k = k + 2\pi/\Delta$ (in white) shows an agreement and thus suggests that the same phenomenon is seen once again.

4.4.3 Material 3: 3D through-the-thickness orthogonal interlock composite

In this subsection, the tested plate sample is made of Material 3 which is a classic 3D through-the-thickness orthogonal interlock fabric infused with epoxy resin. The geometrical attributes of Material 3 can be visualised in Fig.4.9.e-.f. The plate measures 250 × 250 × 4.98 mm as presented in Sec.4.1. A unit cell of this composite as been modelled in Sec.4.3.2 and is shown in Fig.4.1.c. The same study as for the two previous materials is performed on this material. This FE model is composed of 35 × 35 × 60 elements, which means a total of 73500 elements and 237168 DoFs.

In Fig.4.14, the dispersion curves of the five first modes propagating in the x direction are plotted. For each mode, a modeshape is represented for a side only of the considered unit cell (bottom side in this case, see Fig.2.8). This allows to identify that the two higher-order modes present on the figure at cut-off frequencies of around 150 kHz and 153 kHz are respectively SH_1 and A_1.

In Fig.4.15, it is observed that the mesoscale, the static macroscale and the static macroscale per layer models provide dispersion curves that are similar for A_0 and S_0. A significant difference can be observed between the mesoscale and static macroscale per layer models for the shear mode in the x and y directions (see Fig.4.15.a and .d), unfortunately this mode could not be observed experimentally. Also the forth (SH_1) and fifth (A_1) modes appear to be predicted differently with the static macroscale model in Fig.4.15, but performing this test for higher frequency ranges resulted in a highly damped signal that could not propagate at sufficient distance and we were not able to observe these modes experimentally. SH_1 could not have been be observed using this set-up as it is not measured (similarly to SH_0). This material did not allow us to conclude which model gives the best prediction.

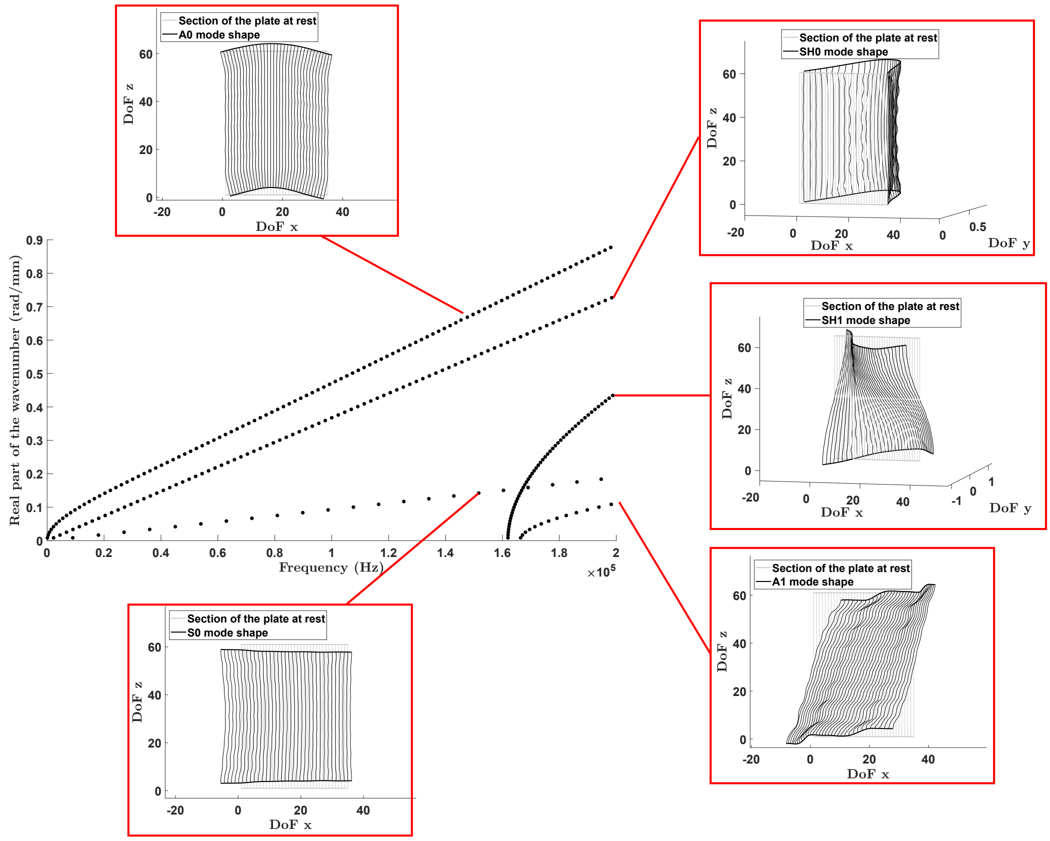

Figure 4.14: Dispersion curves of the five first modes of Material 3 in the x direction of propagation, modelled at mesoscale. For each mode, a modeshape associated to a frequency point is plotted.

The computation times for all three models presented in this section are displayed in Table 4.2. The computations for the mesoscale models were run on the HPC of the University of Nottingham, it used 6 cores in parallel, each needing around 60 GB of RAM. The times shown are the elapsed times for calculating the dispersion relations in five different directions of propagation. To obtain the dispersion relations in another direction would be relatively costless timewise. Indeed, the most consuming task is to project the stiffness and mass matrices of the unit cell on the $\mathbf{B}$ basis obtained through the Craig-Bampton method to reduce the size of the set of internal DoFs (see Eq.(2.61)). The computation time is mainly driven by the number of boundary DoFs of the unit cell. While these 3D woven composites are quite complex, and thus require a large number of nodes and elements to be described accurately, they are relatively thin materials (around 2 and 5 mm) with only five to thirteen yarn layers. Performing the same type of computation on materials with many more layers would dramati-

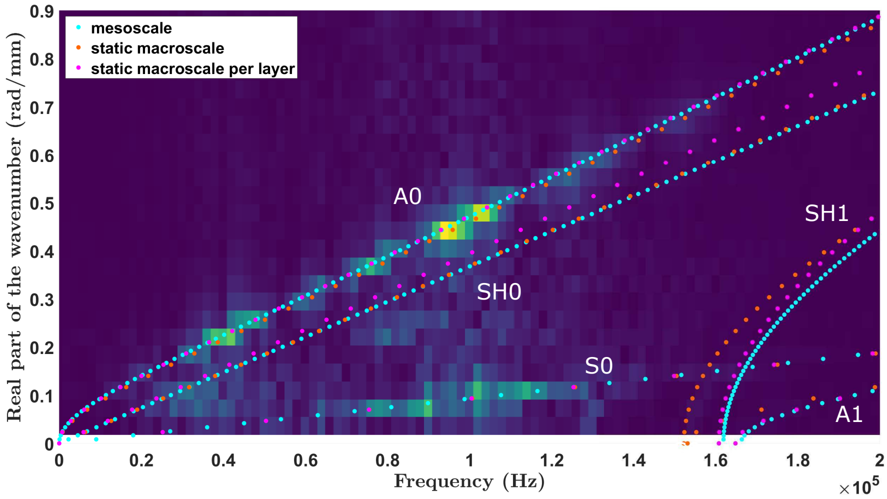

(a) x direction

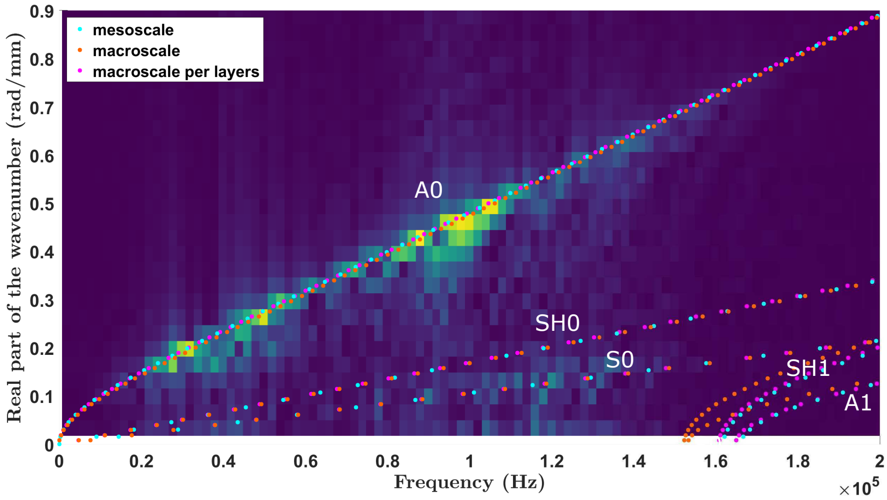

(b) 30°

Figure 4.15: Dispersion relations for Material 3: (results in the background) experimentally obtained, (×) obtained with the mesoscale method, (magenta dots) obtained with the static macroscale per layer method and (yellow dots) obtained with the static macroscale method. (a) Waves propagating in the x direction. (b) Waves propagating at a 30° angle to the x direction. (c) Waves propagating at a 45° angle to the x direction. (d) Waves propagating in the y direction.

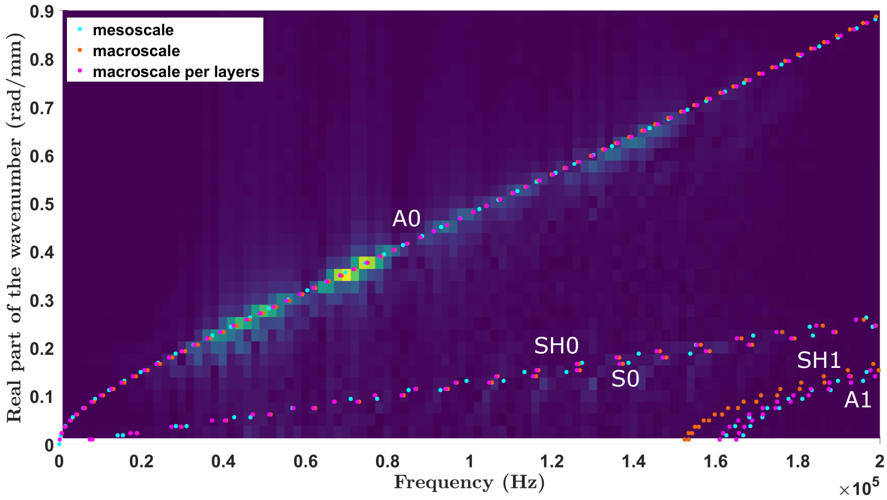

(c) 45°

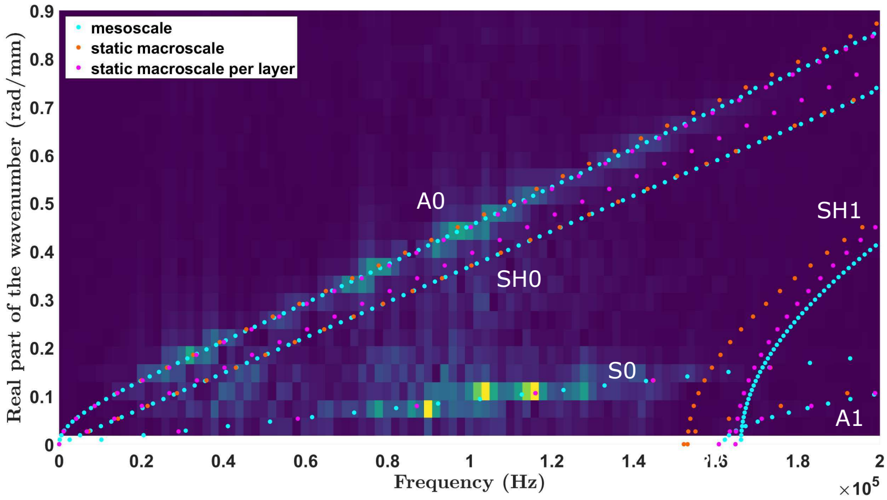

(d) y direction

Figure 4.15: Dispersion relations for Material 3: (results in the background) experimentally obtained, (×) obtained with the mesoscale method, (magenta dots) obtained with the static macroscale per layer method and (yellow dots) obtained with the static macroscale method. (a) Waves propagating in the x direction. (b) Waves propagating at a 30° angle to the x direction. (c) Waves propagating at a 45° angle to the x direction. (d) Waves propagating in the y direction.

cally increase the computational time. Also, the difference in computational cost between a macroscale and a mesoscale model is enormous. One should consider using the static macroscale per layer methodology for a rough but quick estimation of the dispersion curves if knowledge of the stop-bands and modeshapes is not primordial. However, if this information is important, the costly part of the mesoscale computation has to be performed only once for a particular composite.

	Elapsed time (6 cores)	CPU time (1 core)
Material 1 mesoscale	23 hours	around 3 days
Material 2 mesoscale	31 hours	around 4 days
Material 3 mesoscale	2 days	around 6 days
Any material macroscale	-	40-80 seconds

Table 4.2: Computation time for all the models presented in this chapter.

4.5 Conclusions

In this chapter a multiscale approach allowing for predicting the dispersion relations of 3D woven composites is presented and compared with experimental results. Three different materials are studied and three levels of modelling are presented. The static macroscale model resolves less structure details and is shown to be inaccurate in its predictions of the dispersion relations for the first and second presented materials.

While chapter 3 showed that static macroscale and macroscale per layer models provide wrong predictions in comparison to mesoscale models, experimentally it is hard to conclude which model amongst the mesoscale and static macroscale per layer is more accurate as we were not able to compare more than two modes (S_0 and A_0). It would have been possible to observe more modes at higher frequencies, however, the damping in the plates was too high. Another reason is the lack of resolution provided by the experimental results. It would be possible to have a higher resolution with larger plates as the inspected length defines the wavenumber resolution. This limitation comes from the manufacturing equipment used.

It is shown that the computation times, even though relatively long for the mesoscale approach, are feasible. It should be noted that even though the static macroscale per layer model is much faster to compute, the geometrical modelling step is the same for both models and it does take some time to complete as well. However in both cases, once this costly calculation is finished, the dispersion relations and their modeshapes are obtained for any direction of propagation at a minimal cost.

It can be concluded that:

- Macroscale models using material properties obtained by static virtual testing provide inaccurate dispersion relations predictions.
- Both the static macroscale per layer and mesoscale methods have provided good predictions for A_0 and S_0 in comparison to experimental results. This study, however, does not allow to conclude which gives the best predictions.
- The computational times are feasible even when considering a real composite structure.

Chapter 5

Accounting for periodic textile composite structures within continuous wave propagation schemes

It has been established in chapters 3 and 4 that the dispersion characteristics of textile composites cannot be computed accurately using static macroscale models. For this reason, methods such as the SAFE or some formulations of the WFE while extremely time efficient, cannot be used to obtain the dispersion relations of such complex materials. The methodology presented in Sec.3.3 was introduced to mitigate this issue by using a mesoscale model of the composite, accurately representing the yarns and matrix geometries. This methodology, while revealing itself to provide accurate dispersion characteristics predictions, needs much more computational resources than a macroscale one. That is an important drawback when multilayered composites are of interest. Indeed the dispersion characteristics have to be computed for the composite as a whole and since the computational cost are directly dependent to the number of boundary nodes of the discretised unit cell, this implies that the more layers, the bigger the size of the problem, e.g. doubling the number of layers squares the size of the problem to solve.

On the other hand, methods such as SAFE or WFE using macroscale modelling are extremely efficient to compute the dispersion relations of laminates as long as the elastic moduli are known for each individual layer. The approach proposed in this chapter takes advantage of the accuracy of the methodology for computing dispersion relations in complex textile composites from Sec.3.3 and the efficiency of the SAFE method to compute the dispersion characteristics of macroscale laminate models.

In this chapter, the Lamb wave dispersion characteristics of textile composites modelled at a mesoscopic scale are inverted by the mean of a GA in order to obtain their approximated effective elastic constants to be used in a macroscale model. The GA iteratively uses the SAFE method to update the dispersion curves for a set of candidate solutions. In the first section (Sec.5.1), the homogenisation methodology is thoroughly described. In the second section (Sec.5.2), the methodology is validated using a simple orthotropic plate structure. The following sections (Sec.5.3-5.5) are case studies of three different textile composites.

5.1 Homogenisation methodology based on GA

GAs are widely used for error optimisation problems. These algorithms are search algorithms based on the mechanics of natural selection described by Darwin [110]. They are conceptually simple and useful in problems where no analytical model exists or when the search space is too complex for other search algorithms such as simulated annealing or gradient based methods. These characteristics make GA a good candidate for determining the elastic moduli of a material from its dispersion relations. A schematic representation of the elastic moduli identification framework based on the GA method is shown in Fig.5.1. The input to the method are the mesoscale dispersion characteristics of the material computed using Sec.3.3 in a few directions of propagation. The objective function is built on the relative discrepancies between the dispersion characteristics computed using a macroscale model along with the SAFE method for a tentative set of elastic moduli and the mesoscale ones. The GA procedure iteratively updates the sets of elastic moduli in the SAFE formulation in order to minimise the objective function as presented in [110]. The iteration terminates when a stopping-condition is fulfilled, it can be when the value of the objective function for a tentative set of elastic moduli overcomes a threshold or after a pre-defined number of iterations for example.

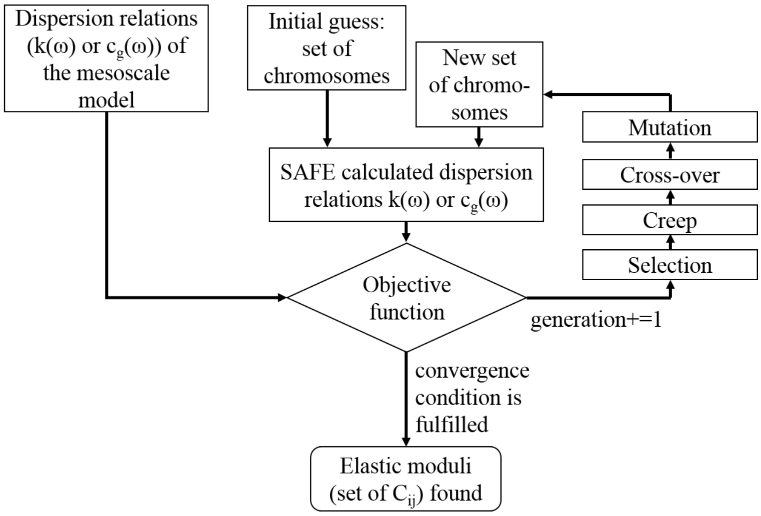

Figure 5.1: Schematic representation of the elastic moduli (C_{ij}) identification framework based on the GA method.

In this GA study, a chromosome is a set of nine elastic moduli (also called C_{ij}) describing the stiffness matrix of an orthotropic material. Each individual moduli is a gene. A set of multiple chromosomes is called a population, as depicted in Fig.5.2.

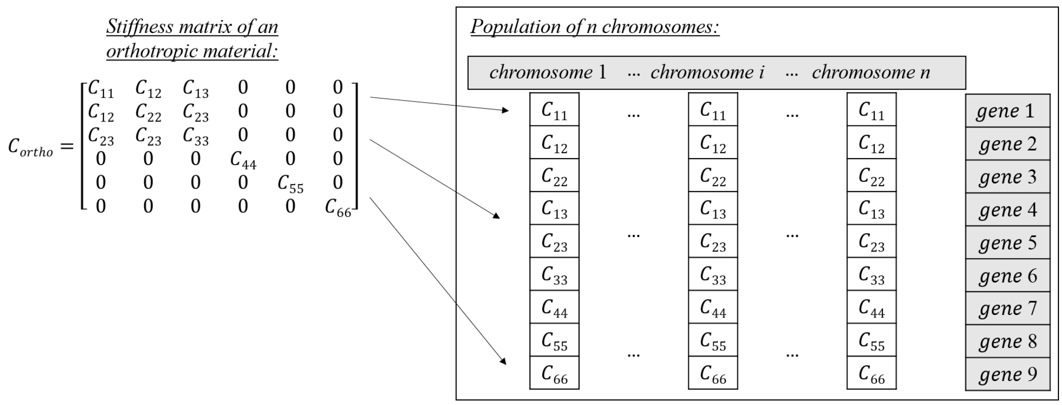

Figure 5.2: GA terms used in this chapter for a chromosome representing the elastic constants of an orthotropic material.

5.1.1 Initialisation

Even though it is not necessary to attain convergence, using an initial guess allows for speeding up the process, given that the initial guess is close to the solution.

Since the material is modelled to obtain its mesoscale dispersion characteristics, it is convenient to use its effective elastic moduli obtained by static virtual testing (method detailed in [29, 30] and explained in Sec.A.1 in Appendix) as initial guess but not necessary. A small set of chromosomes of the initial population is set equal to the initial guess while the rest of the population is randomly generated from a narrow neighbouring interval whose median value is the initial guess.

5.1.2 Objective function

The objective function defines discrepancy between the mesoscopic dispersion relations computed for a textile composite and the macroscopic dispersion characteristics computed for a tentative set of elastic moduli. The identification of the optimal set of elastic moduli is realised through the minimisation of this objective function. The mesoscale dispersion relations are inputs to the GA procedure and are not updated while the macroscale dispersion curves are computed iteratively using the SAFE method for each updated set of elastic moduli. Different types of dispersion characteristics can be used for comparison: the wavenumber or the group velocity (defined in Eq.(2.20)) displayed in Fig.5.3 are two possibilities. While the group velocity parameter is traditionally used [92, 109, 111] for GA-based homogenisation methods (for the simple reason that this parameter is straightforward to obtain experimentally), the wavenumber parameter is also a good candidate. Both approaches are investigated in this chapter.

The error function to be minimised is the Mean of the Relative Error (MRE) for each point of an individual dispersion curve and is written as follows:

$$\mathrm{MRE}(\theta) = \sum_{i=1}^{n} \left| \frac{\lambda_i^{\mathrm{meso}}(\theta) - \lambda_i^{\mathrm{macro}}(\theta)}{\lambda_i^{\mathrm{meso}}(\theta)} \right| /n. \tag{5.1}$$

with λ the dispersion parameter for the considered mode, θ the angle of propagation of consideration and n the number of compared data points.

The relative error function is computed separately for the three fundamental modes (S_0, SH_0 and A_0) and in a few directions of propagation. The objective function is set to the maximum of any of these values, thus minimising all modes simultaneously. All modes have to be considered as it would be useless to obtain a

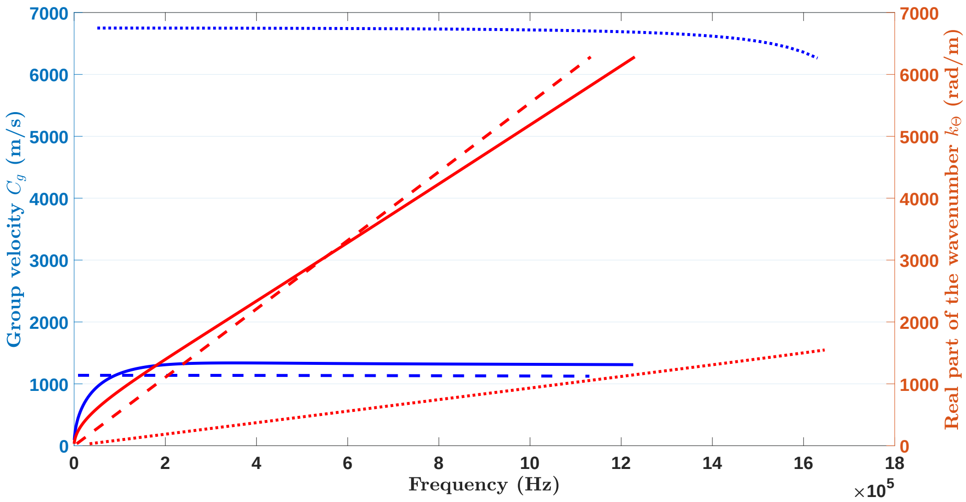

Figure 5.3: Dispersion relations (group velocity plotted in blue and wavenumber in red) of the three first modes in the x direction of propagation for a plate constituted of an orthotropic material. Comparisons on the sensitivity of both parameters are provided in Sec.5.2 to determine which is best for this application. (–) A_0, (- -) SH_0, (..) S_0.

set of moduli that reconstructs one mode only. Using the sum of all relative errors has been considered but revealed itself to slow down the optimisation process.

5.1.3 Selection

The fitness function is directly derived from the objective function and determines the likeliness of a chromosome to be selected for the next generation [109]. The selection process can be visualised as a roulette wheel in which each chromosome covers an area of the wheel proportional to its probability to be selected. The chromosomes for the next generation are selected one by one by turning the wheel. All generations population contain an equal number of chromosomes thus a chromosome with a high probability of selection might be selected more than once to be passed onto the next generation.

5.1.4 Creep

A creeping operation is performed on each new candidate solution. A threshold is established and a random number is generated. If the random number exceeds the threshold then the considered set of elastic moduli is randomly scaled in the range of [1-δ_{creep}, 1+δ_{creep}], δ_{creep} being the creep amount. Using that method allows for a search outside the search space [109] (e.g. if a gene of the candidate solution is close to the high limit of its search space, after the creep operation, the gene might be scaled up to $1+\delta_{creep}$ thus be outside the initial search space).

5.1.5 Crossover

Some of the selected chromosomes mate to create new offspring whose genes are a combination of its parent genes, this is the crossover process. The crossover rate defines the number of parent chromosomes to be selected for crossover. Two parent chromosomes are 'cut' at a single random crossover point and their genes are interchanged [109].

5.1.6 Mutation

Finally some of the chromosomes are mutated to avoid stagnation of the solution to a local minima. The mutation rate defines the number of genes to be mutated and their positions across the chromosomes are selected randomly. The genes selected for mutation are each replaced by a newly generated one [109].

5.2 Implementation method

To show its applicability, the method is first performed on a simulated orthotropic plate whose theoretical elastic moduli are known. Its dispersion characteristics are computed using the WFE method. In the following subsections, the elastic moduli are approximated using two different approaches to validate and compare them. The first approach, named 'brute-force' in this chapter in reference to search techniques that are not the most clever and computationally expensive [107], tries the ambitious task of reconstructing all nine parameters at once. The second uses the sensitivity of each modes to the different parameters to optimise a reduced number of parameters at once.

5.2.1 Brute-force

The thickness of the plate and the density of the material are fixed (0.5 mm and 3212 kg/m^3) because known and the nine elastic moduli presented in Table 5.1 in the 'theoretical' column are sought. These moduli represent a unidirectional carbon fibre reinforced polymer composite whose fibre arrangement makes it slightly non-transverse isotropic. Table 5.1 shows the results obtained for five different and independent runs of the GA and the percentage of error to the theoretical value. In order to validate the method, no initial guess was used. The crossover and mutation rates are both set to 0.1, the creep amount is set to 0.3 and the generated population size is of 50 chromosomes. The algorithm is launched considering the wavenumber dispersion relations for five runs and the group velocity dispersion relations for five other runs to provide for comparison.

	Theoretical	#1	#2	#3	#4	#5
C_{11} (GPa)	147.36	146.18	147.61	146.93	147.39	148.12
error (%)		0.80	0.18	0.29	0.02	0.52
C_{12} (GPa)	3.43	2.46	2.93	3.85	3.63	8.64
error (%)		28.23	14.49	12.18	5.68	151.65
C_{22} (GPa)	9.51	8.68	8.21	8.34	9.31	10.11
error (%)		8.71	13.70	12.29	2.15	6.30
C_{13} (GPa)	3.47	1.11	0.73	1.18	1.77	5.88
error (%)		67.84	78.84	65.85	48.83	69.59
C_{23} (GPa)	4.02	1.49	1.31	1.01	1.89	4.87
error (%)		63.04	67.49	74.94	52.98	21.17
C_{33} (GPa)	11.66	5.77	5.19	5.53	4.80	12.89
error (%)		50.52	55.49	52.54	58.85	10.54
C_{44} (GPa)	3.19	3.18	3.36	3.30	3.20	3.21
error (%)		0.20	5.44	3.44	0.31	0.56
C_{55} (GPa)	5.58	5.60	5.69	5.72	5.48	5.59
error (%)		0.35	1.99	2.52	1.88	0.22
C_{66} (GPa)	4.16	4.13	4.14	4.10	4.13	4.09
error (%)		0.72	0.41	1.51	0.57	1.54
Generations	-	103	118	286	222	222
Time (h)	-	25	30	59	49	46

Table 5.1: Results of the GA for five independent runs for the reconstruction of the elastic moduli of an orthotropic material whose real moduli are displayed on the left-hand side, when $k(\omega)$ is considered.

The results are firstly displayed for the wavenumber approach in Table 5.1. It can be observed that this methodology, while providing a realistic order of

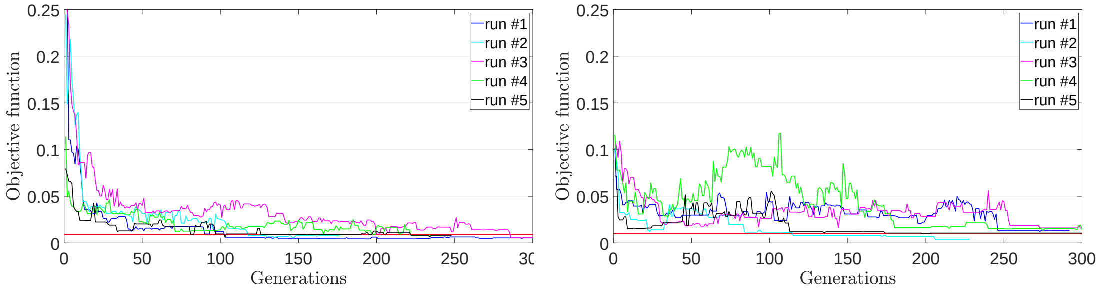

(a) (b)

Figure 5.4: Value of the objective function as a function of the generation for the five GA independent runs for the reconstruction of the elastic moduli of the orthotropic material. (a) $k(\omega)$ is considered. Convergence is observed for all runs after 290 generations. 100 generations were needed for at least one run to converge. The horizontal red line is plotted at 1% of error. (b) $c_g(\omega)$ is considered. After 300 generations, the objective function is smaller than 1% for only two runs, all three other runs struggle to converge.

magnitude for the elastic moduli, yields strong relative error for many of them ($> 10\%$). Some elastic moduli such as C_{11} and C_{66} however, are in all five runs guessed with a very low relative error ($< 2\%$), C_{44} and C_{55} are guessed with a tolerable error ($< 6\%$). One can conclude that these parameters are extremely sensible in comparison to the others.

Trying to optimise nine coefficients at once is a very ambitious task and the convergence is obtained after many generations (at least 100) as seen in Fig.5.4.a, and thus is time consuming. Moreover, only two elastic moduli are reconstructed with a good accuracy and two more only with a relatively low error. One can conclude that this approach is neither time efficient, nor yields accurate results. However, the objective function value is smaller than 1% at convergence for each run. This indicates that even though the correct solution was not found, at least a solution exists.

For the sake of comparison, the exact same methodology is applied once more with the only difference that group velocity ($c_g(\omega)$) curves are compared for minimisation in the objective function, instead of the wavenumber ($k(\omega)$) relations. Figure 5.4.b shows the evolution of the objective function at each new generation. In comparison to the $k(\omega)$ approach, it is observed that three out of the five runs do not reach the threshold of 1% of error in less than 300 generations. It seems that the algorithm is more efficient to find solutions when $k(\omega)$ relations are considered rather than $c_g(\omega)$ relations. This is logical as $c_g(\omega)$ is a derivative of $k(\omega)$ (see Eq.(2.20)), thus $c_g(\omega)$ is less sensitive. The solutions for both converged runs (using $c_g(\omega)$) are displayed in Table 5.2 and it is observed that no greater accuracy is obtained for the parameters in comparison to the elastic moduli obtained in Table 5.1. In conclusion, comparing $k(\omega)$ relation instead of $c_g(\omega)$ in the objective function of the GA allows for faster convergence while providing a similar accuracy.

	Theoretical	**#2**	**#5**
C_{11} (GPa)	147.36	146.73	151.30
error (%)		0.43	2.68
C_{12} (GPa)	3.43	2.13	3.75
error (%)		37.96	9.23
C_{22} (GPa)	9.51	10.00	10.68
error (%)		5.17	12.25
C_{13} (GPa)	3.47	3.54	8.24
error (%)		2.04	137.61
C_{23} (GPa)	4.02	4.76	5.91
error (%)		18.46	46.87
C_{33} (GPa)	11.66	12.70	14.62
error (%)		8.90	25.43
C_{44} (GPa)	3.19	3.19	3.25
error (%)		0.14	1.80
C_{55} (GPa)	5.58	5.61	5.66
error (%)		0.49	1.38
C_{66} (GPa)	4.16	4.15	4.08
error (%)		0.30	1.81
Generations	-	224	200
Time	-	49h	41h

Table 5.2: Results of the GA, for the unique run to converge before 300 iterations, for the reconstruction of the elastic moduli of an orthotropic material whose real moduli are displayed on the left-hand side, when $c_g(\omega)$ is considered.

5.2.2 Sensitivity

The brute-force approach showed that the dispersion relations have a very low sensitivity to some of the moduli if considered altogether. A sensitivity study is performed in order to uncover the effect of each parameters to be optimised on the dispersion relations. This step is of the upmost importance as the sensitivities of the unknown parameters are different and this strongly affects the performance of the GA as stated in [109]. Each individual moduli is alternatively increased by a coefficient, and the relative difference induced on the dispersion curves is computed for the first three modes for a discrete set of directions of propagation ranging from 0° to 90°. Figures 5.5-5.7 display this information and the relative difference is shown in logarithmic scale to emphasise the order of magnitude of effect of each coefficient. Each sensitivity study is both performed considering the wavenumber and the group velocity as outputs.

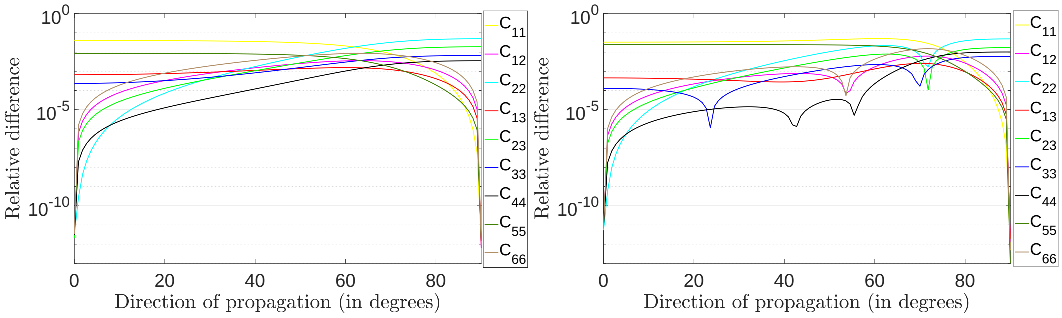

(a) (b)

Figure 5.5: Sensitivity of the A_0 mode to the different elastic moduli at a frequency of 50kHz (a) when $k(\omega)$ is considered (b) when $c_g(\omega)$ is considered.

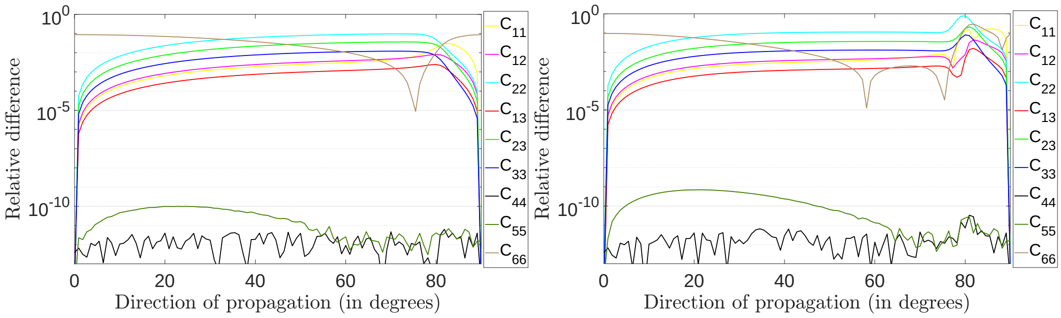

(a) (b)

Figure 5.6: Sensitivity of the SH_0 mode to the different elastic moduli at a frequency of 50kHz (a) when $k(\omega)$ is considered (b) when $c_g(\omega)$ is considered.

First of all, it can be observed that the sensitivities are similar when considering either the wavenumber or the group velocity as reference data. In Fig.5.5 and 5.7, it can be observed that at 50kHz, C_{11} and C_{55} have a significant impact on the A_0 and S_0 modes dispersion curves in the x direction of propagation (0°), while the effect of the other moduli in comparison is considered insignificant. This is logical as the main strain component involved in the S_0 mode in the x direction

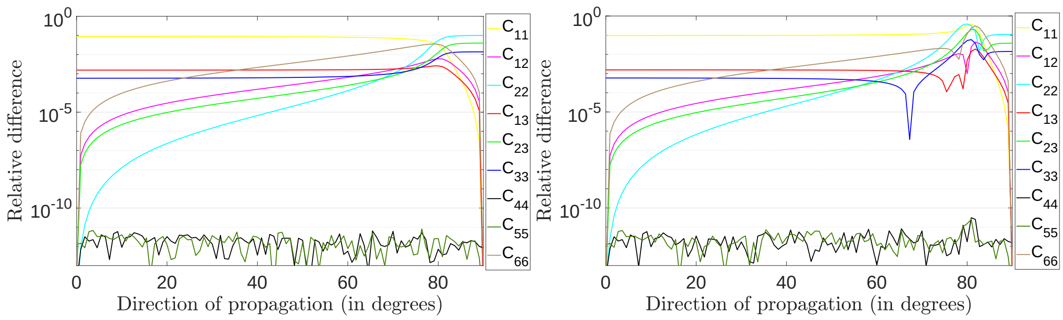

(a) (b)

Figure 5.7: Sensitivity of the S_0 mode to the different elastic moduli at a frequency of 50kHz (a) when $k(\omega)$ is considered (b) when $c_g(\omega)$ is considered.

of propagation is ϵ_{xx} and the main strain components involved in the A_0 mode in the x direction of propagation are ϵ_{xx} and ϵ_{xz} which are respectively strongly related to C_{11} and C_{55}. The homogenisation methodology is launched, with C_{11} and C_{55} being the two unique genes of the chromosome and the other moduli being arbitrarily fixed. Only two modes (S_0 and A_0) are compared in only one direction of propagation (0°), which makes every iteration much faster than in Sec.5.2.1. Tables 5.3 and 5.4 present the results for the $k(\omega)$ and $c_g(\omega)$ approaches respectively for five separate launches of the process each using different random values for the fixed C_{ij}. The algorithm converges in a low number of iterations and provides excellent solutions (less that 1% of relative error in every case).

	Theoretical	**#1**	**#2**	**#3**	**#4**	**#5**
C_{11} (GPa)	147.36	148.16	148.02	147.76	146.92	147.50
error (%)		0.54	0.45	0.28	0.30	0.10
C_{55} (GPa)	5.58	5.61	5.62	5.60	5.58	5.52
error (%)		0.46	0.67	0.33	0.02	0.99
Generations	-	8	9	5	2	10
Time	-	30min	34min	19min	7min	38min

Table 5.3: Results of the GA for five independent runs for the reconstruction of two elastic moduli (C_{11} and C_{55}) of the orthotropic material whose real moduli are displayed on the left-hand side, when $k(\omega)$ is considered.

It can be observed that both approaches (comparing $k(\omega)$ or $c_g(\omega)$ in the objective function) provides very accurate results in a low number of iterations. Even though it seems that the $c_g(\omega)$ approach requires more iterations to converge, the sample size (five runs in each case) is small and the number of iterations is too low to conclude whether the $k(\omega)$ or $c_g(\omega)$ approach is the most efficient.

	Theoretical	**#1**	**#2**	**#3**	**#4**	**#5**
C_{11} (GPa)	147.36	147.41	147.67	146.73	147.87	147.19
error (%)		0.03	0.21	0.43	0.34	0.11
C_{55} (GPa)	5.58	5.58	5.55	5.62	5.59	5.59
error (%)		0.07	0.48	0.68	0.24	0.23
Generations	-	13	11	10	12	24
Time	-	46min	39min	38min	42min	84min

Table 5.4: Results of the GA for five independent runs for the reconstruction of two elastic moduli (C_{11} and C_{55}) of the orthotropic material whose real moduli are displayed on the left-hand side, when $c_g(\omega)$ is considered.

Figures 5.5 and 5.7 also show that C_{22}, C_{23}, C_{33} and C_{44} have a significant impact on the A_0 and S_0 modes dispersion curves in the y direction of propagation (90°). The homogenisation algorithm described in Sec.5.1 is once again launched in five separate runs. Only two modes (S_0 and A_0) are compared in a sole direction of propagation (90°) and the results are displayed in Tables 5.5 and 5.6 for both the $k(\omega)$ and the $c_g(\omega)$ approaches. It can be seen that the algorithm needs more iterations to converge than in the previous case where only two elastic constant were reconstructed. Excellent solutions are provided for the coefficients once again, in particular for C_{22} whose approximated values all contain less than 1% of error in comparison to the theoretical constants. One again, both the wavenumber and the group velocity approaches have an equivalent accuracy and number of iterations and one can not conclude on which is more suitable.

	Theoretical	**#1**	**#2**	**#3**	**#4**	**#5**
C_{22} (GPa)	9.51	9.51	9.45	9.48	9.47	9.42
error (%)		0.10	0.69	0.34	0.42	0.93
C_{23} (GPa)	4.02	4.15	3.96	3.97	3.92	3.90
error (%)		3.23	1.62	1.18	2.48	2.98
C_{33} (GPa)	11.66	11.92	11.69	11.56	11.52	11.51
error (%)		2.26	0.24	0.81	1.16	1.27
C_{44} (GPa)	3.19	3.23	3.20	3.20	3.24	3.25
error (%)		1.11	0.27	0.23	1.46	1.90
Generations	-	21	30	39	64	27
Time	-	80min	115min	149min	245min	103min

Table 5.5: Results of the GA for five independent runs for the reconstruction of four elastic moduli (C_{22}, C_{23}, C_{33} and C_{44}) of the orthotropic material whose real moduli are displayed on the left-hand side, when $k(\omega)$ is considered.

Figure 5.6 shows that only C_{66} has a significant impact on the SH_0 mode

	Theoretical	**#1**	**#2**	**#3**	**#4**	**#5**
C_{22} (GPa) error (%)	9.51	9.59 0.88	9.49 0.19	9.40 1.16	9.41 1.02	9.47 0.37
C_{23} (GPa) error (%)	4.02	4.03 0.33	3.93 2.31	3.92 2.50	3.81 5.10	3.99 0.87
C_{33} (GPa) error (%)	11.66	11.54 1.00	11.46 1.69	11.51 1.26	11.23 3.67	11.57 0.80
C_{44} (GPa) error (%)	3.19	3.19 0.01	3.29 2.99	3.25 1.93	3.25 1.93	3.21 0.51
Generations	-	25	34	3	68	8
Time	-	96min	130min	11min	260min	31min

Table 5.6: Results of the GA for five independent runs for the reconstruction of four elastic moduli (C_{22}, C_{23}, C_{33} and C_{44}) of the orthotropic material whose real moduli are displayed on the left-hand side, when $c_g(\omega)$ is considered.

dispersion curves in both the x and y directions. Again, this was expected as the main strain component involved in the SH_0 mode in both the x and y directions of propagation is ϵ_{xy} which is related to C_{66} according to Hooke's law. Thus the GA compares only the SH_0 mode in two directions of propagation (x and y, respectively at 0° and 90°) and the results are displayed in Tables 5.7 and 5.8. The convergence is attained after a low number of iterations with a good precision on the results (less than 1%). Figures 5.5-5.7 show that, in this case study, C_{12} and C_{13} variations have negligible effects on the dispersion of any modes in any direction of propagation and thus are not considered.

	Theoretical	**#1**	**#2**	**#3**	**#4**	**#5**
C_{66} (GPa) error (%)	4.16	4.12 0.91	4.12 0.96	4.12 0.91	4.11 1.10	4.12 0.91
Generations	-	5	1	4	3	4
Time	-	9min	2min	7min	5min	7min

Table 5.7: Results of the GA for five independent runs for the reconstruction of one elastic moduli (C_{66}) of the orthotropic material whose real moduli is displayed on the left-hand side, when $k(\omega)$ is considered.

Using the sensitivity of each mode to the different elastic moduli allows for dividing the problem and thus considerably reduces the computation time. It also provides very accurate approximations in comparison to the method employed in Sec.5.2.1. One must however be aware that the sensitivity study in that case is straightforward to execute as the parameters to be found are known. Both in Sec.5.2.1 and in the current section, no advantages of using the group velocity

	Theoretical	#1	#2	#3	#4	#5
C_{66} (GPa)	4.16	4.13	4.13	4.14	4.13	4.13
error (%)		0.62	0.76	0.49	0.79	0.83
Generations	-	1	3	1	2	1
Time	-	2min	6min	2min	4min	2min

Table 5.8: Results of the GA for five independent runs for the reconstruction of one elastic moduli (C_{66}) of the orthotropic material whose real moduli is displayed on the left-hand side, when $c_g(\omega)$ is considered.

data over of the wavenumber data were raised. Thus the wavenumber data, being direct outputs from the WFE method, are the one used for the next case studies in this chapter.

5.3 Case study: 2D plain woven composite

Textile composite's dispersion characteristics show complex behaviour (such as stop-bands) that cannot be described by a macroscale substitution model. However, for low to middle frequency ranges, before any cut-off frequencies or stop-bands, the dispersion relations seem rather approachable. In this section, a 2D plain woven composite, whose unit cell is displayed in Fig.3.15, is approximated using different macroscale substitution models.

Its dispersion characteristics are computed using the mesoscale model as detailed in Sec.3.3. In Fig.5.8, on the left-hand side are displayed the slowness surfaces at a fixed frequency for the three first propagating modes, on the right-hand side the same slowness surfaces for a random orthotropic material. It is observed that the shape of these slowness curves are comparable and thus a first hypothesis is made: an orthotropic macroscale model is an adequate substitution for the 2D plain woven composite mesoscale model.

5.3.1 Approximation with one orthotropic layer

In this first subsection, the textile composite is approximated by a single layer material whose properties are orthotropic. A first attempt is made using its static macroscale substitution model as described in Sec.3.3.4. The resulting stiffness matrix describes a transverse isotropic material and is given in Eq.(5.2) (in GPa).

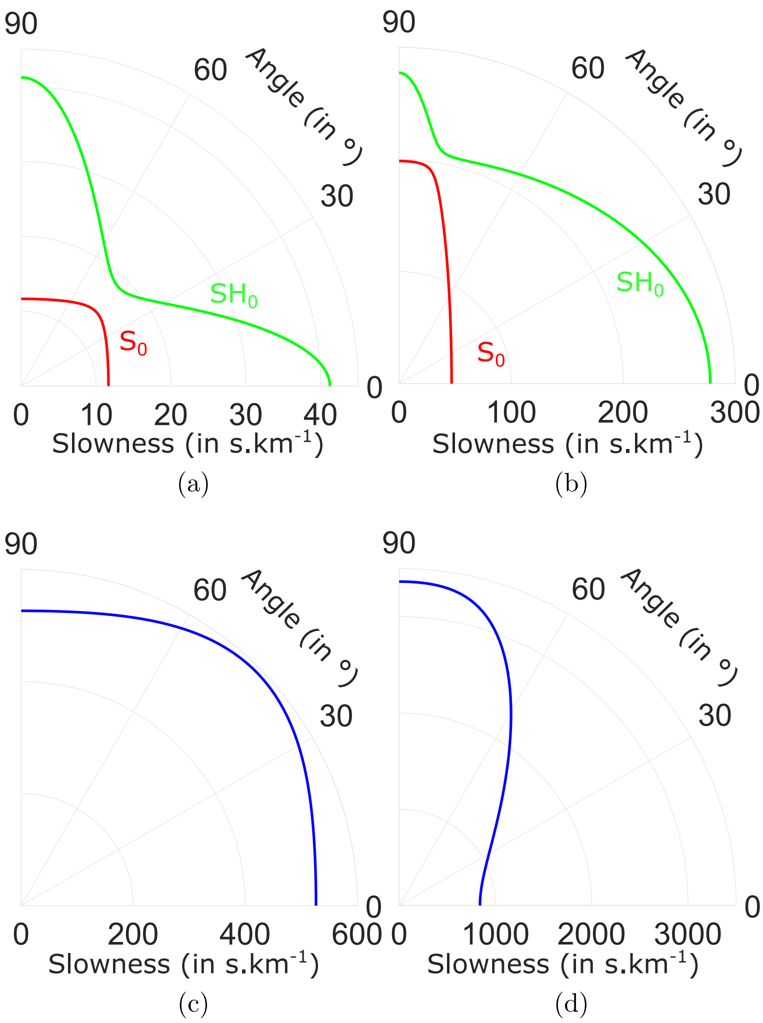

Figure 5.8: Slowness surfaces at a frequency of 8 kHz for the first three modes for the direction of propagation range of [0,90] for the 2D plain woven composite on the left-hand side and for an orthotropic material on the right-hand side (in $s.km^{-1}$). (a) S_0 and SH_0 for the 2D plain woven composite (b) S_0 and SH_0 for an orthotropic material (c) A_0 for the 2D plain woven composite (d) A_0 for an orthotropic material.

$$[C] = \begin{bmatrix} 49.33 & 13.24 & 4.36 & 0 & 0 & 0 \\ 13.24 & 49.33 & 4.36 & 0 & 0 & 0 \\ 4.36 & 4.36 & 1.52 & 0 & 0 & 0 \\ 0 & 0 & 0 & 3.69 & 0 & 0 \\ 0 & 0 & 0 & 0 & 3.69 & 0 \\ 0 & 0 & 0 & 0 & 0 & 5.41 \end{bmatrix}. \tag{5.2}$$

Using the SAFE method, the dispersion curves for a plate structure made of this material (described in Eq.(5.2)) are computed, and plotted for the x direction of propagation in Fig.5.9 along with the dispersion curves of the reference composite described at a mesoscopic scale. It can be seen that even though the dispersion curve in the x direction of propagation for the S_0 mode is accurately predicted using the static macroscale model, it is inaccurate for the A_0 and SH_0 modes.

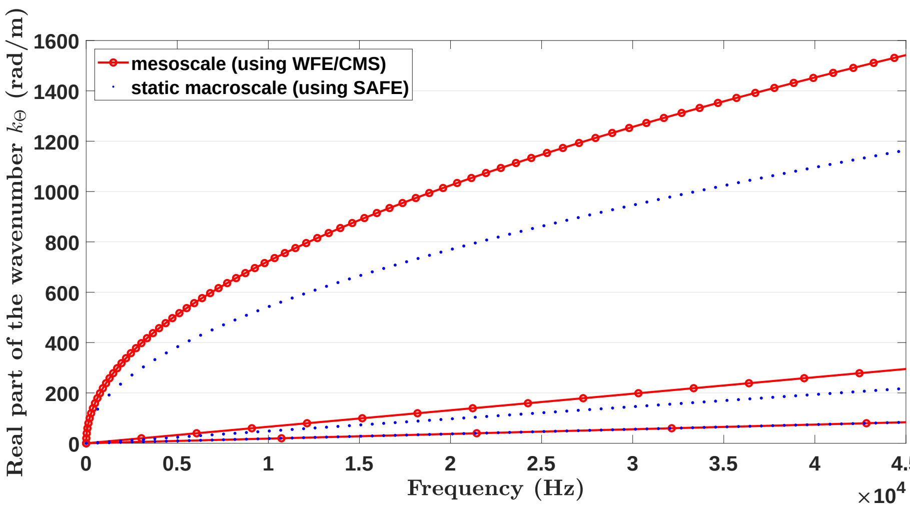

Figure 5.9: Dispersion curves ($k(\omega)$) of the first three modes of the reference mesoscopic model and of its approximated static macroscale model for a 2D plain woven composite, in the x direction of propagation. A strong mismatch between the curves from both models is observed, except for the S_0 mode. The static macroscale model does not predict the dispersion curves accurately.

Making the assumption that the elastic parameters of this textile composite can indeed be approximated by a single layer orthotropic material, the GA approach, thoroughly described in Sec.5.1, is applied to solve this problem in a second homogenisation attempt. The thickness of the plate and the density of the material are fixed (0.22 mm and 3212 kg/m^3) because known and the nine elastic moduli describing an orthotropic material are sought. The brute-force method is firstly employed to obtain the homogenised orthotropic set of elastic moduli displaying the same dispersion characteristics than the 2D plain woven composite. The GA compares the first three modes (S_0, SH_0 and A_0) in three directions of propagation (0°, 45° and 90°).

Figure 5.10 shows the objective function value for each iteration for five independent runs. After 300 iterations, the objective function does not show any sign of a convergence to come as it stays around 20% of error. It seems that no convergence is possible. A possible explanation is that since the material has fibres in two different principal directions ([0/90] as seen in Fig.3.15), it cannot be approximated by a material composed of a single orthotropic layer. Of course it is possible to find a set of orthotropic moduli that would fit the solution for one direction of propagation. However, the solution that is sought here should fit all investigated directions at once.

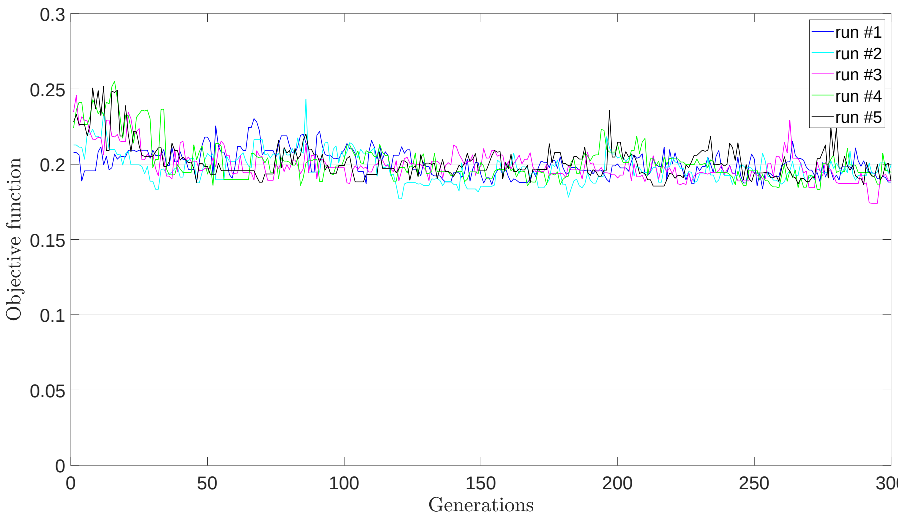

Figure 5.10: Value of the objective function as a function of the generation for the five GA independent runs for the reconstruction of the elastic moduli of the 2D plain woven composite. Convergence is not observed after 300 generations.

5.3.2 Approximation with two identical orthotropic layers

In this second subsection, the textile composite is approximated by a two orthotropic layers laminate whose sequence is [0/90] to emulate the fibres oriented in these directions in the 2D plain woven composite material, as shown in Fig.5.11.

A first attempt to solve this problem is again performed by static virtual testing. This can however not be carried out in a straightforward manner due to the interweaving yarns, thus an intermediate step has to be observed: the yarns are straightened out so that the composite can be divided in the out-of-plane direction in two independent layers whose material constants are obtained using the static macroscale per layer homogenisation method described in Sec.3.3.4

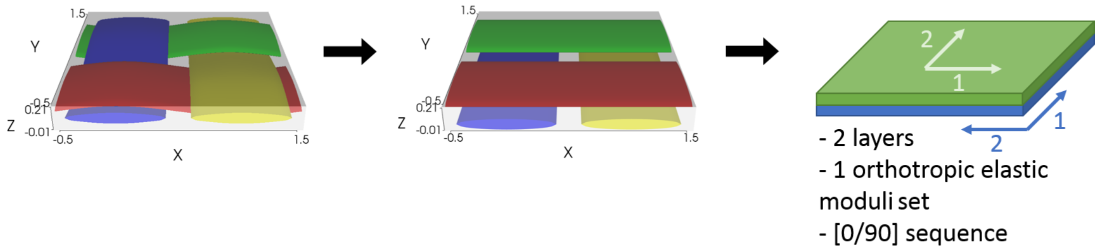

Figure 5.11: 2D plain woven composite model breakdown for approximation by a static macroscale per layer model.

From Fig.5.12, it can be observed that using these static macroscale per layer properties, the dispersion curves in the x direction of propagation are not in agreement, for any of the three modes. Thus the GA homogenisation methodology is performed in order to obtain the elastic moduli that correspond to these dispersion curves using a two orthotropic layers laminate as surrogate model. The approach is firstly tested on a model whose layers are effectively orthotropic and the converged results displayed in Table 5.9 for only one run. C_{11} and C_{66} are reconstructed with great accuracy, while the others are very far from the reference moduli. It seems that using this method does not allow for reconstructing the parameters whose sensitivity to change is not as great as C_{11} and C_{66}.

Figure 3.15 and Eq.(5.2) show that the material presents a symmetry along the 45° axis and thus holds the same dispersion characteristics on each side of that symmetry axis. The assumption that both orthotropic layers have the same elastic properties is made and both thicknesses are set to 0.11 mm for a total of 0.22 mm, only their local material orientations are different. The brute-force method is applied, comparing the first three modes in four directions of propagation (0°, 18°, 30° and 45°).

For the initialisation step of the GA, the chromosomes are set to random values in order not to bias the results. The results are displayed in Table 5.10 and it

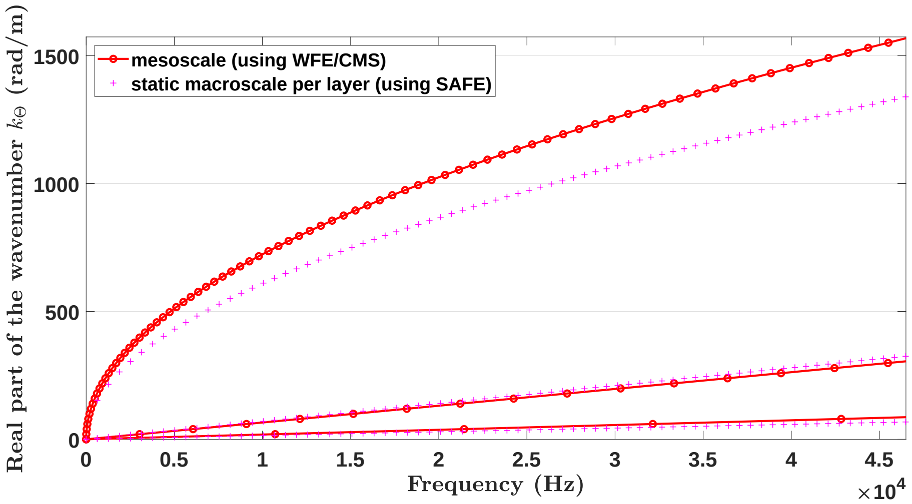

Figure 5.12: Dispersion curves ($k(\omega)$) of the first three modes of the reference mesoscopic model and of its approximated static macroscale per layer model for a 2D plain woven composite.

	Theoretical	**Reconstructed by GA**	**Relative error**
C_{11} (GPa)	114.92	115.67	0.65%
C_{12} (GPa)	2.35	3.04	29.55%
C_{22} (GPa)	6.41	7.65	19.37%
C_{13} (GPa)	2.79	3.72	33.35%
C_{23} (GPa)	1.93	3.44	78.05%
C_{33} (GPa)	6.71	9.44	40.73%
C_{44} (GPa)	2.24	2.28	1.53%
C_{55} (GPa)	2.77	2.32	16.21%
C_{66} (GPa)	2.60	2.61	0.31%
Generations		62	

Table 5.9: Results of the GA for the reconstruction of the elastic moduli of a two layers (sequence [0/90]) composite material whose properties are orthotropic and real moduli are displayed on the left-hand side, when $k(\omega)$ is considered.

can be seen that relatively good estimations of C_{11} and C_{66} are found as their standard deviation is rather small ($< 5\%$). The standard deviation for the other parameters however is high ($> 25\%$), and while the sample size is too small (N=5) to conclude on whether the means and standard deviations represent meaningful statistical values, it shows that no convergence is observed. The dispersion curves for the parameters found and presented in Table 5.10 are shown in Fig.5.13. It can be seen that the reconstructed solutions seem in good agreement with the mesoscopic model and that they provide a much better approximation than the ones obtained by static virtual testing following the method described in Fig.5.11. However, the objective function converges at a relatively high value of around

1.7% for each of the runs. This likely indicates that no exact solution can be found.

	#1	**#2**	**#3**	**#4**	**#5**	Mean	SD
C_{11} (GPa)	73.19	79.30	73.45	70.69	72.11	73.75	2.9 (4.0%)
C_{12} (GPa)	10.09	16.87	8.96	9.59	17.37	12.58	3.7 (29.7%)
C_{22} (GPa)	3.89	11.65	4.46	9.71	51.53	16.25	17.9 (110.1%)
C_{13} (GPa)	6.01	8.19	2.82	3.01	1.43	4.29	2.46 (57.2%)
C_{23} (GPa)	5.50	8.86	8.11	12.62	7.86	8.59	2.31 (26.9%)
C_{33} (GPa)	12.50	7.99	19.83	19.73	1.24	12.26	7.11 (58.0%)
C_{44} (GPa)	1.22	12.57	4.04	1.20	2.29	4.26	4.28 (100.4%)
C_{55} (GPa)	4.72	1.96	7.01	3.32	2.01	3.80	1.90 (49.8%)
C_{66} (GPa)	2.92	2.98	2.94	2.97	2.92	2.95	0.03 (0.85%)
Obj.fun (%)	1.72	1.95	1.82	1.67	1.62		
Generations	115	62	70	84	49		
Time (h)	64	34	38	45	27		

Table 5.10: Results of the GA for five independent runs for the reconstruction of the elastic moduli of the 2D plain woven composite material when $k(\omega)$ is considered. The mean and standard deviation are computed for each parameters and displayed on the right-hand side. The value of objective function at convergence for each run is displayed in the 'Obj.fun' row. 'SD' stands for standard deviation.

5.3.3 Applications

When considering a laminated composite, if the elastic moduli are known for the different layers, then the dispersion characteristics can be computed for the assembly in a fast and straightforward way using SAFE or WFE methods. Since the approximated elastic moduli obtained in Sec.5.3.2 provide similar dispersion characteristics to the reference material, they are used in the next subsections to predict the results for different configurations and arrangements of this material. Firstly, they are used to compute the dispersion characteristics in a plate that is an assembly of multiple layers of this material and in the secondly in a beam configuration.

Plate configuration

In this section, the 'reconstructed' material constants displayed in Table 5.10 are used to compute the dispersion characteristics for three different plate configurations (infinite length in the x and y directions, finite thickness in the z

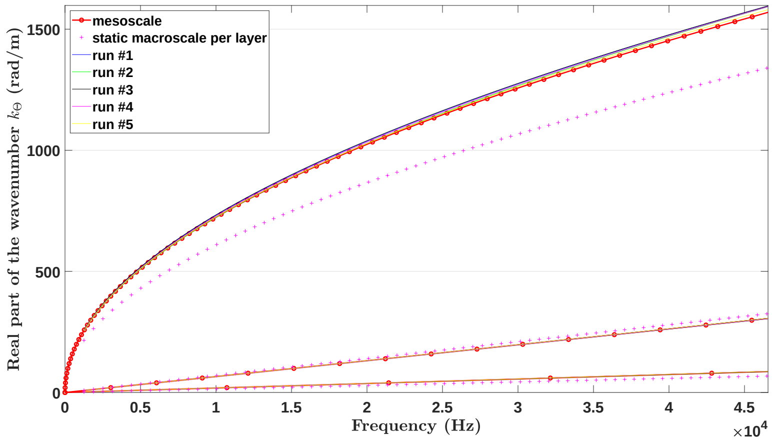

(a) x direction of propagation

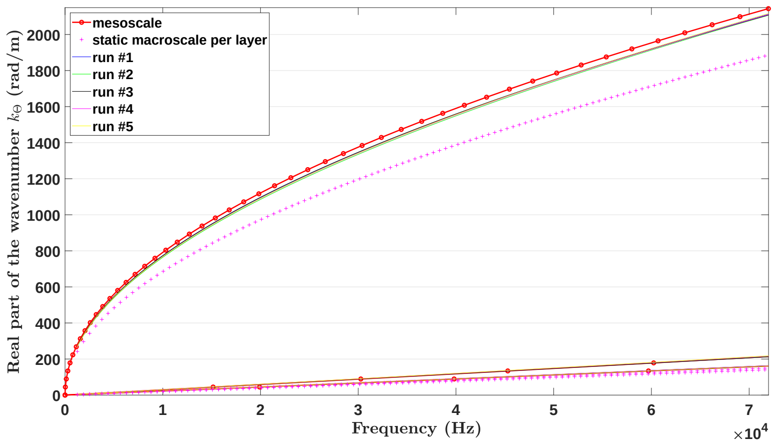

(b) 45° direction of propagation

Figure 5.13: Dispersion curves ($k(\omega)$) of the first three modes of the reference mesoscopic model, its approximated static macroscale per layer model and using the results (displayed in Table 5.10) from all five runs for a 2D plain woven composite.

direction): an assembly of two layers of 2D plain woven composite material, an assembly of three layers of the same material and finally an assembly of five layers of this material as displayed in Fig.5.15.a. Figure 5.14 shows the dispersion curve for the first two configurations (two and three layers assemblies), and Fig.5.15.b for the five layers assembly configuration. It can be seen that the dispersion curves are considerably diverging from the ones obtained for the mesoscale model, and in particular the A_0 mode. The dispersion curves obtained using the static macroscale and macroscale per layer models are plotted in Fig.5.14-5.15 too. Table 5.11 displays the error of the computed A_0 curves for the different runs to the reference mesoscale dispersion curve. It is clear that the dispersion curves obtained for any of the substitution models can not predict the dispersion characteristics in any of the three configurations. One can assume that lower error (objective function was situated around 1.7% at the end of every run) should be obtained for accurate prediction of the dispersion curves or more features of the dispersion curves should be compared such as the higher-order modes. Observation of the predictions for the two, three and five layers assemblies using the set of moduli obtained with run number five (yellow curves) show relatively good agreement with the mesoscale predictions. This bolsters the idea that a solution could be found given attaining a lower error in the search algorithm.

	#1	**#2**	**#3**	**#4**	**#5**	macro	macro/layer
2 layers - A_0	5.0%	3.2%	5.3%	6.5%	1.6%	9.4%	8.6%
3 layers - A_0	5.7%	5.2%	8.8%	7.9%	1.7%	9.2%	7.3%
5 layers - A_0	6.9%	8.0%	13.7%	10.0%	2.6%	11.24%	5.8%

Table 5.11: A_0 mode wavenumber prediction relative error to the reference mesoscale model for the different stacking configurations.

Beam

In this subsection, the 'reconstructed' material constants displayed in Table 5.10 are used to generate the dispersion curves for a beam configuration (infinite length in the x direction, finite width and thickness respectively in the y and z directions). All dispersion curves are plotted in Fig.5.16, and it is observed that the predictions from the 'reconstructed' material constants are in a good agreement with the reference mesoscale dispersion curves. The relative errors are displayed in Table 5.12. The first flexural mode's dispersion curve has a relative error to the reference lower or equal to 4% for any of the five runs, which is far better than for the static macroscale models (macroscale and macroscale per layer both have an error larger than 15%). This is true for the second flexural mode, the shear mode and the pressure mode too. Once again, one can assume that accurate predictions could be obtained given a lower error in the objective function is attained (objective function was situated around 1.7% at the end of every run).

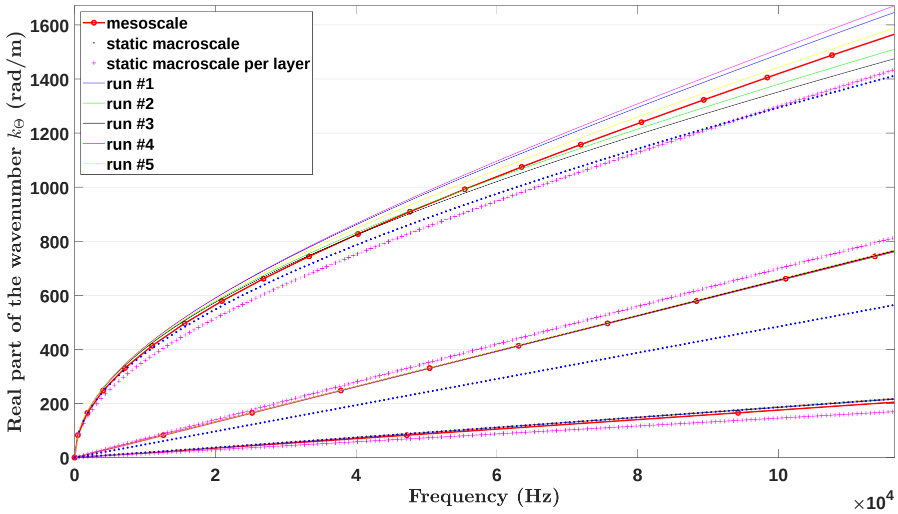

(a)

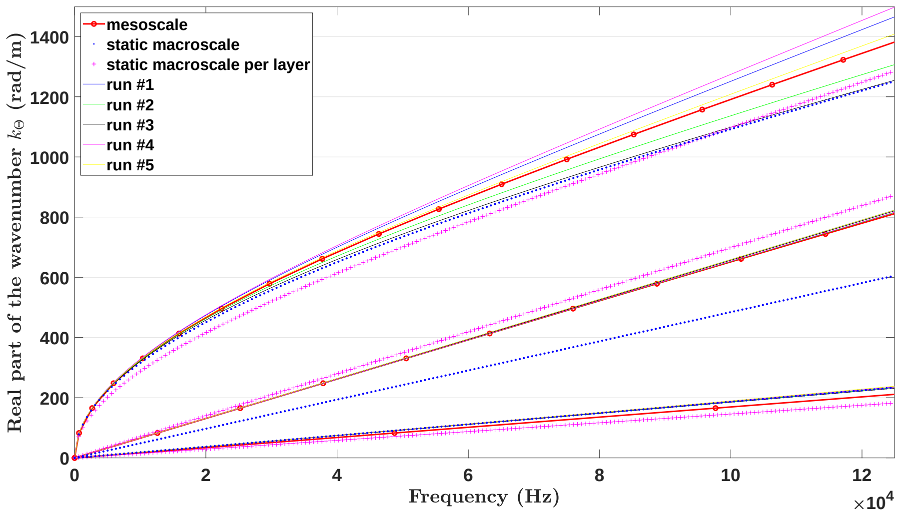

(b)

Figure 5.14: Dispersion curves ($k(\omega)$) in the x direction of propagation of the first three modes of the reference mesoscopic model, its approximated static macroscale model, its approximated static macroscale per layer model and using the results (displayed in Table 5.10) from all five runs for different stacking configurations of the 2D plain woven composite. (a) Two layers [0/0], (b) Three layers [0/0/0].

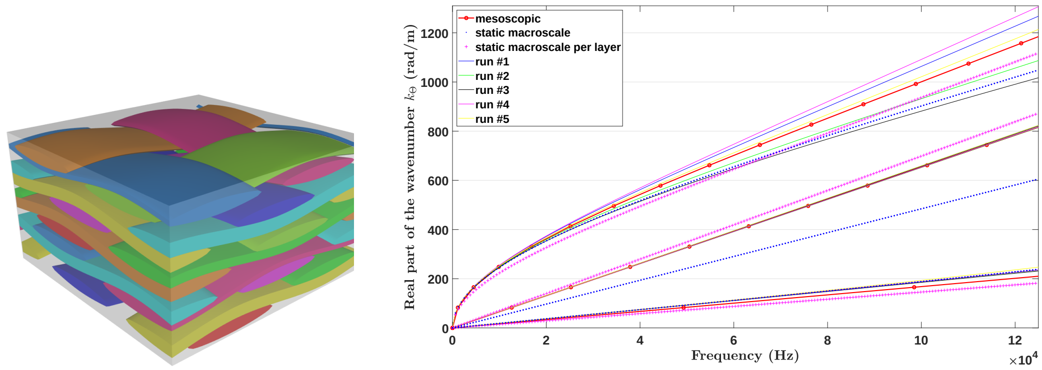

(a) (b)

Figure 5.15: (a) Unit cell of a five layers assembly of the 2D plain woven composite. (b) Dispersion curves ($k(\omega)$) in the x direction of propagation of the first three modes of the reference mesoscopic model, its approximated static macroscale model, its approximated static macroscale per layer model and using the results (displayed in Table 5.10) from all five runs for a five layers laminated plate configuration of the 2D plain woven composite.

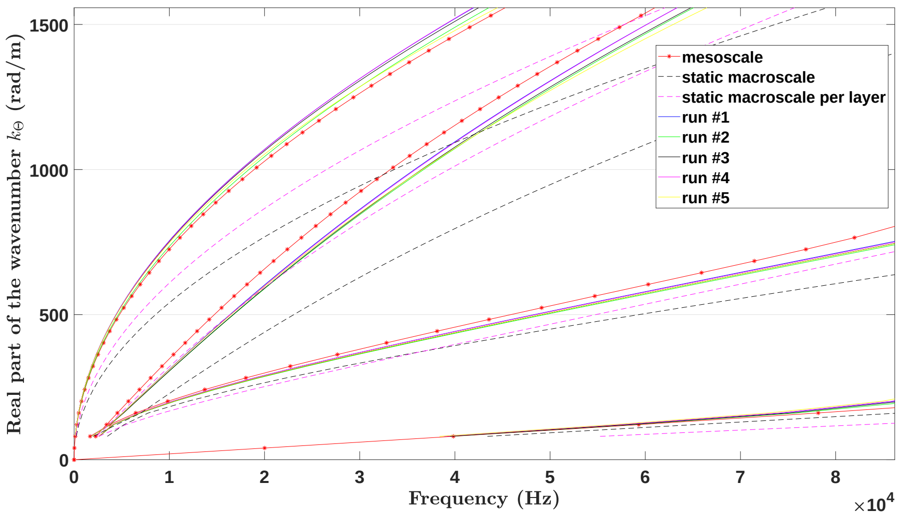

Figure 5.16: Dispersion curves ($k(\omega)$) of the first four modes of the reference mesoscopic model, its approximated static macroscale model, its approximated static macroscale per layer model and using the results (displayed in Table 5.10) from all five runs for a beam configuration of the 2D plain woven composite.

	#1	#2	#3	#4	#5	macro	macro/layer
Mode 1	3.9%	1.8%	3.3%	4.0%	1.3%	25.7%	15.4%
Mode 2	2.7%	4.7%	4.3%	2.8%	5.8%	28.2%	12.5%
Mode 3	4.3%	5.8%	5.2%	4.6%	5.3%	16.2%	9.9%
Mode 4	8.0%	4.3%	6.2%	8.6%	11.1%	10.0%	29.2%

Table 5.12: First four modes wavenumber prediction relative error to the reference mesoscale model for a beam configuration.

5.4 Case study: 2D twill woven composite

The same two orthotropic layers substitution model is used along the GA to obtain the elastic moduli for the 2D twill woven composite displayed in Fig.5.17. The thickness dimensions are the same as in Sec.5.3.2 and the density is of 3280 kg/m^3. The dispersion curves computed for the approximated elastic moduli found from five independent runs (whose results are displayed in Table 5.13) in the x direction of propagation are plotted in Fig.5.18 and it provides significantly better approximations than both static macroscale models. Table 5.13 shows once again that C_{11} and C_{66} seem to be predicted with a good accuracy as the standard deviation is low. However, the objective function attains 2.45% of error after a low number of iterations (around generation 50) for each of the runs as can be observed in Fig.5.19 but stays around this value even after a large number of iterations as can be seen in Table 5.13.

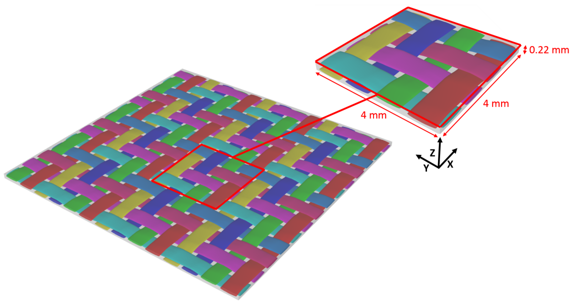

Figure 5.17: 2D twill woven composite and its corresponding unit cell.

The results from these five runs are used to compute the dispersion relations in a different configuration: a composite made of two layers of 2D twill weave. The dispersion curve for this composite in the x direction of propagation are displayed alongside the approximated ones in Fig.5.20. Similarly to the observations made in Sec.5.3.3, the dispersion characteristics predictions for this two 2D twill weave layers model are inaccurate especially for the A_0 mode. Once again, one could assume that accurate predictions could be obtained given a lower error in the objective function is attained (objective function was situated around 2.45% at the end of every run). However, despite the mechanisms avoiding the objective function to be trapped at a local minima (e.g. creep and mutation), it seems that it does get trapped anyway (see Fig.5.19). In Table 5.13, the value of the objective

	#1	#2	#3	#4	#5	Mean	SD
C_{11} (GPa)	77.55	79.67	79.06	79.20	78.62	78.82	0.72 (0.91%)
C_{12} (GPa)	14.58	15.48	15.27	16.56	15.60	15.50	0.64 (4.11%)
C_{22} (GPa)	5.35	5.94	5.45	9.18	6.91	6.57	1.42 (21.61%)
C_{13} (GPa)	1.75	7.79	3.62	2.73	5.21	4.22	2.12 (50.16%)
C_{23} (GPa)	2.04	3.75	1.46	8.08	5.79	4.22	2.45 (57.95%)
C_{33} (GPa)	16.50	19.82	10.08	14.39	16.51	15.46	3.20 (20.72%)
C_{44} (GPa)	1.37	1.14	2.05	1.29	1.01	1.37	0.36 (26.31%)
C_{55} (GPa)	2.49	1.87	1.55	15.27	3.09	4.85	5.23 (107.84%)
C_{66} (GPa)	3.03	2.90	3.11	3.13	2.92	3.02	0.09 (3.13%)
Obj.fun (%)	2.44	2.45	2.44	2.45	2.44		
Generations	414	343	460	533	494		
Time (h)	128	101	122	154	135		

Table 5.13: Results of the GA for five independent runs for the reconstruction of the elastic moduli of the 2D twill woven composite material when $k(\omega)$ is considered. The mean and standard deviation are computed for each parameters and displayed on the right-hand side. The value of objective function at convergence for each run is displayed in the 'Obj.fun' row. 'SD' stands for standard deviation.

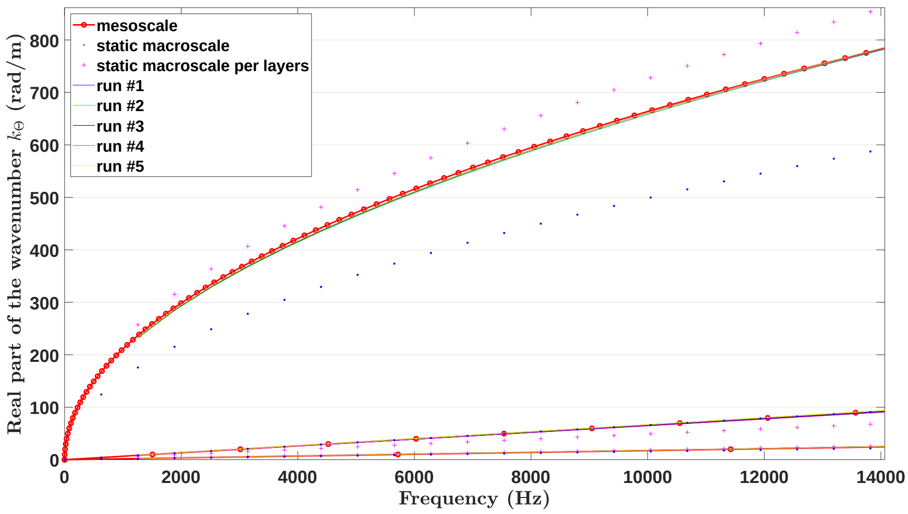

Figure 5.18: Dispersion curves ($k(\omega)$) of the first three modes of the reference mesoscopic model, its approximated static macroscale model, its approximated static macroscale per layer model and using the results (displayed in Table 5.13) from all five runs for a 2D twill woven composite plate.

function at which the algorithm is trapped for each run is almost the same (around 2.45%), while the moduli are quite different (high standard deviation). This could indicate that no exact solution can be found. The lack of solution could be a consequence of the strong assumption that the 2D twill woven composite can be substituted by a two orthotropic layers material.

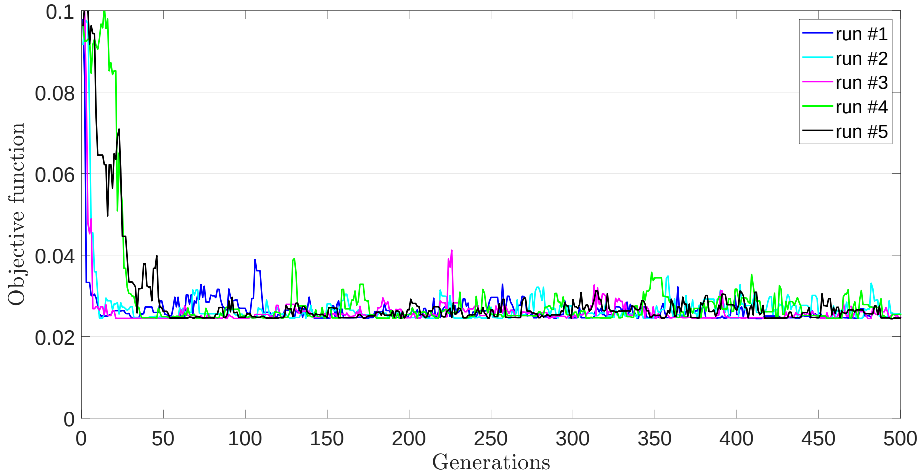

Figure 5.19: Value of the objective function as a function of the generation for the five GA independent runs for the reconstruction of the elastic moduli of the 2D twill woven composite. Convergence is not observed after 500 generations as the error is of more than 2.4% for any generation. This very likely indicates that no exact solution can be found.

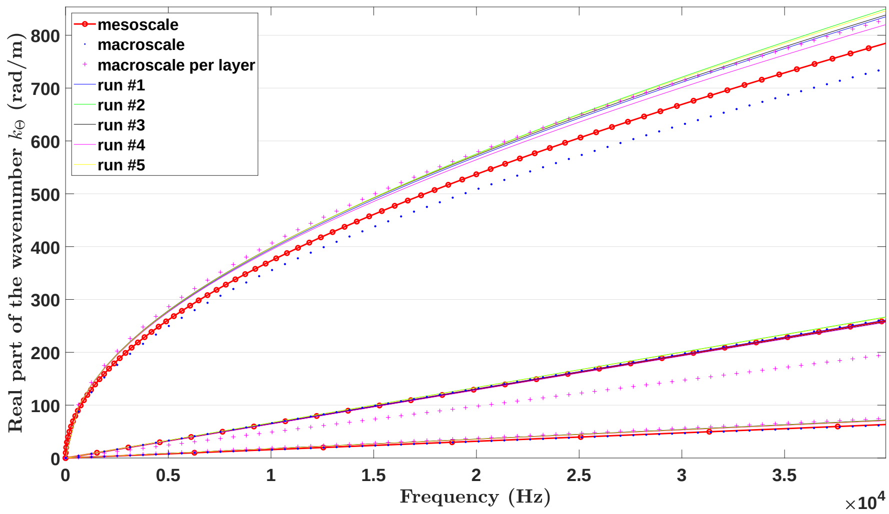

Figure 5.20: Dispersion curves ($k(\omega)$) of the first three modes of the reference mesoscopic model, its approximated static macroscale model, its approximated static macroscale per layer model and using the results (displayed in Table 5.13) from all five runs for a two layers laminated plate configuration of the 2D twill woven composite.

5.5 Case study: triaxial braided composite

It was shown in Sec.5.3 that in order to approximate the elastic moduli of a textile composite, the model of substitution might need to be multilayered. In that section, it was rather obvious that the material could be approached by a two identical layers laminate whose sequence is [0/90]. In this section, the material of consideration is a triaxial braided composite (shown in Fig.3.33) and the definition of the model of substitution is not obvious. While it seems rather safe to assume that the model can be approximated by a laminate composed of three layers, whose sequence is [-60/0/60] (which are the three yarns orientations), similarly to [191], and whose first and third layers (representing the braider yarns) have the same elastic moduli, it is difficult to assume more. Having a substitution model composed of two different materials means that twice as many elastic moduli are to be guessed using the GA, this means chromosomes composed of eighteen genes, which is very ambitious to solve. Another less realistic but more convenient hypothesis can be made: all three layers are composed of the same material, they however have different thicknesses in order to retain a realistic fibre count per orientation. Taking into account the braider yarns versus axial yarns ratio, one gets in this particular case a layer thickness repartition as follows [0.1472 , 0.1056, 0.1472] mm. The density is of 3266 kg/m^3.

Once again, five runs are launched. It can be seen in Fig.5.21 that after more than three hundred iterations, no convergence is acquired as the objective function does not even reach below 7% of error. This indicates that no exact solution can be found using these parameters.

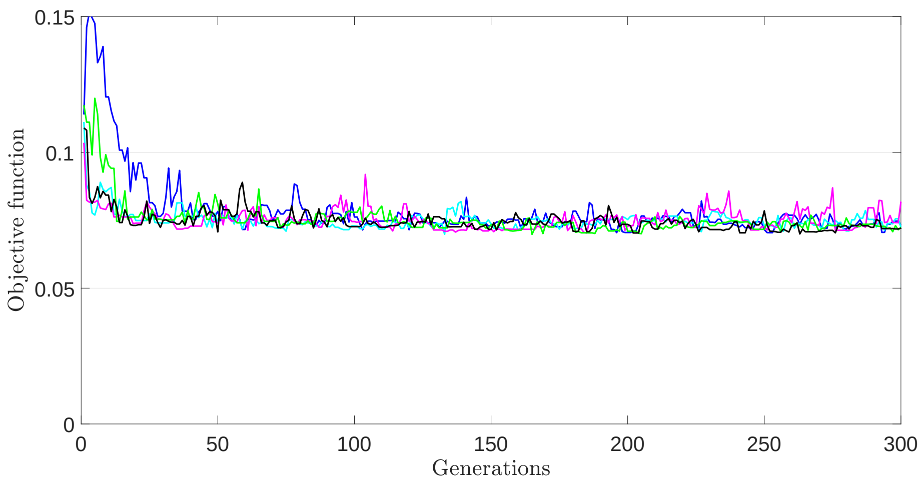

Figure 5.21: Value of the objective function as a function of the generation for the five GA independent runs for the reconstruction of the elastic moduli of the triaxial braided composite. Convergence is not observed after 300 generations as the error is of more than 7%.

Another GA simulation was launched, with ten genes instead of nine in the chromosome. The last gene being the thickness h of the intermediate layer so that the layer thickness breakdown is as follows [(0.4-h)/2 , h, (0.4-h)/2]. It did not converge as the error represented by the objective function remained higher than 7%.

5.6 Conclusions

In this chapter, a characterisation method for the homogenisation of textile composite models using multiscale modelling of their dispersion characteristics and a genetic algorithm is presented. It can be concluded that:

- Using the dispersion curves and genetic algorithm allows for reconstructing the elastic properties of orthotropic materials in a straightforward way.
- As observed in previous chapters, macroscale models using elastic moduli obtained by static virtual testing do not provide a good approximation for textile composites.
- Elastic moduli are not straightforward to obtain by inverting dispersion curves using a GA for 2D woven composites. The approximations they provide however are better than using static macroscale models.
- C_{11} and C_{66} in particular are two elastic moduli whose inversion is performed with a low error or standard deviation in this study.
- Some more complex textile composites, such as a triaxial braided composite, appear not to be approachable by simple multilayered macroscale models.
- While this homogenisation procedure is efficient to characterise an orthotropic material from its dispersion relations or at least to find a possible solution, the lack of convergence or the high converged relative error to the reference model when a textile composite is considered indicates that these complex materials cannot be approximated by simple macroscale models.

- When considering a textile composite, even if the elastic moduli of a close substitution macroscale model are found, this does not mean that this solution can be successfully used in laminated assembly or in different configurations of the same material for dispersion characteristics predictions.

Chapter 6

Effect of the mesoscale architecture of composites on structural damping

In the previous chapters, no damping was assumed in the models for simplicity. However, composite materials usually present high damping properties due to the viscoelastic characteristics of the matrix, thus damping is an important parameter to consider in the analysis of composite structures. Therefore, a damping model is proposed in this chapter. In the first section, damping is introduced in the mesoscale WFE/CMS methodology. It is followed by sections that present numerical examples and validations.

6.1 Damping modelling and loss factor calculation methods

A complex modulus damping model (see Eq.(2.23) in the literature) is introduced in the equation of motion of the problem (Eq.(2.29)). The imaginary part $\mathbf{K}''$ of the global stiffness matrix $\mathbf{K}$ in the case of a textile composite composed of two component materials (yarn and matrix) is written as follows

$$\mathbf{K}'' = \eta_{yarn}\mathbf{K}'_{yarn} + \eta_{mat}\mathbf{K}'_{mat}, \tag{6.1}$$

with η_{yarn} and η_{mat} respectively the yarn and matrix loss factor. $\mathbf{K'}_{yarn}$ and $\mathbf{K'}_{mat}$ being respectively the stiffness matrix of the yarn and matrix elements. It should be noted that in this method, the loss factor data for the constituent elements must be pre-determined.

Once the damping has been modelled, the mesoscale WFE/CMS methodology can be applied to the problem. Several formulations of the WFE scheme, all leading to a different eigenvalue problem (see Sec.2.3), can be employed. In this chapter, the adopted formulation is the same as the one employed throughout the thesis, meaning it involves specified real wavenumber as shown in Sec.3.3 and the frequency set of the propagating waves is calculated from the standard linear eigenvalue problem. The equation of motion is thus solved for complex angular frequencies $\omega = \omega_{re} + \mathrm{i}\omega_{im}$ (*re* subscript stands for real and *im* for imaginary). As depicted in [113], the ratio between the imaginary (representing the dissipated energy) and real coefficients (representing the stored energy) gives the loss factor of the material. The loss factor associated with a propagating wave is calculated as proposed in [137, 192]. The squared angular frequency is given

$$\omega^2 = (\omega_{re} + \mathrm{i}\omega_{im})^2 = 2\mathrm{i}\omega_{re}\omega_{im} + \omega_{re}^2 - \omega_{im}^2, \tag{6.2}$$

The loss factor η is the ratio between the imaginary and real coefficients, which gives:

$$\eta(\omega, \theta) = 2\frac{\omega_{re}\omega_{im}}{(\omega_{re}^2 - \omega_{im}^2)}. \tag{6.3}$$

The loss factor is dependent on both the considered direction of propagation θ and the angular frequency ω.

In the following sections, four case studies using the method displayed here are presented. In the first section, a macroscale model of a laminate composite is studied, an eigenproblem formulation comparison is provided as well as a numerical validation. The next three sections present three different textile composites modelled at a mesoscopic scale and a numerical validation is proposed for the last model.

6.2 Case study: macroscale modelling of a composite laminate for damping prediction and numerical validation

6.2.1 Comparison of two eigenvalue problem formulations

The methodology presented in this chapter is compared to the one presented in [137] for a simple case of a composite laminate made of two layers of the same lamina stacked in the following sequence [0/90]. The lamina is considered at a macroscopic scale, its orthotropic elastic properties are given in Table D.1 in Appendix. The model is a beam of 0.5 mm thickness and 1 mm width, it has ten elements in the thickness, twenty in the width and one element only is needed in the length to describe a section of the beam.

The adopted formulation for solving the eigenvalue problem shown in Eq.(2.29) involves known and real wavenumber and the associated complex angular frequency vector is sought ($\omega(k)$), this is the standard linear eigenvalue problem used in Sec.3.3 for textile composites. The damping characteristics are computed using Eq.(6.3). Another available formulation is a polynomial eigenvalue problem and it involves real prescribed frequency ($k(\omega)$). The associated complex wavenumber vector is sought as presented in [98, 137]. A disadvantage of this second approach compared to the first is that the considered unit cell whose dispersion characteristics are sought cannot display a complex internal structure similarly to a textile composite. It can however deal with laminate composites described at a macroscopic scale and thus is used here for comparison.

This numerical example compares the loss factor computation methodology that uses the $\omega(k)$ formulation with the $k(\omega)$ formulation presented in [137]. Using the second formulation methodology, $\eta(\omega, \theta)$ is computed as follows:

$$\eta(\omega, \theta) = \frac{\mathbf{V_j^*}\mathbf{K}''(\omega)\mathbf{V_j}}{\mathbf{V_j^*}\mathbf{K}'(\omega)\mathbf{V_j}} \tag{6.4}$$

where * denotes the conjugate transpose and $\mathbf{V_j}$ is the modeshape.

This particular comparison is not made to show the advantages of the mesoscale methodology over the macroscale one but rather to verify that both methodologies provide identical results for a same model. In Fig.6.1 are displayed the dispersion characteristics and the loss factor for both methodologies. The results are in excellent agreement.

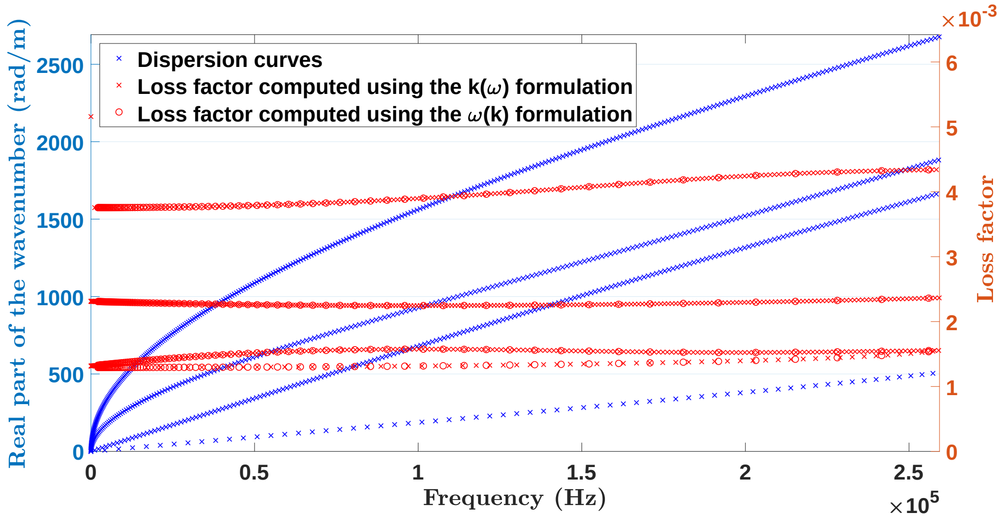

Figure 6.1: Comparison of the loss factor computed for the four first modes using the $k(\omega)$ and $\omega(k)$ formulations. An excellent agreement is observed.

6.2.2 Numerical validation using guided waves in a laminated composite beam through transient FE analysis

In order to validate the method used in this chapter, the dispersion relations and the loss factor of a longitudinal wave are investigated in a beam structure made of a composite laminate material by transient FEA.

Transient FEA

A beam made of a two layers laminated composite is modelled. Its width is of 1 mm, while its thickness is of 0.5 mm and its length, which should be long enough to avoid wave reflection on the far end side, is of 200 mm.

Longitudinal waves are chosen for the study as they are straightforward to induce to a beam model. A force envelope is applied on one end side of the beam (on every nodes of that surface) in the direction of the beam length. The magnitude of the load is variable over time so that the signal can carry a narrow band frequency, and has a short time pulse. To avoid the coupling of various modes, displacement in directions of the beam width and thickness are set as null independently of time ($U_2 = U_3 = 0$). This is also allowing for shorter computation time.

The signal is composed of a signal carrying the frequency of interest, mixed with a Hanning window function to ensure a narrow frequency band (see Fig.6.2) and no leaking. The carrier signal is sinusoidal and composed of eleven cycles. The displacement in the length direction is measured over time at a large set of positions along the length of the beam. Using these displacement amplitudes over time data, the damping can be observed (see Fig.6.3) and the loss factor calculated for each studied frequency.

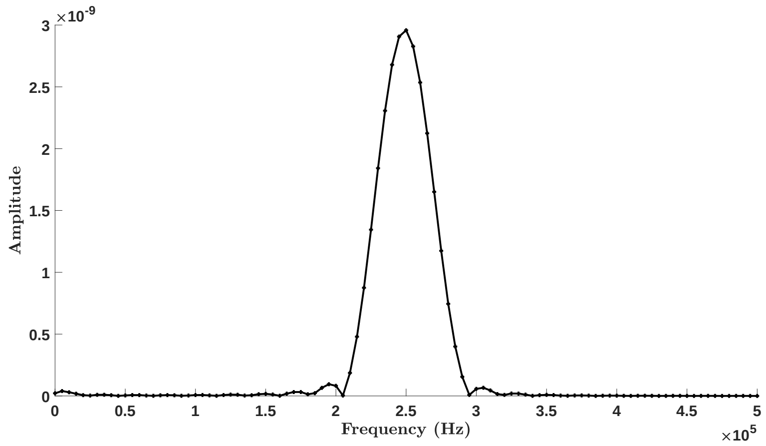

Figure 6.2: Discrete Fourier transform of the narrow frequency band input signal (carrying a frequency of 250 kHz).

As stated in [147], the attenuation of propagating waves in a thin structure is mainly caused by four factors. One factor is the geometric spreading of the wave, which describes the loss of amplitude due to the growth of the wave front length spreading in all directions from a localised source. However, unlike in a plate-like structure, guided waves in a beam-like structure propagate in a single direction (i.e. along the beam length), thus geometric spreading does not occur. Another factor is the wave dispersion, which does not occur either in our case as the carrier signal has a very narrow frequency band and is lower than the cut-off frequency. Another is the dissipation of the energy into an adjacent media, which does not occur here as there are no adjacent media. Lastly, the fourth

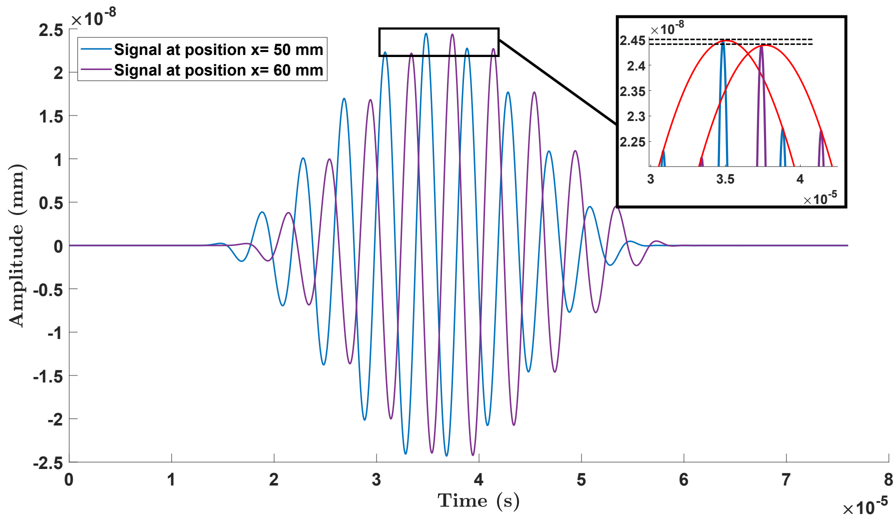

Figure 6.3: Wave propagating along the length of the damped laminated beam (x direction), the wavepacket carries a narrowband frequency of 250 kHz. The displacement in the length direction is measured for two points situated respectively at $x=$ 50 mm and 60 mm distance function of time. A zoom of the maximum amplitude of the envelop of the two wavepackets shows damping.

factor of attenuation is the material damping which is introduced here using the pre-determined materials loss factors. This last factor should be the only source of damping in this model.

For an accurate comparison, the model mesh size should be the same for the two compared methods (transient FEA and WFE/CMS). In this FE model, the viscous damping is modelled using Rayleigh's proportional damping as proposed in [146, 147], but neglecting the mass damping in order to obtain the same damping model than used within the WFE/CMS approach (see Sec.D.1 in Appendix), thus

$$\xi = \frac{\beta\omega}{2}. \tag{6.5}$$

β coefficient is calculated as follows

$$\beta = \frac{2\xi}{\omega} = \frac{\eta}{\omega}. \tag{6.6}$$

For each frequency point for which the attenuation is sought, β has to be recalculated and it differs as well for each material component of the structure (since they have different loss factors η).

Once the damping has been introduced in the FE model, the transient FEA can be performed for the different frequency points. The loss factor is computed by studying the attenuated amplitude of a traveling wave at different positions along the considered structure. The method for computing the damping ξ from the transient FEA is presented here. The amplitude A_p at a selected point p on the beam can be expressed as

$$A_p = A\mathrm{e}^{\mathrm{i}(\omega t - kx_p)}, \tag{6.7}$$

with x_p the position of the point p along the length of the beam. The ratio of amplitude of two points placed at different positions is thus written

$$\frac{A_2}{A_1} = \mathrm{e}^{\mathrm{i}(kx_1 - kx_2)}, \tag{6.8}$$

it follows

$$\ln\left(\frac{A_2}{A_1}\right) = -\mathrm{i}k\delta_x, \tag{6.9}$$

with δ_x the distance between the two considered points.

Assuming $k = k_{re} + \mathrm{i}k_{im}$ and that the dissipation is only due to the imaginary part

$$k_{im} = \frac{\ln\left(\frac{A_2}{A_1}\right)}{\delta_x}. \tag{6.10}$$

ξ is calculated as proposed in [193]

$$\xi = \left|\frac{k_{im}}{k_{re}}\right|. \tag{6.11}$$

Combining Eq.(6.10) and Eq.(6.11), ξ is given by

$$\xi = \left|\frac{\ln\left(\frac{A_2}{A_1}\right)}{k_{re}\delta_x}\right|. \tag{6.12}$$

The maximum amplitudes A_1 and A_2 are calculated using the envelope of the displacement amplitude over time at respectively the positions x_1 and x_2 of the beam.

Results

The loss factor is calculated by comparing the displacement amplitude over time at different positions along the beam (at least a thousand points). The transient analysis is firstly performed for a small set of five frequencies ranging from 300kHz to 500kHz with a unique loss factor for both layers of the laminate ($\eta = 0.003$). Using an identic loss factor for every constituents of the material should produce an equal and constant loss factor for the whole material, independently of the frequency. However, a difference is observed in the transient FEA (see Fig.D.1 in Appendix) as the resulting loss factor is equal to 0.003 at low frequency but ever slightly increasing as the frequency grows, which the model formulation should prevent. It is believed that this difference is induced by the FE software in use that does not allow to model structural damping in the conventional way but only allows to use the Rayleigh damping formulation in explicit analysis, and these results are used to adjust the determination of the β coefficient for later computations.

The simulation is performed once again, this time using different input loss factor for the different layers orientations (see Table D.1 in Appendix) and the adjusted β coefficient (see Table D.5 in Appendix). The mean and mean-squared error of the computed loss factor using Eq.(6.12) (for the thousand points) are plotted on Fig.6.4 along with the results from the presented methodology (the mean-squared error is shown with error bars).

A good agreement between the loss factor curve (plotted against frequency) computed with the damped WFE/CMS methodology and the one computed from the transient FEA is observed.

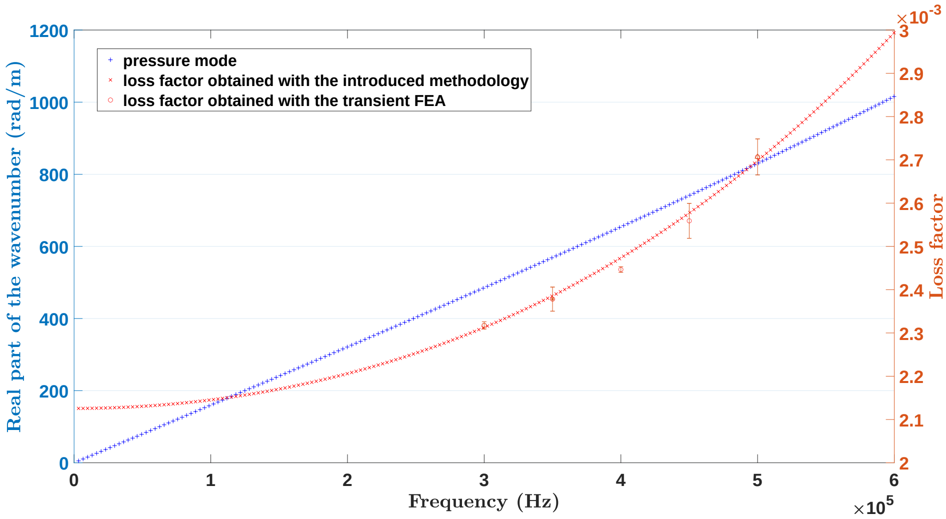

Figure 6.4: Loss factor in a two layers laminate beam, function of the frequency, propagating in the x direction, associated to the pressure mode. (+) the dispersion curve, ($\times$) the loss factor computed with the methodology introduced in this chapter, (o) the loss factor computed from the transient FEA.

6.3 Case study: mesoscale modelling of a 2D plain woven composite for damping prediction

As a first textile composite example, a unit cell of a 2D plain woven composite (Fig.3.15) is modelled at a mesoscopic scale and the loss factor is calculated as a function of the propagation angle and the frequency. The dimensions of the unit cell are $2 \times 2 \times 0.2$ mm. This FE model is composed of 6250 elements ($25 \times 25 \times 10$), 3336 elements are yarn elements while the 2914 remaining elements are matrix elements. This gives a fibre volume fraction of 0.5338. $\eta_{yarn} = 0.0001$ and $\eta_{mat} = 0.02$ are used as pre-determined loss factor for the yarns and matrix constituents respectively. The materials properties are given in Tables D.2 and D.3 in Appendix.

Thanks to the method presented in Sec.6.1, the loss factor associated to the first flexural mode can be calculated, as a function of the wave direction of propagation and the frequency, as shown in Fig.6.5. A mirror symmetry to the 45° direction of propagation plane can be observed for the loss factor values. This is in agreement with the geometry of the unit cell, itself presenting a symmetry to the 45° axis.

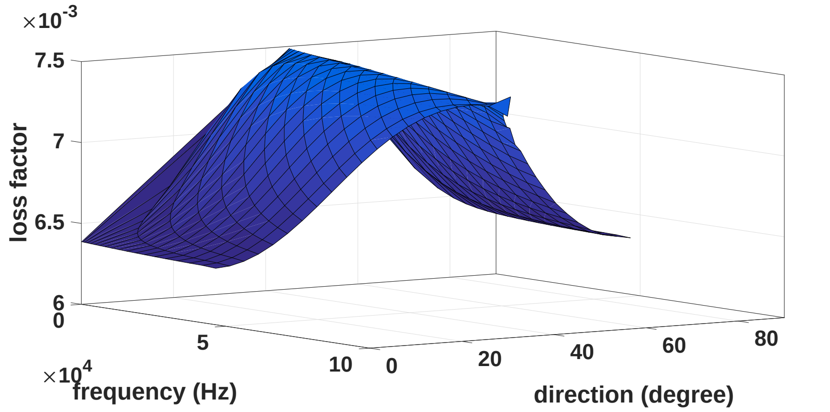

Figure 6.5: Loss factor in a 6250 elements model of a 2D plain woven fabric, function of the wave direction of propagation and the frequency, associated to the flexural mode of the composite plate.

In Fig.6.6, the loss factor, associated to the flexural mode, function of the frequency, propagating in the x direction is displayed for a larger frequency range. The dispersion curve for this mode is shown as well on the figure allowing for comparison. A Bragg type stop-band is present in the dispersion curve (for details on the difference between Bragg and local stop-bands, the reader is referred to Sec.2.2.2), and the loss factor seem to have an asymptotic behaviour next to it. For the loss-factor to reach extreme values for frequencies around a stop-band where the signal is fully attenuated seems logical. It can be observed that the loss factor is lower at higher frequencies (after the stop-band), this has previously been observed in [137] for laminates.

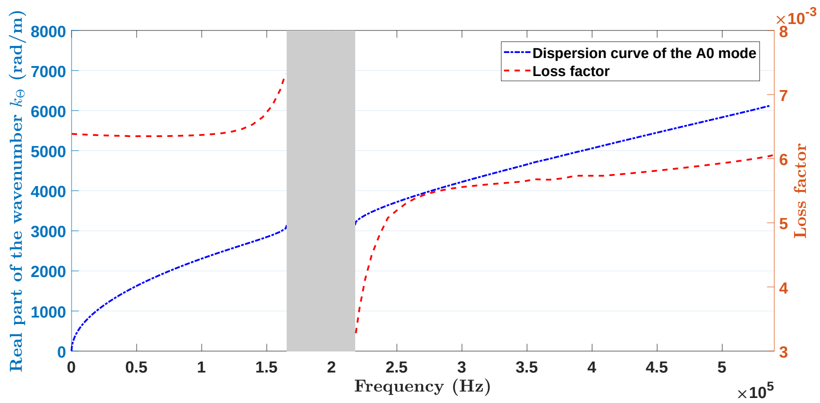

Figure 6.6: Loss factor in a 6250 elements model of a 2D plain woven fabric, function of the frequency, propagating in the x direction, associated to the flexural mode of the composite plate.

Three parametric studies are subsequently presented. The first compares the effect of the fibre volume fraction. The second shows the impact of different pre-determined component loss factors values and lastly the effect of the wave direction of propagation on the loss factor is demonstrated.

6.3.1 Effect of the fibre volume fraction

Two new models have been created based on the one described above. The difference between these models is the width of the yarns (and thus the number of fibres), which has an impact on the fibre volume fraction (see Fig.6.7), and therefore on the structural damping performance. The external dimensions of the unit cells are the same for these three models.

Textile geometry	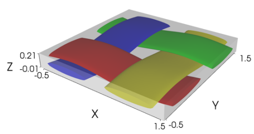	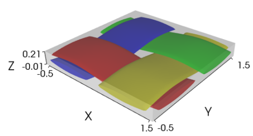	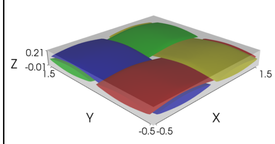
Fibre volume fraction	0.4813	0.5338	0.5709

Figure 6.7: Parametric study: change of the yarns width (the model in the middle of the figure is the reference model used in the previous part of the subsection).

The results of this study are displayed in Fig.6.8-6.10. As expected, the lower the fibre volume fraction is, the more effective the model is in dissipating energy, and this is true for the first flexural, shear and pressure modes. All three models, however, present similar loss factor curve shapes for the three first modes.

The loss factor curves of the three models present an asymptotic behaviour around the Bragg stop-band for the first flexural mode (see Fig.6.8). The loss factor has a lower value on the higher frequency part of the figure, after the stop-band. While the loss factor intensity of the curves is shifted as a function of fibre volume fraction, the stop-band occurs at the same frequency range for all three models. Indeed, Bragg stop-bands are due to the interactions between incident and reflected waves that create destructive interference and are linked to the length scale of periodicity. For all three models shown in Fig.6.7, the yarn widths are different but the unit cell lengths (and thus the periodicity) remain the same, thus the stop-bands occur at the same frequency range. Two small bumps can be seen in the curves around 360 and 390 kHz. These are due the interaction between the flexural mode and two other modes that are crossing when observed in the IBZ (details about this phenomenon are given in Sec.6.4 and illustrated in Fig.6.16).

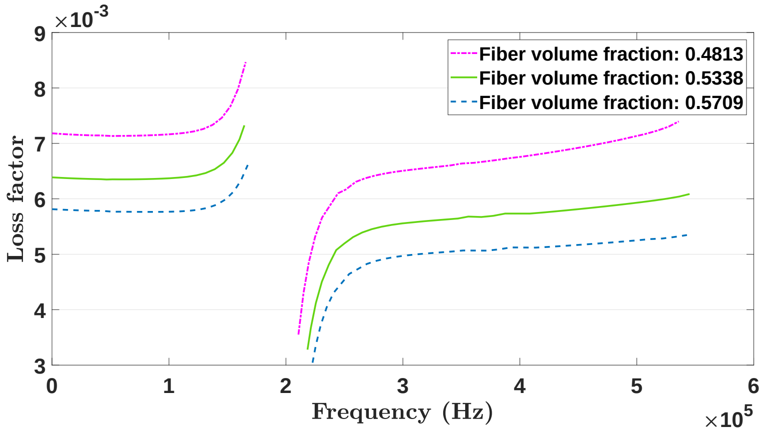

Figure 6.8: Loss factor displayed for three 6250 elements models of a 2D plain woven fabric composite as a function of frequency, associated to the flexural mode of the composite plate (angle of propagation null: x direction): structure with larger fibres (- -), reference structure (–), thinner fibres (-.).

In Fig.6.9, the dissipative characteristics slightly decrease until reaching a frequency of around 300 kHz. The loss factor then increases and it seems to tend to a high value. This is because a local stop-band is present in the dispersion curve. Unlike what was observed in Fig.6.8, the frequency at which the stop-band starts is slightly different for the three models. Indeed a shift in frequency is observed: the higher the fibre volume fraction, the higher the frequency of the stop-band. This shift is justified by the properties of the stop-bands, indeed, local resonant stop-bands usually appear when the unit cell displays one or more resonant unit and thus depend on the internal architecture of the cell. The internal architecture is slightly changed by the different yarns width, thus the stop-bands are different as well.

The loss factor associated to the first pressure wave slightly grows (see Fig.6.10), then the growing rate suddenly increases and the loss factor seems to tend to a high value around the stop-band. On the right side of the stop-band, the same phenomenon can be observed. It seems to tend to a high value around the local stop-band and then settles after the frequency of 350 kHz. The loss factor at 500 kHz is more than the double of the loss factor at 50 kHz. Similarly to what

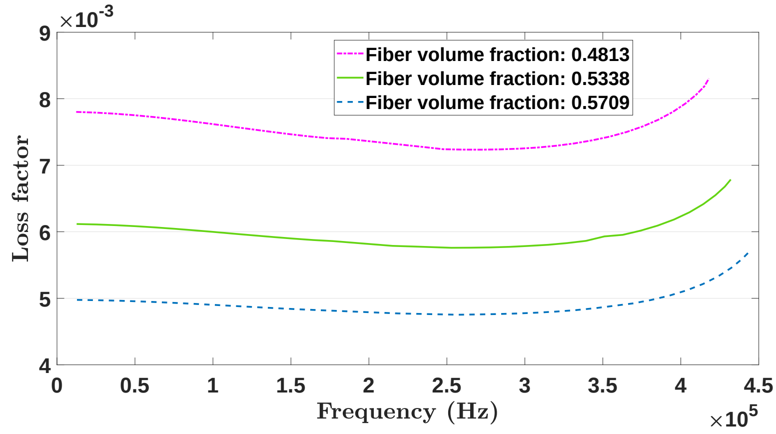

Figure 6.9: Loss factor displayed for three 6250 elements models of a 2D plain woven fabric composite as a function of frequency, associated to the shear mode of the composite plate (angle of propagation null: x direction): structure with larger fibres (- -), reference structure (–), thinner fibres (-.).

was observed in Fig.6.9, the stop-band frequency range is slightly different for the three models. Once again, a shift in frequency is observed: the higher the fibre volume fraction, the higher the frequency range of the stop-band location. The stop-bands in Fig.6.10 also are local resonant stop-bands, thus a change in the internal architecture changes the stop-bands as well. Also, at around 446 kHz, two small peaks are observed. They appear when the wavenumber of the pressure mode curve reaches a limit of the IBZ ($k = \pi/\Delta$), they are the consequences of a small Bragg stop-band. If plotted with a finer wavenumber resolution, the asymptotic behaviour of the loss factor would be observed around the stop-band.

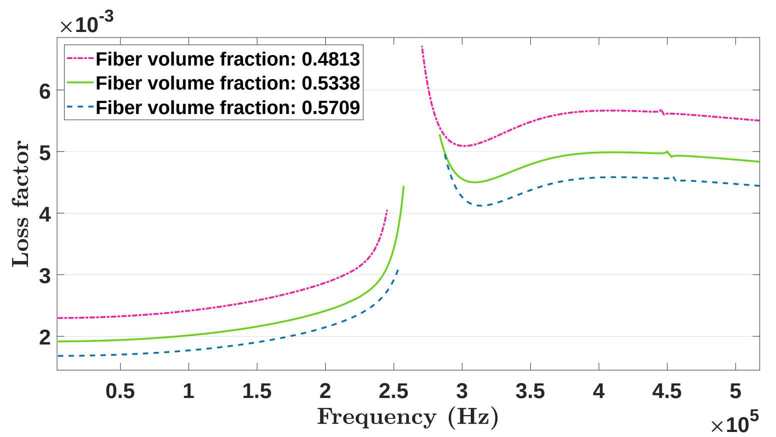

Figure 6.10: Loss factor displayed for three 6250 elements models of a 2D plain woven fabric composite as a function of frequency, associated to the pressure mode of the composite plate (angle of propagation null: x direction): structure with larger fibres (- -), reference structure (–), thinner fibres (-.).

As expected, this parametric study clearly shows that the fibre volume fraction has an impact on the structural damping, and it also shows the strong influence of the frequency over this same parameter. Another interesting result is the effect of a change in yarn width on the frequency of a local stop-band.

6.3.2 Effect of the pre-determined components loss factor

Another parametric study has been conducted on the original model of the 2D plain woven fabric, by altering the pre-determined loss factor of the matrix (η_{mat}) and yarn (η_{yarn}) components. The loss factor function of the frequency is displayed in Fig.6.11.a. It appears that a relation of proportionality exists between the loss factor of the assembly and the pre-determined loss factors of the constituent components and that this relation is independent from the initial loss factors chosen for each components.

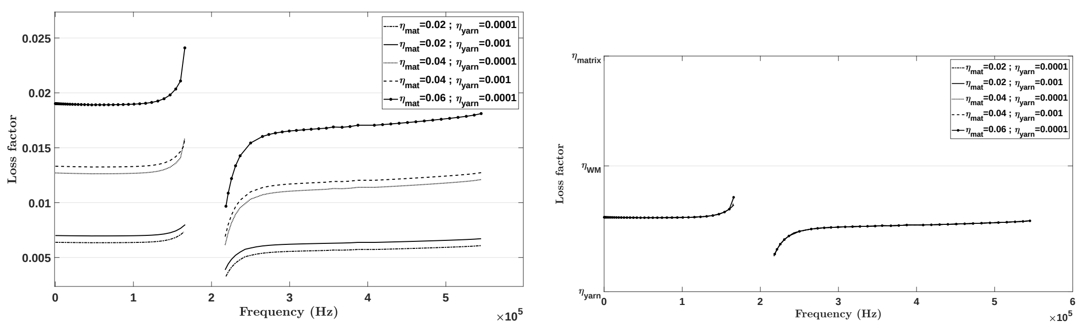

(a) Loss factor (b) Scaled loss factor

Figure 6.11: Loss factor displayed for a 6250 elements model of a 2D plain woven fabric (with changing components loss factor), function of frequency, associated to the flexural mode of the composite plate (propagation along the x direction). WM stands for weigthed mean.

In Fig.6.11.b is displayed the same parametric study with the loss factors adjusted to a scale going from the yarn loss factor as the low limit to the matrix loss factor as the high limit using feature scaling:

$$\eta_{scaled}(\omega) = \frac{\eta(\omega) - \eta_{yarn}}{\eta_{mat} - \eta_{yarn}}. \tag{6.13}$$

It can be observed that all curves are superposed, and it is the case also for the loss factors of the other two first modes. This shows that the structural damping curve shape of the structure is mostly independent from the initial choice of the constituent components loss factors.

6.3.3 Effect of the direction of propagation

Finally, the effect of the direction of propagation is studied. As the model presents a symmetry axis, the dispersion curves and loss factors are symmetric as well. The directions of propagation with an angle superior to 45° will not be studied. However, directions of propagation such as [0°, 30°, 45°] can be studied (see Fig.6.12). The results of this study are displayed in Fig.6.13.

It can be observed that the higher the angle of propagation (amongst the studied ones), the higher the first flexural wave attenuation, and yet, both values of the loss factor for the 30° and 45° angles of propagation start decreasing for a frequency around 100 kHz until reaching and following the curve representing the loss factor at an angle of propagation of 0°. In the right-hand part of the figure, the same order is followed. The angle of propagation which impose the most damping is of 45°, followed by 30° and then 0°. From 500 kHz, the damping curves for the 0° and 30° angle of propagation seem to be crossing and the order is changed: the angle of propagation which impose the most damping is of 45°, followed by 0° and then 30°. It can be concluded that the damping is clearly affected by the direction of propagation in a complex textile composite. Small peaks can be observed in the loss factor curves around 450 kHz, these are due to a light coupling of the flexural mode with other modes in the IBZ. An in-depth study of this phenomenon is presented in Sec.6.5.

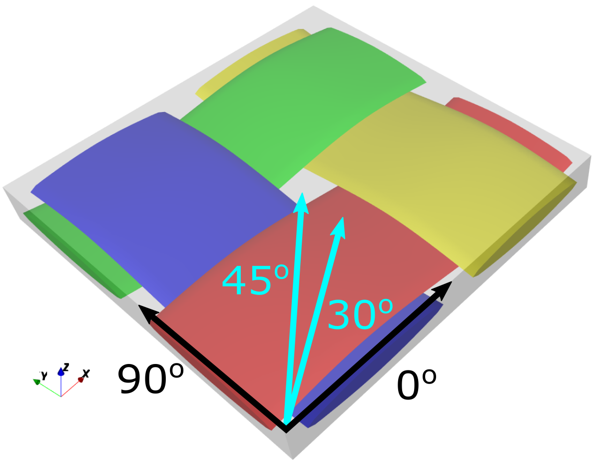

Figure 6.12: Angles of propagation in the unit cell of a 2D plain woven composite.

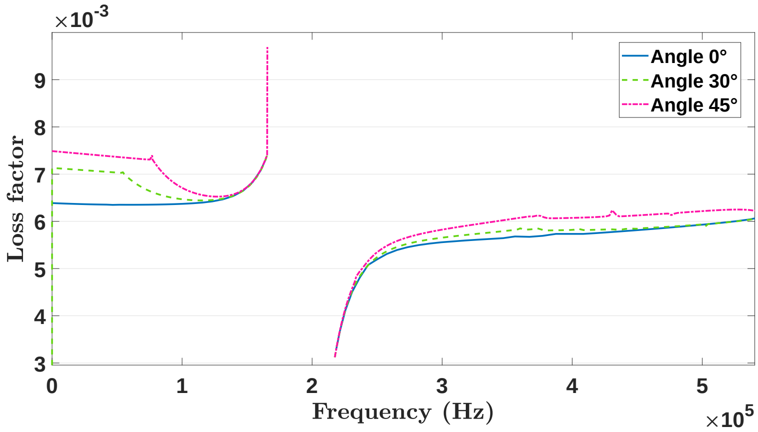

Figure 6.13: Loss factor displayed for a 6250 elements model of a 2D plain woven composite (with changing direction of propagation), function of frequency, associated to the flexural mode of the composite plate.

6.4 Case study: mesoscale modelling of a 3D woven composite for damping prediction

The second example of a textile composite is a 3D woven composite which is modelled at a mesoscopic scale using TexGen (see Fig.3.30). The dimensions of the unit cell are $2 \times 1.5 \times 0.6$ mm. The loss factor was calculated as a function of the propagation angle and the frequency. This FE model is composed of 15625 elements ($25 \times 25 \times 25$), 7834 elements represent the yarns while the 7791 remaining elements are matrix elements. $\eta_{yarn} = 0.0001$ and $\eta_{mat} = 0.02$ are used as pre-determined loss factor for respectively the yarns and matrix constituents. This gives a fibre volume fraction of 0.5014. The materials properties are given in Tables D.2 and D.3 in Appendix.

In Fig.6.14, the loss factor, associated to the flexural mode in the y direction, is shown as a function of frequency. The dispersion curve for this mode is shown as well on the figure allowing for comparison. The results obtained here are comparable to the ones obtained with the 2D weave model. The dispersion curve presents a Bragg stop-band and the loss factor has an asymptotic behaviour around it once again. The loss factor curve is also mostly situated in the $[\eta_{yarn}, \eta_{weightedmean}]$ range.

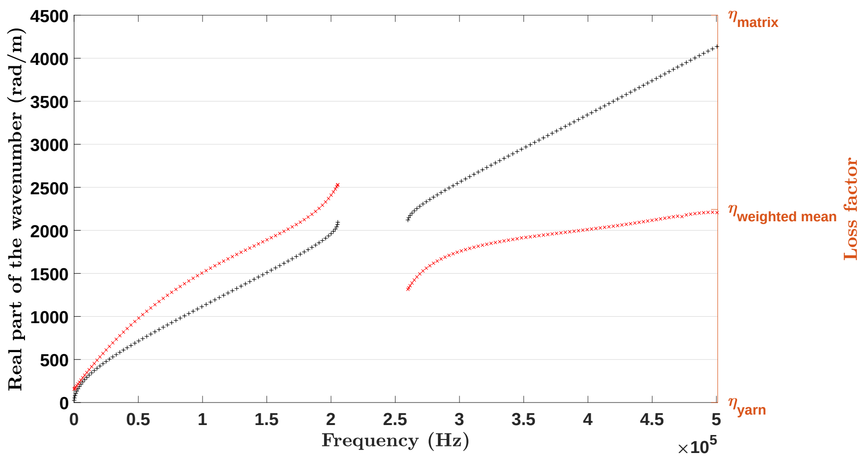

Figure 6.14: Loss factor in a 15625 elements model of a 3D woven fabric composite, function of the frequency, propagating in the y direction, associated to the flexural mode.

Figure 6.15 shows the loss factor, associated to the shear mode in the y direction, as a function of frequency. The dispersion curve for this mode is shown as well on the figure allowing for comparison. The dispersion curve presents a Bragg stop-band and the loss factor has an asymptotic behaviour around it.
At 380 kHz, a light peak is observed. This is caused by the interaction of this shear mode with another mode, provoking both modes to veer away.

A parametric study showing the dispersion curves veering away for low predetermined components loss factors and crossing for higher ones is presented in Fig.6.16 for the same model. Only the bending and the pressure modes in the x direction are plotted, in a restrained frequency range where a local stop-band is present. The modes dispersion curves and their assigned loss factor curves are displayed for four couples of pre-determined components loss factors. It can be observed that when the modes veer away, their loss factors are joined, while this does not happen when they cross. When they cross, a peak in the loss factor

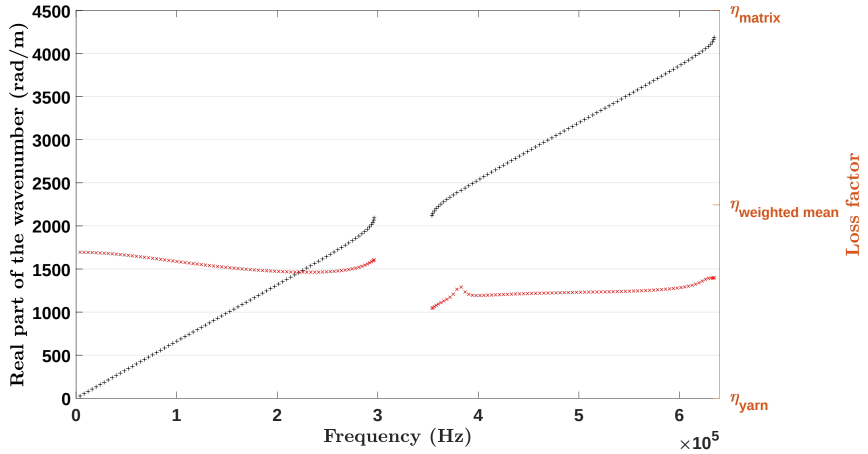

Figure 6.15: Loss factor in a 15625 elements model of a 3D woven fabric composite, function of the frequency, propagating in the y direction, associated to the shear mode.

curve can be observed but the higher the pre-determined components loss factors are, the more faded this local peak will be. This phenomenon is known and other examples where veering is influenced and sometimes suppressed by the effect of damping are presented in [116] and [194].

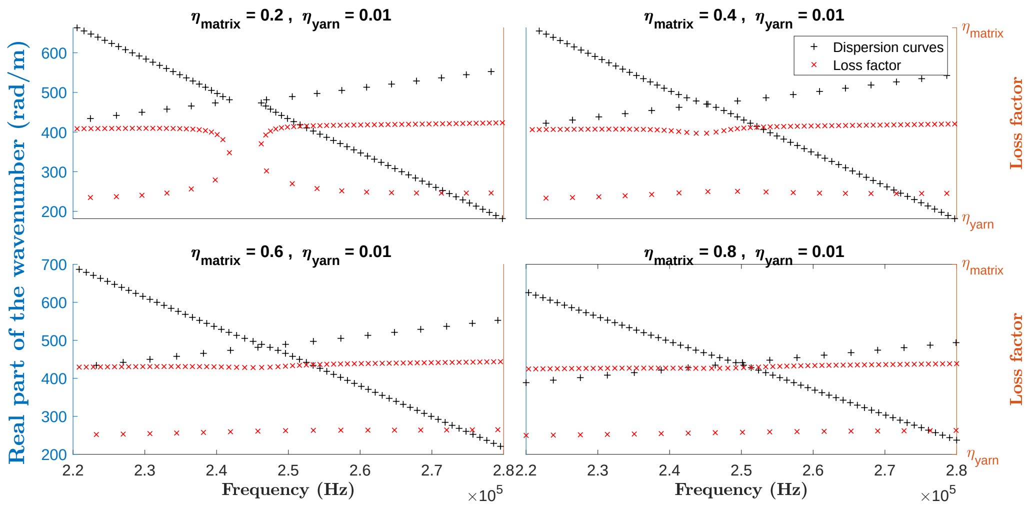

Figure 6.16: Loss factor in a 15625 elements model of a 3D woven composite, function of the frequency, associated to the flexural and pressure modes propagating in the x direction for four different configurations of pre-determined components loss factors. (+) dispersion curves, ($\times$) loss factors.

Figure 6.17 shows the loss factor, associated to the pressure mode in the y direction, is shown as a function of frequency. It is presented for both this 3D weave model and for the triaxial braided fabric model from the next section as well. The dispersion curves for this modes are shown as well on the figure allowing for comparison. It can be observed that the loss factor for the braid fabric is higher than for the 3D weave, even though the fibre volume fraction is higher for the braid fabric model. This is surprising as it is the matrix material that has the highest component loss factor. It shows that the mesoscale architecture of yarns within the textile composite has a strong effect on the damping.

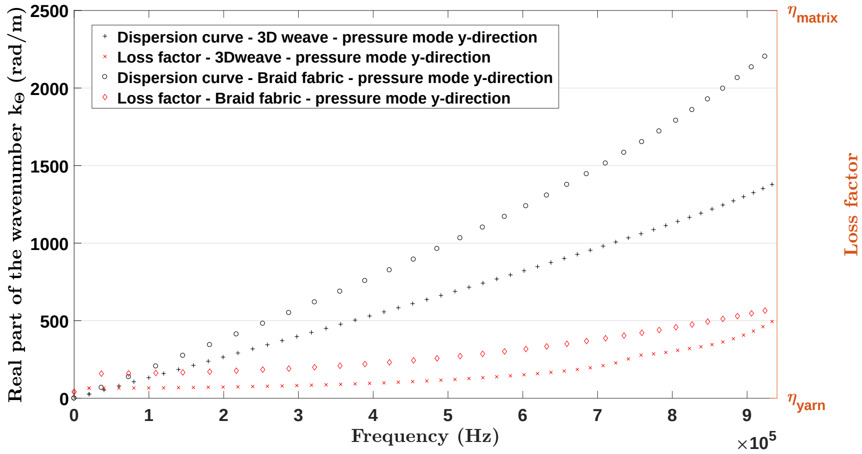

Figure 6.17: Comparison of the loss factor in a 15625 elements model of a 3D woven composite and in a 12000 elements model of a triaxial braid fabric, function of the frequency, propagating in the y direction, associated to the pressure mode.

6.5 Case study: mesoscale modelling of a triaxial braided composite for damping prediction and numerical validation

As a third textile composite case study, a unit cell of a triaxial braided composite is modelled (Fig.3.33) and the loss factor of the flexural wave is calculated as a function of the propagation angle and the frequency. The dimensions of the unit cell are $2 \times 0.6 \times 0.4$ mm. This FE model is composed of 12000 elements ($40 \times 20 \times 15$), 6665 are yarn elements while the 5335 remaining elements are matrix elements. This gives a fibre volume fraction of 0.5554. $\eta_{yarn} = 0.0001$ and $\eta_{mat} = 0.02$ are used as pre-determined loss factor for respectively the yarns and matrix constituents. The materials properties are given in Tables D.2 and D.3 in Appendix.

In Fig.6.18, the loss factor, associated to both the flexural and the shear modes propagating in the x direction, function of the frequency, is displayed. The dispersion curves for these modes are shown as well on the figure allowing for comparison. Both are displayed on the same figure as there is a strong coupling between these two modes (around 150 kHz and again around 750 kHz). The coupling is creating local stop-bands (circled in yellow) as the dispersion curves veer away (when displayed in the BZ) instead of crossing. This is the result of the two eigenvalue loci approaching closely and it causes the properties of the two modes to be swapped, including eigenvectors or the loss factors [194, 195] as can be seen on this same figure. Other stop-bands can be observed around 300 kHz and 850 kHz for the flexural mode and around 600 kHz and 1.1 MHz for the shear mode. These are Bragg stop-bands (circled in green), intrinsic to the periodic properties of the structure. Around these stop-bands, the loss factor has an asymptotic behaviour once again. Finally, it can be noted that the loss factor curves are largely located below the loss factor weighted mean, which would indicates that the loss factor of the yarns has a stronger influence on the final loss factor in that direction of propagation. The same phenomenon does arise with the pressure mode as well which is displayed in Fig.6.19.

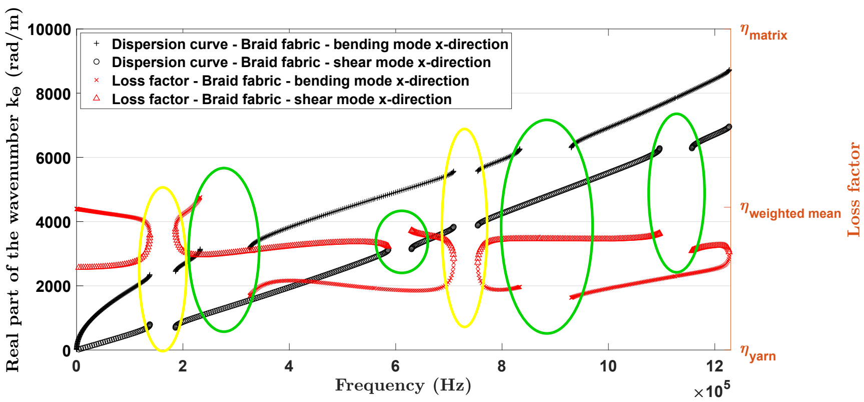

Figure 6.18: Loss factor in a 12000 elements model of a triaxial braid fabric, function of the frequency, propagating in the x direction, associated both to the flexural and shear modes. The Bragg stop-bands are circled in green and the local stop-bands are circled in yellow.

In Fig.6.19 are displayed the loss factors, associated to the pressure modes of the triaxial braided composite, propagating in both the x and the y directions. It can be observed that the loss factor is lower for the pressure wave propagating in the y direction until it reaches 800 kHz and takes over on the loss factor of the pressure wave propagating in the x direction. This shows again direction dependency of the loss factor.

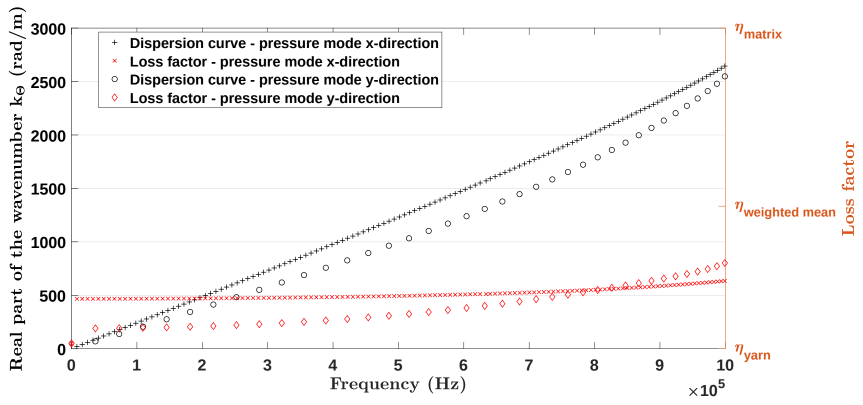

Figure 6.19: Comparison of the loss factor in a 12000 elements model of a triaxial braid fabric, function of the frequency, associated to the pressure mode, propagating in the x direction and in the y direction.

In order to provide for numerical validation, a beam made of a triaxial braided composite is modelled, its width is of 0.6 mm, its thickness is of 0.4 mm and its length is of 200 mm. The nodal displacements in the y and z directions are fixed as null. The WFE/CMS method allows for computing the dispersion relations and the loss factor over frequency and it is used for the described beam model as shown in Fig.6.20. A transient FEA computation is performed once with a broadband signal and the displacement is measured for a set of positions along the length of the beam (B-scan). Post-treating these results with the 2D FFT allows for obtaining the dispersion relations as displayed in Fig.6.20. The comparison is made with the dispersion curves obtained with the WFE/CMS on the same figure. A very good agreement is observed, the loss factors can now be compared. It can also be noted that symmetries and translations in the different BZs, effects of the periodicity, appear in the dispersion curves computed from the transient FEA as previously observed in Sec.3.3.5.

Finally, a numerical validation using the transient FE method presented in Sec.6.2.2 is performed for 13 frequency points ranging from 200 to 800 kHz. From the transient FEA performed with a narrow band input signal at different frequencies, the β coefficients are adjusted as shown in Table D.7 in Appendix

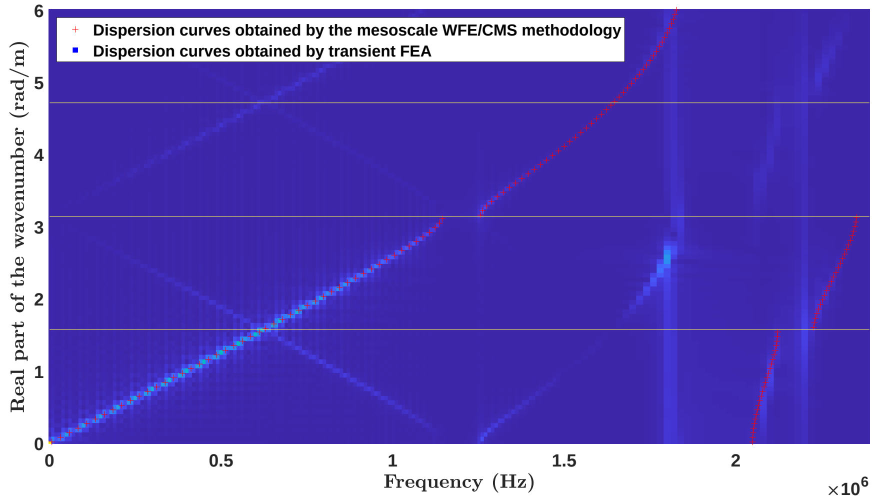

Figure 6.20: Dispersion curves for the triaxial braided composite beam with blocked displacement in the second and third directions. The background pixelised image results from the two-dimensional Fast Fourier Transform of the B-scan, while the red dots result from the WFE/CMS methodology presented in Sec.3.3. A perfect agreement is observed. Yellow lines are plotted at BZ limits ($k = \pi/\Delta$, $k = 2\pi/\Delta$ and $k = 3\pi/\Delta$).

and the loss factor is computed using Eq.(6.12). The maximum amplitudes are calculated using the envelope of the displacement amplitudes over time. The loss factor is calculated by comparing the displacement amplitude over time at more than two thousand points along the beam. The mean is plotted on Fig.6.21 along with the results from the presented methodology. The mean-squared error is, however, not plotted because extremely low and thus barely visible.

A very good agreement between the loss factor curve computed with the methodology presented in this chapter and the one computed from the transient FEA is observed once again. The calculation of these dispersion and damping properties using the WFE/CMS methodology took 30 min on a 1 core and 8GB RAM system for a wide frequency range, while it took around 5 hours on a 8 cores and 160 GB of RAM on a HPC system to get the loss factor for only one frequency point using transient FEA.

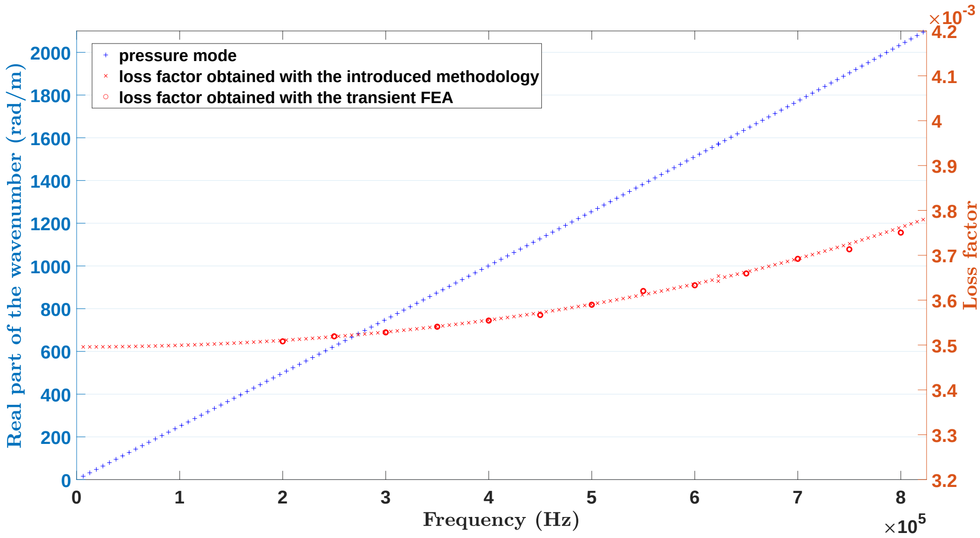

Figure 6.21: Loss factor in a triaxial braided composite beam, function of the frequency, propagating in the x direction, associated to the pressure mode. (+) the dispersion curve, ($\times$) the loss factor computed with the methodology introduced in this chapter, (o) the loss factor computed from the transient FEA.

6.6 Conclusions

In this chapter a method allowing for prediction of the structural damping in textile composites at a mesoscopic scale is presented. Four composite models are presented: a laminate, a 2D plain woven composite, a 3D woven composite and a triaxial braided composite. For all four models, the dispersion relations are computed as well as the variation of the loss factor versus the frequency for the first three modes.

The damping predictions are compared for waves propagating in different directions of the same composite and for varying fibre volume fraction. The damping is also studied around complex phenomena such as stop-bands.

It can be concluded that:

- The damping is strongly affected by the direction of propagation of the waves and dependent on the frequency in a textile composite.
- The damping is affected by the fibre volume fraction of the textile. But even though the numerical values of the damping loss factor change, the shape of the curves remain quite similar if the mesoscale architecture is similar as well.

- When a textile dispersion curve shows stop-bands, the damping loss factor has a characteristic behaviour depending on the stop-band type. Asymptotic in the case of a Bragg stop-band and either strongly increasing or decreasing on both sides of a local stop-band.
- The shape of the loss factor curves is mostly independent from the predetermined loss factors of the components.
- The mesoscale architecture of the textile composite has a strong influence over the damping.

Chapter 7

Concluding remarks

7.1 Summary

In this thesis, numerical methodologies for the simulation of elastic waves in textile composites have been proposed, applied to numerous structures and validated. A mesoscale WFE/CMS methodology has been presented, its one-dimensional formulation numerically validated by transient finite element analysis, its two-dimensional formulation experimentally validated and the limitations and issues were discussed. A multiscale approach was proposed for comparison and it was demonstrated that mesoscale modelling is needed for dispersion characterisation as well as for damping predictions when considering textile composites.

Two macroscale modelling approaches were presented alongside the mesoscale methodology. The first method uses a virtual static testing approach to obtain one set of effective mechanical properties for a textile composite, and is called in this thesis 'the static macroscale' approach. The second method divides a textile composite into individual layers, against its own integrity, and obtains an individual set of moduli for each layer by virtual static testing. The resulting model is equivalent to a laminate whose layers are homogeneous and is named 'static macroscale per layer'. It was shown that both macroscale modelling approaches provide dispersion characteristics that are very different in comparison to the ones obtained by the introduced mesoscale approach, yet the static macroscale per layer performs reasonably well. Neither were able to predict for the complex phenomena (e.g. stop-bands) uncovered by the mesoscale approach.

In comparison to experimental results, both the static macroscale per layer and mesoscale approaches have provided accurate predictions for A_0 and S_0. While it is not possible to conclude whether the mesoscale methodology provides more accurate predictions than the static macroscale per layer on the experimental level, as no more than two modes (S_0 and A_0) could be compared, it is expected to perform better at unveiling stop-band phenomenon and in higher frequency ranges. It would have been possible to observe more modes at higher frequencies but the damping in the composite plates is too high and thus the waves do not propagate far enough. Another reason that prevents concluding is the lack of resolution provided by the experimental results.

However, in reality, if the effective moduli for a textile composite were to be extracted by static experimental testing instead of virtual testing, only one set of moduli would be obtained, characterising a macroscale model. It is impracticable to obtain experimentally the effective mechanical properties necessary to construct our macroscale per layer model. This model can be constructed using a numerical approach and a mesoscale modelling is needed to compute the effective properties for each individual layers.

Only the introduced mesoscale WFE/CMS methodology provides excellent accuracy in comparison to the results obtained by transient finite element analysis and allows for predicting stop-bands. This methodology shares the same unit cell modelling step with the macroscale approaches but the dispersion characterisation step is more costly while still feasible.

Of course, other homogenisation methodologies exist and one in particular has been considered in the spirit of reducing the computation time, especially for large layered assemblies of textile composites. Indeed, while the computation of a mesoscale model is feasible timewise for a textile composite whose geometry is complex, it becomes less viable when considering a layered material composed of a large assembly of textile composites. Macroscale models cannot describe complex phenomena implied by the periodicity of a structure but are very efficient to compute dispersion relations of large assembly. In that context, a homogenisation method based on dispersion curves inversion by the mean of an optimisation

algorithm was introduced. It was shown again that no simple macroscale model can act as substitute for a complex textile composite.
At last, a damping model was presented within the mesoscale WFE/CMS methodology and it was demonstrated that internal architecture of a textile composite has a strong effect on wave attenuation, and thus a mesoscale approach is needed.

7.2 Future work

The exhibited work has shown the need for mesoscale modelling to investigate the wave properties of textile composite waveguides. The proposed methodology is reliable and has a lot of potential applications. In this section, possible future research related to this methodology are proposed:

- Extending the mesoscale WFE/CMS methodology to various applications such as curved structures for dispersion characterisation of pipelines made of textile composites for example.

- A set of experimental dispersion characterisations performed on textile composite structures of large dimensions would provide results with acceptable resolution and thus a more robust experimental validation of the methodology. Measurements of higher-order modes would also be most useful for validation of the model. These experimental results could be used for correlation of the measured damping with the presented prediction model as well.

- Building a robust homogenisation technique for reduction of the computation time for structures composed of large layered assemblies of textile composites is in order.

- A next step toward early damage detection in textile composite structures is the building of prediction scheme for guided wave interactions with damage such as fibres breakage or delamination in order to build a complete forward model.

Bibliography

[1] V. Giurgiutiu, *Structural health monitoring: with piezoelectric wafer active sensors*. Elsevier, 2007.

[2] V. Giurgiutiu, *Structural Health Monitoring of Aerospace Composites*. Academic Press, 2015.

[3] J. L. Rose, J. J. Ditri, A. Pilarski, K. Rajana, and F. Carr, "A guided wave inspection technique for nuclear steam generator tubing," *NDT & E International*, vol. 27, no. 6, pp. 307–310, 1994.

[4] E. Kannan, B. W. Maxfield, and K. Balasubramaniam, "Shm of pipes using torsional waves generated byin situmagnetostrictive tapes," *Smart Materials and Structures*, vol. 16, no. 6, pp. 2505–2515, 2007.

[5] J. K. Van Velsor, R. L. Royer, S. E. Owens, and J. L. Rose, "Pipe test a magnetostrictive phased array system for guided wave testing and structural health monitoring of pipe," 2013.

[6] C. Willberg, S. Duczek, J. Vivar-Perez, and Z. Ahmad, "Simulation methods for guided wave-based structural health monitoring: a review," *Applied Mechanics Reviews*, vol. 67, no. 1, p. 010803, 2015.

[7] A. C. Loos and G. S. Springer, "Curing of epoxy matrix composites," *Journal of composite materials*, vol. 17, no. 2, pp. 135–169, 1983.

[8] A. P. Mouritz, M. K. Bannister, P. J. Falzon, and K. H. Leong, "Review of applications for advanced three-dimensional fibre textile composites," *Composites Part A: Applied Science and Manufacturing*, vol. 30, no. 12, pp. 1445–1461, 1999.

[9] Y. Liu, M. de Araujo, and H. Hu, *2 - Advanced fibrous architectures for composites in aerospace engineering*, pp. 17–58. Woodhead Publishing, 2016.

[10] M. Ansar, W. Xinwei, and Z. Chouwei, "Modeling strategies of 3d woven composites: a review," *Composite structures*, vol. 93, no. 8, pp. 1947–1963, 2011.

[11] E. J. Barbero, *Introduction to composite materials design*. CRC press, 2017.

[12] S. V. Lomov, G. Huysmans, Y. Luo, R. S. Parnas, A. Prodromou, I. Verpoest, and F. R. Phelan, "Textile composites: modelling strategies," *Composites Part A: applied science and manufacturing*, vol. 32, no. 10, pp. 1379–1394, 2001.

[13] N. Charalambakis, "Homogenization techniques and micromechanics. a survey and perspectives," *Applied Mechanics Reviews*, vol. 63, no. 3, 2010.

[14] X. Ji, A. M. Khatri, E. S. M. Chia, R. K. H. Cha, B. T. B. Yeo, S. C. Joshi, and Z. Chen, "Multi-scale simulation and finite-element-assisted computation of elastic properties of braided textile reinforced composites," *Journal of Composite Materials*, vol. 48, no. 8, pp. 931–949, 2013.

[15] M. Y. Matveev, *Effect of variabilities on mechanical properties of textile composites*. Thesis, University of Nottingham, 2015.

[16] J. I. Mugica, C. S. Lopes, F. Naya, M. Herraez, V. Martinez, and C. Gonzalez, "Multiscale modelling of thermoplastic woven fabric composites: From micromechanics to mesomechanics," *Composite Structures*, vol. 228, p. 111340, 2019.

[17] W. Voigt, "Ueber die beziehung zwischen den beiden elasticitatsconstanten isotroper korper," *Annalen der Physik*, vol. 274, no. 12, pp. 573–587, 1889.

[18] A. Reuss, "Berechnung der fliessgrenze von mischkristallen auf grund der plastizitatsbedingung fur einkristalle," *ZAMM Journal of Applied Mathematics and Mechanics/Zeitschrift fur Angewandte Mathematik und Mechanik*, vol. 9, no. 1, pp. 49–58, 1929.

[19] T. J. Whitney and T.-W. Chou, "Modeling of 3-d angle-interlock textile structural composites," *Journal of Composite Materials*, vol. 23, no. 9, pp. 890–911, 1989.

[20] A. Endruweit and A. C. Long, "Analysis of compressibility and permeability of selected 3d woven reinforcements," *Journal of Composite Materials*, vol. 44, no. 24, pp. 2833–2862, 2010.

[21] Z. Hashin and B. W. Rosen, "The elastic moduli of fiber-reinforced materials," *Journal of applied mechanics*, vol. 31, no. 2, pp. 223–232, 1964.

[22] R. M. Christensen and K. H. Lo, "Solutions for effective shear properties in three phase sphere and cylinder models," *Journal of the Mechanics and Physics of Solids*, vol. 27, no. 4, pp. 315–330, 1979.

[23] J. C. H. Affdl and J. L. Kardos, "The halpin-tsai equations: a review," *Polymer Engineering & Science*, vol. 16, no. 5, pp. 344–352, 1976.

[24] C. C. Chamis, "Mechanics of composite materials: past, present, and future," *Journal of Composites, Technology and Research*, vol. 11, no. 1, pp. 3–14, 1989.

[25] Y. L. Shen, M. Finot, A. Needleman, and S. Suresh, "Effective elastic response of two-phase composites," *Acta Metallurgica et Materialia*, vol. 42, no. 1, pp. 77–97, 1994.

[26] L. E. Asp, L. A. Berglund, and R. Talreja, "Prediction of matrix-initiated transverse failure in polymer composites," *Composites Science and Technology*, vol. 56, no. 9, pp. 1089–1097, 1996.

[27] M. Dong and S. Schmauder, "Modeling of metal matrix composites by a self-consistent embedded cell model," *Acta Materialia*, vol. 44, no. 6, pp. 2465–2478, 1996.

[28] S. Li, "On the unit cell for micromechanical analysis of fibre-reinforced composites," *Proceedings of the Royal Society of London. Series A: Mathematical, Physical and Engineering Sciences*, vol. 455, no. 1983, pp. 815–838, 1999.

[29] S. Li and A. Wongsto, "Unit cells for micromechanical analyses of particle-reinforced composites," *Mechanics of Materials*, vol. 36, no. 7, pp. 543–572, 2004.

[30] S. Li and E. Sitnikova, "An excursion into representative volume elements and unit cells," in *Comprehensive Composite Materials II*, vol. 1, Elsevier, 2017.

[31] H. Yuanchen, J. Kyo Kook, and H. Sung Kyu, "Effects of fiber arrangement on mechanical behavior of unidirectional composites," *Journal of Composite Materials*, vol. 42, no. 18, pp. 1851–1871, 2008.

[32] E. H. Glaessgen, C. M. Pastore, O. H. Griffin, and A. Birger, "Geometrical and finite element modelling of textile composites," *Composites Part B: Engineering*, vol. 27, no. 1, pp. 43–50, 1996.

[33] P. Tan, L. Tong, and G. P. Steven, "Modelling for predicting the mechanical properties of textile composites: a review," *Composites Part A: Applied Science and Manufacturing*, vol. 28, no. 11, pp. 903–922, 1997.

[34] X. Lei, W. Rui, L. Yong, and L. Jin, "The effect of woven structures on the vibration characteristics of glass fabric/epoxy composite plates," *Defence Science Journal*, vol. 61, no. 5, pp. 499–504, 2011.

[35] J. J. Crookston, A. C. Long, and I. A. Jones, "A summary review of mechanical properties prediction methods for textile reinforced polymer composites," *Proceedings of the Institution of Mechanical Engineers, Part L: Journal of Materials: Design and Applications*, vol. 219, no. 2, pp. 91–109, 2005.

[36] G. Hivet and P. Boisse, "Consistent mesoscopic mechanical behaviour model for woven composite reinforcements in biaxial tension," *Composites Part B: Engineering*, vol. 39, no. 2, pp. 345–361, 2008.

[37] F. T. Peirce, "The geometry of cloth structure," *Journal of the Textile Institute Transactions*, vol. 28, no. 3, pp. T45–T96, 1937.

[38] T. Ishikawa and T.-W. Chou, "Stiffness and strength behaviour of woven fabric composites," *Journal of Materials Science*, vol. 17, no. 11, pp. 3211–3220, 1982.

[39] J.-M. Yang, C.-L. Ma, and T.-W. Chou, "Fiber inclination model of three-dimensional textile structural composites," *Journal of Composite Materials*, vol. 20, no. 5, pp. 472–484, 1986.

[40] B. N. Cox, W. C. Carter, and N. A. Fleck, "A binary model of textile composites: I. formulation," *Acta Metallurgica et Materialia*, vol. 42, no. 10, pp. 3463–3479, 1994.

[41] J. Whitcomb, K. Srirengan, and C. Chapman, "Evaluation of homogenization for global/local stress analysis of textile composites," *Composite Structures*, vol. 31, no. 2, pp. 137–149, 1995.

[42] R. A. Naik, "Failure analysis of woven and braided fabric reinforced composites," *Journal of Composite Materials*, vol. 29, no. 17, pp. 2334–2363, 1995.

[43] R. T. Farouki, "The bernstein polynomial basis: A centennial retrospective," *Computer Aided Geometric Design*, vol. 29, no. 6, pp. 379–419, 2012.

[44] W.-S. Kuo and B.-J. Pon, "Elastic moduli and damage evolution of three-axis woven fabric composites," *Journal of Materials Science*, vol. 32, no. 20, pp. 5445–5455, 1997.

[45] P. Tan, L. Tong, and G. P. Steven, "Modeling approaches for 3d orthogonal woven composites," *Journal of Reinforced Plastics and Composites*, vol. 17, no. 6, pp. 545–577, 1998.

[46] S. V. Lomov, A. V. Gusakov, G. Huysmans, A. Prodromou, and I. Verpoest, "Textile geometry preprocessor for meso-mechanical models of woven composites," *Composites Science and Technology*, vol. 60, no. 11, pp. 2083–2095, 2000.

[47] I. Verpoest and S. V. Lomov, "Virtual textile composites software wisetex: Integration with micro-mechanical, permeability and structural analysis," *Composites Science and Technology*, vol. 65, no. 15, pp. 2563–2574, 2005.

[48] S. Lomov, T. Truong, I. Verpoest, T. Peeters, D. Roose, P. Boisse, and A. Gasser, "Mathematical modelling of internal geometry and deformability of woven performs," *International Journal of Forming Processes*, vol. 6, no. 3-4, pp. 413–442, 2003.

[49] F. Robitaille, A. C. Long, I. A. Jones, and C. D. Rudd, "Automatically generated geometric descriptions of textile and composite unit cells," *Composites Part A: Applied Science and Manufacturing*, vol. 34, no. 4, pp. 303–312, 2003.

[50] F. Robitaille, B. R. Clayton, A. C. Long, B. J. Souter, and C. D. Rudd, "Geometric modelling of industrial preforms: Woven and braided textiles," *Proceedings of the Institution of Mechanical Engineers, Part L: Journal of Materials: Design and Applications*, vol. 213, no. 2, pp. 69–83, 1999.

[51] M. Sherburn, *Geometric and Mechanical Modelling of Textiles.* Thesis, The University of Nottingham, 2007.

[52] S. D. Green, M. Y. Matveev, A. C. Long, D. Ivanov, and S. R. Hallett, "Mechanical modelling of 3d woven composites considering realistic unit cell geometry," *Composite Structures*, vol. 118, pp. 284–293, 2014.

[53] W. Wijaya, P. A. Kelly, and S. Bickerton, "A novel methodology to construct periodic multi-layer 2d woven unit cells with random nesting configurations directly from ct-scans," *Composites Science and Technology*, vol. 193, p. 108125, 2020.

[54] K. F. Graff, *Wave motion in elastic solids.* Courier Corporation, 2012.

[55] L. Cremer and M. Heckl, *Structure-borne sound: structural vibrations and sound radiation at audio frequencies.* Springer Science & Business Media, 2013.

[56] W. C. Young, R. G. Budynas, and A. M. Sadegh, *Roark's formulas for stress and strain*, vol. 7. McGraw-Hill New York, 2002.

[57] G. B. Warburton, *The Dynamical Behaviour of Structures: Structures and Solid Body Mechanics Series.* Elsevier, 2014.

[58] L. Hinke, B. R. Mace, and M. J. Brennan, "Finite element analysis of waveguides," *Institute of Sound and Vibration Research*, 2004.

[59] S. P. Timoshenko, "LXVI. On the correction for shear of the differential equation for transverse vibrations of prismatic bars," *The London, Edinburgh, and Dublin Philosophical Magazine and Journal of Science*, vol. 41, no. 245, pp. 744–746, 1921.

[60] S. P. Timoshenko, "X. On the transverse vibrations of bars of uniform cross-section," *The London, Edinburgh, and Dublin Philosophical Magazine and Journal of Science*, vol. 43, no. 253, pp. 125–131, 1922.

[61] G. R. Cowper, "The shear coefficient in timoshenkoś beam theory," *Journal of Applied Mechanics*, vol. 33, no. 2, pp. 335–340, 1966.

[62] H. Lamb, "On waves in an elastic plate," *Proceedings of the Royal Society of London. Series A*, vol. 93, no. 648, p. 114, 1917.

[63] J. M. Whitney and N. J. Pagano, "Shear deformation in heterogeneous anisotropic plates," *Journal of applied mechanics*, vol. 37, no. 4, pp. 1031–1036, 1970.

[64] W. H. Prosser, "The propagation characteristics of the plate modes of a-coustic emission waves in thin aluminum plates and thin graphite/epoxy composite plates and tubes," *The Journal of the Acoustical Society of America*, vol. 92, no. 6, pp. 3441–3442, 1992.

[65] H. Mei, M. F. Haider, R. James, and V. Giurgiutiu, "Pure s0 and sh0 detections of various damage types in aerospace composites," *Composites Part B: Engineering*, vol. 189, p. 107906, 2020.

[66] G. Floquet, "Sur les équations différentielles linéaires à coefficients périodiques," *Annales scientifiques de l'École normale supérieure*, vol. 12, pp. 47–88, 1883.

[67] F. Bloch, "Uber die quantenmechanik der elektronen in kristallgittern," *Zeitschrift fur Physik*, vol. 52, no. 7, pp. 555–600, 1929.

[68] D. J. Mead, "Wave propagation in continuous periodic structures: research contributions from southampton, 1964-1995," *Journal of Sound and Vibration*, vol. 190, no. 3, pp. 495–524, 1996.

[69] M. I. Hussein, M. J. Leamy, and M. Ruzzene, "Dynamics of phononic materials and structures: Historical origins, recent progress, and future outlook," *Applied Mechanics Reviews*, vol. 66, no. 4, 2014.

[70] L. Brillouin, *Wave propagation in periodic structures: electric filters and crystal lattices*. Dover Publications, 1953.

[71] L. Rayleigh, "XVII. On the maintenance of vibrations by forces of double frequency, and on the propagation of waves through a medium endowed with a periodic structure," *Philosophical Magazine*, vol. 24, no. 147, pp. 145–159, 1887.

[72] G. Wang, D. Yu, J. Wen, Y. Liu, and X. Wen, "One-dimensional phononic crystals with locally resonant structures," *Physics Letters A*, vol. 327, no. 5, pp. 512–521, 2004.

[73] Y. Xiao, J. Wen, D. Yu, and X. Wen, "Flexural wave propagation in beams with periodically attached vibration absorbers: band-gap behavior and band formation mechanisms," *Journal of Sound and Vibration*, vol. 332, no. 4, pp. 867–893, 2013.

[74] L. Van Belle, C. Claeys, E. Deckers, and W. Desmet, "On the impact of damping on the dispersion curves of a locally resonant metamaterial: Modelling and experimental validation," *Journal of Sound and Vibration*, vol. 409, pp. 1–23, 2017.

[75] O. Sigmund and J. Sondergaard Jensen, "Systematic design of phononic band gap materials and structures by topology optimization," *Philosophical Transactions of the Royal Society of London. Series A: Mathematical, Physical and Engineering Sciences*, vol. 361, no. 1806, p. 1001, 2003.

[76] Z. C. He, X. Xiao, and E. Li, "Design for structural vibration suppression in laminate acoustic metamaterials," *Composites Part B: Engineering*, vol. 131, pp. 237–252, 2017.

[77] X. An, H. Fan, and C. Zhang, "Elastic wave and vibration bandgaps in planar square metamaterial-based lattice structures," *Journal of Sound and Vibration*, vol. 475, p. 115292, 2020.

[78] M. Cong, X. Wu, and R. Liu, "Dispersion analysis of guided waves in the finned tube using the semi-analytical finite element method," *Journal of Sound and Vibration*, vol. 401, pp. 114–126, 2017.

[79] T. Kundu, S. Banerjee, and K. V. Jata, "An experimental investigation of guided wave propagation in corrugated plates showing stop bands and pass bands," *The Journal of the Acoustical Society of America*, vol. 120, no. 3, pp. 1217–1226, 2006.

[80] C. T. Sun, J. D. Achenbach, and G. Herrmann, "Time-harmonic waves in a stratified medium propagating in the direction of the layering," *Journal of Applied Mechanics*, vol. 35, no. 2, pp. 408–411, 1968.

[81] C. T. Sun, J. D. Achenbach, and G. Herrmann, "Continuum theory for a laminated medium," *Journal of Applied Mechanics*, vol. 35, no. 3, pp. 467–475, 1968.

[82] J. R. Banerjee, "Dynamic stiffness formulation for structural elements: a general approach," *Computers & Structures*, vol. 63, no. 1, pp. 101–103, 1997.

[83] F. W. Williams and J. R. Banerjee, "Free vibration of composite beams - an exact method using symbolic computation," *Journal of Aircraft*, vol. 32, no. 3, pp. 636–642, 1995.

[84] J. R. Banerjee, "Free vibration of sandwich beams using the dynamic stiffness method," *Computers & Structures*, vol. 81, no. 18, pp. 1915–1922, 2003.

[85] W. T. Thomson, "Transmission of elastic waves through a stratified solid medium," *Journal of Applied Physics*, vol. 21, no. 2, pp. 89–93, 1950.

[86] M. J. S. Lowe, "Matrix techniques for modeling ultrasonic waves in multilayered media," *IEEE transactions on ultrasonics, ferroelectrics, and frequency control*, vol. 42, no. 4, pp. 525–542, 1995.

[87] S. B. Dong and R. B. Nelson, "On natural vibrations and waves in laminated orthotropic plates," *Journal of Applied Mechanics*, vol. 39, no. 3, pp. 739–745, 1972.

[88] G. R. Liu, J. Tani, T. Ohyoshi, and K. Watanabe, "Characteristic wave surfaces in anisotropic laminated plates," *Journal of Vibration and Acoustics*, vol. 113, no. 3, pp. 279–285, 1991.

[89] G. R. Liu and J. D. Achenbach, "A strip element method for stress analysis of anisotropic linearly elastic solids," *Journal of applied mechanics*, vol. 61, no. 2, pp. 270–277, 1994.

[90] K. Jezzine, *Approche modale pour la simulation globale de controles non-destructifs par ondes elastiques guidees*. Thesis, Bordeaux 1, 2006.

[91] I. Bartoli, A. Marzani, F. Lanza di Scalea, and E. Viola, "Modeling wave propagation in damped waveguides of arbitrary cross-section," *Journal of Sound and Vibration*, vol. 295, no. 3-5, pp. 685–707, 2006.

[92] M. Sale, P. Rizzo, and A. Marzani, "Semi-analytical formulation for the guided waves-based reconstruction of elastic moduli," *Mechanical Systems and Signal Processing*, vol. 25, no. 6, pp. 2241–2256, 2011.

[93] R. M. Orris and M. Petyt, "A finite element study of harmonic wave propagation in periodic structures," *Journal of Sound and Vibration*, vol. 33, no. 2, pp. 223–236, 1974.

[94] R. M. Orris and M. Petyt, "Random response of periodic structures by a finite element technique," *Journal of Sound and Vibration*, vol. 43, no. 1, pp. 1–8, 1975.

[95] A. Y. Abdel-Rahman, *Matrix analysis of wave propagation in periodic systems.* Thesis, University of Southampton, 1979.

[96] J. M. Mencik and M. N. Ichchou, "Multi-mode propagation and diffusion in structures through finite elements," *European Journal of Mechanics - A/Solids*, vol. 24, no. 5, pp. 877–898, 2005.

[97] B. R. Mace, D. Duhamel, M. J. Brennan, and L. Hinke, "Finite element prediction of wave motion in structural waveguides," *The Journal of the Acoustical Society of America*, vol. 117, no. 5, pp. 2835–2843, 2005.

[98] E. Manconi and B. R. Mace, "Modelling wave propagation in two-dimensional structures using finite element analysis," *Journal of Sound and Vibration*, vol. 318, no. 4-5, pp. 884–902, 2008.

[99] M. N. Ichchou, J. Berthaut, and M. Collet, "Multi-mode wave propagation in ribbed plates. part ii: Predictions and comparisons," *International Journal of Solids and Structures*, vol. 45, no. 5, pp. 1196–1216, 2008.

[100] M. N. Ichchou, J. Berthaut, and M. Collet, "Multi-mode wave propagation in ribbed plates: Part i, wavenumber-space characteristics," *International Journal of Solids and Structures*, vol. 45, no. 5, pp. 1179–1195, 2008.

[101] L. Houillon, M. N. Ichchou, and L. Jezequel, "Wave motion in thin-walled structures," *Journal of Sound and Vibration*, vol. 281, no. 3-5, pp. 483–507, 2005.

[102] D. Chronopoulos, M. Ichchou, B. Troclet, and O. Bareille, "Predicting the broadband response of a layered cone-cylinder-cone shell," *Composite Structures*, vol. 107, pp. 149–159, 2014.

[103] Y. Yang, B. R. Mace, and M. J. Kingan, "Vibroacoustic analysis of periodic structures using a wave and finite element method," *Journal of Sound and Vibration*, vol. 457, pp. 333–353, 2019.

[104] Y. C. Chu and S. I. Rokhlin, “Stability of determination of composite moduli from velocity data in planes of symmetry for weak and strong anisotropies,” *The Journal of the Acoustical Society of America*, vol. 95, no. 1, pp. 213–225, 1994.

[105] Y. C. Chu and S. I. Rokhlin, “A method for determination of elastic constants of a unidirectional lamina from ultrasonic bulk velocity measurements on [0/90] cross-ply composites,” *The Journal of the Acoustical Society of America*, vol. 96, no. 1, pp. 342–352, 1994.

[106] S. I. Rokhlin and W. Wang, “Double through-transmission bulk wave method for ultrasonic phase velocity measurement and determination of elastic constants of composite materials,” *The Journal of the Acoustical Society of America*, vol. 91, no. 6, pp. 3303–3312, 1992.

[107] K. Balasubramaniam and N. S. Rao, “Inversion of composite material elastic constants from ultrasonic bulk wave phase velocity data using genetic algorithms,” *Composites Part B: Engineering*, vol. 29, no. 2, pp. 171–180, 1998.

[108] J. H. Tam, Z. C. Ong, Z. Ismail, B. C. Ang, and S. Y. Khoo, “Identification of material properties of composite materials using nondestructive vibrational evaluation approaches: A review,” *Mechanics of Advanced Materials and Structures*, vol. 24, no. 12, pp. 971–986, 2017.

[109] J. Vishnuvardhan, C. V. Krishnamurthy, and K. Balasubramaniam, “Genetic algorithm based reconstruction of the elastic moduli of orthotropic plates using an ultrasonic guided wave single-transmitter-multiple-receiver shm array,” *Smart Materials and Structures*, vol. 16, no. 5, p. 1639, 2007.

[110] A. Marzani and L. De Marchi, “Characterization of the elastic moduli in composite plates via dispersive guided waves data and genetic algorithms,” *Journal of Intelligent Material Systems and Structures*, vol. 24, no. 17, pp. 2135–2147, 2012.

[111] A. A. Eremin, E. V. Glushkov, N. V. Glushkova, and R. Lammering, “Evaluation of effective elastic properties of layered composite fiber-reinforced

plastic plates by piezoelectrically induced guided waves and laser doppler vibrometry," *Composite Structures*, vol. 125, pp. 449–458, 2015.

[112] R. Cui and F. Lanza di Scalea, "On the identification of the elastic properties of composites by ultrasonic guided waves and optimization algorithm," *Composite Structures*, vol. 223, p. 110969, 2019.

[113] A. Treviso, B. Van Genechten, D. Mundo, and M. Tournour, "Damping in composite materials: Properties and models," *Composites Part B: Engineering*, vol. 78, pp. 144–152, 2015.

[114] H. Schiessel, R. Metzler, A. Blumen, and T. F. Nonnenmacher, "Generalized viscoelastic models: their fractional equations with solutions," *Journal of physics A: Mathematical and General*, vol. 28, no. 23, p. 6567, 1995.

[115] X. Tang and X. Yan, "A review on the damping properties of fiber reinforced polymer composites," *Journal of Industrial Textiles*, vol. 49, no. 6, pp. 693–721, 2018.

[116] F. Simonetti and P. Cawley, "On the nature of shear horizontal wave propagation in elastic plates coated with viscoelastic materials," *Proceedings of the Royal Society of London. Series A: Mathematical, Physical and Engineering Sciences*, vol. 460, no. 2048, pp. 2197–2221, 2004.

[117] G. C. Wright, "The dynamic properties of glass and carbon fibre reinforced plastic beams," *Journal of Sound and Vibration*, vol. 21, no. 2, pp. 205–212, 1972.

[118] R. M. Crane and J. W. Gillespie, "Characterization of the vibration damping loss factor of glass and graphite fiber composites," *Composites Science and Technology*, vol. 40, no. 4, pp. 355–375, 1991.

[119] R. D. Adams and D. G. C. Bacon, "Effect of fibre orientation and laminate geometry on the dynamic properties of cfrp," *Journal of Composite Materials*, vol. 7, no. 4, pp. 402–428, 1973.

[120] R. D. Adams and M. R. Maheri, "Dynamic flexural properties of anisotropic fibrous composite beams," *Composites Science and Technology*, vol. 50, no. 4, pp. 497–514, 1994.

[121] R. D. Adams and M. R. Maheri, "Damping in advanced polymer-matrix composites," *Journal of Alloys and Compounds*, vol. 355, no. 1, pp. 126–130, 2003.

[122] J.-M. Berthelot and Y. Sefrani, "Damping analysis of unidirectional glass and kevlar fibre composites," *Composites Science and Technology*, vol. 64, no. 9, pp. 1261–1278, 2004.

[123] S. Wray, J. N. Ashton, and H. El-Sobky, "An investigation of the influence of anisotropy and frequency on damping in short glass fibre reinforced polypropylene," *Composite Structures*, vol. 15, no. 1, pp. 43–60, 1990.

[124] R. G. Ni and R. Adams, "The damping and dynamic moduli of symmetric laminated composite beams-theoretical and experimental results," *Journal of Composite Materials*, vol. 18, no. 2, pp. 104–121, 1984.

[125] J. H. Yim, "A damping analysis of composite laminates using the closed form expression for the basic damping of poisson's ratio," *Composite Structures*, vol. 46, no. 4, pp. 405–411, 1999.

[126] J.-M. Berthelot, M. Assarar, Y. Sefrani, and A. E. Mahi, "Damping analysis of composite materials and structures," *Composite Structures*, vol. 85, no. 3, pp. 189–204, 2008.

[127] M. R. Maheri, "The effect of layup and boundary conditions on the modal damping of frp composite panels," *Journal of Composite Materials*, vol. 45, no. 13, pp. 1411–1422, 2010.

[128] S. J. Hwang and R. F. Gibson, "The effects of three-dimensional states of stress on damping of laminated composites," *Composites Science and Technology*, vol. 41, no. 4, pp. 379–393, 1991.

[129] S. J. Hwang and R. F. Gibson, "Contribution of interlaminar stresses to damping in thick laminated composites under uniaxial extension," *Composite Structures*, vol. 20, no. 1, pp. 29–35, 1992.

[130] J.-L. Tsai and Y.-K. Chi, "Effect of fiber array on damping behaviors of fiber composites," *Composites Part B: Engineering*, vol. 39, no. 7, pp. 1196–1204, 2008.

[131] R. Chandra, S. P. Singh, and K. Gupta, "Micromechanical damping models for fiber-reinforced composites: a comparative study," *Composites Part A: Applied Science and Manufacturing*, vol. 33, no. 6, pp. 787–796, 2002.

[132] A. E. Mahi, M. Assarar, Y. Sefrani, and J.-M. Berthelot, "Damping analysis of orthotropic composite materials and laminates," *Composites Part B: Engineering*, vol. 39, no. 7, pp. 1069–1076, 2008.

[133] H. Guan and R. F. Gibson, "Micromechanical models for damping in woven fabric-reinforced polymer matrix composites," *Journal of Composite Materials*, vol. 35, no. 16, pp. 1417–1434, 2001.

[134] H. Yu and C. Zhou, "Complex stiffness method for damping properties of woven composites," *Journal of Reinforced Plastics and Composites*, vol. 36, no. 19, pp. 1421–1430, 2017.

[135] G. D. Gounaris and N. K. Anifantis, "Structural damping determination by finite element approach," *Computers & Structures*, vol. 73, no. 1, pp. 445–452, 1999.

[136] A. Marzani, E. Viola, I. Bartoli, F. Lanza di Scalea, and P. Rizzo, "A semi-analytical finite element formulation for modeling stress wave propagation in axisymmetric damped waveguides," *Journal of Sound and Vibration*, vol. 318, no. 3, pp. 488–505, 2008.

[137] E. Manconi and B. R. Mace, "Estimation of the loss factor of viscoelastic laminated panels from finite element analysis," *Journal of Sound and Vibration*, vol. 329, no. 19, pp. 3928–3939, 2010.

[138] H. Mei and V. Giurgiutiu, “Guided wave excitation and propagation in damped composite plates,” *Structural Health Monitoring*, vol. 18, no. 3, pp. 690–714, 2018.

[139] C. D. Johnson and D. A. Kienholz, “Finite element prediction of damping in structures with constrained viscoelastic layers,” *AIAA Journal*, vol. 20, no. 9, pp. 1284–1290, 1982.

[140] S. H. Crandall, “The role of damping in vibration theory,” *Journal of Sound and Vibration*, vol. 11, no. 1, pp. 3–18, 1970.

[141] S. H. Crandall, “The hysteretic damping model in vibration theory,” *Proceedings of the Institution of Mechanical Engineers, Part C: Mechanical Engineering Science*, vol. 205, no. 1, pp. 23–28, 1991.

[142] S. J. Hwang and R. F. Gibson, “The use of strain energy-based finite element techniques in the analysis of various aspects of damping of composite materials and structures,” *Journal of Composite Materials*, vol. 26, no. 17, pp. 2585–2605, 1992.

[143] W. Kelvin, “On the theory of viscoelastic fluids,” *Math. A. Phys. Pap*, vol. 3, pp. 27–84, 1875.

[144] W. Voigt, “Ueber innere reibung fester körper, insbesondere der metalle,” *Annalen der Physik*, vol. 283, no. 12, pp. 671–693, 1892.

[145] J. L. Rose, *Ultrasonic Guided Waves in Solid Media*. Cambridge University Press, 2014.

[146] S. Adhikari, “Damping modelling using generalized proportional damping,” *Journal of Sound and Vibration*, vol. 293, no. 1, pp. 156–170, 2006.

[147] M. Gresil and V. Giurgiutiu, “Prediction of attenuated guided waves propagation in carbon fiber composites using rayleigh damping model,” *Journal of Intelligent Material Systems and Structures*, vol. 26, no. 16, pp. 2151–2169, 2015.

[148] E. E. Ungar and E. M. Kerwin, "Loss factors of viscoelastic systems in terms of energy concepts," *The Journal of the Acoustical Society of America*, vol. 34, no. 7, pp. 954–957, 1962.

[149] I. C. Finegan and R. F. Gibson, "Analytical modeling of damping at micromechanical level in polymer composites reinforced with coated fibers," *Composites Science and Technology*, vol. 60, no. 7, pp. 1077–1084, 2000.

[150] V. Cotoni, R. S. Langley, and P. J. Shorter, "A statistical energy analysis subsystem formulation using finite element and periodic structure theory," *Journal of Sound and Vibration*, vol. 318, no. 4-5, pp. 1077–1108, 2008.

[151] C. W. Zhou, J. P. Lainé, M. N. Ichchou, and A. M. Zine, "Multi-scale modelling for two-dimensional periodic structures using a combined mode/wave based approach," *Computers & Structures*, vol. 154, pp. 145–162, 2015.

[152] B. R. Mace and E. Manconi, "Modelling wave propagation in two-dimensional structures using finite element analysis," *Journal of Sound and Vibration*, vol. 318, no. 4-5, pp. 884–902, 2008.

[153] D. Duhamel, B. R. Mace, and M. J. Brennan, "Finite element analysis of the vibrations of waveguides and periodic structures," *Journal of Sound and Vibration*, vol. 294, no. 1-2, pp. 205–220, 2006.

[154] C. Droz, J. P. Lainé, M. N. Ichchou, and G. Inquiete, "A reduced formulation for the free-wave propagation analysis in composite structures," *Composite Structures*, vol. 113, pp. 134–144, 2014.

[155] E. Manconi and B. R. Mace, "Wave characterization of cylindrical and curved panels using a finite element method," *J Acoust Soc Am*, vol. 125, no. 1, pp. 154–63, 2009.

[156] E. Manconi, *Modelling wave propagation in two-dimensional structures using a wave/finite element technique*. Thesis, Universitá di Parma, 2008.

[157] C. Droz, C. Zhou, M. N. Ichchou, and J. P. Lainé, "A hybrid wave-mode formulation for the vibro-acoustic analysis of 2d periodic structures," *Journal of Sound and Vibration*, vol. 363, pp. 285–302, 2016.

[158] R. R. Craig Jr and M. C. Bampton, "Coupling of substructures for dynamic analyses," *AIAA journal*, vol. 6, no. 7, pp. 1313–1319, 1968.

[159] C. Zhou, J. P. Lainé, M. Ichchou, and A. Zine, "Wave finite element method based on reduced model for one-dimensional periodic structures," *International Journal of Applied Mechanics*, vol. 7, no. 02, p. 1550018, 2015.

[160] Y. Fan, M. Collet, M. Ichchou, L. Li, O. Bareille, and Z. Dimitrijevic, "Energy flow prediction in built-up structures through a hybrid finite element/wave and finite element approach," *Mechanical Systems and Signal Processing*, vol. 66, pp. 137–158, 2016.

[161] J. Becker and L. Gaul, "Cms methods for efficient damping prediction for structures with friction," *Proceedings of the IMAC-XXVI, Orlando*, 2008.

[162] W. Sachse and Y. Pao, "On the determination of phase and group velocities of dispersive waves in solids," *Journal of applied Physics*, vol. 49, no. 8, pp. 4320–4327, 1978.

[163] D. Alleyne and P. Cawley, "A two-dimensional fourier transform method for the measurement of propagating multimode signals," *The Journal of the Acoustical Society of America*, vol. 89, no. 3, pp. 1159–1168, 1991.

[164] P. Gomez Garcia and J.-P. Fernandez-Alvarez, "Floquet-bloch theory and its application to the dispersion curves of nonperiodic layered systems," *Mathematical Problems in Engineering*, vol. 2015, 2015.

[165] J. M. Mencik, "On the low- and mid-frequency forced response of elastic structures using wave finite elements with one-dimensional propagation," *Computers & Structures*, vol. 88, no. 11-12, pp. 674–689, 2010.

[166] J. N. Reddy, *Theory and analysis of elastic plates and shells.* CRC press, 2006.

[167] H. Lin, L. P. Brown, and A. C. Long, "Modelling and simulating textile structures using texgen," *Advanced Materials Research*, vol. 331, pp. 44–47, 2011.

[168] H. Lin, X. Zeng, M. Sherburn, A. C. Long, and M. J. Clifford, "Automated geometric modelling of textile structures," *Textile Research Journal*, vol. 82, no. 16, pp. 1689–1702, 2012.

[169] S. D. Green, M. Y. Matveev, A. C. Long, D. Ivanov, and S. R. Hallett, "Mechanical modelling of 3d woven composites considering realistic unit cell geometry," *Composite Structures*, vol. 118, pp. 284–293, 2014.

[170] L. P. Brown and M. Sherburn, "Texgen v3.9.0," Feb. 2017. This software is currently funded by EPSRC Research Software Engineering Fellowship - Software for Textile Modelling and Simulation, EP/N019040/1.

[171] J. J. Crookston, W. Ruijter, A. C. Long, N. A. Warrior, and I. A. Jones, "A comparison of mechanical property prediction techniques using conformal tetrahedra and voxel-based finite element meshes for textile composite unit cells," *Proceedings of finite element modeling of textiles and textile composites*, pp. 26–28, 2007.

[172] K.-S. Lee, D.-S. Han, and S.-K. Kim, "Physical origin and generic control of magnonic band gaps of dipole-exchange spin waves in width-modulated nanostrip waveguides," *Physical Review Letters*, vol. 102, no. 12, p. 127202, 2009.

[173] F. S. Ma, H. S. Lim, V. L. Zhang, S. C. Ng, and M. H. Kuok, "Magnonic band structure investigation of one-dimensional bi-component magnonic crystal waveguides," *Nanoscale Research Letters*, vol. 7, no. 1, p. 498, 2012.

[174] Z. K. Wang, V. L. Zhang, H. S. Lim, S. C. Ng, M. H. Kuok, S. Jain, and A. O. Adeyeye, "Nanostructured magnonic crystals with size-tunable bandgaps," *ACS Nano*, vol. 4, no. 2, pp. 643–648, 2010.

[175] C. Xiaogang, L. W. Taylor, and L.-J. Tsai, "An overview on fabrication of three-dimensional woven textile preforms for composites," *Textile Research Journal*, vol. 81, no. 9, pp. 932–944, 2011.

[176] X. Zeng, L. P. Brown, A. Endruweit, M. Matveev, and A. C. Long, "Geometrical modelling of 3d woven reinforcements for polymer composites:

Prediction of fabric permeability and composite mechanical properties," *Composites Part A: Applied Science and Manufacturing*, vol. 56, pp. 150–160, 2014.

[177] P. K. Mallick, *Fiber-reinforced composites: materials, manufacturing, and design*. CRC press, 2007.

[178] H. Miyagawa, T. Mase, C. Sato, E. Drown, L. T. Drzal, and K. Ikegami, "Comparison of experimental and theoretical transverse elastic modulus of carbon fibers," *Carbon*, vol. 44, no. 10, pp. 2002–2008, 2006.

[179] X. Ji, C. Wang, B. A. P. Francis, E. S. M. Chia, L. Zheng, J. Yang, S. C. Joshi, and Z. Chen, "Mechanical and interfacial properties characterisation of single carbon fibres for composite applications," *Experimental Mechanics*, vol. 55, no. 6, pp. 1057–1065, 2015.

[180] R. Maurin, P. Davies, N. Baral, and C. Baley, "Transverse properties of carbon fibres by nano-indentation and micro-mechanics," *Applied Composite Materials*, vol. 15, no. 2, pp. 61–73, 2008.

[181] J. F. Villeneuve and R. Naslain, "Shear moduli of carbon, si-c-o, si-c-ti-o and alumina single ceramic fibers as assessed by torsion pendulum tests," *Composites Science and Technology*, vol. 49, no. 2, pp. 191–203, 1993.

[182] Q. T. Nguyen, E. Vidal-Salle, P. Boisse, C. H. Park, A. Saouab, J. Breard, and G. Hivet, "Mesoscopic scale analyses of textile composite reinforcement compaction," *Composites Part B: Engineering*, vol. 44, no. 1, pp. 231–241, 2013.

[183] R. D. B. Sevenois, D. Garoz, F. A. Gilabert, S. W. F. Spronk, S. Fonteyn, M. Heyndrickx, L. Pyl, D. Van Hemelrijck, J. Degrieck, and W. Van Paepegem, "Avoiding interpenetrations and the importance of nesting in analytic geometry construction for representative unit cells of woven composite laminates," *Composites Science and Technology*, vol. 136, pp. 119–132, 2016.

[184] N. Naouar, E. Vidal-Salle, J. Schneider, E. Maire, and P. Boisse, "Meso-scale fe analyses of textile composite reinforcement deformation based on x-ray computed tomography," *Composite Structures*, vol. 116, pp. 165–176, 2014.

[185] H. J. Maris, "Enhancement of heat pulses in crystals due to elastic anisotropy," *The Journal of the Acoustical Society of America*, vol. 50, no. 3B, pp. 812–818, 1971.

[186] B. Chapuis, N. Terrien, and D. Royer, "Modeling and experimental investigations of lamb waves focusing in anisotropic plates," *Journal of Physics: Conference Series*, vol. 269, no. 1, p. 012020, 2011.

[187] M. A. Torres-Arredondo, H. Jung, and C.-P. Fritzen, "A study of attenuation and acoustic energy anisotropy of lamb waves in multilayered anisotropic media for ndt and shm applications," 2011.

[188] O. Putkis, R. P. Dalton, and A. J. Croxford, "The anisotropic propagation of ultrasonic guided waves in composite materials and implications for practical applications," *Ultrasonics*, vol. 65, pp. 390–399, 2016.

[189] N. Etaix, A. Leblanc, and M. Fink, "Thickness or phase velocity measurements using the green's function comparison method," *IEEE transactions on ultrasonics, ferroelectrics, and frequency control*, vol. 57, no. 8, pp. 18804–1812, 2010.

[190] T. Druet, *Tomographie passive par ondes guidées pour des applications de contrôle santé intégré*. Thesis, Université de Valenciennes et du Hainaut-Cambresis, 2017.

[191] K. Goldberg Robert, J. Blinzler Brina, and K. Binienda Wieslaw, "Modification of a macromechanical finite element–based model for impact analysis of triaxially braided composites," *Journal of Aerospace Engineering*, vol. 25, no. 3, pp. 383–394, 2012.

[192] D. Chronopoulos, “Design optimization of composite structures operating in acoustic environments,” *Journal of Sound and Vibration*, vol. 355, pp. 322–344, 2015.

[193] D. Chronopoulos, I. Antoniadis, M. Collet, and M. Ichchou, “Enhancement of wave damping within metamaterials having embedded negative stiffness inclusions,” *Wave Motion*, vol. 58, pp. 165–179, 2015.

[194] E. Manconi and S. Sorokin, “On the effect of damping on dispersion curves in plates,” *International Journal of Solids and Structures*, vol. 50, no. 11-12, pp. 1966–1973, 2013.

[195] J. L. du Bois, S. Adhikari, and N. A. J. Lieven, “On the quantification of eigenvalue curve veering: A veering index,” *Journal of Applied Mechanics*, vol. 78, no. 4, p. 041007, 2011.

[196] S. Li, “Boundary conditions for unit cells from periodic microstructures and their implications,” *Composites Science and Technology*, vol. 68, no. 9, pp. 1962–1974, 2008.

[197] S. Li, L. F. C. Jeanmeure, and Q. Pan, “A composite material characterisation tool: Unitcells,” *Journal of Engineering Mathematics*, vol. 95, no. 1, pp. 279–293, 2015.

[198] M. Minus and S. Kumar, “The processing, properties, and structure of carbon fibers,” *Jom*, vol. 57, no. 2, pp. 52–58, 2005.

[199] D. D. L. Chung, *Carbon fiber composites.* Elsevier, 2012.

[200] C. T. Sun and R. S. Vaidya, “Prediction of composite properties from a representative volume element,” *Composites Science and Technology*, vol. 56, no. 2, pp. 171–179, 1996.

[201] I. P. Kumar, S. P. Kushwaha, P. Mohite, and S. Kamle, “Longitudinal shear modulus of single aramid, carbon and glass fibres by torsion pendulum tests,” *World Academy of Science, Engineering and Technology International Journal of Mechanical, Aerospace, Industrial and Mechatronics Engineering*, vol. 8, pp. 1–6, 2014.

[202] C. L. Tsai and I. M. Daniel, "Determination of shear modulus of single fibers," *Experimental Mechanics*, vol. 39, no. 4, pp. 284–286, 1999.

[203] L. Yu, D. Liu, K. Peng, and Y. He, "An improved torsion pendulum based on image processing for single fibers," *Measurement Science and Technology*, vol. 27, no. 7, p. 075601, 2016.

Appendix A

Appendix: chapter 2

A.1 Static virtual testing

A macroscale model is defined by its homogenised mechanical properties. Traditionally, material characterisation refers to material testing as a way to obtain the material properties. The establishment of a unit cell is an alternative for acquiring those properties, even though it does not replace a physical testing completely. This method can be seen as virtual testing of the material. The analyses are conducted on the mesoscale model in order to evaluate the effective material properties of the macroscale model. Some basic assumptions are that the macroscale model is effectively homogeneous (in this case the periodicity of the structure at the mesoscale can justify this assumption) and the stress and strain states imposed to it are uniform [30]. It is important to note that according to the periodic pattern, the boundary conditions are different for an identic unit cell. The periodic boundary condition equations are generated based on the method developed by Li et al. in [29, 196, 197, 30]. The considered periodic pattern is formed by translational symmetries of the unit cell along x- and y-axis.

A.1.1 Displacement boundary conditions for unit cells

The boundary conditions must be given for each pair of faces of the unit cell. The considered textile can be seen as a simple cubic packing of cells as described in [29], only without periodicity along the z-axis in our case. $2b_x$, $2b_y$ and $2b_z$ (see Fig.A.1) give the dimensions of the unit cell in the x, y and z directions respectively. This implies that any point *P'(x',y',z')* in the textile outside the considered unit cell has an image *P(x,y,z)* in the unit cell:

$$(x', y', z') = (x + 2ib_x, y + 2jb_y, z) \tag{A.1}$$

where i and j are the number of unit cells separating P' from P in the x and y directions, respectively.

The relative displacement between P and P' in the mesoscale unit cell (displacement noted as (u, v, w)) must be the same as the relative displacement between those same points in the macroscale unit cell (displacement noted as (U, V, W)) [30], i.e.,

$$\left\{ \begin{matrix} u \\ v \\ w \end{matrix} \right\}\Bigg|_{P'} - \left\{ \begin{matrix} u \\ v \\ w \end{matrix} \right\}\Bigg|_{P} = \left\{ \begin{matrix} U \\ V \\ W \end{matrix} \right\}\Bigg|_{P'} - \left\{ \begin{matrix} U \\ V \\ W \end{matrix} \right\}\Bigg|_{P} = \left\{ \begin{matrix} \Delta U \\ \Delta V \\ \Delta W \end{matrix} \right\} \tag{A.2}$$

The relative displacement field in the macroscale model can be written as [30]:

$$\left\{ \begin{matrix} \Delta U \\ \Delta V \\ \Delta W \end{matrix} \right\} = \begin{bmatrix} \frac{\partial U}{\partial x} & \frac{\partial U}{\partial y} & \frac{\partial U}{\partial z} \\ \frac{\partial V}{\partial x} & \frac{\partial V}{\partial y} & \frac{\partial V}{\partial z} \\ \frac{\partial W}{\partial x} & \frac{\partial W}{\partial y} & \frac{\partial W}{\partial z} \end{bmatrix} \left\{ \begin{matrix} \Delta x \\ \Delta y \\ \Delta z \end{matrix} \right\} \tag{A.3}$$

In order to eliminate rigid body motions, the displacement at an arbitrary point (we choose O whose coordinates are (0,0,0)) are suppressed and the rotations of the x-axis about the y- and z-axis, respectively, and that of the y-axis about the x-axis are constrained at that same point O as follows [29, 196, 197, 30]:

$$\frac{\partial V}{\partial x} = \frac{\partial W}{\partial x} = \frac{\partial W}{\partial y} = 0 \tag{A.4}$$

It is important to clarify that this is not a unique expression for constraining the rigid body rotation, there are multiple ways as presented in [30]. This is, however, the most convenient and thus the one used here. Finally, the relative displacement field becomes

$$\left\{\begin{matrix} u \\ v \\ w \end{matrix}\right\}\Bigg|_{P'} - \left\{\begin{matrix} u \\ v \\ w \end{matrix}\right\}\Bigg|_{P} = \begin{bmatrix} \frac{\partial U}{\partial x} & \frac{\partial U}{\partial y} & \frac{\partial U}{\partial z} \\ 0 & \frac{\partial V}{\partial y} & \frac{\partial V}{\partial z} \\ 0 & 0 & \frac{\partial W}{\partial z} \end{bmatrix} \left\{\begin{matrix} \Delta x \\ \Delta y \\ \Delta z \end{matrix}\right\} = \begin{bmatrix} \epsilon_x^0 & \epsilon_{xy}^0 & \epsilon_{xz}^0 \\ 0 & \epsilon_y^0 & \epsilon_{yz}^0 \\ 0 & 0 & \epsilon_z^0 \end{bmatrix} \left\{\begin{matrix} \Delta x \\ \Delta y \\ \Delta z \end{matrix}\right\} \tag{A.5}$$

$\epsilon_x^0, \epsilon_y^0, \epsilon_z^0, \epsilon_{xy}^0, \epsilon_{yz}^0, \epsilon_{zx}^0$ being the macroscopic strains.

As a result, the faces of the unit cells in this packing configuration are defined by the following translational symmetry transformations: for the parts of the boundary normal to the x-axis (see faces A and B in Fig.A.1), the translation is given as

$$\left\{\begin{matrix} \Delta x \\ \Delta y \\ \Delta z \end{matrix}\right\} = \left\{\begin{matrix} 2b_x \\ 0 \\ 0 \end{matrix}\right\} \tag{A.6}$$

Using Eq.(A.5), the relative displacement boundary conditions is obtained

$$\begin{aligned} \left(u|_{x=b_x} - u|_{x=-b_x}\right) &= 2b_x\epsilon_x^0 \\ \left(v|_{x=b_x} - v|_{x=-b_x}\right) &= 0 \\ \left(w|_{x=b_x} - w|_{x=-b_x}\right) &= 0 \end{aligned} \tag{A.7}$$

Similarly for the pair of faces normal to y-axis (faces C and D),

$$\left\{\begin{matrix} \Delta x \\ \Delta y \\ \Delta z \end{matrix}\right\} = \left\{\begin{matrix} 0 \\ 2b_y \\ 0 \end{matrix}\right\} \tag{A.8}$$

and hence

$$\begin{aligned}
\left(u|_{y=b_y} - u|_{y=-b_y}\right) &= 2b_y\epsilon_{xy}^0 \\
\left(v|_{y=b_y} - v|_{y=-b_y}\right) &= 2b_y\epsilon_{y}^0 \\
\left(w|_{y=b_y} - w|_{y=-b_y}\right) &= 0
\end{aligned} \tag{A.9}$$

Finally, the conditions can be written similarly for the pair of faces normal to z-axis,

$$\begin{aligned}
\left(u|_{z=b_z} - u|_{z=-b_z}\right) &= 2b_z\epsilon_{xz}^0 \\
\left(v|_{z=b_z} - v|_{z=-b_z}\right) &= 2b_z\epsilon_{yz}^0 \\
\left(w|_{z=b_z} - w|_{z=-b_z}\right) &= 2b_z\epsilon_{z}^0
\end{aligned} \tag{A.10}$$

Some redundancies emerge for pairs of edges that are on complementary faces. On faces A and B for example are found respectively edges 1 and 2 which use the same conditions as in Eq.(A.7). However, edges 1 and 3 for example have a special set of boundary conditions. The translation is given by

$$\left\{\begin{array}{c} \Delta x \\ \Delta y \\ \Delta z \end{array}\right\} = \left\{\begin{array}{c} 2b_x \\ 2b_y \\ 0 \end{array}\right\} \tag{A.11}$$

and hence

$$\begin{aligned}
\left(u|_{y=b_y} - u|_{y=-b_y}\right) &= 2b_x\epsilon_{x}^0 + 2b_y\epsilon_{xy}^0 \\
\left(v|_{y=b_y} - v|_{y=-b_y}\right) &= 2b_y\epsilon_{y}^0 \\
\left(w|_{y=b_y} - w|_{y=-b_y}\right) &= 0
\end{aligned} \tag{A.12}$$

It is of utmost importance that the mesh is similar for each pair of faces or edges.

A.1.2 Effective material properties

The macroscopic strains $\epsilon_x^0, \epsilon_y^0, \epsilon_z^0, \epsilon_{xy}^0, \epsilon_{yz}^0$ and ϵ_{zx}^0 appearing in the boundary conditions Eq.(A.7-A.12) are physical entities and are called key DoFs [197], e.g. considered as six individual nodes, each having a single DoF. Six independent load cases $F_x, F_y, F_z, F_{xy}, F_{yz}$ and F_{zx} are applied successively to the key DoFs, these

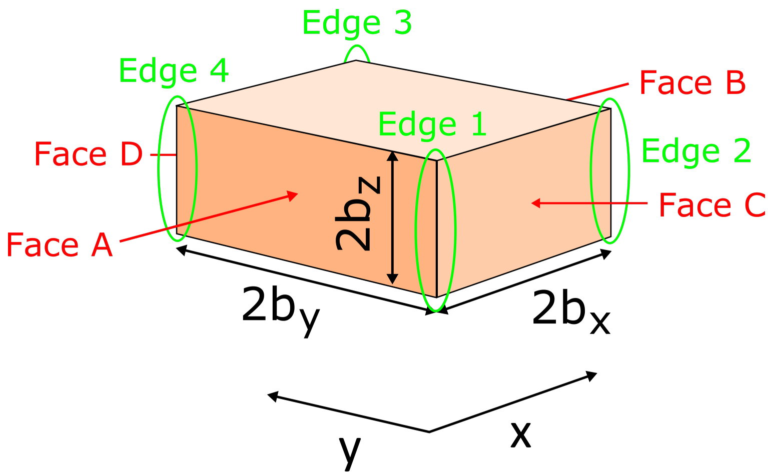

Figure A.1: Unit cell faces and edges numbering.

concentrated forces are related to the macroscopic stresses $\sigma_x^0, \sigma_y^0, \sigma_z^0, \sigma_{yz}^0, \sigma_{zx}^0$ and σ_{xy}^0 and the volume of the unit cell. This is performed in order to build the compliance matrix $[\mathbf{S}]$ of the macroscopic material by using the generalized Hooke's law: $\{\epsilon\} = [\mathbf{S}]\{\sigma\}$ (see Eq.(A.13)).

The material of the textile composite is considered orthotropic in its principal axes once homogenised, which makes the evaluation of the coefficients straightforward. Indeed, an orthotropic material is characterised by nine engineering elastic constants only.

$$\left\{\begin{array}{c}\epsilon_1\\ \epsilon_2\\ \epsilon_3\\ \epsilon_{23}\\ \epsilon_{31}\\ \epsilon_{12}\end{array}\right\} = \begin{bmatrix} \frac{1}{E_1} & -\frac{\nu_{21}}{E_2} & -\frac{\nu_{31}}{E_3} & 0 & 0 & 0\\ -\frac{\nu_{12}}{E_1} & \frac{1}{E_2} & -\frac{\nu_{32}}{E_3} & 0 & 0 & 0\\ -\frac{\nu_{13}}{E_1} & -\frac{\nu_{23}}{E_2} & \frac{1}{E_3} & 0 & 0 & 0\\ 0 & 0 & 0 & \frac{1}{G_{23}} & 0 & 0\\ 0 & 0 & 0 & 0 & \frac{1}{G_{13}} & 0\\ 0 & 0 & 0 & 0 & 0 & \frac{1}{G_{12}} \end{bmatrix} \left\{\begin{array}{c}\sigma_1\\ \sigma_2\\ \sigma_3\\ \sigma_{23}\\ \sigma_{31}\\ \sigma_{12}\end{array}\right\} \tag{A.13}$$

For example, the first equation would be:

$$\frac{1}{E_1}\sigma_1 - \frac{\nu_{21}}{E_2}\sigma_2 - \frac{\nu_{31}}{E_3}\sigma_3 = \epsilon_1 \tag{A.14}$$

which gives in our case and when $F_y = F_z = F_{xy} = F_{yz} = F_{zx} = 0$:

$$\frac{\sigma_x^0}{E_x^0} = \frac{F_x}{V_{tot}E_x^0} = \epsilon_x^0 \tag{A.15}$$

The density for the macroscale model is calculated using the volume ratio of each material in the mesoscale model (weighted average formula), as follows

$$\rho_{macro} = \frac{\rho_f V_f + \rho_m V_m}{V_{tot}} \tag{A.16}$$

Appendix B

Appendix: chapter 3

B.1 Material properties

$\mathbf{C_{11}}$ (GPa)	$\mathbf{C_{12}}$ (GPa)	$\mathbf{C_{22}}$ (GPa)	$\mathbf{C_{13}}$ (GPa)	$\mathbf{C_{23}}$ (GPa)	$\mathbf{C_{33}}$ (GPa)
8.27	2.90	74.40	3.57	3.33	7.27
$\mathbf{C_{44}}$ (GPa)	$\mathbf{C_{55}}$ (GPa)	$\mathbf{C_{66}}$ (GPa)	**density** (kg/m^3)	height (mm)	
2.42	2.14	2.46	1351	0.395	

Table B.1: Stiffness parameters defining the orthotropic material of layer 1 (bottom layer) in Sec.3.1.2, its density and its height.

$\mathbf{C_{11}}$ (GPa)	$\mathbf{C_{12}}$ (GPa)	$\mathbf{C_{22}}$ (GPa)	$\mathbf{C_{13}}$ (GPa)	$\mathbf{C_{23}}$ (GPa)	$\mathbf{C_{33}}$ (GPa)
114.87	2.75	9.59	3.33	3.86	8.64
$\mathbf{C_{44}}$ (GPa)	$\mathbf{C_{55}}$ (GPa)	$\mathbf{C_{66}}$ (GPa)	**density** (kg/m^3)	height (mm)	
2.58	3.96	3.26	1461	0.410	

Table B.2: Stiffness parameters defining the orthotropic material of layer 2 in Sec.3.1.2, its density and its height.

$\mathbf{C_{11}}$ (GPa)	$\mathbf{C_{12}}$ (GPa)	$\mathbf{C_{22}}$ (GPa)	$\mathbf{C_{13}}$ (GPa)	$\mathbf{C_{23}}$ (GPa)	$\mathbf{C_{33}}$ (GPa)
7.71	3.10	85.88	3.59	3.17	7.29
$\mathbf{C_{44}}$ (GPa)	$\mathbf{C_{55}}$ (GPa)	$\mathbf{C_{66}}$ (GPa)	**density** (kg/m^3)	height (mm)	
2.46	2.15	2.43	1352	0.380	

Table B.3: Stiffness parameters defining the orthotropic material of layer 3 in Sec.3.1.2, its density and its height.

$\mathbf{C_{11}}$ (GPa)	$\mathbf{C_{12}}$ (GPa)	$\mathbf{C_{22}}$ (GPa)	$\mathbf{C_{13}}$ (GPa)	$\mathbf{C_{23}}$ (GPa)	$\mathbf{C_{33}}$ (GPa)
115.12	2.78	9.49	3.33	3.86	8.64
$\mathbf{C_{44}}$ (GPa)	$\mathbf{C_{55}}$ (GPa)	$\mathbf{C_{66}}$ (GPa)	**density** (kg/m^3)	height (mm)	
2.56	3.96	3.23	1459	0.410	

Table B.4: Stiffness parameters defining the orthotropic material of layer 4 in Sec.3.1.2, its density and its height.

$\mathbf{C_{11}}$ (GPa)	$\mathbf{C_{12}}$ (GPa)	$\mathbf{C_{22}}$ (GPa)	$\mathbf{C_{13}}$ (GPa)	$\mathbf{C_{23}}$ (GPa)	$\mathbf{C_{33}}$ (GPa)
8.40	3.01	79.74	3.59	3.32	7.33
$\mathbf{C_{44}}$ (GPa)	$\mathbf{C_{55}}$ (GPa)	$\mathbf{C_{66}}$ (GPa)	**density** (kg/m^3)	height (mm)	
2.47	2.18	2.51	1387	0.375	

Table B.5: Stiffness parameters defining the orthotropic material of layer 5 (top layer) in Sec.3.1.2, its density and its height.

$\mathbf{E_1}$ (GPa)	$\mathbf{E_2}$ (GPa)	$\mathbf{E_3}$ (GPa)	ν_{12}	ν_{13}
200	10	10	0.3	0.4
ν_{23}	$\mathbf{G_{12}}$ (GPa)	$\mathbf{G_{13}}$ (GPa)	$\mathbf{G_{23}}$ (GPa)	**density** (kg/m^3)
0.4	5	5	5	4600

Table B.6: Elastic properties of the yarn material used in Sec.3.3.

E (GPa)	ν	**density** (kg/m^3)
3	0.2	1600

Table B.7: Elastic properties of the matrix material used in Sec.3.3.

B.2 Texgen interface

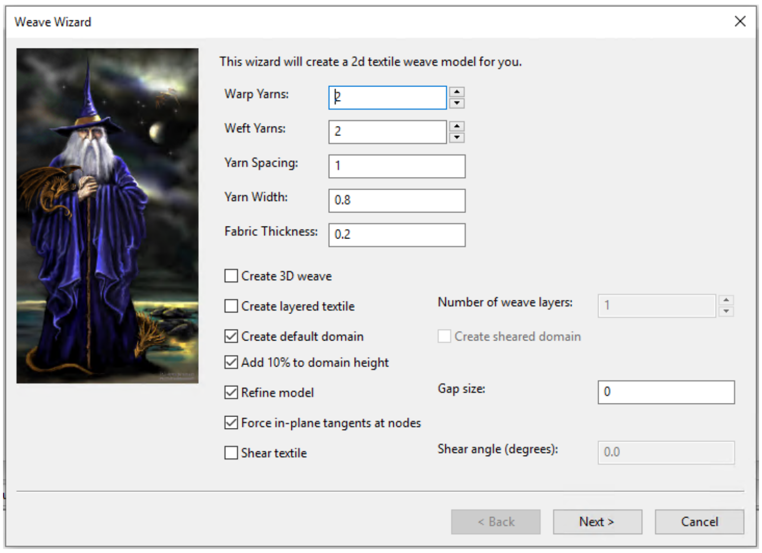

Figure B.1: 2D textile weave properties.

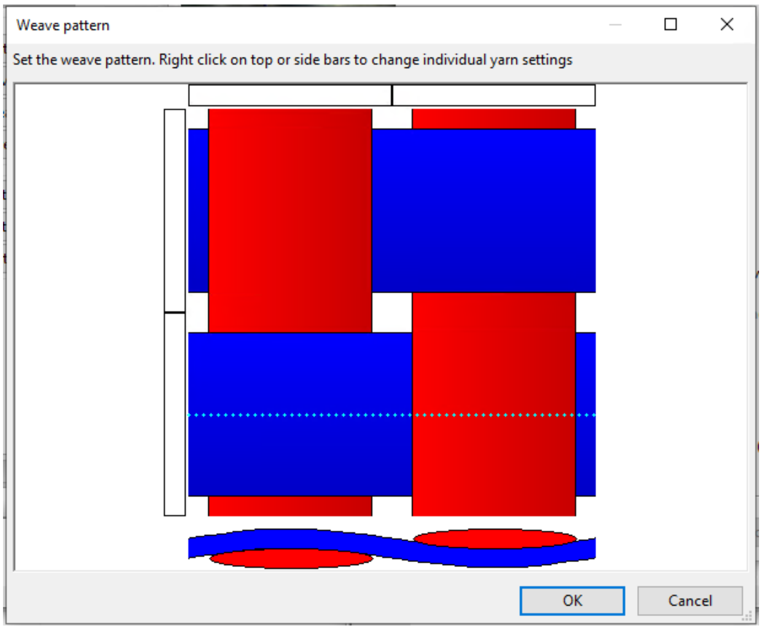

Figure B.2: 2D textile weave pattern.

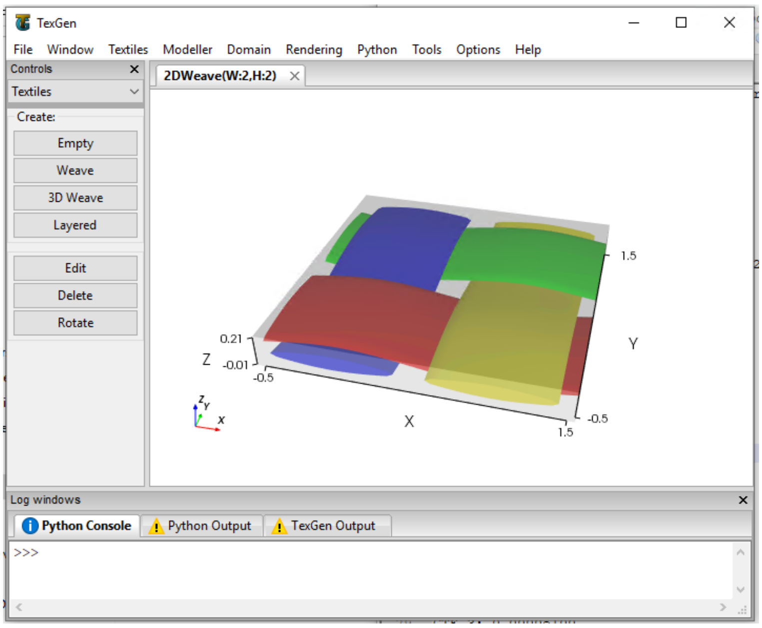

Figure B.3: 2D textile weave model.

B.3 Mesh convergence study

B.3.1 Convergence study: linear tetrahedral mesh

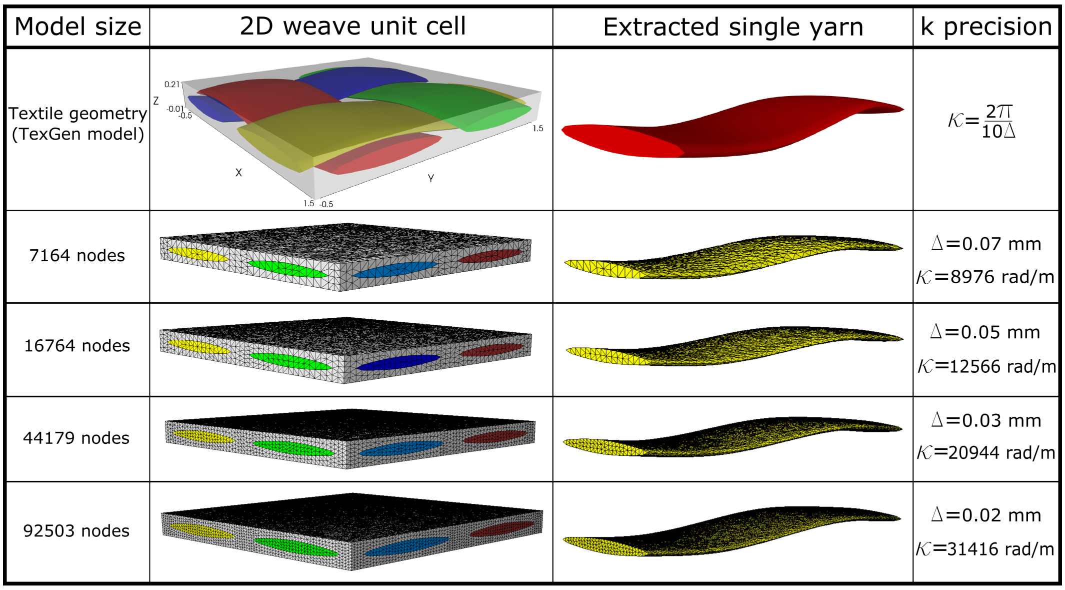

Figure B.4: Linear tetrahedral discretisations of the 2D plain woven model with different degrees of mesh refinement.

Model size (nodes)	$\mathbf{E_1}$ (GPa)	$\mathbf{E_2}$ (GPa)	$\mathbf{E_3}$ (GPa)	ν_{12}	ν_{13}
7164	48.5	48.5	5.71	0.148	0.370
	ν_{23}	$\mathbf{G_{12}}$ (GPa)	$\mathbf{G_{13}}$ (GPa)	$\mathbf{G_{23}}$ (GPa)	
	0.370	2.93	2.31	2.31	
16764	$\mathbf{E_1}$ (GPa)	$\mathbf{E_2}$ (GPa)	$\mathbf{E_3}$ (GPa)	ν_{12}	ν_{13}
	48.6	48.6	5.72	0.150	0.370
	ν_{23}	$\mathbf{G_{12}}$ (GPa)	$\mathbf{G_{13}}$ (GPa)	$\mathbf{G_{23}}$ (GPa)	
	0.370	2.94	2.31	2.31	
44179	$\mathbf{E_1}$ (GPa)	$\mathbf{E_2}$ (GPa)	$\mathbf{E_3}$ (GPa)	ν_{12}	ν_{13}
	48.6	48.6	5.72	0.152	0.370
	ν_{23}	$\mathbf{G_{12}}$ (GPa)	$\mathbf{G_{13}}$ (GPa)	$\mathbf{G_{23}}$ (GPa)	
	0.370	2.93	2.30	2.30	
92503	$\mathbf{E_1}$ (GPa)	$\mathbf{E_2}$ (GPa)	$\mathbf{E_3}$ (GPa)	ν_{12}	ν_{13}
	48.6	48.6	5.72	0.152	0.370
	ν_{23}	$\mathbf{G_{12}}$ (GPa)	$\mathbf{G_{13}}$ (GPa)	$\mathbf{G_{23}}$ (GPa)	
	0.370	2.93	2.30	2.30	

Table B.8: Effective elastic properties of the different meshes. Used for the static convergence study in Sec.3.3.1

B.3.2 Convergence study: quadratic tetrahedral mesh

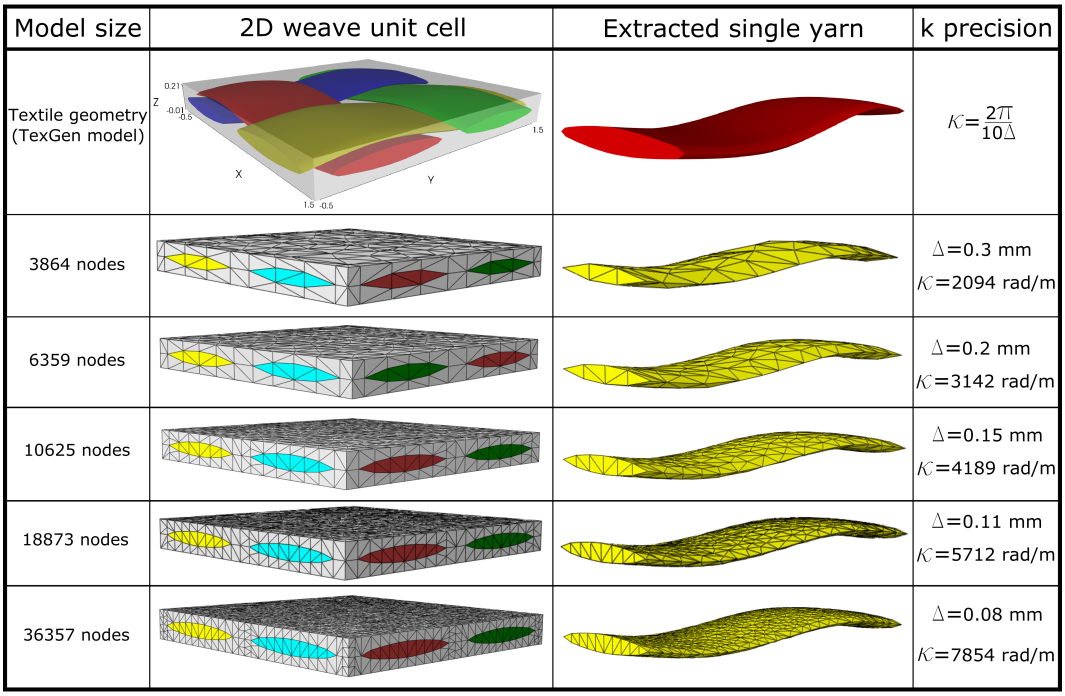

Figure B.5: Quadratic tetrahedral discretisations of the 2D plain woven model with different degrees of mesh refinement.

Model size (nodes)	$\mathbf{E_1}$ (GPa)	$\mathbf{E_2}$ (GPa)	$\mathbf{E_3}$ (GPa)	ν_{12}	ν_{13}
3864	39.2	38.7	5.31	0.109	0.370
	ν_{23}	$\mathbf{G_{12}}$ (GPa)	$\mathbf{G_{13}}$ (GPa)	$\mathbf{G_{23}}$ (GPa)	
	0.360	7.62	2.19	2.18	
6359	$\mathbf{E_1}$ (GPa)	$\mathbf{E_2}$ (GPa)	$\mathbf{E_3}$ (GPa)	ν_{12}	ν_{13}
	42.8	42.1	5.61	0.114	0.319
	ν_{23}	$\mathbf{G_{12}}$ (GPa)	$\mathbf{G_{13}}$ (GPa)	$\mathbf{G_{23}}$ (GPa)	
	0.312	8.77	2.30	2.30	
10625	$\mathbf{E_1}$ (GPa)	$\mathbf{E_2}$ (GPa)	$\mathbf{E_3}$ (GPa)	ν_{12}	ν_{13}
	43.9	45.1	5.83	0.114	0.313
	ν_{23}	$\mathbf{G_{12}}$ (GPa)	$\mathbf{G_{13}}$ (GPa)	$\mathbf{G_{23}}$ (GPa)	
	0.318	9.36	2.41	2.41	
18873	$\mathbf{E_1}$ (GPa)	$\mathbf{E_2}$ (GPa)	$\mathbf{E_3}$ (GPa)	ν_{12}	ν_{13}
	45.7	46.4	5.89	0.118	0.321
	ν_{23}	$\mathbf{G_{12}}$ (GPa)	$\mathbf{G_{13}}$ (GPa)	$\mathbf{G_{23}}$ (GPa)	
	0.325	9.03	2.45	2.45	
36357	$\mathbf{E_1}$ (GPa)	$\mathbf{E_2}$ (GPa)	$\mathbf{E_3}$ (GPa)	ν_{12}	ν_{13}
	46.3	48.0	5.89	0.117	0.324
	ν_{23}	$\mathbf{G_{12}}$ (GPa)	$\mathbf{G_{13}}$ (GPa)	$\mathbf{G_{23}}$ (GPa)	
	0.329	10.5	2.45	2.44	

Table B.9: Effective elastic properties of the different meshes. Used for the static convergence study in Sec.3.3.1

B.3.3 Convergence study: linear hexahedral mesh

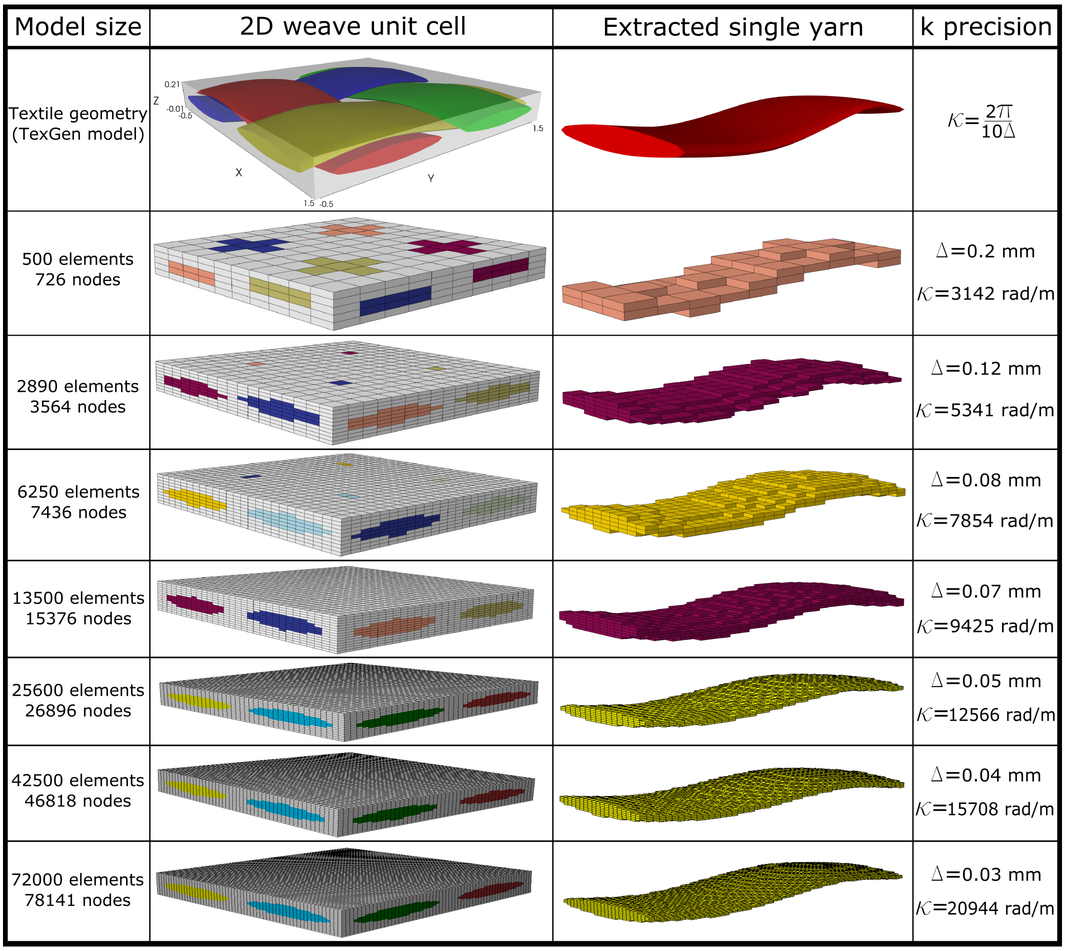

Figure B.6: Linear hexahedral discretisations of the 2D plain woven model with different degrees of mesh refinement.

Model size (nodes)	$\mathbf{E_1}$ (GPa)	$\mathbf{E_2}$ (GPa)	$\mathbf{E_3}$ (GPa)	ν_{12}	ν_{13}
726	37.3	37.3	6.05	0.136	0.362
	ν_{23}	$\mathbf{G_{12}}$ (GPa)	$\mathbf{G_{13}}$ (GPa)	$\mathbf{G_{23}}$ (GPa)	V_{yarn}
	0.362	2.54	2.43	2.43	0.448
3564	$\mathbf{E_1}$ (GPa)	$\mathbf{E_2}$ (GPa)	$\mathbf{E_3}$ (GPa)	ν_{12}	ν_{13}
	45.9	45.9	5.89	0.140	0.361
	ν_{23}	$\mathbf{G_{12}}$ (GPa)	$\mathbf{G_{13}}$ (GPa)	$\mathbf{G_{23}}$ (GPa)	V_{yarn}
	0.361	2.93	2.37	2.37	0.528
7436	$\mathbf{E_1}$ (GPa)	$\mathbf{E_2}$ (GPa)	$\mathbf{E_3}$ (GPa)	ν_{12}	ν_{13}
	46.1	46.1	5.84	0.138	0.358
	ν_{23}	$\mathbf{G_{12}}$ (GPa)	$\mathbf{G_{13}}$ (GPa)	$\mathbf{G_{23}}$ (GPa)	V_{yarn}
	0.358	2.94	2.34	2.34	0.533
15376	$\mathbf{E_1}$ (GPa)	$\mathbf{E_2}$ (GPa)	$\mathbf{E_3}$ (GPa)	ν_{12}	ν_{13}
	46.0	46.0	5.77	0.146	0.363
	ν_{23}	$\mathbf{G_{12}}$ (GPa)	$\mathbf{G_{13}}$ (GPa)	$\mathbf{G_{23}}$ (GPa)	V_{yarn}
	0.363	2.85	2.31	2.31	0.521
26896	$\mathbf{E_1}$ (GPa)	$\mathbf{E_2}$ (GPa)	$\mathbf{E_3}$ (GPa)	ν_{12}	ν_{13}
	47.6	47.6	5.84	0.143	0.365
	ν_{23}	$\mathbf{G_{12}}$ (GPa)	$\mathbf{G_{13}}$ (GPa)	$\mathbf{G_{23}}$ (GPa)	V_{yarn}
	0.365	2.96	2.35	2.35	0.541
46818	$\mathbf{E_1}$ (GPa)	$\mathbf{E_2}$ (GPa)	$\mathbf{E_3}$ (GPa)	ν_{12}	ν_{13}
	46.8	46.8	5.79	0.145	0.363
	ν_{23}	$\mathbf{G_{12}}$ (GPa)	$\mathbf{G_{13}}$ (GPa)	$\mathbf{G_{23}}$ (GPa)	V_{yarn}
	0.363	2.90	2.32	2.32	0.532
78141	$\mathbf{E_1}$ (GPa)	$\mathbf{E_2}$ (GPa)	$\mathbf{E_3}$ (GPa)	ν_{12}	ν_{13}
	47.4	47.4	5.80	0.146	0.365
	ν_{23}	$\mathbf{G_{12}}$ (GPa)	$\mathbf{G_{13}}$ (GPa)	$\mathbf{G_{23}}$ (GPa)	V_{yarn}
	0.365	2.94	2.33	2.33	0.537

Table B.10: Effective elastic properties of the different meshes. Used for the static convergence study, before correction of the inaccurate yarn volume fraction (V_{yarn}) in Sec.3.3.1.

B.3.4 Models computation time

C3D4		**C3D10**		**C3D8**	
Nodes	Time	Nodes	Time	Nodes	Time
		726	2min 1CPU		
		3564	7 min 1CPU	3864	10 min 1CPU
7164	19 min 1CPU	7436	20 min 1CPU	6359	25 min 1CPU
16764	1h44 1CPU	15376	1h40 1CPU	10625	30 min 6CPU
44179	16h 1CPU	26896	4h50 6CPU	18873	1h 6CPU
92503	60h 1CPU	46818	8h50 6CPU	36357	3h45 6CPU
		78141	29h15 6CPU		

Table B.11: Computation times for the different models.

B.4 3D woven composite models

SIZE	3D weave unit cell	Extracted single yarn	k precision
TexGen model	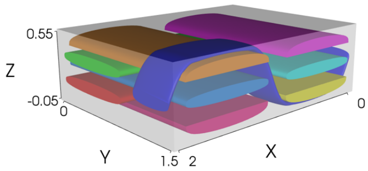	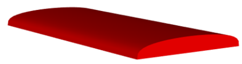	
15625 elements	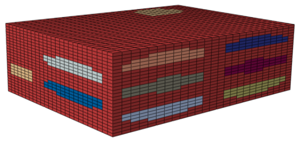	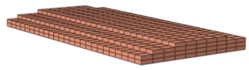	Δ = 0.00008 m $k = \frac{2\pi}{10\Delta}$ = 7854 rad/m

Figure B.7: Linear hexahedral voxel discretisation of the 3D woven model.

Unit cell Y X	Material homogenised properties
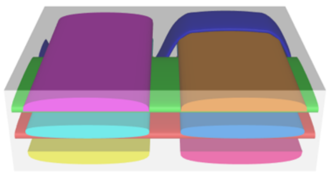	C_{11}=35.36, C_{12}=2.34, C_{22}=70.35, C_{13}=1.96, C_{23}=2.102, C_{33}=5.65, C_{44}=2.74, C_{55}=2.24, C_{66}=2.53 (in GPa) and ρ=3104 kg/m^3

Figure B.8: Elastic moduli for the static macroscale model of the 3D woven composite. Homogenisation method presented in Fig.3.28.

Layers Y X	Material homogenised properties
1 	C_{11}=6.65, C_{12}=2.01, C_{22}=94.54, C_{13}=1.61, C_{23}=2.22, C_{33}=5.75, C_{44}=2.24, C_{55}=2.09, C_{66}=2.53 (in GPa) and ρ=3065 kg/m^3
2 	C_{11}=94.26, C_{12}=1.84, C_{22}=5.31, C_{13}=2.64, C_{23}=1.66, C_{33}=6.72, C_{44}=1.99, C_{55}=2.82, C_{66}=2.04 (in GPa) and ρ=3005 kg/m^3
3 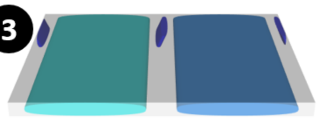	C_{11}=7.55, C_{12}=3.04, C_{22}=144.08, C_{13}=2.66, C_{23}=3.93, C_{33}=8.91, C_{44}=3.70, C_{55}=2.86, C_{66}=3.04 (in GPa) and ρ=3750 kg/m^3
4 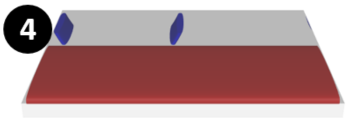	Same as material 2.
5 	Same as material 1.

Figure B.9: Elastic moduli for the static macroscale per layer model of the 3D woven composite. Homogenisation method presented in Fig.3.28.

Appendix C

Appendix: chapter 4

C.1 Material properties

C.1.1 Material properties datasheets

MATERIAL 1	**Supplier**	**Product ref**	**Filament count**	**Tensile Modulus** (GPa)	**Density** (g/cm^3)
Warp tows	Tairylan	TC35-12K	2 x 12K	246	1.801
Weft tows	Tairylan	TC35-12K	12K	246	1.801
Binder tows	Tairylan	TC33-6K	6K	230	1.798
Resin	Easy Composites	IN2		3.35	1.10
MATERIAL 2					
Warp tows	Tairylan	TC35-12K	4 x 12K	246	1.801
Weft tows	Tairylan	TC35-12K	12K	246	1.801
Warp interwoven tows	Tairylan	TC33-6K	6K	230	1.798
Binder tows	Tairylan	TC33-6K	6K	230	1.798
Resin	Gurit	Prime 20LV		3.5	1.144
MATERIAL 3					
Warp tows	Teijin	HTS40	12K	240	1.77
Weft tows	Teijin	HTA40	2 x 6K	240	1.77
Binder tows	Teijin	HTA40	1K	240	1.77
Resin	Easy Composites	IN2		3.35	1.10

Table C.1: Mechanical properties from the datasheets provided by the fibers manufacturers and resin providers.

C.1.2 Mechanical properties in the literature

Lit ref	**Product ref**	E_1	$E_{2,3}$	$G_{12,13}$	$\nu_{12,13}$	ν_{23}
[15]	Toray T300	230	15	13	0.24	0.24
[180]	Toray M40	294	15			
[180]	Toray M60	277	14			
[180]	Mitsubishi Pitch KL637	640	10.7			
[198]		200-500	10-15			
[31]		303	15.2	9.7	0.2	0.2
[199]	T300	230		17		
[199]	T400	226		21.4		
[199]	AS	215		21		
[199]	M30	290		17		
[199]	M40	400		15.8		
[199]	M46	450		14.8		
[199]	T800H	290		17		
[199]	M-40J	390		17		
[199]	M-46J	450		17		
[169]		238	13	13	0.2	0.2
[200]	AS4	235	14	28	0.2	0.25
[181]	T300	231		16		
[201]				18.5		
[202]				10.1		
[14]		227.53	16.6	24.8	0.2	0.25
[203]	T300			15.8		
[15]	Resin epoxy	3.5	3.5			0.35
[31]	Resin epoxy	3.31	3.31			0.35

Table C.2: Fiber and resin mechanical properties obtained from the literature.

C.1.3 Mechanical properties of the yarns

	Yarn	V_f^{yarn}	E_1	$E_{2,3}$	$G_{12,13}$	G_{23}	$\nu_{12,13}$	ν_{23}	**density**
Yarn - Mat1	Warp	0.643	159	7.76	4.83	3.40	0.247	0.434	1.55
	Weft	0.421	105	5.79	2.72	2.33	0.281	0.481	1.39
	Binder	0.610	141	7.32	4.29	3.20	0.253	0.446	1.53
Yarn - Mat2	Warp	0.705	173	8.84	6.27	3.78	0.239	0.405	1.61
	Warp tows	0.364	85.1	5.62	2.50	2.17	0.291	0.485	1.38
	Weft	0.683	169	8.52	5.76	3.68	0.242	0.415	1.59
	Weft compressed	1.00	246	15.0	18.0	6.00	0.200	0.250	1.80
	Binder	0.797	182	10.8	10.9	4.30	0.225	0.340	1.67
Yarn - Mat3	Warp	0.705	169	8.84	6.27	3.78	0.239	0.405	1.57
	Weft	0.635	153	7.84	4.81	3.41	0.249	0.435	1.53
	Binder	1.00	240	15.0	18.0	6.00	0.200	0.250	1.77

Table C.3: Engineering constants for the yarns of the mesoscale model.

Appendix D

Appendix: chapter 6

D.1 Damping models

D.1.1 Damping in the WFE/CMS model

Damping is introduced as an imaginary term in the stiffness matrix

$$\mathbf{K} = \mathbf{K}' + \mathrm{i}\mathbf{K}'', \tag{D.1}$$

and

$$\mathbf{K}'' = \eta_{yarn}\mathbf{K}'_{yarn} + \eta_{mat}\mathbf{K}'_{mat}, \tag{D.2}$$

so

$$\mathbf{K} = \mathbf{K}' + \mathrm{i}(\eta_{yarn}\mathbf{K}'_{yarn} + \eta_{mat}\mathbf{K}'_{mat}), \tag{D.3}$$

which we write for simplicity as

$$\mathbf{K} = \mathbf{K}' + \mathrm{i}\eta\mathbf{K}'. \tag{D.4}$$

Introducing Eq.(D.4) in the equation of motion gives

$$\left[\mathbf{K}' + \mathrm{i}\eta\mathbf{K}' - \omega^2\mathbf{M}\right]\mathbf{q} = \mathbf{f}. \tag{D.5}$$

D.1.2 Damping in the transient FEA

Using Rayleigh's damping model:

$$\mathbf{C} = \alpha\mathbf{M} + \beta\mathbf{K}, \tag{D.6}$$

and choosing $\alpha = 0$ and $\beta = \frac{\eta}{\omega}$, one obtains

$$\mathbf{C} = \frac{\eta}{\omega}\mathbf{K}. \tag{D.7}$$

Introducing Eq.(D.7) in the equation of motion gives

$$\left[\mathbf{K} + \mathrm{i}\eta\frac{\omega}{\omega}\mathbf{K} - \omega^2\mathbf{M}\right]\mathbf{q} = \mathbf{f} \tag{D.8}$$

and finally

$$\left[\mathbf{K} + \mathrm{i}\eta\mathbf{K} - \omega^2\mathbf{M}\right]\mathbf{q} = \mathbf{f}. \tag{D.9}$$

D.2 Material properties

$\mathbf{C_{11}}$ (GPa)	$\mathbf{C_{12}}$ (GPa)	$\mathbf{C_{22}}$ (GPa)	$\mathbf{C_{13}}$ (GPa)	$\mathbf{C_{23}}$ (GPa)	$\mathbf{C_{33}}$ (GPa)
80.7	12.9	18.7	3.6	5.1	1.5
$\mathbf{C_{44}}$ (GPa)	$\mathbf{C_{55}}$ (GPa)	$\mathbf{C_{66}}$ (GPa)	**density** (kg/m^3)	η_x (%)	η_y (%)
3.0	4.9	5.4	3212	0.118	0.62

Table D.1: Nine independent elastic stiffness parameters defining orthotropic elasticity of the material in Sec.6.2, its density and damping properties.

$\mathbf{E_1}$ (GPa)	$\mathbf{E_2}$ (GPa)	$\mathbf{E_3}$ (GPa)	ν_{12}	ν_{13}
200	10	10	0.3	0.4
ν_{23}	$\mathbf{G_{12}}$ (GPa)	$\mathbf{G_{12}}$ (GPa)	$\mathbf{G_{23}}$ (GPa)	**density** (kg/m^3)
0.4	5	5	5	4600

Table D.2: Elastic properties of the yarn material used in Sec.6.3-6.5.

E (GPa)	ν	**density** (kg/m^3)
3	0.2	1600

Table D.3: Elastic properties of the matrix material used in Sec.6.3-6.5.

D.3 Adjusted β coefficient

D.3.1 Macroscale damping modelling of a composite laminate

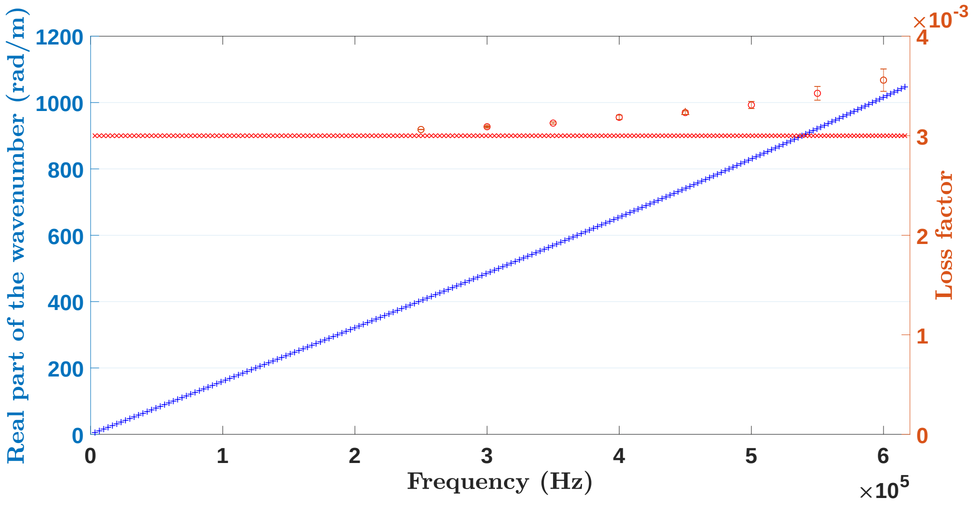

Figure D.1: Loss factor in a two layers laminate beam, function of the frequency, propagating in the x direction, associated to the pressure mode. The loss factor of both layers is of $\eta = 0.003$. (+) the dispersion curve, ($\times$) the loss factor computed with the methodology introduced in this chapter, (o) the loss factor computed from the transient FEA.

Frequency (kHz)	$\beta_{\eta=0.003}$	Relative difference (%)
250	1.91E-09	2.10
300	1.59E-09	2.27
350	1.36E-09	4.3
400	1.19E-09	6.33
450	1.06E-09	7.77
500	9.55E-10	9.33
550	8.68E-10	14.20
600	7.96E-10	19.07

Table D.4: β coefficients computed using Eq.(6.6) and the loss factor relative difference.

In Sec.6.2.2, a transient analysis was performed for a two layers laminate beam with a unique loss factor of $\eta = 0.003$. Using an identic loss factor for every constituents of the material should produce an equal and constant loss factor for the whole material, independently of the frequency. However, a difference is observed in the transient FEA when using the β coefficients displayed in Table

D.4 (see Fig.D.1), which the model formulation should prevent. The results are used to adjust the determination of the β coefficient for later computations as displayed in Table D.5.

Frequency (kHz)	$\beta_{\eta=0.003}$	$\beta_{\eta=0.00118}$	$\beta_{\eta=0.0062}$
250	1.87E-09	7.36E-10	3.87E-09
300	1.56E-09	6.12E-10	3.22E-09
350	1.31E-09	5.14E-10	2.70E-09
400	1.12E-09	4.42E-10	2.32E-09
450	9.85E-10	3.87E-10	2.03E-09
500	8.83E-10	3.47E-10	1.82E-09
550	7.60E-10	2.99E-10	1.57E-09
600	6.68E-10	2.63E-10	1.38E-09

Table D.5: β coefficients adjusted from Table D.4 and Fig.D.1.

D.3.2 Mesoscale damping modelling of a triaxial braided composite

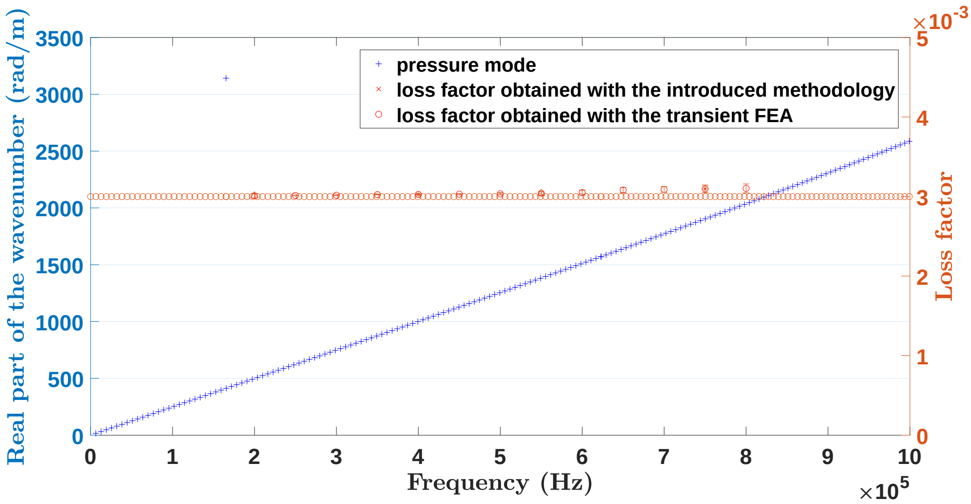

Figure D.2: Loss factor in a triaxial braided composite beam, function of the frequency, propagating in the x direction, associated to the pressure mode. The loss factor of both constituent materials (yarn and matrix) is of $\eta = 0.003$. (+) the dispersion curve, ($\times$) the loss factor computed with the methodology introduced in this chapter, (o) the loss factor computed from the transient FEA.

In Sec.6.5, a transient analysis was performed for a triaxial braided composite beam with a unique loss factor of $\eta = 0.003$ for each constituents of the material. This should produce an equal and constant loss factor for the whole material,

Frequency (kHz)	$\beta_{\eta=0.003}$	Relative difference (%)
200	2.39E-09	0.30
250	1.91E-09	0.43
300	1.59E-09	0.57
350	1.36E-09	0.80
400	1.19E-09	0.93
450	1.06E-09	1.43
500	9.55E-10	1.83
550	8.68E-10	2.23
600	7.96E-10	2.87
650	7.35E-10	3.27
700	6.82E-10	3.97
750	6.37E-10	5.67
800	5.97E-10	6.63

Table D.6: β coefficients computed using Eq.(6.6) and the loss factor relative difference.

independently of the frequency. However, a difference is observed in the transient FEA when using the β coefficients displayed in Table D.6 (see Fig.D.2), which the model formulation should prevent. The results are used to adjust the determination of the β coefficient for later computations as displayed in Table D.7.

Frequency (kHz)	$\beta_{\eta=0.003}$	$\beta_{\eta=0.02}$	$\beta_{\eta=0.0001}$
200	2.38E-09	1.59E-08	7.93E-11
250	1.90E-09	1.27E-08	6.34E-11
300	1.58E-09	1.06E-08	5.28E-11
350	1.35E-09	9.02E-09	4.51E-11
400	1.18E-09	7.88E-09	3.94E-11
450	1.05E-09	6.97E-09	3.49E-11
500	9.38E-10	6.25E-09	3.13E-11
550	8.49E-10	5.66E-09	2.83E-11
600	7.74E-10	5.16E-09	2.58E-11
650	7.11E-10	4.74E-09	2.37E-11
700	6.56E-10	4.37E-09	2.19E-11
750	6.02E-10	4.02E-09	2.01E-11
800	5.60E-10	3.73E-09	1.87E-11

Table D.7: β coefficients adjusted from Table D.6 and Fig.D.2.